Journal of Powder Materials

Volume 32, Number 4 August 2025

Research Articles

277 Laser Processing of an $Al_{0.1}CoCrFeNi$ High Entropy Alloy + Cu Composite Powders via Laser Powder Bed Fusion
Kwangtae Son, Ji-Woon Lee, Soon-Jik Hong, Somayeh Pasebani

288 Cost-effective Fabrication of Near β-Ti Alloy via L-PBF: Process Optimization of In-Situ Alloying Ti-3Fe
Sehun Kim, Ukju Gim, Taehu Kang, Jongik Lee, Sanghee Jeong, Jimin Han, Bin Lee

299 Fabrication and Pore Characteristics of Metal Powder Filters with a Cross-Sealed Honeycomb Shape Using Material Extrusion Additive Manufacturing
Minji Kim, Min-Jeong Lee, Su-Jin Yun, Poong-Yeon Kim, Hyeon Ju Kim, Juyong Kim, Jung Woo Lee, Jung-Yeul Yun

309 Evaluation of Mechanical Properties of Pure Ni Coatings on a Type 316H Stainless Steel Substrate via High-Velocity Oxy-fuel and Directed Energy Deposition Processes
Won Chan Lee, Seung Ju Nam, Ji-Hyun Yoon, Jeoung Han Kim

315 Enhanced Compressive Strength of Fired Iron Ore Pellets: Effects of Blending Fine and Coarse Particle Concentrates
Ngo Quoc Dung, Tran Xuan Hai, Nguyen Minh Thuyet, Nguyen Quang Tung, Arvind Barsiwal, Nguyen Hoang Viet

330 The Recycling Process and Powderization Technology of Stellite 6 Scrap: A Thermodynamic and Heat Transfer Analysis
YongKwan Lee, Hyun-chul Kim, Myungsuk Kim, Soong Ju Oh, Kyoungtae Park, JaeJin Sim

344 Influence of Powder Particle Size on the Microstructure of UO_2 Fuel Pellets with High Gd_2O_3 Content
Ji-Hwan Lee, Jae Ho Yang, Ji-Hae Yoon, Dong-Joo Kim, Dong-wook Shin, Dong Seok Kim

354 Effect of Fe and Cr on ω Phase Formation in Metastable β-Ti Alloy
Sun-Young Park, Young-Bum Chun

361 CODE OF ETHICS

367 INSTRUCTIONS FOR AUTHORS

kpmi
Korean Powder Metallurgy & Materials Institute

Journal of Powder Materials
VOL. 32 NO. 4 / AUGUST 2025
Page 277-374
kpmi

pISSN 2799-8525 | eISSN 2799-8681
VOL. 32 NO. 4 / AUGUST 2025

Journal of Powder Materials

한국분말재료학회지

https://powdermat.org

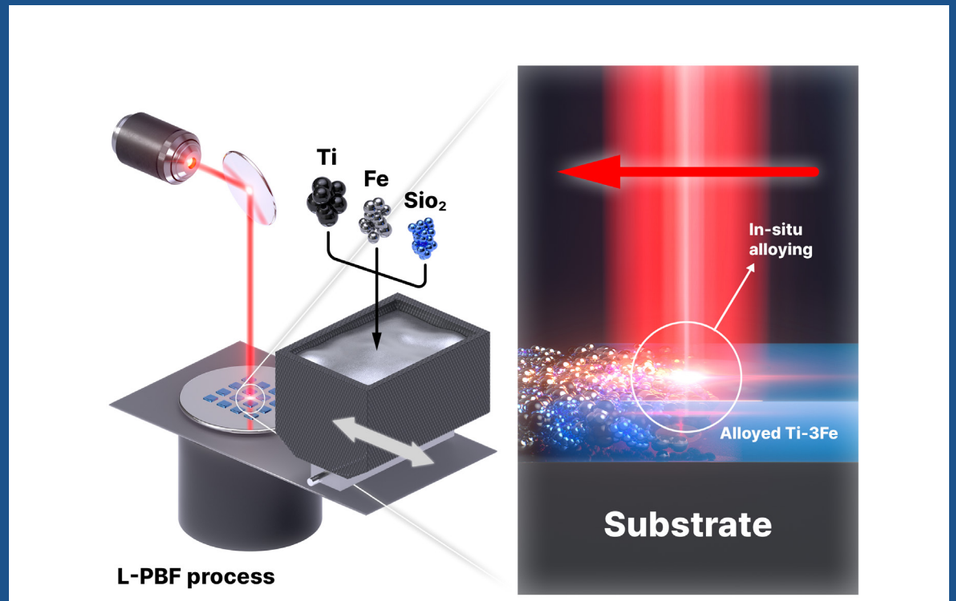

S. Kim et al, 32(4) p. 288

kpmi Korean Powder Metallurgy & Materials Institute

Journal of
Powder Materials

ISSN 2799-8525 (Print)
ISSN 2799-8681 (Online)

VOL. 32 NO. 4 (Total 171) / August 2025

Aims and Scope
The Journal of Powder Materials (JPM) is dedicated to sharing cutting-edge research and advanced technologies in the fields of powder metallurgy and powder-related materials science and engineering. By serving as a vital platform for both researchers and industry professionals worldwide, JPM aims to bridge the gap between fundamental research and practical applications. The journal offers valuable insights for material scientists, technologists, engineers, designers, and manufacturers.

JPM covers the entire spectrum of powder materials and processing technologies, including but not limited to: powder production (including precursor materials), milling, granulation, cold and hot compaction, sintering, cold and hot isostatic pressing, pulsed and other assisted consolidation, additive manufacturing, injection molding, and powder-based coating technologies. The journal also encompasses research on characterization, testing, quality assurance, and diverse industrial applications. Furthermore, *JPM* actively promotes research incorporating data-driven methodologies, including computational materials science, machine learning, and artificial intelligence (AI), which are increasingly shaping the future of powder materials research and process optimization.

ISO abbreviation of journal title
✓ Topic

Powder Materials
- Fe-based powders
- Non-ferrous powders
- Ceramic powders
- Particulate Composite
- Tool/Cemented Carbides
- Porous powders
- Electric/Electronic powders
- Bio materials
- Magnetic powders
- Energy conversion/storage powders
- Multi-functional powders
- Organic/inorganic powders

Powder Technology
- Powder synthesis
- Powder characterization/analysis
- Powder compaction
- Powder pretreatment
- Sintering
- Densification process
- PIM
- Post-treatment
- Novel powder technology
- Nanostructured powders
- Simulation of powder/process
- Powder test
- Powder business/industry

The official title of the journal is 'Journal of Powder Materials' and the abbreviated title is 'J. Powder Mater.'.

Year of launching (history)
Journal of Powder Materials was launched in 1993.

The frequency of publication
Journal of Powder Materials is published bi-monthly in February, April, June, August, October, and December. Supplementary issues are also published at times.

Availability of the full-text in the web, URL address
The published articles from the initial to the present issue are available free of charge at http://ejournal.kpmi.or.kr.

Index in database
The articles published in Journal of Powder Materials are indexed and/or abstracted in Google Scholar, KISTI, and KCI.

Fund support
"본 사업은 기획재정부의 복권기금 및 과학기술정보통신부의 과학기술진흥기금으로 추진하여 사회적 가치 실현과 국가 과학기술 발전에 기여합니다."
"This work is supported by the 'Lottery Fund' of the 'Ministry of Strategy and Finance' and the 'Science and Technology Promotion Fund' of the 'Ministry of Science and ICT', contributing to the realization of social value and the development of national science and technology."

kpmi
Korean Powder Metallurgy
& Materials Institute

Subscription info
The annual subscription fee for this journal is Korean Won ₩50,000 (US$ 50.00 or equivalent). Back issues are available on request. The number of circulated print copies is 600. Full published papers from the initial to the present issue are available free of charge at http://ejournal.kpmi.or.kr. Correspondence concerning business matters should be addressed to Ms. Youn-Ho Kim, Manager, The Korean Powder Metallurgy & Materials Institute, Unit 706, (635-4, Yeoksam-Dong) 22, 7Gil, Teheran-Ro, Gangnam-Gu, Seoul 06130, Korea (Tel: +82-2-539-4603, Fax: +82-0303-0947-4603, e-mail: kpmi@kpmi.or.kr).

Submission
Manuscripts should be submitted via the online Manuscript Central website (https://submit.powdermat.org). Other correspondence can be sent by e-mail (ktkim@kims.re.kr or kpmi@kpmi.or.kr) to the Editor-in-Chief, Dr. Kyung Tae Kim, Korea Institute of Materials Science, Changwon, Gyeongnam 51508, Korea. All manuscripts are peer-reviewed.

Contact info (Editorial office)
The Korean Powder Metallurgy & Materials Institute Unit 706, 22, 7Gil, Teheran-Ro, Gangnam-Gu, Seoul 06130, Korea
Tel: +82-2-539-4603, Fax: +82-0303-0947-4603, E-mail: kpmi@kpmi.or.kr

Printed by M2PI
#805, 26 Sangwon 1-gil, Seongdong-gu, Seoul 04779, Korea
Tel: +82-2-6966-4930, Fax: +82-2-6966-4945, E-mail: support@m2-pi.com, Homepage: http://m2-pi.com

Journal of
Powder Materials

Editorial Board

Contents

Journal of
Powder Materials

VOL. 32 NO.4 / August 2025

Research Articles

277 Laser Processing of an $Al_{0.1}CoCrFeNi$ High Entropy Alloy + Cu Composite Powders via Laser Powder Bed Fusion
Kwangtae Son, Ji-Woon Lee, Soon-Jik Hong, Somayeh Pasebani

288 Cost-effective Fabrication of Near β-Ti Alloy via L-PBF: Process Optimization of In-Situ Alloying Ti-3Fe
Sehun Kim, Ukju Gim, Taehu Kang, Jongik Lee, Sanghee Jeong, Jimin Han, Bin Lee

299 Fabrication and Pore Characteristics of Metal Powder Filters with a Cross-Sealed Honeycomb Shape Using Material Extrusion Additive Manufacturing
Minji Kim, Min-Jeong Lee, Su-Jin Yun, Poong-Yeon Kim, Hyeon Ju Kim, Juyong Kim, Jung Woo Lee, Jung-Yeul Yun

309 Evaluation of Mechanical Properties of Pure Ni Coatings on a Type 316H Stainless Steel Substrate via High-Velocity Oxy-fuel and Directed Energy Deposition Processes
Won Chan Lee, Seung Ju Nam, Ji-Hyun Yoon, Jeoung Han Kim

315 Enhanced Compressive Strength of Fired Iron Ore Pellets: Effects of Blending Fine and Coarse Particle Concentrates
Ngo Quoc Dung, Tran Xuan Hai, Nguyen Minh Thuyet, Nguyen Quang Tung, Arvind Barsiwal, Nguyen Hoang Viet

330 The Recycling Process and Powderization Technology of Stellite 6 Scrap: A Thermodynamic and Heat Transfer Analysis
YongKwan Lee, Hyun-chul Kim, Myungsuk Kim, Soong Ju Oh, Kyoungtae Park, JaeJin Sim

344 Influence of Powder Particle Size on the Microstructure of UO_2 Fuel Pellets with High Gd_2O_3 Content
Ji-Hwan Lee, Jae Ho Yang, Ji-Hae Yoon, Dong-Joo Kim, Dong-wook Shin, Dong Seok Kim

354 Effect of Fe and Cr on ω Phase Formation in Metastable β-Ti Alloy
Sun-Young Park, Young-Bum Chun

361 CODE OF ETHICS

367 INSTRUCTIONS FOR AUTHORS

Contents

Journal of
Powder Materials

VOL. 32 NO.4 / August 2025

Research Articles

277 Laser Processing of an $Al_{0.}1CoCrFeNi$ High Entropy Alloy + Cu Composite Powders via Laser Powder Bed Fusion
Kwangtae Son, Ji-Woon Lee, Soon-Jik Hong, Somayeh Pasebani

288 Cost-effective Fabrication of Near β-Ti Alloy via L-PBF: Process Optimization of In-Situ Alloying Ti-3Fe
Sehun Kim, Ukju Gim, Taehu Kang, Jongik Lee, Sanghee Jeong, Jimin Han, Bin Lee

299 Fabrication and Pore Characteristics of Metal Powder Filters with a Cross-Sealed Honeycomb Shape Using Material Extrusion Additive Manufacturing
Minji Kim, Min-Jeong Lee, Su-Jin Yun, Poong-Yeon Kim, Hyeon Ju Kim, Juyong Kim, Jung Woo Lee, Jung-Yeul Yun

309 Type 316H 스테인리스강 기판 위에 high velocity oxy-fuel 및 directed energy deposition 공정을 통한 순수 Ni 적층 및 기계적 특성 평가
이원찬, 남승주, 윤지현, 김정한

315 Enhanced Compressive Strength of Fired Iron Ore Pellets: Effects of Blending Fine and Coarse Particle Concentrates
Ngo Quoc Dung, Tran Xuan Hai, Nguyen Minh Thuyet, Nguyen Quang Tung, Arvind Barsiwal, Nguyen Hoang Viet

330 열역학 및 열 전달 해석을 활용한 Stellite 6 스크랩 재활용 공정과 분말화 기술 연구
이용관, 김현철, 김명석, 오승주, 박경태, 심재진

344 고함량 Gd_2O_3 첨가 UO_2 핵연료 소결체의 혼합 분말 입도에 따른 미세구조 영향 분석
이지환, 양재호, 윤지해, 김동주, 신동욱, 김동석

354 Fe 와 Cr 첨가량이 β 타이타늄 합금의 ω상 형성에 미치는 영향
박선영, 천영범

361 CODE OF ETHICS

367 INSTRUCTIONS FOR AUTHORS

Research Article

pISSN 2799-8525 · eISSN 2799-8681
J Powder Mater 2025;32(4):277-287

Journal of
Powder Materials

Laser Processing of an $Al_{0.1}$CoCrFeNi High Entropy Alloy + Cu Composite Powders via Laser Powder Bed Fusion

Kwangtae Son[1,2,*], **Ji-Woon Lee**[3,4], **Soon-Jik Hong**[3,4], **Somayeh Pasebani**[1,2]

[1]School of Mechanical, Industrial, and Manufacturing Engineering, Oregon State University, Corvallis, OR 97331, USA
[2]Advanced Technology and Manufacturing Institute, Corvallis, OR 97330, USA
[3]Division of Advanced Materials Engineering, Kongju National University, Cheonan 31080, Republic of Korea
[4]Center for Advanced Materials and Parts of Powders, Kongju National University, Cheonan 31080, Republic of Korea

This study examined process–structure relationships in laser powder bed fusion of $Al_{0.1}$CoCrFeNi + Cu composites, focusing on densification, elemental distribution, and solidification cracking. Mechanically mixed $Al_{0.1}$CoCrFeNi and Cu powders were processed across a range of laser powers (100–250 W) and scan speeds (200–800 mm/s). Increased volumetric energy density (VED) improved densification, with a plateau near 200 J/mm^3 yielding ~96% relative density; however, this value was still below application-grade thresholds. At low VED, insufficient thermal input and short melt pool residence times promoted Cu segregation, while higher VED facilitated improved elemental mixing. Elemental mapping showed partial co-segregation of Ni with Cu at low energies. Solidification cracks were observed across all processing conditions. In high VED regimes, cracking exhibited a minimal correlation with segregation behavior and was primarily attributed to steep thermal gradients, solidification shrinkage, and residual stress accumulation. In contrast, at low VED, pronounced Cu segregation appeared to exacerbate cracking through localized thermal and mechanical mismatch.

Keywords: Laser powder bed fusion; High-entropy alloys; Solidification cracking; Cu segregation; Microstructural integrity

Received: April 8, 2025
Revised: July 1, 2025
Accepted: July 1, 2025

***Corresponding author:**
Kwangtae Son
E-mail: kwangtas@alumni.usc.edu

1. Introduction

The AlCoCrFeNi alloy and its derivatives within the high-entropy alloy (HEA) class have emerged as a focal point in recent alloy design efforts due to their compositional complexity and tunable properties [1, 2]. Among the principal elements, aluminum has been shown to exert the most pronounced effect on both the microstructure and mechanical behavior of the alloy. In the Al_xCoCrFeNi system, progressive addition of Al induces a transformation in the primary crystal structure—from a face-centered cubic (fcc) lattice at lower Al concentrations to a body-centered cubic (bcc) lattice at higher concentrations. Specifically, the fcc structure dominates for $x \leq 0.4$, a dual-phase (fcc + bcc) region appears within $0.5 \leq x \leq 0.9$, and a single bcc phase becomes stable for $x \geq 0.9$ [3]. Building upon earlier studies focused on pure single-phase matrices, recent alloy development strategies have increasingly emphasized the deliberate formation of multi-phase microstructures and/or intermetallic precipitates to enhance performance [4, 5].

Among the fcc-structured Al_xCoCrFeNi high-entropy alloys, the $Al_{0.1}$ composition has emerged as a particularly attractive candidate due to its advantageous combination of mechanical resilience and microstructural stability, especially under cryogenic and moderately elevated temperature regimes [6, 7]. The stability of the single-phase FCC matrix facilitates deformation through dislocation glide and mechanical twinning, mechanisms that synergistically enhance strain hardening capacity and confer exceptional resistance to brittle fracture, even at cryogenic temperatures [6]. Additionally, its demonstrated hot workability and resistance to thermomechanical cracking underscore its suitability for industrial forming operations such as hot forging

https://doi.org/10.4150/jpm.2025.00101

and rolling [7]. Despite these favorable mechanical attributes, a notable limitation lies in its inherently modest thermal conductivity, which may hinder its deployment in applications where efficient heat dissipation is critical—such as heat exchangers in power plants, thermal shielding structures, or load-bearing supports interfacing with superconducting components [8]. A promising strategy to overcome this constraint is inspired by the recent study conducted by Mirzababaei et al. [9], who achieved a 2.5- to 6.6-fold enhancement in thermal conductivity of 316L stainless steel through the incorporation of 60 vol% Cu via laser powder bed fusion (LPBF). This substantial increase highlights the potential of Cu-rich alloying in promoting thermal transport, suggesting that similar compositional modification of the $Al_{0.1}$CoCrFeNi alloy may enable the development of multifunctional materials that simultaneously meet structural and thermal performance requirements.

Traditionally, the fabrication of HEAs including $Al_{0.1}$CoCrFeNi alloy has been primarily achieved through arc melting and mechanical alloying techniques [10]. In the arc melting route, constituent elements are first weighed according to the desired atomic ratios and then melted under an inert atmosphere, typically argon, using a high-temperature electric arc. Alternatively, mechanical alloying enables the synthesis of HEA powders via high-energy ball milling, wherein repeated fracturing and cold welding of elemental or pre-alloyed powders result in intimate mixing and alloy formation. These powders can then be consolidated through spark plasma sintering, hot isostatic pressing, or conventional sintering. Despite the success of these techniques in establishing the foundational understanding of HEAs, both routes face challenges related to compositional homogeneity, limited microstructural tunability, and labor-intensive post-processing requirements. Recent efforts have thus explored Cu additions to $Al_{0.1}$CoCrFeNi alloys via arc melting, revealing that Cu induces the formation of coherent Cu-rich nanoprecipitates within the FCC matrix, which effectively enhance yield strength through precipitation strengthening [11]. However, increasing Cu content can reduce ductility due to strain localization and microcrack formation at precipitate–matrix interfaces [11]. These limitations have motivated the exploration of advanced processing methods—particularly additive manufacturing—as a means to produce compositionally complex alloys with refined microstructures and geometrically flexible architectures [6].

In this study, Cu-added $Al_{0.1}$CoCrFeNi composites were fabricated using the LPBF) process to establish an optimized processing window across a range of laser powers (100–250 W) and scanning speeds (200–800 mm/s). The objective was to evaluate the feasibility of producing high-performance, Cu-enriched $Al_{0.1}$CoCrFeNi-based alloys through in situ laser processing of blended elemental powders, thereby exploring the potential of compositional tuning for enhanced multifunctional properties. A Cu content of 21.8 wt%—corresponding to approximately 19.6 at%—was selected not only to enable sufficient Cu enrichment for Cu-rich phase formation, but also to shift the overall composition toward a near-equiatomic $Al_{0.1}$CoCrFeNiCu configuration.

2. Experimental

2.1. Preparation of Mixed $Al_{0.1}$CoCrFeNi + Cu composite powders

The $Al_{0.1}$CoCrFeNi powder was synthesized via a high-purity gas atomization process at Kongju National University (Cheonan, South Korea). High-purity elemental metals were weighed according to the stoichiometric composition and induction-melted at approximately 1600 °C to produce a homogeneous molten alloy. The melt was then discharged through a boron-nitride nozzle (8 mm diameter) into a gas atomization chamber, where high-pressure argon gas (1.3 MPa) was employed to atomize the stream into fine droplets. These droplets rapidly solidified into spherical powders, which were collected at the base of the chamber. The atomized powders exhibited a smooth, spherical morphology with a particle size distribution characterized by D_{10}, D_{50}, and D_{90} values of 16.9 μm, 34.0 μm, and 58.5 μm, respectively.

For the preparation of $Al_{0.1}$CoCrFeNi + Cu composite powders, commercially available copper powders (99.7% purity, −325 mesh) were procured from Royal Metal Powders Inc. (Maryville, TN, USA) and blended with $Al_{0.1}$CoCrFeNi powders at a weight ratio of 21.8 wt% Cu to 78.2 wt% $Al_{0.1}$CoCrFeNi. This composition was selected to develop a HEA system in which no single element dominates the overall chemistry. Powder mixing was conducted using a Retsch PM 100 planetary ball mill (Haan, Germany). To prevent fragmentation or mechanical deformation of particles, no grinding media were introduced into the milling jar. A total of 500 g of blended powder was loaded, and the mixing was performed at 100 rpm for 1 hour. The SEM image and chemical composition maps of mixed $Al_{0.1}$CoCrFeNi + Cu powders are given in Fig. 1. This procedure ensured uniform dispersion of the Cu particles within the $Al_{0.1}$CoCrFeNi matrix, resulting in a homogeneously blended precursor powder suitable for subsequent laser processing.

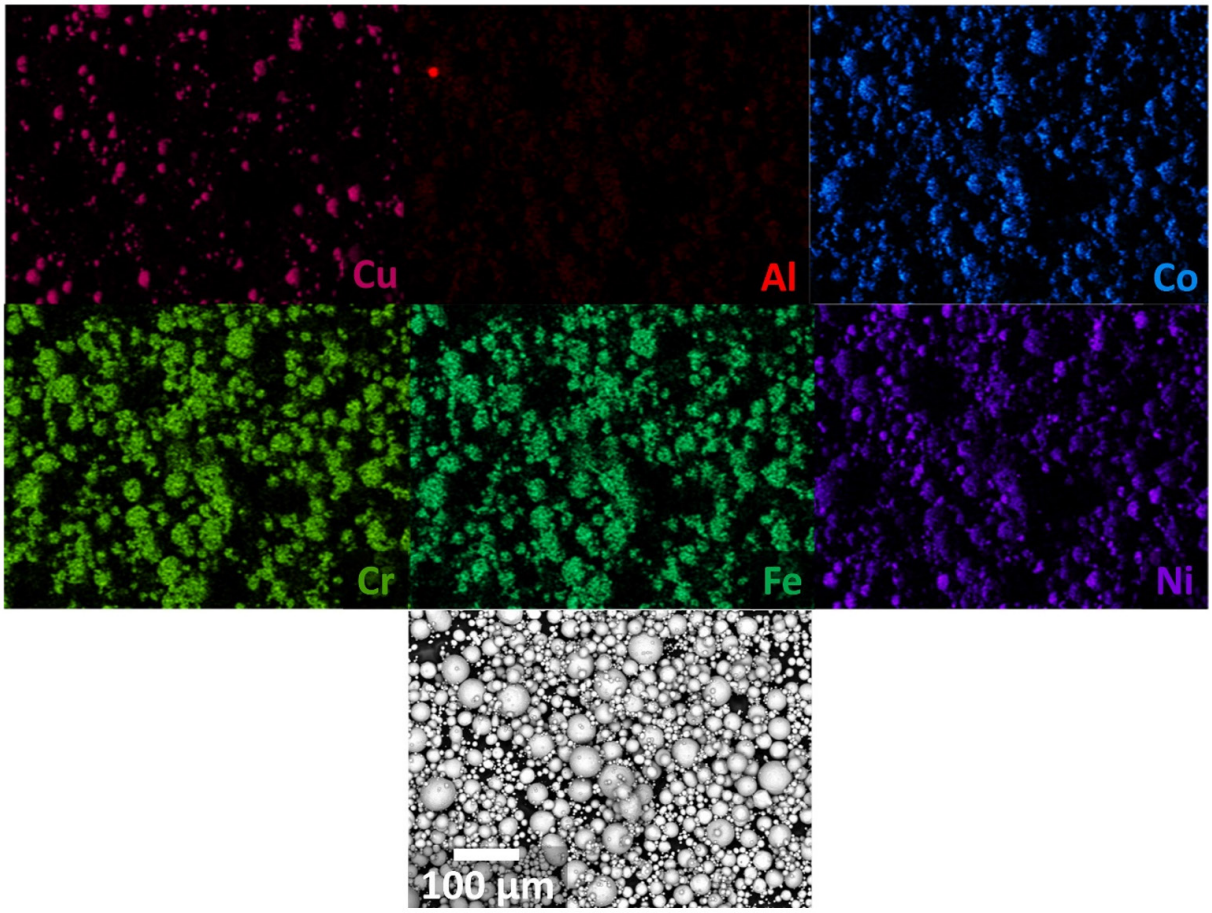

Fig. 1. Scanning electron micrograph with energy-dispersive X-ray spectroscopy elemental mapping of $Al_{0.1}$CoCrFeNiCu composite powder feedstock for laser powder bed fusion.

2.2. LPBF process of $Al_{0.1}$CoCrFeNiCu Composite Mixture

The fabrication of $Al_{0.1}$CoCrFeNi + Cu composite structures was carried out using a 2ONELAB LPBF system (Coherent, Germany). The machine is equipped with an infrared fiber laser operating at a wavelength of 1070 nm and a focused beam diameter of approximately 40 μm. For the purpose of laser process parameter optimization, sixteen cubic samples—each measuring 7 mm × 7 mm × 7 mm—were fabricated simultaneously in a single build. These samples were spatially separated by approximately 10 mm to minimize thermal interactions during fabrication.

The LPBF process employed a layer thickness of 40 μm and a hatch spacing of 40 μm. To systematically investigate the influence of processing conditions on part geometry and melt behavior, four laser power levels (100 W, 150 W, 200 W, and 250 W) and four scanning speeds (200 mm/s, 400 mm/s, 600 mm/s, and 800 mm/s) were selected. These combinations enabled a comprehensive evaluation of laser-material interaction under varying volumetric energy density (VED) conditions. The corresponding VED values for each parameter set are summarized in Table 1.

2.3. Microstructure Characterization

Following LPBF fabrication, the specimens were detached from the build platform using a Sodick VL600Q electrical discharge machining (EDM) system (Yokohama, Japan). To expose the internal features for microstructural evaluation, cross-sectional samples were sectioned along the central plane of each 7 mm cube in the build direction using the same EDM system. The extracted sections were then mounted in conductive carbon-filled phenolic resin using a hot compression mounting press to ensure mechanical stability during subsequent metallographic processing.

The mounted specimens underwent sequential grinding with silicon carbide (SiC) abrasive papers, beginning with coarse 120 grit and advancing to 1200 grit to achieve a flat and uni-

Table 1. Laser processing parameters applied in this study

Laser power (W)	Scanning speed (mm/s)	Hatch spacing (μm)	Layer thickness (μm)	VED[1)] (J/mm^3)	Rotational angle	Laser travel method
100	200	40	40	312.50	67.5	Bi-directional
100	400			156.25		
100	600			104.17		
100	800			78.13		
150	200			468.75		
150	400			234.38		
150	600			156.25		
150	800			117.19		
200	200			625.00		
200	400			312.50		
200	600			208.33		
200	800			156.25		
250	200			781.25		
250	400			390.63		
250	600			260.42		
250	800			195.31		

Volumetric energy density (VED) is an energy parameter to quantify the laser processing parameter, calibrated with an equation of $P/(v{\cdot}h{\cdot}t)$. where P is the laser power; v is the scanning speed; h is the hatch spacing; t is the layer thickness.

form surface. This was followed by mechanical polishing using 1 μm diamond suspension, and final surface finishing was completed with 0.05 μm colloidal silica to obtain a mirror-like finish suitable for high-resolution microstructural analysis.

Optical microscopy was performed using a Zeiss optical microscope (Oberkochen, Germany) to assess part relative density and surface integrity. For statistical reliability, a minimum of 10 cross-sectional images were acquired at 50× magnification from each sample to account for repeatability and measurement uncertainty.

To further investigate elemental distribution within the printed structures, scanning electron microscopy (SEM) was conducted using a Hitachi TM4000 tabletop SEM (Tokyo, Japan) equipped with a Bruker energy-dispersive spectroscopy (EDS) detector (Billerica, MA). This allowed qualitative mapping of elemental homogeneity and potential segregation at the microstructural scale.

3. Results and Discussion

3.1 Cross-Sectional Analysis of LPBF-Fabricated $Al_{0.1}$CoCrFeNiCu Composite Structures

The cross-sectional micrographs of the LPBF-fabricated $Al_{0.1}$CoCrFeNi + Cu composites (Fig. 2) revealed a strong dependency of defect morphology on the applied VED. At lower VEDs—particularly those corresponding to laser powers of 100–200 W combined with scanning speeds of 400–800 mm/s—pronounced lack-of-fusion (LOF) defects were observed. These defects arise from insufficient energy input, leading to incomplete melting and poor interlayer bonding [12]. The resulting melt pools are typically shallow and narrow, which inhibits capillary-driven consolidation and results in unbonded regions between tracks and layers. Conversely, processing conditions with higher VEDs, such as 250 W at scanning speeds of 200–400 mm/s, induced deeper, more unstable melt pools characteristic of keyhole-mode melting. In this regime, excessive energy input causes vapor-induced recoil pressure and dynamic melt pool instabilities, promoting the formation of gas entrapment and spherical porosity—commonly referred to as keyholes [13]. These observations are consistent with previous findings in HEA systems [14], where porosity was shown to increase significantly at both insufficient and excessive energy input levels due to LOF and keyhole phenomena, respectively. Importantly, none of the fabricated samples achieved a fully dense structure, as solidification cracking persisted across the processing window, suggesting that in addition to energy input, factors such as elemental segregation [15], thermal gradients, and residual stress accumulation [16] play critical roles in governing microstructural integrity during LPBF.

The consistent presence of solidification cracking observed

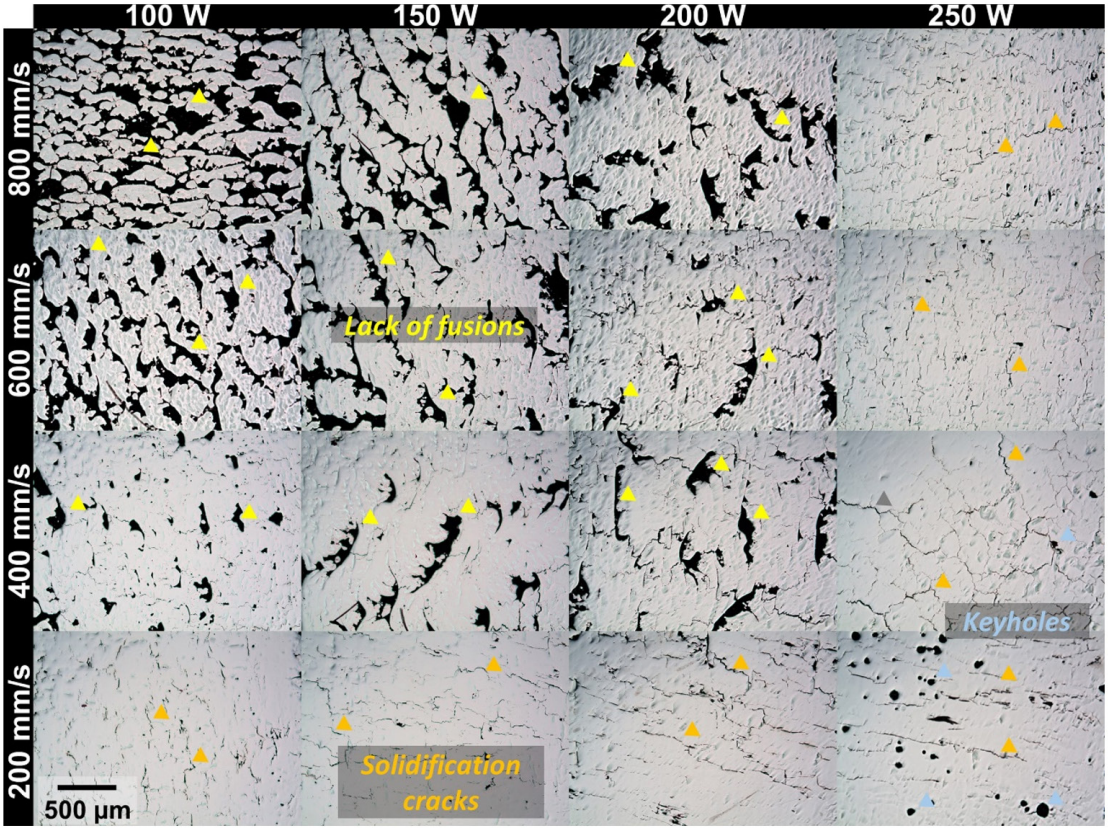

Fig. 2. Cross-sectional view observation of fabricated composites at laser conditions of 100 – 250 W and 200 – 800 mm/s using optical microscopy, revealing artifacts such as lack of fusions, solidification cracks, and keyholes. The building direction is vertical to the image.

in the LPBF-fabricated $Al_{0.1}$CoCrFeNi + Cu composites, even under conditions optimized to mitigate LOF and keyhole porosity, underscores the critical role of alloy chemistry and solidification dynamics in crack formation. Solidification cracking in HEAs is often attributed to a combination of low melting-point eutectic films, wide solidification temperature ranges, and high thermal gradients inherent to laser-based additive manufacturing processes [14]. In multicomponent systems such as $Al_{0.1}$CoCrFeNi + Cu, the differential solidification behavior between constituent elements can lead to compositional segregation at grain boundaries, particularly of Cu, which has a relatively low melting point and poor solubility in several transition metals. Guo et al. [15] demonstrated that microsegregation of Si and N in an FeCoCrNiMn-based HEA induced localized eutectic formation and weakened intergranular cohesion during the terminal stages of solidification. A similar mechanism is likely at play in the current alloy system, where segregation of Cu to interdendritic regions reduces the local solidus temperature and promotes the formation of thin liquid films along grain boundaries. These liquid films are susceptible to tensile stress-induced rupture during cooling, especially under the high thermal gradients and rapid solidification conditions characteristic of LPBF. Furthermore, the insufficient backfilling of liquid into the solidification front due to poor fluidity of Cu-rich melt may exacerbate crack propagation.

To gain a comprehensive understanding of how laser processing parameters affect the structural integrity of LPBF-fabricated $Al_{0.1}$CoCrFeNi + Cu composites, two data visualizations were constructed: a relative density plot as a function of VED (Fig. 3a) and a laser power–scan speed process map (Fig. 3b). As shown in Fig. 3a, the relative density of the printed parts generally increases with VED, reaching a plateau at approximately 200 J/mm^3. This behavior suggests that energy input beyond this threshold does not significantly enhance densification, likely due to saturation in melt pool penetration and consolidation efficiency.

However, to disentangle the individual contributions of laser power and scan speed—factors that are otherwise convolved in the VED expression—the relative density data were further plotted as a two-variable process map in Fig. 3b. The results re-

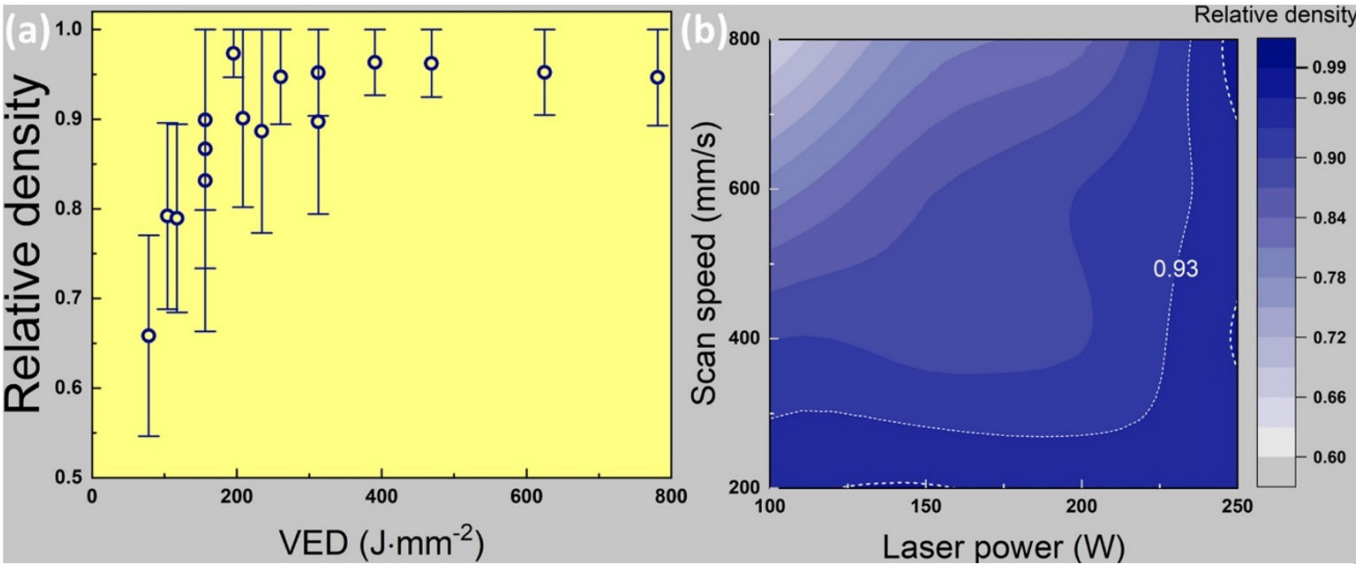

Fig. 3. Relative density variation in laser powder bed fusion-printed $Al_{0.1}$CoCrFeNi + Cu composite with (a) volumetric energy density profile (b) a processing window of laser power and scan speed. The maximum relative density of the printed part is ≈ 0.96 where indicated with dashed lines.

veal a distinct trend: relative density decreases with increasing scan speed and decreasing laser power. Notably, at lower laser powers (100 W and 150 W), the relative density is highly sensitive to scan speed variations, indicating insufficient melting and reduced energy coupling at high scan velocities. In contrast, at higher laser powers (e.g., 250 W), the effect of scan speed on relative density becomes less pronounced, approaching an apparent insensitivity within the examined range.

This phenomenon can be partially explained by the laser absorptivity behavior of metallic powders under varying power inputs. As demonstrated by Trapp et al. [17], the laser absorptivity of stainless steel 316L powders increases exponentially from 0.3 to 0.8 as laser power increases from 50 W to 220 W. A similar effect is likely present in the $Al_{0.1}$CoCrFeNi + Cu system, where higher laser powers enhance powder-bed absorptivity, promoting more efficient energy coupling and stable melt pool formation. Consequently, this increased absorptivity at higher powers diminishes the dependence of melt pool behavior—and thus relative density—on scan speed. It also reduces the likelihood of LOF defects, which are more prevalent under conditions of poor absorptivity and shallow melting.

Despite these improvements, the maximum relative density achieved in this study was approximately 0.96, which remains below the industrially acceptable threshold (> 0.99) for critical structural applications. This shortfall is attributed not only to suboptimal melting dynamics but also to inherent issues in powder morphology, including incomplete packing and potential moisture content. Prior studies [18, 19] have shown that residual moisture in composite powders can lead to spattering and irregular melt pool behavior, ultimately increasing porosity. These results collectively emphasize the need for optimized powder handling and pre-processing protocols, in addition to refined laser parameters, to achieve full densification in LPBF-fabricated compositionally complex alloys.

3.2. Elemental Distribution Observation of Low and High VED Conditions

While the overall relative density of the LPBF-fabricated $Al_{0.1}$CoCrFeNi + Cu composites was found to be strongly influenced by VED and associated laser absorptivity behaviors, densification alone does not fully account for the nature and severity of microstructural defects. As previously discussed, LOF and keyhole-induced porosity were prevalent under low and high energy input conditions, respectively. However, beyond void morphology, the presence of these processing-induced artifacts may also be linked to elemental segregation, particularly in compositionally complex systems where multi-element interactions govern phase stability and local melting behavior. To further elucidate this relationship, EDS elemental mapping was performed on samples fabricated under the lowest and highest VED conditions. This comparative analysis aims to correlate the distribution of major alloying elements with the observed

defect structures, providing deeper insight into the role of localized chemical inhomogeneity in the formation of process-induced artifacts.

To further understand the influence of laser energy input on the distribution of alloying elements and potential defect mechanisms, EDS elemental mapping was performed on specimens fabricated under the lowest and highest VED conditions. At the lowest VED setting (100 W, 800 mm/s), where the largest LOF defects and the lowest overall relative density were observed, significant Cu segregation was identified (Fig. 4). In contrast to the uniform distribution of the primary HEA-forming elements (Al, Co, Cr, Fe, Ni), Cu appeared concentrated in localized regions, often separated from the surrounding matrix. Partial co-segregation between Cu and Ni was also noted, which is thermodynamically plausible given the favorable mixing enthalpy between these two elements, as reported by Mirzababaei et al. [9]. Although X-ray diffraction analysis of the Cu-enriched phases within the $Al_{0.1}$CoCrFeNi matrix presents inherent challenges due to their limited volume fraction and potential overlap with matrix peaks, EDS clearly identified the presence of Cu-rich regions, consistent with prior observations reported by Lee et al. [20]. In that study, an increased Cu feed rate during the LPBF process led to a higher volume fraction of Cu-enriched islands within a stainless steel matrix, which was correlated with enhanced thermal conductivity. By analogy, the Cu-rich domains observed in Fig. 4 of the present work may similarly contribute to improved thermal transport, owing to the intrinsically high thermal conductivity of Cu and its localized enrichment within the composite microstructure.

The observed Cu segregation under low VED conditions is attributed primarily to insufficient melt pool residence time and reduced thermal enthalpy, both of which hinder the full dissolution and mixing of Cu into the HEA matrix. Trapp et al. [16] demonstrated that laser absorptivity—and therefore energy absorption—of metallic powders increases significantly with laser power. At lower power levels, limited absorptivity results

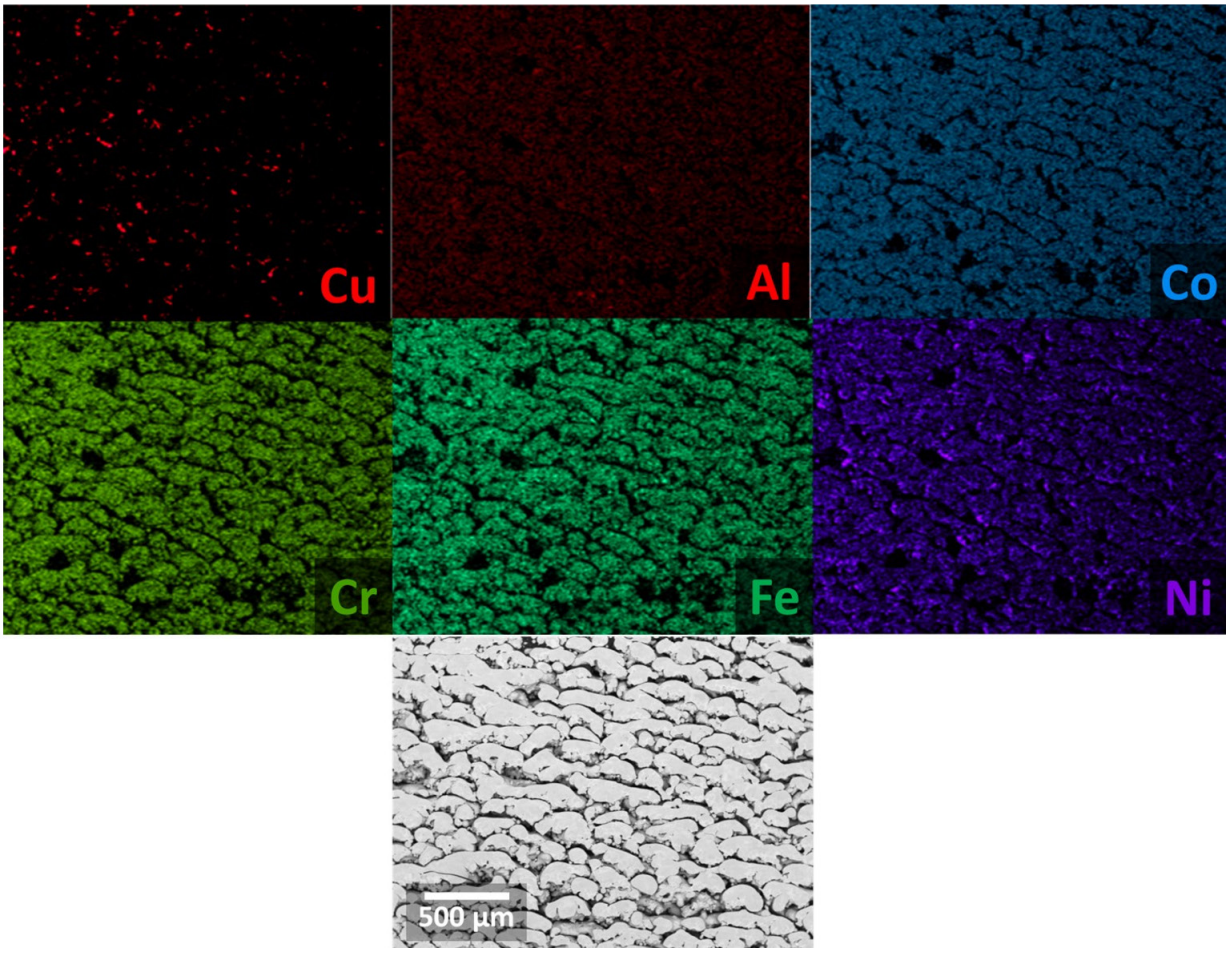

Fig. 4. Scanning electron microscopy–energy-dispersive X-ray spectroscopy mapping result for the lowest volumetric energy density condition (100 W, 800 mm/s), showing Cu segregation with some Ni concentration separated from other $Al_{0.1}$CoCrFeNi-driven elements.

in shallow and short-lived melt pools, which do not provide the thermal or temporal conditions required for effective diffusion and homogenization of dissimilar powder constituents. Additionally, as described by Afrasiabi et al. [11], inadequate energy input reduces melt pool convection and Marangoni flow, further suppressing elemental intermixing.

In contrast, under the highest VED condition (250 W, 200 mm/s), elemental mapping revealed a much more homogeneous distribution of Cu throughout the matrix (Fig. 5), suggesting effective melting, mixing, and solute incorporation due to deeper and more thermally stable melt pools. Importantly, while Cu segregation was evident at low VED, no direct correlation was observed between this segregation and the occurrence of solidification cracking. Cracks were detected even in regions where elemental distributions were homogenous, implying that cracking in the current $Al_{0.1}$CoCrFeNi + Cu system arises from mechanisms other than segregation-induced liquation.

One plausible explanation is the development of high thermal gradients and solidification-induced stresses intrinsic to LPBF processing of compositionally complex alloys. As highlighted by Guo et al. [15], cracking susceptibility in HEAs may also be governed by a combination of solidification shrinkage and grain boundary cohesion, independent of visible segregation. Platl et al. [21] similarly reported that intergranular cracking in FeCoMo alloys could occur due to intrinsic brittleness and residual stress development, even in the absence of any significant impurity phases or compositional heterogeneities. Additionally, as noted by Khodashenas and Mirzadeh [14], post-solidification tensile stresses generated during rapid thermal cycling in LPBF are sufficient to nucleate and propagate cracks in regions with unfavorable grain orientations or insufficient ductility at high cooling rates.

Now, Fig. 6a and 6b present EDS elemental maps highlighting Cu-enriched regions (defined as areas containing >50 wt% Cu) under two representative LPBF conditions: a high VED condition (200 W, 200 mm/s) and a low VED condition

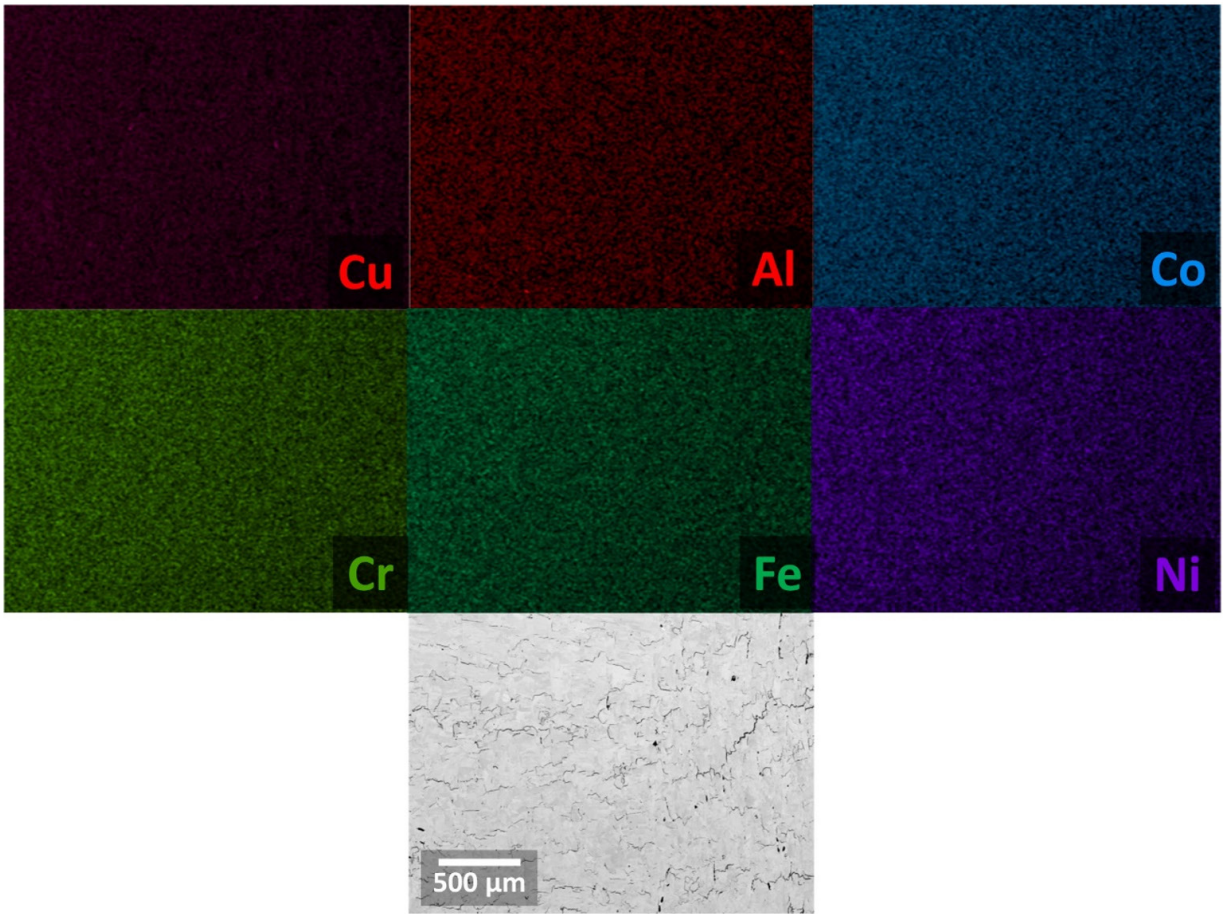

Fig. 5. Scanning electron microscopy–energy-dispersive X-ray spectroscopy mapping result for the highest volumetric energy density condition (250 W, 200 mm/s), showing the absence of Cu segregation.

(150 W, 800 mm/s), respectively. In the low VED condition (Fig. 6a), extensive LOF cracking is observed in close proximity to Cu-segregated zones, suggesting that the presence of unmixed Cu phases contributes to localized mechanical incompatibility and crack initiation. In contrast, under the high VED condition (Fig. 6b), where cracking is narrower and less prevalent, there is neither a high density of Cu-segregated regions nor spatial correlation between Cu enrichment and crack location. This indicates that in the high VED regime, cracking is more likely driven by rapid solidification-induced embrittlement rather than compositional heterogeneity. A schematic summarizing the distinct cracking mechanisms under both processing conditions is provided in Fig. 6c.

Therefore, in the present alloy system, solidification cracking under high VED conditions is more likely attributed to the combined effects of rapid cooling, thermal stress accumulation, and insufficient strain accommodation at the solid–liquid interface, rather than elemental segregation. In contrast, at lower VED, pronounced Cu segregation is observed and appears to exacerbate crack formation, both in severity and frequency, by promoting localized mechanical and thermal mismatches during solidification. These results highlight the critical impor-

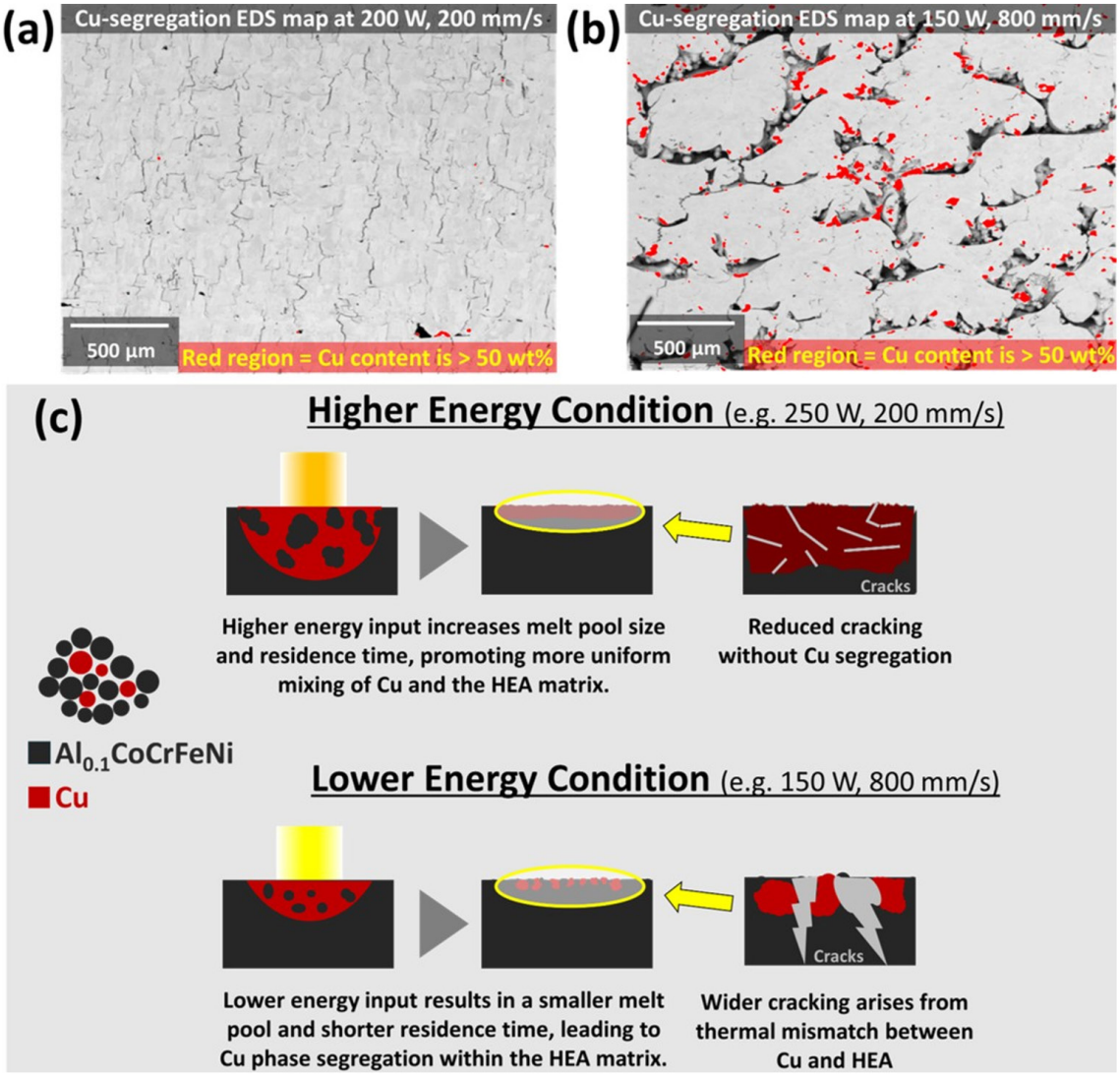

Fig. 6. Correlation between Cu segregation and solidification cracking behavior under different volumetric energy density (VED) conditions in laser powder bed fusion-processed $Al_{0.1}$CoCrFeNi + Cu composites. (a) EDS elemental map under a low VED condition (150 W, 800 mm/s). (b) EDS mapping under a high VED condition (200 W, 200 mm/s) (c) Schematic illustration comparing the dominant cracking mechanisms under low and high VED conditions. Red regions in (a) and (b) are where Cu concentration is higher than 50 wt%.

tance of optimizing thermal gradients and promoting grain refinement to mitigate cracking in LPBF-processed, compositionally complex alloys. Potential strategies to mitigate cracking frequency in LPBF-fabricated alloys include preheating the build substrate to reduce thermal gradients and suppress thermal shock during processing [22], modifying laser parameters—such as employing pulsed rather than continuous wave lasers to control energy input and cooling rates [23]—and incorporating strengthening dispersoids, such as oxide particles, to enhance crack resistance through microstructural stabilization [24].

5. Conclusion

In this study, $Al_{0.1}$CoCrFeNi + Cu composite were fabricated via LPBF using systematically varied laser powers (100–250 W) and scan speeds (200–800 mm/s) to explore the process-structure relationships governing densification, elemental distribution, and defect formation. The key findings and conclusions are summarized as follows:

1. Relative density improved with increasing VED, reaching a plateau near 200 J/mm^3, while low VED led to pronounced LOF and Cu segregation due to insufficient melt pool residence time. In contrast, high-VED conditions promoted uniform Cu dissolution and suppressed segregation.
2. Cracking persisted even under homogeneous compositions at high VED, driven mainly by thermal gradients, shrinkage, and stress buildup. At low VED, Cu segregation further promoted cracking via local thermal and mechanical mismatch.
3. Suppressing defects in LPBF-fabricated HEA composites requires not only appropriate energy input but also strategies to refine grains, reduce thermal stress, and tailor alloying elements to minimize cracking susceptibility.

Funding

None.

Conflict of Interest

The authors have no conflicts of interest to declare.

Data Availability Statement

The data in this research will be available upon request to corresponding author.

Author Information and Contribution

First Author: PhD candidate; conceptualization, writing–original draft

Second Author: Professor; supervision, writing–review & editing

Third Author: Professor; writing–original draft, funding acquisition, supervision

Acknowledgments

The corresponding author gratefully acknowledges the invaluable research support provided by Prof. Brian K. Paul and Prof. Somayeh Pasebani. Their guidance and provision of access to the LPBF facilities were instrumental in the successful execution of this work. Their contributions significantly enhanced both the experimental design and the technical depth of this study.

References

[1] C.-J. Tong, Y.-L. Chen, J.-W. Yeh, S.-J. Lin, S.-K. Chen, T.-T. Shun, C.-H. Tsau and S.-Y. Chang: Metall. Mater. Trans. A, **36** (2005) 881.

[2] Y.-F. Kao, T.-J. Chen, S.-K. Chen and J.-W. Yeh: J. Alloys Compd., **488** (2009) 57.

[3] W.-R. Wang, W.-L. Wang, S.-C. Wang, Y.-C. Tsai, C.-H. Lai and J.-W. Yeh: Intermetallics, **26** (2012) 44.

[4] E. P. George, D. Raabe and R. O. Ritchie: Nat. Rev. Mater., **4** (2019) 515.

[5] Z. Li, A. Ludwig, A. Savan, H. Springer and D. Raabe: J. Mater. Res., **33** (2018) 3156.

[6] W.-R. Wang, W.-L. Chen, S.-C. Wang, Y.-C. Tsai, C.-H. Lai and J.-W. Yeh: Intermetallics, **19** (2012) 698.

[7] A. Sourav, S. Yebaji and S. Thangaraju: Mater. Sci. Eng. A, **793** (2020) 139877.

[8] Z. Sun, C. Shi, L. Gao, S. Lin and W. Li: J. Alloys Compd., **901** (2022) 163554.

[9] S. Mirzababaei, V. V. K. Doddapaneni, K. Lee, G. E. Paul, H. Pirgazi, K.-S. Tan, O. Ertorer, C.-H. Chang, B. K. Paul and S. Pasebani: Addit. Manuf., **70** (2023) 103576.

[10] C. Li, M. Ferry, J. J. Kruzic and X. Li: J. Mater. Sci., **57** (2022) 9903.

[11] Q. K. Wang, L. F. Tang, Y. L. Bian, M. Majeed, H. W. Tang, Y.

Cai, N. B. Zhang, L. Lu and S. N. Luo: Mater. Sci. Eng. A, **934** (2025) 148280.
[12] M. Afrasiabi, D. Keller, C. Lüthi, M. Bambach and K. Wegener: Procedia CIRP, **113** (2022) 378.
[13] W. E. King, H. D. Barth, V. M. Castillo, G. F. Gallegos, J. W. Gibbs, D. E. Hahn, C. Kamath and A. M. Rubenchik: J. Mater. Process. Technol., **214** (2014) 2915.
[14] H. Khodashenas and H. Mirzadeh: J. Mater. Res. Technol., **21** (2022) 3795.
[15] L. Guo, J. Gu, B. Gan, S. Ni, Z. Bi, Z. Wang and M. Song: J. Alloys Compd., **865** (2021) 158892.
[16] Y. S. Lee and W. Zhang: Addit. Manuf., **12** (2016) 178.
[17] J. Trapp, A. M. Rubenchik, G. Guss and M. J. Matthews: Appl. Mater. Today, **9** (2017) 341.
[18] N. R. Comins: Philos. Mag., **25** (1972) 817.
[19] S. Ly, S. A. Khairallah, A. M. Rubenchik, G. Guss and M. J. Matthews: Sci. Rep., **7** (2017) 4085.
[20] K. Lee, V. V. K. Doddapaneni, S. Mirzababaei, S. Pasebani, C.-H. Chang and B. K. Paul: Addit. Manuf., **86** (2024) 104202.
[21] J. Platl, D. Rainer, H. Leitner, C. Turk, F. Galbusera, A. G. Demir, B. Previtali and R. Schnitzer: Berg. Huettenmaenn. Monatsh., **167** (2022) 325.
[22] A. V. Müller, G. Schlick, R. Neu, C. Anstätt, T. Klimkait, J. Lee, B. Pascher, M. Schmitt and C. Seidel: Nucl. Mater. Ener., **19** (2019) 184.
[23] H. Huang, B. Nie, P. Wan, L.-M. Yang, S. Bai and J. Liu: Proc. SPIE, **9353** (2015) 93530A.
[24] Z. Hu, Y. Zhao, K. Guan, Z. Wang and Z. Ma: Addit. Manuf., **36** (2020) 101579.

Research Article

pISSN 2799-8525 · eISSN 2799-8681
J Powder Mater 2025;32(4):288-298

Journal of
Powder Materials

Cost-effective Fabrication of Near β-Ti Alloy via L-PBF: Process Optimization of In-Situ Alloying Ti-3Fe

Sehun Kim, Ukju Gim, Taehu Kang, Jongik Lee, Sanghee Jeong, Jimin Han, Bin Lee*

Department of Advanced Materials Engineering Kyung Hee University, Yongin 17104, Republic of Korea

This study presents a cost-effective approach to fabricating near β-Ti alloys via in-situ alloying during laser powder bed fusion (L-PBF). A blend of non-spherical pure Ti, 3 wt.% Fe, and 0.1 wt.% SiO_2 nanoparticles was used to induce β-phase stabilization and improve flowability. Twenty-five process conditions were evaluated across a volumetric energy density range of 31.75-214.30 J/mm^3, achieving a maximum relative density of 99.21% at 89.29 J/mm^3. X-ray diffraction analysis revealed that the β-Ti phase was partially retained at room temperature, accompanied by lattice contraction in the α'-Ti structure, indicating successful Fe incorporation. Elemental mapping confirmed that the Fe distribution was homogeneous, without significant segregation. Compared to pure Ti, the Ti-3Fe sample exhibited a 49.2% increase in Vickers hardness and notable improvements in yield and ultimate tensile strengths. These results demonstrate the feasibility of in-situ alloying with low-cost elemental powders to produce high-performance near β-Ti alloys using L-PBF.

Keywords: Laser powder bed fusion; β-Ti alloy; Flowability; In-situ alloying; Mechanical properties

Received: July 10, 2025
Revised: August 11, 2025
Accepted: August 11, 2025

***Corresponding author:**
Bin Lee
E-mail: leebin@khu.ac.kr

1. Introduction

Titanium (Ti) and its alloys are widely employed in various sectors, including aerospace, biomedical fields, and mobility, due to their high specific strength, exceptional corrosion resistance, and superior biocompatibility [1, 2]. Ti is an allotropic metal, exhibiting two primary equilibrium phases: the α phase, which exhibits a hexagonal close-packed (HCP) structure at lower temperatures, and the β phase, which exhibits a body-centered cubic (BCC) structure at higher temperatures. The mechanical properties of Ti alloys are influenced by the ratio of alloying elements incorporated to stabilization of each phase [3, 4]. Ti alloys are typically classified as α-Ti, α+β-Ti, or β-Ti alloys based on the phase stability at room temperature. The β-Ti alloys investigated in this study are characterized by improved processability and biocompatibility due to the stabilization of the β phase. These alloys are further classified as near β, metastable β, or stable β Ti alloys, depending on the content of elements that stabilize the β phase.

The molybdenum equivalent (Mo_{eq}) formula, as defined in equation (1), is employed to categorize β-Ti alloys.

$$\begin{aligned} Mo_{eq} = {} & 1.0(\text{wt.\% Mo}) + 0.67(\text{wt.\% V}) \\ & + 0.44(\text{wt.\% W}) + 0.28(\text{wt.\% Nb}) + 0.22(\text{wt.\% Ta}) \\ & + 2.9(\text{wt.\% Fe}) + 1.6(\text{wt.\% Cr}) + 1.25(\text{wt.\% Ni}) \\ & + 1.70(\text{wt.\% Mn}) + 1.70(\text{wt.\% Co}) - 1.0(\text{wt.\% Al}) \end{aligned} \quad (1)$$

This formula provides a numerical measure that quantifies the degree of stabilization of the β phase, based on the addition of molybdenum (Mo), a well-known β-stabilizer. A higher Mo_{eq} value signifies enhanced β phase stability. According to this value, β-Ti alloys can be classified as detailed in Table 1 [5]. For instance, in this investigation, the incorporation of iron (Fe), a β phase stabilizing element, at a concentration of 3 wt.% yields an Mo_{eq} value of approximately 8.7, resulting in the formation of a near β-Ti alloy. This near β-Ti alloy is characterized by a microstructure wherein the α phase is distributed within the β matrix, thereby improving the alloy's strength and lowering the β-transus temperature, which confers advantages in hot forging

https://doi.org/10.4150/jpm.2025.00213

Table 1. Classification of β-Ti based on Mo_{eq} values [5]

Type of Ti	Mo_{eq} value
β-rich Ti	0~5
Near β-Ti	5~10
Metastable β-Ti	10~30
Stable β-Ti	> 30

and precision forming operations [6]. β-stabilizers are typically categorized into isomorphous elements (e.g., Mo, Nb, V), which are fully soluble in Ti, and eutectoid elements (e.g., Fe, Co), which exhibit partial solubility [5, 7]. Specifically, Fe, being an eutectoid element, is more abundant in the Earth's crust compared to isomorphous elements, rendering it a cost-effective choice. Additionally, Fe contributes to solid solution strengthening, which has led to extensive research into the incorporation of Fe into Ti alloys to develop low-cost β-Ti alloys [8–13].

Meanwhile, Ti and its alloys present significant machining challenges at room temperature. Their low machinability hinders the production of intricate shapes required by advanced industries when using conventional methods such as casting or forging. Several studies have explored the use of additive manufacturing (AM) technologies, employing metal powders, to overcome these limitations in Ti alloy production [14-16]. One such method is laser powder bed fusion (L-PBF), which involves the selective irradiation of a laser onto thin layers of metal powder, each approximately 30 μm in thickness, to construct three-dimensional structures. Among various additive manufacturing techniques, L-PBF offers superior dimensional accuracy and high design flexibility, making it particularly suitable for fabricating complex Ti alloy geometries. In the production of β-Ti alloys via the L-PBF process, it is essential to use pre-alloyed spherical powders containing β phase stabilizing elements as alloying constituents to ensure a smooth process. However, the production of pre-alloyed powders is generally costly and, depending on the composition ratio, can be difficult to achieve, which often results in the inability to produce powders with specific compositions.

Therefore, in this study, β-Ti alloys were fabricated using an in-situ alloying process applied to non-spherical pure Ti powder, which was individually mixed with β phase stabilizing elements, rather than utilizing pre-alloyed powders, to facilitate alloying during the L-PBF process. This approach not only allows for the precise design of alloys with the desired composition ratios but also ensures cost-effectiveness, as the powders are not subjected to alloying or spheroidization processes and are mixed separately [17]. Indeed, studies utilizing the advantages of the L-PBF based in-situ alloying process for alloy design and production have been documented. For example, a Ti-34Nb alloy was successfully produced using the in-situ alloying technique with Ti and niobium (Nb) powders, where the challenges of porosity and unmelted particles were addressed by adjusting process parameters [18]. Similarly, another study demonstrated the potential of producing functional composites with hardness gradients by utilizing Ti and Mo powders in the in-situ alloying process, facilitated by layer-by-layer energy control [19]. Research has also been conducted to examine process variables and mechanical properties during manufacturing, not solely focused on alloy design. However, when using elemental powders with varying melting points and densities, these powders can melt and diffuse during processing, leading to alloying and potentially causing local concentration gradients or microstructural inhomogeneities, depending on the process conditions [20]. To ensure successful in-situ alloying, it is crucial to optimize L-PBF process parameters, such as laser power and scan speed, and to analyze the relative density and microstructure of the resulting specimens.

In this study, the Fe content was set at 3 wt.% to produce a near β-Ti alloy that stabilizes the β phase while allowing the coexistence of the α phase. The mixed powder used in the in-situ alloying process was prepared by incorporating 0.1 wt.% SiO_2 hydrophobically treated oxide nanoparticles to improve the flowability of the non-spherical pure Ti powder. In a previous study, our research team confirmed the enhancement of flowability and oxide-based strength through the dry coating of SiO_2 nanoparticles with non-spherical hydrogenation-dehydrogenation (HDH) Ti-6Al-4V powder [21]. We employed the same technique to prepare the mixed powder for this study. Optimal process conditions were determined by combining 25 process variables within the volumetric energy density (VED) range of 31.75-214.30 J/mm^3, ensuring that specimens with a relative density of 99 % or higher were produced. Additionally, pure Ti specimens were fabricated under the same conditions and used as a control group to assess differences in microstructure and mechanical properties based on the alloy composition. The phase composition and elemental distribution of the fabricated specimens were analyzed using X-ray diffraction (XRD) and energy dispersive spectroscopy (EDS), and the microstructure of the layered specimens was examined using optical microscopy (OM) and scanning electron microscopy (SEM). Vickers hardness measurements and tensile tests were conduct-

ed to evaluate the mechanical properties and confirm changes resulting from the addition of Fe.

2. Experimental

In this experiment, non-spherical pure Ti powder (<45 μm, Samhwa Steel), spherical Fe powder (40-50 μm, Avention), and hydrophobic surface-treated SiO_2 nanoparticles (5-15 nm, Skyspring Nanomaterials) were used. To assess the size and distribution of the base Ti and alloying element Fe powders, particle size analysis (PSA; Particle Size Analysis, Shympatec, HELOS QUIXEL) was conducted. To improve the flowability of the non-spherical pure Ti powder, SiO_2 nanoparticles were dry-coated at a 0.1 wt.% ratio using a turbula mixer at 3000 rpm for 3 hours. Fe powder was then mixed with the SiO_2-treated Ti powder at a 3 wt.% ratio under the same conditions.

To evaluate the flow characteristics of the mixed powder and its suitability for the PBF process, Hall flowmeter measurements were conducted, and apparent density and tap density were measured using a tap densimeter. The time it took for 50 g of powder to fall through a standard funnel with a 25 mm diameter orifice was measured five times, and the average time was used for Hall flowmeter analysis. For a quantitative evaluation of flow characteristics, the Hausner ratio, calculated as the ratio of apparent density to tap density, was derived and compared.

The mixed powder was used to fabricate specimens with dimensions of 10 × 10 × 5 mm using an L-PBF machine (AnyX-120, CSCAM). The additive manufacturing process was carried out in a high-purity argon atmosphere, with recoating speed, layer thickness, and hatch spacing fixed at 30 mm/s, 0.03 mm, and 0.14 mm, respectively. Laser power and scan speed were set as process variables, resulting in the fabrication of 25 specimens with different laser powers and scan speeds.

For phase analysis of the fabricated specimens, X-ray diffraction (XRD; D8 ADVANCE, Bruker) was performed within a 20-90° diffraction angle range at 3 °/min, and elemental distribution was analyzed using energy dispersive spectroscopy (EDS; ZEISS, Gemini360). Microstructural analysis was carried out using scanning electron microscopy (SEM; ZEISS, LEO "SUPRA 55"), and optical microscopy (OM; ZEISS, Axioscope 5).

To compare the mechanical properties before and after alloying, Vickers hardness measurements were performed with a 500 gf load and 10-second dwell time for 10 cycles, and the average value was calculated. Tensile tests were conducted using ASTM E8 specimens (Fig. 1) produced under the same conditions, and the average value was derived after three measurements using a tensile testing machine (SHIMADZU CORPORATION, AG-Retrofit).

3. Results and Discussion

3.1 Powder preparation

The morphologies of the Ti and Fe powder used in this study are shown in the SEM images in Fig. 2(a) and (b). Fig. 2 (a) particles produced via HDH process exhibit a non-spherical morphology, whereas (b) particles produced by gas atomization feature a rounded, spherical shape. Fig. 2(c) presents the particle size analysis results, indicating that the d50 of Ti is 32.19 μm and that of Fe is 42.66 μm. Given that the size difference between the Ti base material and the Fe alloy element powder is several μm, powders with a relatively small particle size difference were selected to ensure the stability of the mixed powder and the process. No Fe peaks were detected in the X-ray diffraction (XRD) pattern after powder mixing (Fig. 2(d)), which can be attributed to the low Fe content of 3 wt.%.

The results of the flowability evaluation, which confirm the applicability of the L-PBF process to the mixed powder, are presented in Table 2. A previous study conducted by our research team [21] demonstrated that the addition of 0.1 wt.% SiO_2 nanoparticles to non-spherical Ti-6Al-4V powder significantly improved its flow characteristics, making it suitable for the L-PBF process. Therefore, a similar evaluation of the flowability of Ti-3Fe powder, both before and after dry coating with 0.1 wt.% SiO_2 nanoparticles, was performed. The Ti-3Fe powder mixture without SiO_2 addition exhibited extremely poor flow properties, making measurement with a Hall flowmeter unfeasible. In contrast, the Ti-3Fe + 0.1 wt.% SiO_2 powder mixture showed flow properties comparable to those reported in

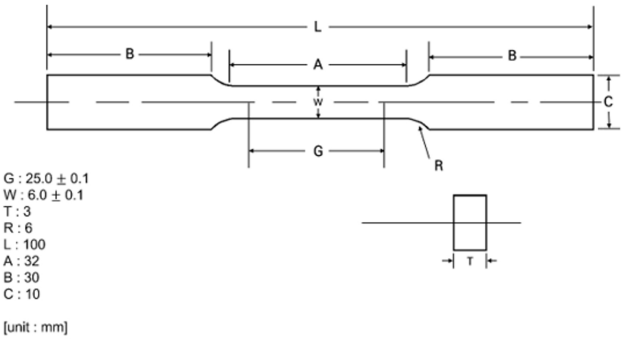

Fig. 1. Schematic of the tensile specimen according to ASTM E8 standards

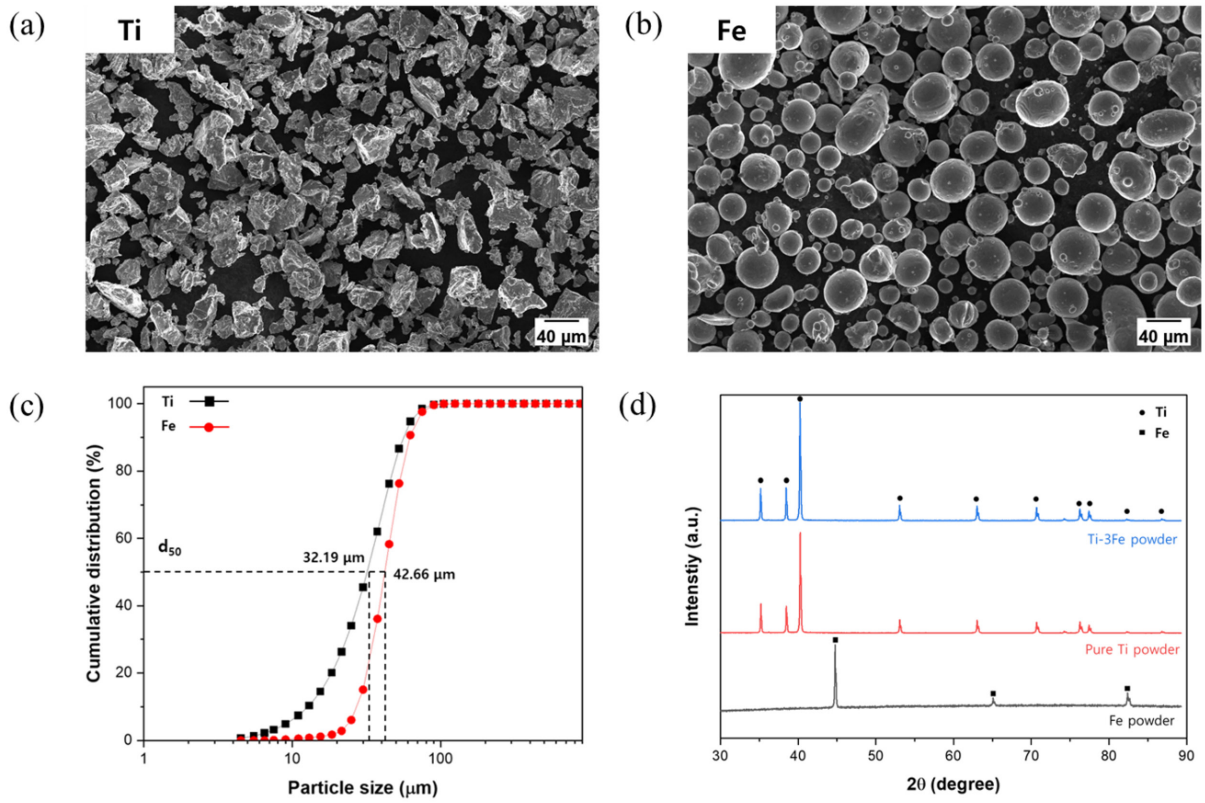

Fig. 2. (a), (b) Scanning electron microscopy image of Ti and Fe powder, (c) particle size analysis results of the powder, (d) X-ray diffraction patterns before and after mixing of the powders

Table 2. Flow characteristics of Ti-3Fe mixed powder before and after the addition of SiO_2

	Ti-3Fe	Ti-3Fe + 0.1 wt.% SiO_2
Hall flowmeter (Standard, s/50 g)	No flow	92.61 ± 3.14
Hall flowmeter (Carney, s/50 g)	No flow	16.75 ± 0.94
Hausner ratio	1.40	1.15

previous studies. Specifically, the Hausner ratio, which is calculated by dividing the apparent density by the tap density, indicates excellent flowability when it approaches 1 [22]. The mixed powder with SiO_2 addition exhibited even better flow properties, with a value of 1.15 – approximately 0.05 lower than the values reported in previous studies. The flow property evaluation results when SiO_2 nanoparticles were added to Ti-3Fe powder were comparable to, or in some cases superior to, those observed in previous studies that successfully achieved layering. Therefore, we conclude that there should be no issues in applying the L-PBF process to this material.

3.2 L-PBF process and sample fabrication

Even when the same material is used, characteristics such as microstructure and relative density can vary depending on the process conditions for specimens produced by the L-PBF process. This variation arises because the morphology and geometric structure of the melt pool formed during the process are influenced by the process variables. Therefore, it is essential to determine the optimal combination of the four key L-PBF process variables: laser power (P), scan speed (v), hatch spacing (h), and layer thickness (t). The volumetric energy density (VED), calculated using equation (2), serves as a quantitative thermodynamic indicator and is primarily used to optimize the L-PBF process [23].

$$\mathrm{VED} = \frac{\mathrm{P}}{\mathrm{v} \cdot \mathrm{h} \cdot \mathrm{t}} \quad (2)$$

In this study, the process conditions were optimized by fixing the layer thickness and hatch spacing, while laser power and scan speed – the variables related to the laser irradiation – were selected as the primary variables. A total of 25 process conditions, involving different laser power and scan speed settings

within the VED range of 31.75-214.30 J/mm^3, were combined to produce the specimens shown in Table 3.

As mentioned above, VED is a thermodynamic quantitative indicator, meaning it quantifies the amount of energy injected per unit volume. However, it does not account for the geometric behavior determined by the depth of the molten pool formed during the process, nor its internal dynamics [24]. For example, even when two specimens yield the same VED value with different combinations of process variables, their microstructures and mechanical properties may vary depending on the specific variables employed. Therefore, in this study, VED was not used as an absolute indicator for process optimization, but rather as a comparative value between different process conditions. Optimization was performed based on the relative density and microstructure analysis of the produced samples.

3.3 Phase and microstructure analysis

XRD pattern analysis of the produced specimens (Fig. 3) revealed that the α'-Ti peak was dominant overall, although some β-Ti peaks remained at room temperature. This is due to the transformation of the β phase into α' martensite caused by the rapid cooling during the L-PBF process. As no peaks corresponding to the α-Fe phase or the intermetallic compounds TiFe or $TiFe_2$ were observed, it can be inferred that Fe exists in a dissolved state within the Ti lattice rather than as a separate phase. Furthermore, when comparing the XRD patterns of pure Ti specimens produced under the same conditions, it was observed that the α'-Ti peak of Ti-3Fe shifted slightly towards the high-angle region (increased 2θ). Peak shifts to the low- or high-angle regions can result from various factors, but in this study, we focused on the changes in the Ti lattice caused by the addition of Fe to interpret this phenomenon.

The atomic radii of Ti and Fe are generally known to be 147 pm and 126 pm, respectively [25]. According to the Hume-Rothery rule [26], two atoms can form a solid solution through substitution when the difference in their radii is within 15 %. Ti

Table 3. L-PBF process conditions and resulting volumetric energy density (VED)

Sample number	Laser power (W)	Scan speed (mm/s)	Hatch spacing (mm)	Layer thickness (mm)	VED (J/mm^3)	Relative density (%)
1	80	600	0.14	0.03	31.75	93.66
2	80	500	0.14	0.03	38.10	94.63
3	80	400	0.14	0.03	47.62	95.08
4	80	300	0.14	0.03	63.49	96.20
5	80	200	0.14	0.03	95.24	96.96
6	100	600	0.14	0.03	39.68	97.48
7	100	500	0.14	0.03	47.62	97.57
8	100	400	0.14	0.03	59.52	96.47
9	100	300	0.14	0.03	79.37	95.73
10	100	200	0.14	0.03	119.05	97.90
11	120	600	0.14	0.03	47.62	98.68
12	120	500	0.14	0.03	57.14	98.91
13	120	400	0.14	0.03	71.43	97.12
14	120	300	0.14	0.03	95.24	96.31
15	120	200	0.14	0.03	142.86	97.98
16	150	600	0.14	0.03	59.52	98.52
17	150	500	0.14	0.03	71.43	99.12
18	150	400	0.14	0.03	89.29	99.21
19	150	300	0.14	0.03	119.05	98.83
20	150	200	0.14	0.03	178.57	99.01
21	180	600	0.14	0.03	71.43	99.07
22	180	500	0.14	0.03	85.71	98.63
23	180	400	0.14	0.03	107.14	98.62
24	180	300	0.14	0.03	142.87	98.92
25	180	200	0.14	0.03	214.30	98.56

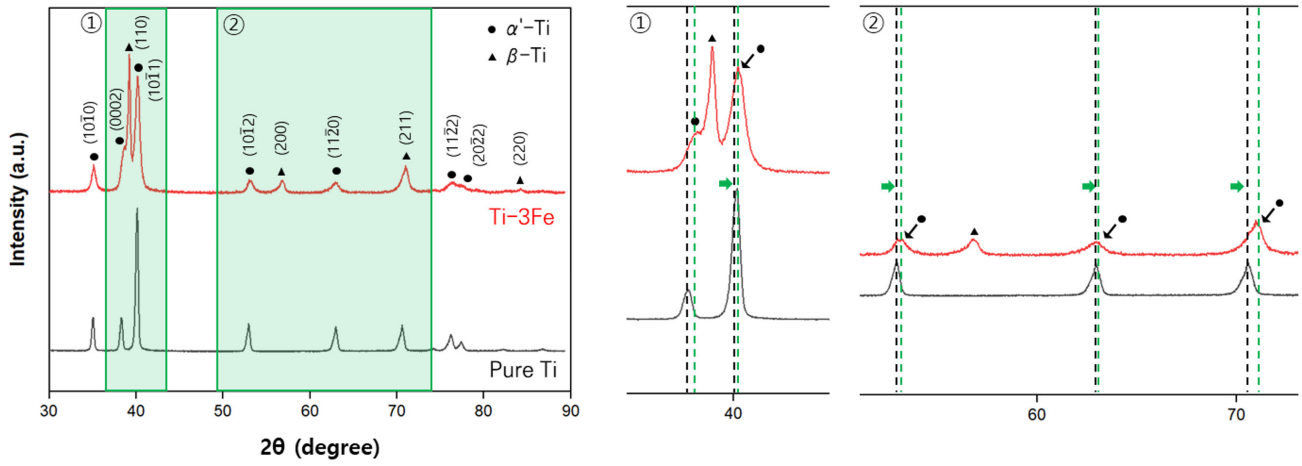

Fig. 3. X-ray diffraction patterns of Ti-3Fe and pure Ti fabricated specimens, and enlarged regions ① and ② for peak shift analysis

and Fe have a radius difference of approximately 14.29 %, which means they fall within the range where solid solution formation is feasible during alloying. Therefore, when the relatively smaller-radius element Fe is dissolved into the Ti matrix, lattice contraction occurs in the solid solution, resulting in distortion and a decrease in interplanar spacing and lattice constants [27]. The interplanar spacing (d) was calculated using peak angle (2θ) of the (0002) and (101¯0) planes of α'-Ti (in Fig. 3) by plugging it into Bragg's law (3). The derived interplanar spacing was then used to calculate the lattice constants (a, c) of the α-Ti HCP structure using equation (4), thereby confirming the change in lattice constants [28].

$$n\lambda = 2dsin\theta \tag{3}$$

$$\frac{1}{d_{hkl}^2} = \frac{4}{3}\cdot\frac{h^2+hk+k^2}{a^2}+\frac{l^2}{c^2} \tag{4}$$

The calculation results are presented in Table 4. The theoretical calculations, based on the peak angle, reveal that the lattice constants a and c of Ti-3Fe decreased by 0.14 % and 0.51 %, respectively, compared to pure Ti with no Fe added. This indicates that the reduction in interplanar spacing and lattice constants, caused by the addition of Fe, resulted in a shift of the XRD peaks towards the high-angle region. This suggests that the Fe elements added during the powder mixing stage formed a solid solution with Ti.

The results of the relative density measurements according to the VED of 25 specimens are shown in Fig. 4(a). While there was a general trend of increasing relative density with higher VED values, no specific correlation, such as a linear proportional relationship, was observed. However, specimens within the 70-90 J/mm^3 range exhibited relatively high relative densities. Specimen #18, with a VED value of 89.29 J/mm^3, had the highest relative density at 99.21 %. EDS mapping of specimen #18 in Fig. 4(b) reveals that the added Fe is uniformly distributed throughout the Ti matrix. Accordingly, specimen #18 was designated as the optimal condition, and all subsequent analyses were performed on specimens fabricated under that setting.

Table 4. Interplanar spacing (d), lattice constants (a, c), and calculation results

	Pure Ti	Ti-3Fe
d_{100} (Å)	2.559 (2θ = 35.09°)	2.557 (2θ = 35.11°)
d_{002} (Å)	2.341 (2θ = 38.40°)	2.329 (2θ = 38.65°)
a (Å)	2.957	2.953
c (Å)	4.682	4.658

Fig. 5 show OM and SEM images of Ti-3Fe and pure Ti specimens fabricated under the same conditions in their as-built state. As shown in Fig. 5(a) and (b), both types of specimens formed a non-equilibrium lamellar α' martensite phase due to the rapid melting and cooling that occurs during the L-PBF process. The same microstructure is observed in the SEM images in Fig. 5(c) and (d), which is typical of specimens produced by L-PBF. Ti alloys containing 3 wt.% Fe exhibit the same α' martensite-dominated microstructure as pure Ti specimens, as they correspond to near β-Ti alloys and undergo no phase transformation. When approximately 9 wt.% or more of Fe is added, dendritic-shaped TiFe or $TiFe_2$ precipitates are typ-

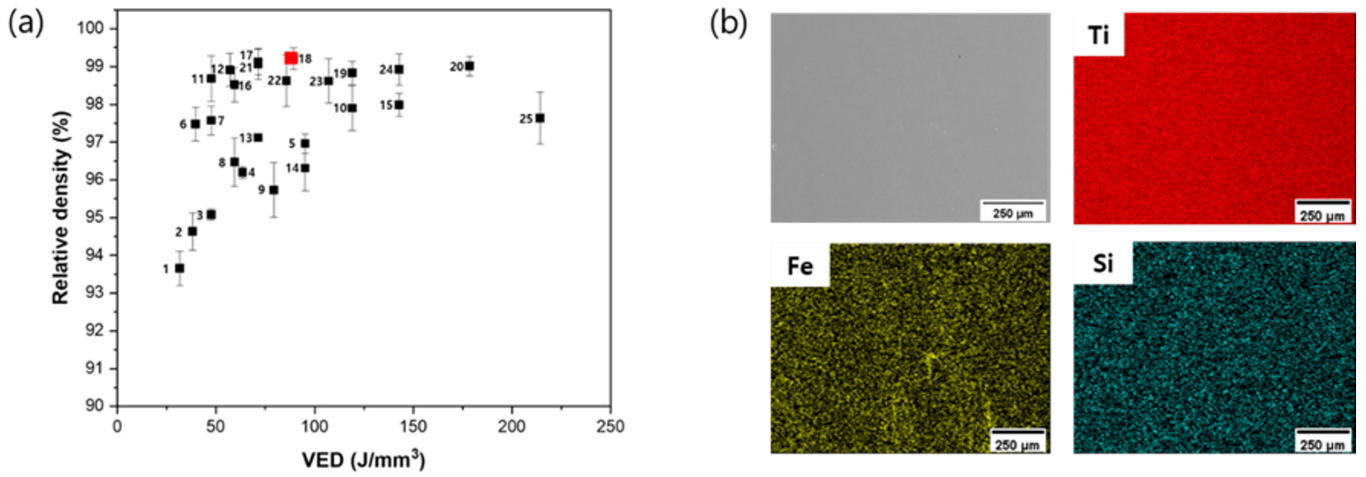

Fig. 4. (a) Relative density measurements as a function of volumetric energy density (VED), (b) energy dispersive spectroscopy mapping of specimen #18

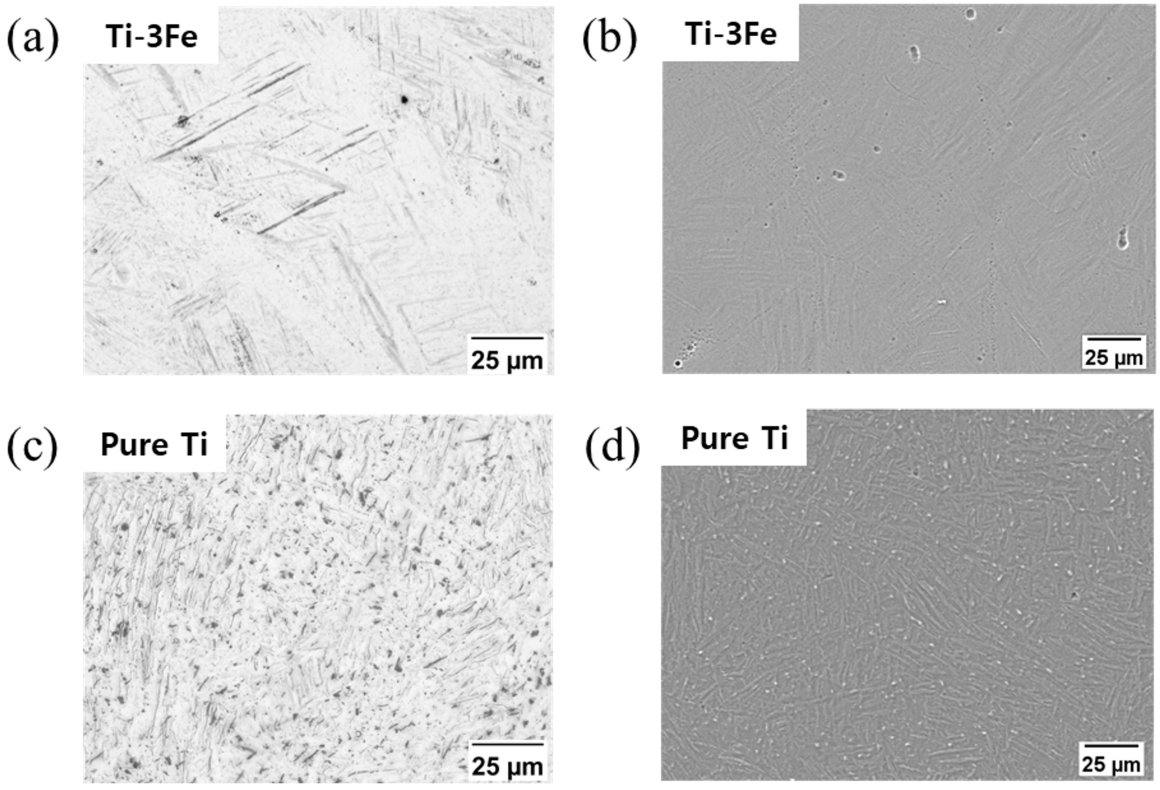

Fig. 5. (a), (c) Optical microscopy images of pure Ti and Ti-3Fe as-built specimens, (b), (d) scanning electron microscopy images of pure Ti and Ti-3Fe as-built specimens

ically observed [29]. However, such intermetallic compounds were not observed in this study due to the low Fe content.

3.4 Mechanical properties

Fig. 6 shows a graph comparing the Vickers hardness of 25 Ti-3Fe specimens with that of 25 pure Ti specimens, both of which were under the same process conditions. The average values obtained from 10 measurements are presented in Table 5. The hardness values for the Ti-3Fe and pure Ti specimens were 470.80 HV and 315.56 HV, respectively, showing an im-

provement in hardness of Ti-3Fe alloy approximately 49.19 % compared to pure Ti. This enhancement is attributed not only to the solid solution strengthening effect caused by the incorporation of Fe into Ti lattice (as confirmed in Section 3.3), but also to oxide dispersion strengthening resulting from the addition of SiO_2 nanoparticles to improve flowability. Two strengthening pathways are distinguished. Fe (composition-driven) acts as a β-stabilizer and dissolves in the Ti matrix; the absence of Fe or Ti-Fe intermetallic reflections together with high-angle XRD peak shifts (lattice contraction) evidences solid-solution formation. This composition change provides a direct contribution to the observed increases in strength/hardness and aligns with the work hardening behavior in some stress-strain curves. SiO_2 (microstructure-driven) promotes martensite grain size reduction under the L-PBF process (pinning-assisted refinement). In our research team's previous study [21], SiO_2 treatment of Ti-based powders produced an ~36.8 % decrease in martensite grain size verified by EBSD IPF maps, accompanied by higher hardness/strength, supporting a grain-refinement-mediated contribution relevant here. Because dispersion-related effects were not quantitatively isolated in the present dataset, we do not assign a numerical partition between the Fe and SiO_2 contributions. This limitation is deemed addressable by targeted nanoscale characterization-e.g., high-resolution TEM/STEM-EDS (and, where appropriate, APT or synchrotron XRD)-which is expected to enable quantitative resolution of dispersion-related contributions.

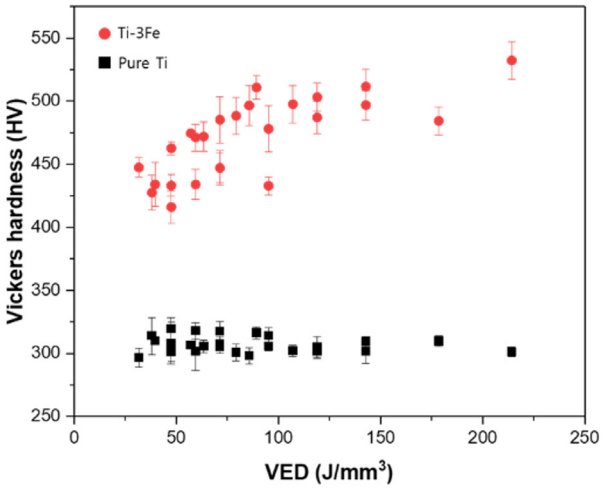

Fig. 6. VED-Vickers hardness graph of Ti-3Fe and pure Ti specimens

Table 5. Comparison of average Vickers hardness values for specimen #18 Ti-3Fe and specimen #18 pure Ti

Specimen	Vickers hardness (HV)
Ti-3Fe	470.80 ± 29.34
Pure Ti	315.56 ± 4.65

The Ti-3Fe alloy exhibits superior strength compared to pure Ti due to the solid solution strengthening effect and the oxide dispersion strengthening effect induced by the addition of SiO_2 nanoparticles, both of which were discussed in the previous section. As shown in Fig. 7 and Table 6, which present the stress-strain curve and tensile properties derived from actual tensile tests, the yield and ultimate tensile strengths of the Ti-3Fe alloy increased by 44.6 % and 52.3 %, respectively, compared to pure Ti. However, the elongation of the Ti-3Fe alloy is slightly lower than that of pure Ti, which can be attributed to lattice distortion caused by addition of Fe, as observed previously. While the addition of Fe enhances strength through solid solution strengthening, it also induces brittle behavior due to stress concentration caused by lattice distortion [30, 31]. In summary, the addition of Fe improves yield strength, tensile strength, and hardness through solid solution strengthening and the oxide dispersion strengthening effect of the added SiO_2 nanoparticles. However, lattice distortion leads to embrittlement, resulting in a decrease in elongation.

Meanwhile, in the stress-strain curve shown in Fig. 7, pure Ti exhibits a nearly horizontal curve with little increase in stress until fracture occurs after yield, shows a tendency for stress to increase even after the yield point. This behavior is typical characteristic of work hardening, which results from delayed necking due to the continuous accumulation of dislocations within the Ti-3Fe alloy during plastic deformation. Work hardening refers to the phenomenon where the strength of a material increases as the degree of deformation increases during plastic deformation. Accordingly, in this study we interpret the work hardening as arising from two indirect effects associated with Fe addition. First, Fe addition primarily elevates the initial yield strength via solid-solution strengthening, while also giving rise to lattice distortion and solute-induced stress fields that can impede dislocation motion and retard dynamic recovery. As Fe is solubilized into the Ti lattice, as previously described, lattice distortion and a stress field arise due to differences in atomic radii, which induce the solid solution strengthening effect [32]. The stress field generated at this stage acts as additional resistance during dislocation movement, delaying their rearrangement and annihilation. As a re-

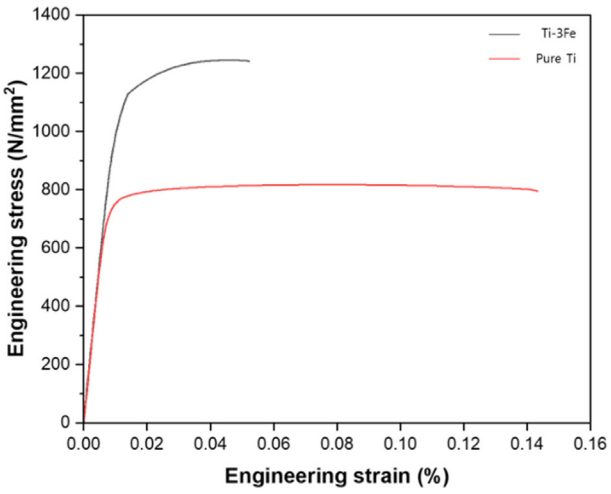

Fig. 7. Stress-strain curve of Ti-3Fe and pure Ti specimens

Table 6. Tensile test results for each specimen: yield strength, ultimate tensile strength, and elongation

Properties	Ti-3Fe	Pure Ti
Yield strength (MPa)	1063.85 ± 50.63	735.73 ± 2.16
Ultimate tensile strength (MPa)	1245.45 ± 44.86	817.66 ± 8.83
Elongation (%)	5.22 ± 0.26	14.33 ± 1.10

sult, the dislocation density retention time increases, and stress continues to accumulate, serving as a mechanism that promotes work hardening. Second, based on reports that solute alloying in Ti alloys reduces the stacking-fault energy (SFE) [33], Fe addition likewise leads to an approximately linear decrease in SFE; since lower SFE generally increases strain hardening [34], we regard this as an additional indirect effect of Fe addition. Therefore, in the elongation region of Fig. 7, the Ti-3Fe alloy shows a post-yield rise in stress indicative of work hardening, confirming that Fe addition not only induces solid-solution strengthening but also contributes to work hardening. In contrast, the pure Ti specimen exhibits an essentially flat post-yield segment, and no discernible work hardening was observed for pure Ti under our test conditions.

4. Conclusion

In this study, near β-Ti was produced by adding 3 wt.% of Fe powder, a eutectoid β-stabilizer, and 0.1 wt.% of SiO_2 nanoparticles to improve flowability to pure Ti powder, and then inducing alloying during the process using an in-situ alloying method. To compare the microstructure and mechanical properties before and after Fe addition, pure Ti specimens were used as a control group for comparative analysis.

- Based on two process conditions (laser power and scan speed) of L-PBF, 25 specimens with different process conditions were produced, and the process conditions were optimized for specimens with a relative density of 99 % or higher. To analyze the effect of the alloying element Fe, pure Ti specimens were produced under the same optimized process conditions, and their microstructure and mechanical properties were compared and analyzed.
- XRD pattern analysis confirmed the presence of the β phase at room temperature and the peak shift phenomenon in the high-angle region. In this study, we interpreted this phenomenon by focusing on the decrease in interplanar spacing and lattice constants due to dissolved Fe in the Ti matrix. The lattice constants a and c of the actual HCP structure were calculated to have decreased by 0.14 % and 0.51 %, respectively, using equations (3) and (4). Additionally, EDS mapping confirmed that Fe was uniformly dissolved throughout the specimen.
- When comparing the mechanical properties of pure Ti specimens and Ti-3Fe specimens, the hardness of Ti-3Fe specimens improved by approximately 49.19% compared to pure Ti specimens, and the yield strength and ultimate tensile strength increased by 44.6 % and 52.3 %, respectively. However, the elongation of the Ti-3Fe specimen showed a slight decrease compared to the pure Ti specimen, which was attributed to brittleness induced by internal stress concentration resulting from lattice distortion.

Funding

This work was supported by the National Research Foundation of Korea (NRF) grant funded by the Korean government (Grant No. RS-2023-00212081) and by Korea Institute of Energy Technology Evaluation and Planning (KETEP) grant funded by the Korean government (MOTIE)(RS-2024-00349003), Support for on-site practical training linked to public enterprises).

Conflict of Interest

B. Lee serves as an editor of the Journal of Powder Materials editing, but has no role in the decision to publish this article. Except for that, no potential conflict of interest relevant to this article was reported.

Data Availability Statement

Data will be made available on request.

Author Information and Contribution

Sehun Kim: MSc student; Conceptualization of the study, original manuscript drafting.

Ukju Gim: MSc student; Preparation and surface treatment of Ti powder; SiO_2 nanoparticle coating.

Taehu Kang: MSc student; L-PBF process trials under varied energy densities, Review & Editing.

Jongik Lee: MSc student; Microstructural characterization by OM, XRD, Review & Editing.

Sanghee Jeong: MSc student; SEM imaging, Review & Editing.

Jimin Han: Undergraduate student; Review & Editing.

Bin Lee: Associate professor; Project supervision and funding acquisition, overall study conceptualization, critical review and editing of the manuscript; correspondence with the journal.

Acknowledgments

None.

ORCID

Bin Lee, https://orcid.org/0000-0002-9906-9651

References

[1] P. Pushp, S. M. Dasharath and C. Arati: Mater. Today Proc., **54** (2022) 537.
[2] J. C. Williams and R. R. Boyer: Metals(Basel), **10** (2020) 705.
[3] C. Veiga, J. P. Davim and A. J. R. Loureiro: Rev. Adv. Mater. Sci., **32** (2012) 133.
[4] J. D. Cotton, R. D. Briggs, R. R. Boyer, S. Tamirisakandala, P. Russo, N. Shchetnikov and J. C. Fanning: JOM, **67** (2015) 1281.
[5] R. P. Kolli and A. Devaraj: Metals, **8** (2018) 506.
[6] P. Pesode and S. Barve: J. Eng. Appl. Sci., **70** (2023) 25.
[7] F. Huber, T. Papke, C. Kauffmann, R. Rothfelder, P. Krakhmalev, M. Merklein and M. Schmidt: Mat. Sci. Eng., **A, 808** (2021) 141374.
[8] S. G Careau, E. Ulate-Kolitsky and B. Tougas: Mater., **24** (2022) 101471.
[9] W. Wang, X. Zhang and J. Sun: Mat. Charact., **142** (2018) 398.
[10] S. Ma, X. Min, M. Lv and J. Dai: Mater. Sci. Eng., **A, 898** (2024) 146372.
[11] G. Al-Makhzumi, K. L. Dahm, F. Yang and L. Bolzoni: Mater. Chem. Phys., **308** (2023) 128244.
[12] H. Wang, H. L. Luo, J. Q. Chen, J. C. Tang, X. Y. Yao, Y. H. Zhou and M. Yan: Mat. Character., **182** (2021) 111526.
[13] H. Hwang, Y. Lee, J. Park and D.-G. Lee: J. Powder Mater., **29** (2022) 325.
[14] C. Ni, J. Zhu, B. Zhang, K. An, Y. Wang, D. Liu, W. Lu, L. Zhu and C. Liu: Virt. Phys. Prototy., **20** (2025) e2446952.
[15] S. Cao, Y. Zou, C. V. S. Lim and X. Wu: Light: Adv. Manuf., **2** (2021) 20.
[16] J. C. Colombo-Pulgarín, C. A. Biffi, M. Vedani, D. Celentano, A. Sánchez-Egea, A. D. Boccardo and J.-P. Ponthot: J. Mater. Eng. Perform., **30** (2021) 6365.
[17] M. S. Knieps, W. J. Reynolds, J. Dejaune, A. T. Clare and A. Evirgen: Mater. Sci. Eng., **A, 807** (2021) 140849.
[18] S. Huang, R. L. Narayan, J. H. K. Tan, S. L. Sing and W. Y. Yeong: Acta Mater., **204** (2021) 116522.
[19] R. Duan, S. Li, B. Cai, Z. Tao, W. Zhu, F. Ren and M. M. Attallah: Composites, Part B, **222** (2021) 109059.
[20] S. Wei, Y. Zhao, B. Zhang, P. Wang and U. Ramamurty: Mat. Sci. Eng. A, **888** (2023) 145795.
[21] U. Gim, S. Kim, T. H. Kang, J. Lee, S. Jeong, J. Han and B. Lee: Powder Metall., **68** (2025) 95.
[22] B. Lee, D.-K. Kim, Y. I. Kim, D. H. Kim, Y. Son, K.-T. Park and T.-S. Kim: J. Powder Mater., **27** (2020) 509.
[23] R. Zhao, C. Chen, W. Wang, T. Cao, S. Shuai, S. Xu, T. Hu, H. Liao, J. Wang and Z. Ren: Addit. Manuf., **51** (2022) 102605.
[24] U. Scipioni Bertoli, A. J. Wolfer, M. J. Matthews, J. P. R. Delplanque and J. M. Schoenung: Mater. Des., **113** (2017) 331.
[25] N. N. Greenwood, N. Neill and A. Earnshaw, Chemistry of the Elements, 2nd edElsevier, (2012).
[26] Q. F. He, Y. F. Ye and Y. Yang: J. Phase Equilib. Diffus., **38** (2017) 416.
[27] A. Kilmametov, Y. Ivanisenko, B. Straumal, A. A. Mazilkin, A. S. Gornakova, M. J. Kriegel, O.B. Fabrichnaya, D. Rafaja and H. Hahn: Scr. Mater., **136** (2017) 46.
[28] Z. Elahi and W. Gull: Spreadsheets in Eudcation. Indexing the X-Ray Diffraction Patterns of Cubic and Hexagonal Structures Using Spreadsheets, (2024).

[29] T. Teramae, T. Tanaka, M. Fukuo, K. Shitata, J. Umeda, S. Li, A. Alhazaa and K. Kondoh: J. Alloys Compd., **858** (2021) 158292.
[30] M. A. Haq, I. Ali, Y. Song and B. S. Kim: Mater. Today Commun., **38** (2024) 107743.
[31] Z. He, W. Yang, C. Liu, X. Wei and J. Wang: Metals(Basel), **14** (2024) 198.
[32] H. M. Kim, Y. J. Lee, J. G. Lee and D. G. Lee: J. Mater. Res. Technol., **33** (2024) 7406.
[33] A. Yu: SCIREA J. Phys., **1** (2016) 1.
[34] D. T. Pierce, J. A. Jiménez, J. Bentley, D. Raabe and J. E. Wittig: Acta Mater., **100** (2015) 178.

Research Article

pISSN 2799-8525 · eISSN 2799-8681
J Powder Mater 2025;32(4):299-308

Journal of
Powder Materials

Fabrication and Pore Characteristics of Metal Powder Filters with a Cross-Sealed Honeycomb Shape Using Material Extrusion Additive Manufacturing

Minji Kim[1,2], Min-Jeong Lee[1,2], Su-Jin Yun[1], Poong-Yeon Kim[1], Hyeon Ju Kim[1], Juyong Kim[3], Jung Woo Lee[2,*], Jung-Yeul Yun[1,*]

[1]Nanomaterials Research Center, Korea Institute of Materials Science KIMS, Changwon 51508, Republic of Korea
[2]Department of Materials Science and Engineering, Pusan National University, Busan 46241, Republic of Korea
[3]3DP R&D Center, REPROTECH, Suwon 16229, Republic of Korea

The development of high-performance metal filters is essential for maintaining ultra-clean environments in semiconductor manufacturing. In this study, cross-sealed honeycomb filters were fabricated using STS316L powder via material extrusion additive manufacturing (MEAM) for semiconductor gas filtration. The effects of filter geometry (4 or 9 channels) and sintering temperature (850°C, 950°C, or 1,050°C) on performance were examined. First, 4-channel and 9-channel filters sintered at the same temperature (950°C) exhibited similar porosities of 50.08% and 50.57%, but the 9-channel filter showed a higher pressure-drop (0.26 bar) and better filtration-efficiency (3.55 LRV) than the 4-channel filter (0.19 bar and 3.25 LRV, respectively). Second, for filters with the same geometry (4-channel) increasing the sintering temperature reduced porosity from 64.52% to 40.33%, while the pressure-drop increased from 0.13 bar to 0.22 bar and filtration-efficiency improved from 2.53 LRV to 3.51 LRV. These findings demonstrate that filter geometry and sintering temperature are key factors governing the trade-off between air permeability, pressure-drop, and filtration efficiency. This work provides insights and data for optimizing MEAM-based high-performance metal powder filter design.

Keywords: Material Extrusion Additive Manufacturing (MEAM); Metal Filter; STS316L; Porosity; Sintering

Received: July 24, 2025
Revised: August 18, 2025
Accepted: August 19, 2025

***Corresponding author:**
Jung-Yeul Yun
E-mail: yjy1706@kims.re.kr

***Corresponding author:**
Jung Woo Lee
E-mail: jungwoolee@pusan.ac.kr

1. Introduction

Porous metals are solid materials containing numerous internal pores, and they have been extensively studied and applied in various industries due to their unique properties such as enhanced surface area for adsorption and catalytic activity, lightweight characteristics, and energy absorption [1-4]. In particular, maintaining an ultra-clean environment is crucial in semiconductor manufacturing processes, and high-performance metal filters are required to effectively remove fine particles and contaminants present in process gases [5-7]. Most commercial filters have simple disk or cylindrical geometries, which limits their ability to simultaneously improve filtration efficiency by capturing impurity particles and reduce the pressure drop, which refers to the difference in gas pressure before and after the filter [8, 9].

With recent advances in additive manufacturing (AM) technology, the demand for metal filters with complex internal architectures and optimized performance has been increasing [10-12]. Among various 3D printing-based filter fabrication methods, such as Powder Bed Fusion (PBF), Directed Energy Deposition (DED), and Material Extrusion Additive Manufacturing (MEAM), PBF and DED typically rely on laser-based equipment, which involves high capital and operating costs and imposes restrictions on usable materials [13-15]. In contrast, MEAM does not require lasers, which results in lower initial investment costs and enables the use of a wide range of feed-

https://doi.org/10.4150/jpm.2025.00234

stock materials. Additionally, the absence of mold fabrication enhances cost efficiency, makes it suitable for prototyping, and provides greater design flexibility for easily creating complex and precise structures [16-20]. Compared with the simple tube- or disk-shaped filters commonly available on the market, the complex internal channel geometry of the filters developed in this study is expected to enhance filtration efficiency by diversifying airflow paths and increasing the contact area with particles. These design advantages can be particularly beneficial in industrial fields such as semiconductor processing, where high-purity and high-efficiency filtration are required [21, 22].

In this study, the fabrication and pore characteristics of STS316L-based metal powder filters with a cross-sealed honeycomb shape using the MEAM process were systematically investigated, focusing on filter geometry and the evolution of pore structure with varying sintering temperatures. Two filter designs with identical outer dimensions (20 mm in diameter and 25 mm in height) but different internal flow channel numbers (4-channel and 9-channel) were produced to analyze the effects of structural complexity on porosity, air permeability, gas pressure drop, and filtration efficiency. Furthermore, three sintering temperatures (850, 950, and 1,050°C) were employed to examine microstructural changes and the corresponding reduction in porosity, followed by quantitative evaluation of variations in air permeability and filtration performance. Through this approach, this study aims to elucidate the combined effects of geometry and sintering conditions, which are two key variables influencing the performance of metal filters, and to provide fundamental data for establishing optimized design strategies for the development of high-performance metal filters.

2. Experimental Section

The manufacturing process of the honeycomb filters produced in this study is illustrated in Fig. 1. The process involves mixing the STS316L metal powder with the binder, pelletizing the mixture, and then shaping it using the Material Extrusion Additive Manufacturing (MEAM) process. This is followed by solvent debinding and thermal debinding to remove the binder, and finally sintering to produce the final filters, which were then subjected to characterization.

The chemical composition of the STS316L metal powder (Daido, Japan) and the M1 binder (Atect, Japan) used in this study are presented in Table 1 and Table 2, respectively. The STS316L powder and M1 binder were mixed in a weight ratio of 86.34 wt.% to 13.66 wt.% to prepare the feedstock. The prepared feedstock was used to fabricate two honeycomb filter structures with different internal flow path complexities: a 4-channel design and a 9-channel design. Fig. 2 shows the modeling images of these filters, where Fig. 2(a) and (b) depict the overall geometry and cross-section of the 4-channel filter, and Fig. 2(c) and (d) show those of the 9-channel filter. The internal channels were designed with cross-shielded sections at the top and bottom to force the fluid to pass through the internal walls. Both filters were designed with the same external dimensions (20 mm in diameter and 25 mm in height), but the total wall volume and mass were increased in the 9-channel design due to the greater number of internal channels.

MEAM-based additive manufacturing was performed using an RPT_CME300 (REPROTECH, Korea) system under the following conditions: nozzle diameter of 0.4 mm, nozzle temperature of 175°C, bed temperature of 65°C, layer height of 125 μm, and printing speed of 35 mm/s. The green parts were immersed in n-heptane for 24 h to perform solvent debinding, removing the low-molecular-weight binder components SA (stearic acid) and PW (paraffin wax), followed by thermal debinding in an argon (Ar) atmosphere, where the temperature was ramped to 800°C at a rate of 1°C/min and held for 1 h to remove the high-molecular-weight binders EVA and PE. Subsequently, the debound specimens were sintered under high vacuum (5×10^{-5} torr) at 850, 950, and 1,050°C for 1 h to evaluate the effects of sintering temperature on the pore structure.

Sintering temperature was set as one of the key process variables to analyze its effect on the pore structure and filtration performance of metal filters. The powder used was STS316L stainless steel, which has a melting point of approximately 1,400°C. Therefore, sintering was conducted below the melting point, selecting a temperature range where neck formation between particles and pore retention are balanced. Generally, the sintering process is divided into initial, intermediate, and final stages, with the intermediate stage being most suitable for filter fabrication, as it ensures sufficient neck growth to secure mechanical strength while maintaining an adequate level of penetrating pores. In contrast, in the final stage, excessive densification eliminates pores, reducing permeability and impairing the filter's functionality. Based on this theoretical background and previous studies, we selected the range of 850–1,050°C corresponding to the intermediate sintering stage. [23, 24]

The particle morphology of the STS316L powder was examined using field emission scanning electron microscopy (FE-SEM, SU-70, Hitachi, Japan) in order to characterize surface features. The particle size distribution was measured using a la-

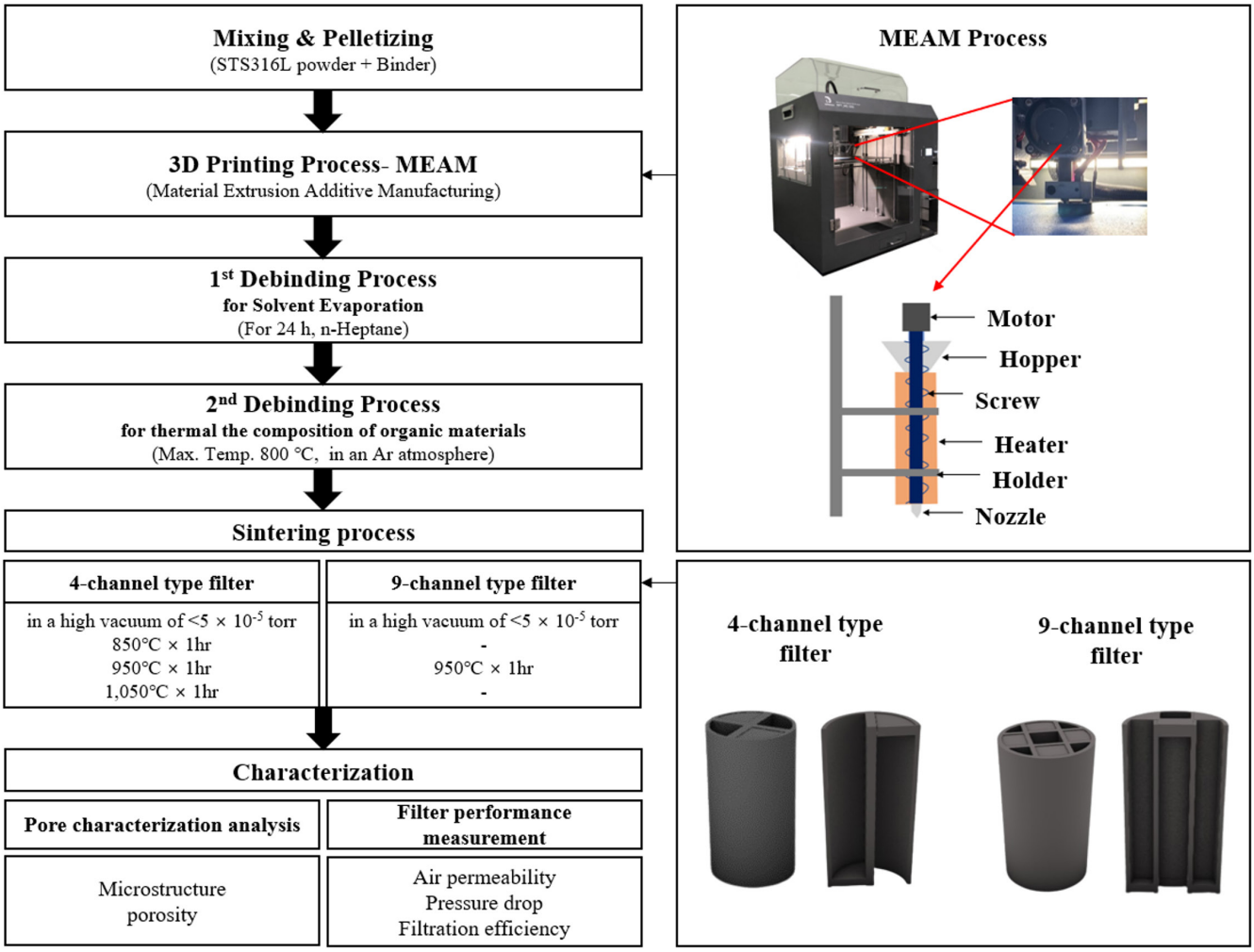

Fig. 1. Schematic flow chart illustrating fabrication of STS316L-based gas filters and conceptual images of the MEAM process used in this study.

ser diffraction particle size analyzer (PSA, LS13 320, Beckman Coulter). The microstructure of the sintered filters was examined using scanning electron microscopy (SEM, JSM-IT300, JEOL, Japan). The porosity was quantified based on SEM cross-sectional images using the ImageJ software. Air permeability was evaluated using a Gas Permeameter (GP-101A, Porous Materials Inc., USA) by measuring the flow rate versus gas pressure curves, and the gas pressure drop (ΔP) and filtration efficiency (Log Reduction Value, LRV) were quantitatively assessed following the international standard test method SEMI F38, which evaluates the particle removal efficiency of gas filters.

3. Results and Discussion

The STS316L powder used in this study served as the key raw material for fabricating filters via the MEAM process. The particle morphology and size distribution of the powder significantly affect not only printability, forming density, and sintering behavior, but also the final porosity and air permeability. Fig. 3(a) shows an FE-SEM (SU-70, Hitachi, Japan) image of the powder surface, which exhibits an overall irregular morphology. This is attributed to rapid and irregular solidification mechanisms inherent to the water atomization process. Fig. 3(b) presents the particle size distribution, measured using a laser diffraction particle size analyzer (PSA, LS13 320, Beckman Coulter), which shows a normal distribution with a single peak in the 10–100 μm range. The median particle size (D_{50}) was approximately 50 μm. These characteristics confirm the suitability of the powder for stable material flow during MEAM processing and for controlled pore structure development during sintering.

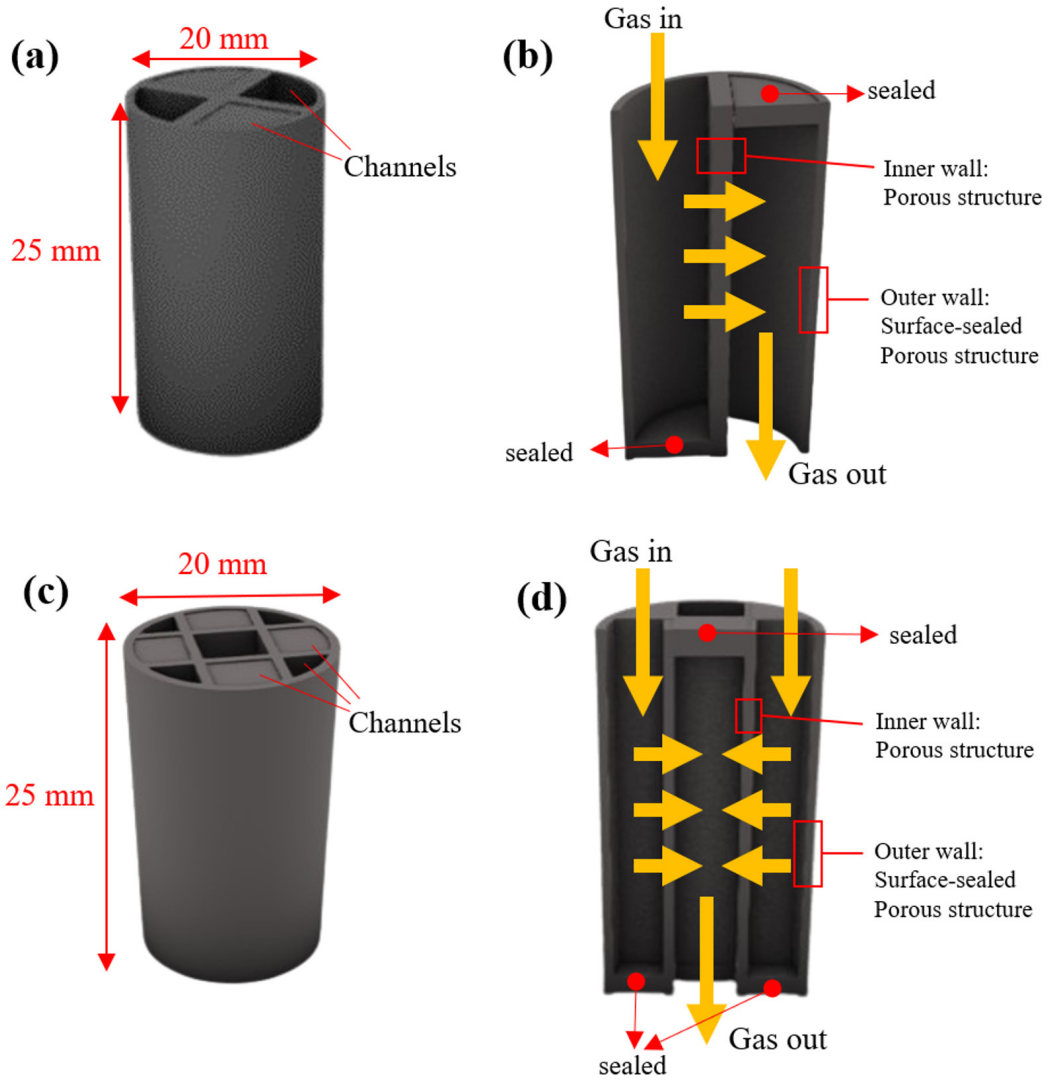

Fig. 2. Schematic images showing modeled filter geometries for the MEAM process. (a) 4-channel type filter, (b) cross-sectional image exhibiting gas flow along with porous structures, (c) 9-channel type filter, (d) cross-sectional image exhibiting gas flow along with porous structures.

Table 1. Component analysis of STS316L powder (Daido, Japan)

Component	C	Si	Mn	Ni	Cr	Cu	Mo	V	Other
wt.%	0.02	0.8	0.2	12	17	-	2.5	-	-

Table 2. Component analysis of M1 Binder (Atect, Japan) used for pelletizing

Component	PW	EVA	PE	SA
wt.%	57	20	20	3

PW, paraffin wax; EVA, ethylene-vinyl acetate; PE, polyethylene; SA, stearic acid.

The metal powder filters fabricated via the MEAM process were designed with two types of internal flow channel structures: 4-channel and 9-channel. Their external appearance and cross-sectional images are shown in Fig. 4. Fig. 4(a) presents the overall morphology and top/bottom views of the 4-channel filter sintered at 950°C, while Fig. 4(c) shows those of the 9-channel filter under the same conditions. As observed in the top and bottom views, both filters adopt a cross-shield configuration, in which the upper and lower sections are alternately blocked. Fig. 4(b) and (d) illustrate the internal wall structures (indicated by red dashed lines) of the 4-channel and 9-channel filters, respectively. Compared with the 4-channel design, the

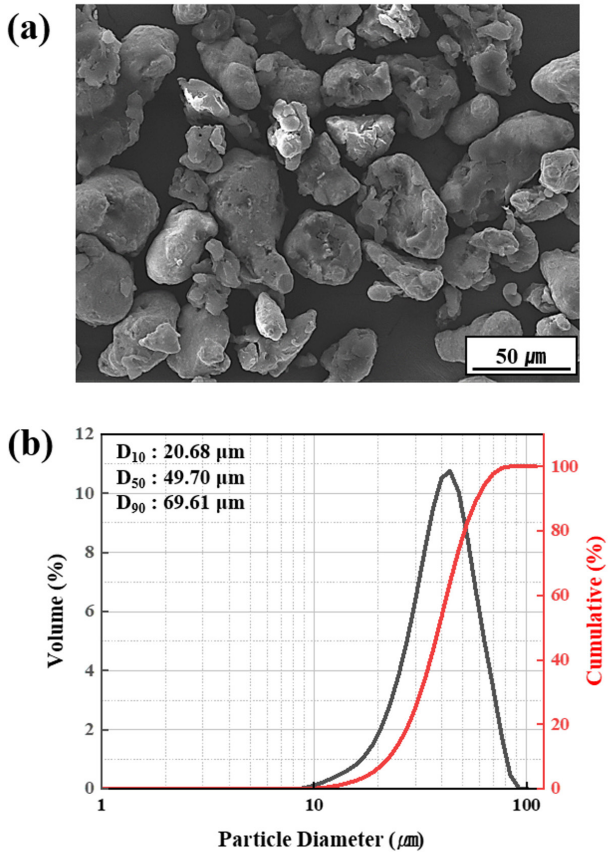

Fig. 3. Characteristics of the STS316L powder used in this study, (a) a surface morphology of water atomized particles (D_{50} ≈ 49.70 μm) showing an irregular shape, (b) particle size distribution curves.

9-channel filter provides more finely divided flow paths, which increase fluid dispersion and particle contact probability. In addition, the cross-shield design guides the fluid to enter through the upper opening, pass through the internal walls, and exit from the lower opening.

Although both filters were designed with identical outer dimensions (20 mm in diameter and 25 mm in height), differences in the number of channels and the total volume of internal walls resulted in variations in mass. The 4-channel filter weighed approximately 13.9 g, while the 9-channel filter weighed 17.1 g, which can be attributed to the increased fraction of metallic walls in the latter. Cross-sectional analysis of the internal walls, as shown in Fig. 4(b) and (d), revealed that the 4-channel filter had an internal wall cross-sectional area of 0.74 cm^2 and a wall volume of 1.85 cm^3, whereas the 9-channel filter had values of 1.26 cm^2 and 3.16 cm^3, respectively. This increased internal wall structure enlarges the effective filtration area for particle capture but simultaneously raises flow resistance, which can impact air permeability.

Fig. 5 presents the microstructures and porosity of specimens sintered at 950°C. The porosity data were obtained by performing three measurements each at the center and edge regions of every specimen, resulting in a total of six measurements per specimen, which were then averaged and expressed with standard deviations. Differences between measurement locations were negligible. In the microstructural images, the STS316L particles appear as bright regions, whereas the pores are observed as dark regions. Fig. 5(a) and (b) show the microstructures of the 4-channel and 9-channel filters, respectively, where no significant differences were observed between the two geometries. This indicates that comparable microstructural uniformity was achieved under identical MEAM and sintering conditions. Fig. 5(c) displays the porosity results, revealing values of 50.42% (standard deviation 0.80) for the 4-channel filter and 50.53% (standard deviation 0.93) for the 9-channel filter, suggesting that the number of internal channels had no meaningful influence on microstructural uniformity or porosity.

Fig. 6 shows the microstructures and porosity of 4-channel type filters sintered at different temperatures (850, 950, and 1,050°C). The microstructures in Fig. 6(a)–(c) reveal progressive densification with increasing temperature, as the STS316L regions become coarser while the pore regions diminish. According to the porosity results shown in Fig. 6(d), quantitative image analysis of the metallic and pore areas indicated a gradual decrease in porosity from 63.68% at 850°C to 50.42% at 950°C, and further to 39.38% at 1,050°C. The corresponding standard deviations were 0.73, 0.80, and 0.96, all below 1, confirming the reliability of the measurements. In particular, specimens sintered at 1,050°C exhibited a pronounced reduction in pore size and number, along with the formation of a continuous metallic network, indicating the development of a high-density structure.

Air permeability represents the relationship between gas flow rate and applied gas pressure across the filter, where a steeper slope in the flow rate–pressure curve indicates superior permeability. As shown in Fig. 7(a), the 4-channel filter exhibited higher flow rates than the 9-channel filter, demonstrating better air permeability. Air permeability represents the relationship between the gas flow rate and the applied pressure across the filter, where a steeper slope in the flow rate–pressure curve indicates superior permeability. As shown in Fig. 8(a) and (b), the 4-channel filter exhibited higher flow rates than the 9-channel filter, thereby demonstrating superior air permeability.

Gas pressure drop (ΔP) is another critical parameter for eval-

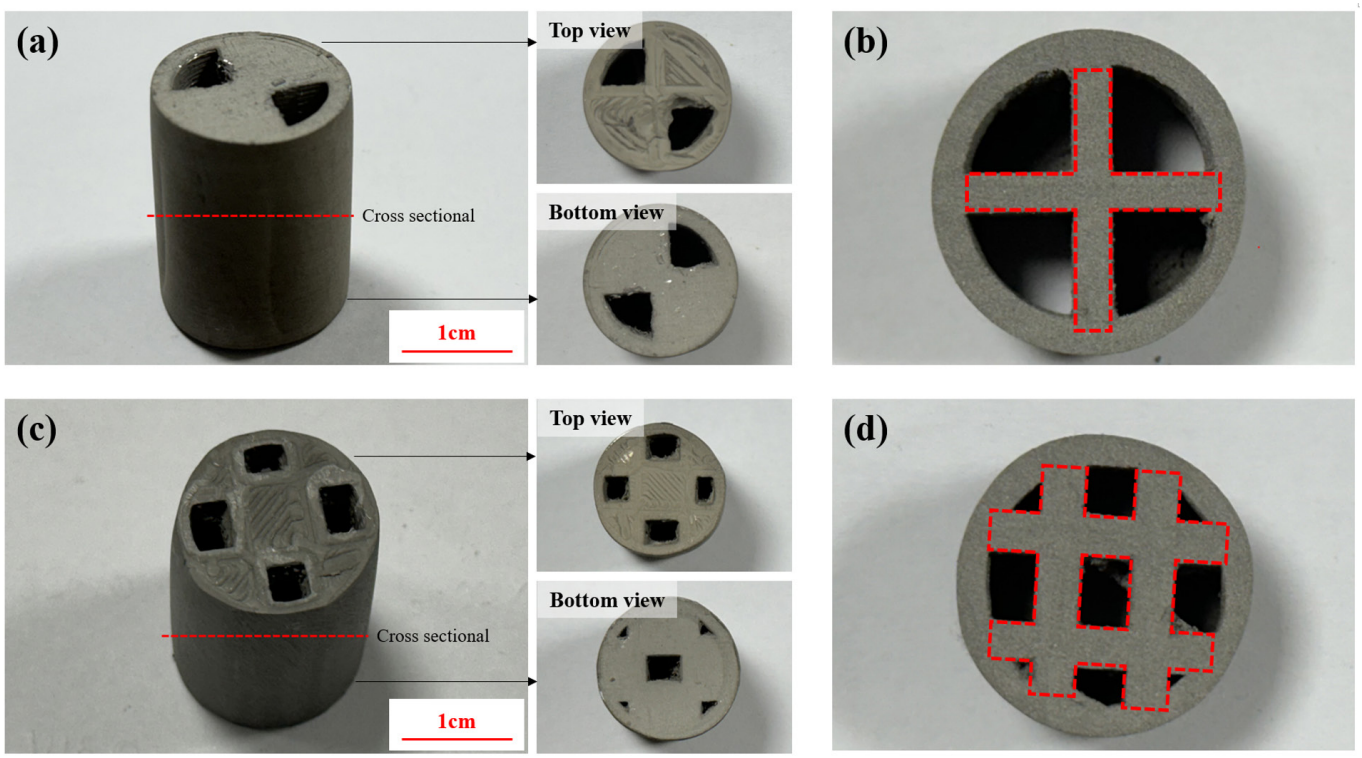

Fig. 4. Photographs of two different pore-structured filters fabricated by the MEAM and sintering process at temperature of 950°C: (a) 4-channel type filter showing top and bottom views, (b) cross sectional photograph indicated by a red-dotted line along the inner walls (c) 9-channel type filters showing top and bottom views, and (d) cross-sectional photograph indicated by a red-dotted line along the inner walls.

uating filter performance and is defined by the equation $\Delta P = P_{upstream} - P_{downstream}$. This represents the difference between the pressure of the gas introduced at the filter inlet ($P_{upstream}$) and the pressure measured at the outlet after passing through the filter ($P_{downstream}$). A higher pressure drop indicates greater energy loss within the filter, reflecting increased resistance to gas flow.

Filtration efficiency, another key performance metric, quantifies the ability of the filter to remove particles from the gas stream. In this study, filtration efficiency was expressed as the Log Reduction Value (LRV), which is calculated by counting the number of particles in the gas before and after filtration and then applying a logarithmic transformation. A higher LRV indicates a greater degree of particle removal, and thus, superior filtration performance.

Experimental results showed that the 9-channel filter exhibited a higher pressure drop compared to the 4-channel filter due to its larger internal wall area and volume, which increased flow resistance. However, this structural characteristic also provided a greater effective surface area for particle capture, thereby improving filtration efficiency. Consequently, the 9-channel filter achieved a filtration efficiency of 3.55 LRV, surpassing the 3.25 LRV of the 4-channel filter. In summary, the 9-channel filter presents a trade-off: while the increased flow resistance results in higher pressure drop, it simultaneously provides enhanced filtration efficiency. This highlights the coexistence of advantages and limitations depending on the intended design objectives.

The effect of sintering temperature is shown in Fig. 8(a) and (b). The results were obtained from tests conducted using the 4-channel filter, with the channel configuration fixed to isolate the effect of sintering temperature. As sintering temperature increased, air permeability decreased while gas pressure drop increased. Filtration efficiency improved from 2.53 LRV at 850°C to 3.25 LRV at 950°C, and to 3.51 LRV at 1,050°C. This behavior results from pore shrinkage and densification due to enhanced neck growth among particles, which reduces porosity but enhances particle interception.

In summary, differences in air permeability, gas pressure drop, and filtration efficiency are governed by internal channel complexity and wall structure. The 9-channel filter achieved higher filtration efficiency but exhibited lower permeability and higher pressure drop, reflecting a trade-off relationship. Similarly, higher sintering temperatures reduce porosity and perme-

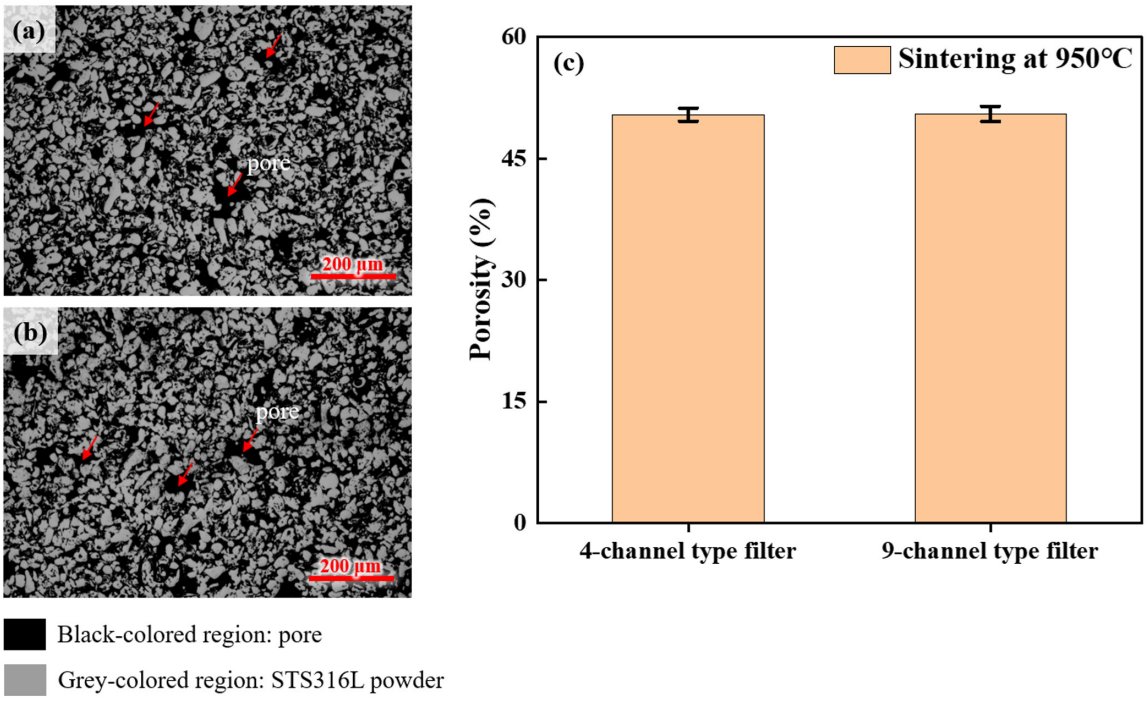

Fig. 5. Comparison of polished surface morphologies (showing similar pore structures) of (a) 4-channel type filter and (b) 9-channel type filter fabricated by the MEAM process, after sintering at 950°C, and (c) comparison of porosity between 4-channel and 9-channel type filters fabricated by the MEAM process, after sintering at 950°C.

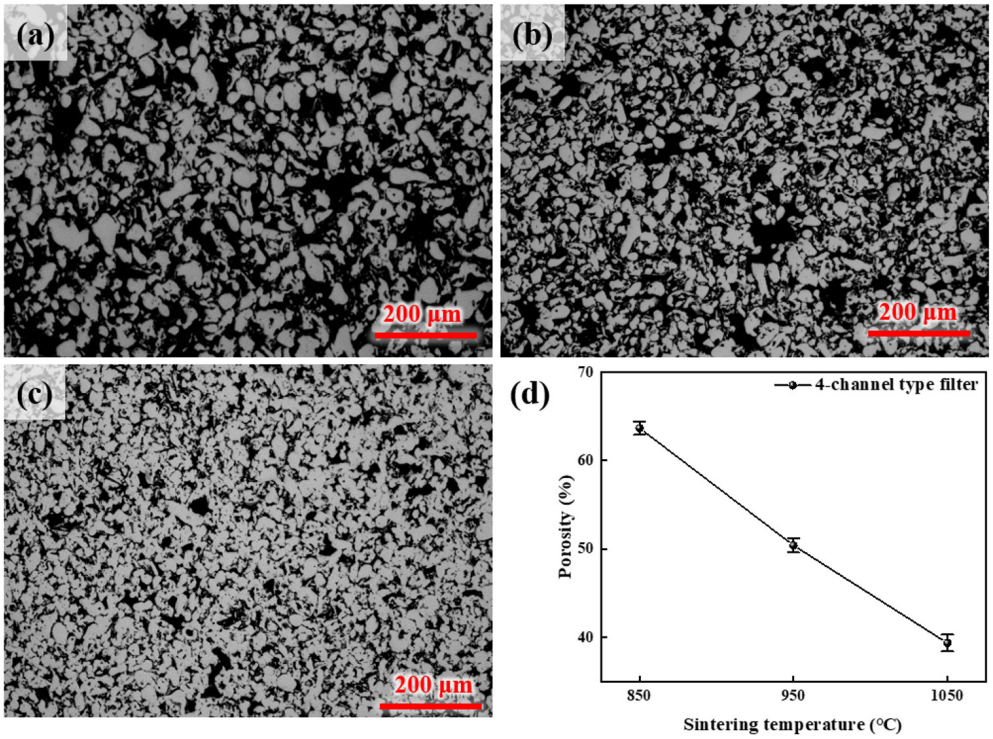

Fig. 6. Polished surface morphologies of 4-channel type filters fabricated by the MEAM process and sintered at (a) 850°C, (b) 950°C, and (c) 1,050°C, showing progressive densification with increasing temperature. (d) Quantitative porosity variation as a function of sintering temperature.

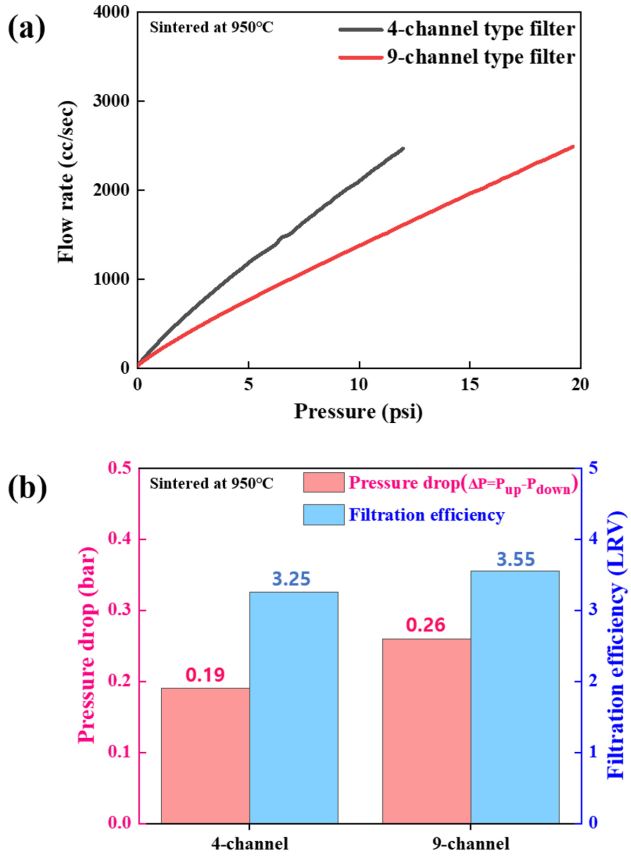

Fig. 7. Filter performance evaluation of 4-channel and 9-channel type filters fabricated by MEAM and sintered at 950°C: (a) air permeability test results showing flow rate–pressure curves, and (b) comparison of pressure drop ($\Delta P = P_{up}–P_{down}$) and filtration efficiency (LRV: log reduction value).

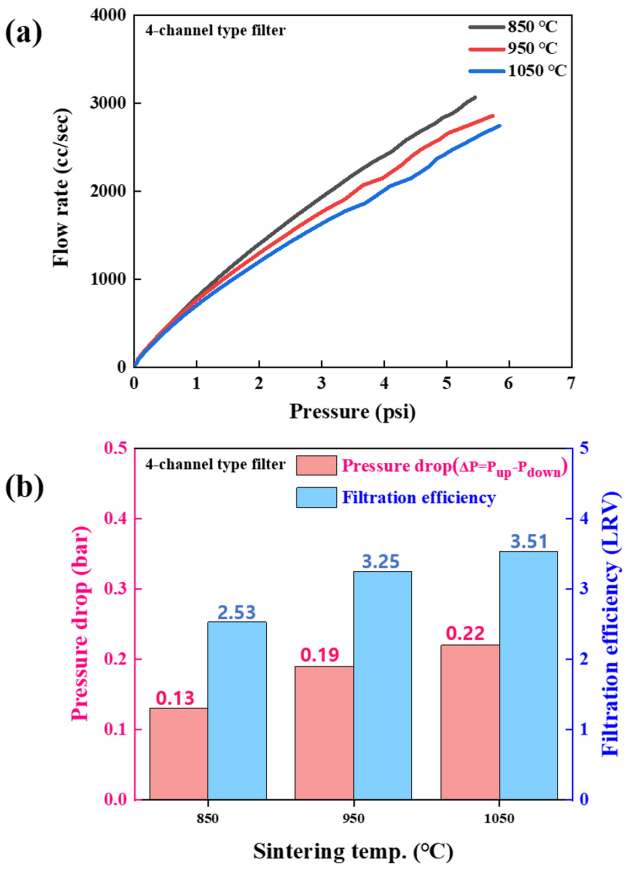

Fig. 8. Filter performance evaluation of 4-channel type filters fabricated by the MEAM process and sintered at different temperatures (850°C, 950°C, and 1,050°C): (a) air permeability test results showing flow rate–pressure curves, and (b) comparison of pressure drop ($\Delta P = P_{up}–P_{down}$) and filtration efficiency (LRV: log reduction value).

ability but improve filtration performance. These findings highlight the importance of simultaneously optimizing filter geometry and sintering conditions for balanced performance.

4. Conclusion

In semiconductor manufacturing processes, removing fine particles and contaminants that may cause wafer defects is critical for maintaining an ultra-clean environment. In this study, honeycomb-type metal filters with identical outer dimensions (20 mm in diameter and 25 mm in height) were fabricated using the Material Extrusion Additive Manufacturing (MEAM) process, and the effects of internal channel numbers (4-channel and 9-channel) on pore characteristics and filtration performance were systematically investigated. From a component designer's perspective, the optimal number of channels may vary depending on the intended application. If air flow is the primary concern, the 4-channel configuration is more advantageous, whereas if filtration efficiency is the priority, the 9-channel configuration is more suitable.

The results showed that the porosity values of the 4-channel and 9-channel filters were 50.57% and 50.08%, respectively, with negligible differences. However, significant variations were observed in air permeability, gas pressure drop, and filtration efficiency. The 4-channel filter, with its simpler internal geometry and smaller wall area (0.74 cm^2) and volume (1.85 cm^3), exhibited lower flow resistance and superior air permeability. Conversely, the 9-channel filter, having a larger wall area (1.26 cm^2), demonstrated higher filtration efficiency (3.55 LRV) but reduced air permeability and increased pressure drop (0.26 bar).

The sintering temperature was also a critical factor: as it increased, the microstructure became denser, and porosity decreased from 64.52% at 850°C to 40.33% at 1,050°C. This densification led to reduced air permeability and increased gas pressure drop (0.13 bar to 0.22 bar), while filtration efficiency improved from 2.53 to 3.51 LRV due to enhanced particle capture by finer pore structures.

These findings confirm that internal geometry and sintering temperature are two key design parameters that jointly affect the trade-off between permeability, pressure loss, and filtration efficiency. The results underscore the need for an optimized design strategy that balances filtration performance and energy consumption. This study provides valuable insights and quantitative effects of geometry and heat treatment conditions on filter performance, offering valuable data for the development of advanced metal filters and structural optimization for high-purity industrial applications, including semiconductor manufacturing.

Funding

This work is supported by the Ministry of Trade, Industry & Energy (MOTIE) of the Republic of Korea (no.00431424).

Conflict of Interest

The authors have no conflicts of interest to declare.

Data Availability Statement

The data that support the findings of this study are not publicly available due to confidentiality greements but are available from the corresponding author on reasonable request.

Author Information and Contribution

Minji Kim: M.S. candidate; conceptualization, writing–original Draft

Min-Jeong Lee: Ph.D. candidate; investigation (experimental assistance)

Su-Jin Yun: Researcher; investigation (experimental assistance)

Poong-Yeon Kim: Researcher; investigation (experimental assistance)

Hyeon Ju Kim: Researcher; investigation (experimental assistance)

Juyong Kim: Researcher; investigation (experimental assistance)

Jung Woo Lee: Professor, corresponding author; supervision, writing – review & editing

Jung-Yeul Yun: Ph.D., corresponding author; funding acquisition, supervision, writing – Review & editing

Acknowledgments

None.

ORCID

Minji Kim, https://orcid.org/0009-0005-5180-3473
Min-Jeong Lee, https://orcid.org/0000-0002-2604-7611
Su-Jin Yun, https://orcid.org/0000-0002-5688-3856
Poong-Yeon Kim, https://orcid.org/0009-0005-9940-8579
Hyeon Ju Kim, https://orcid.org/0000-0002-0799-295X
Juyong Kim, https://orcid.org/0000-0002-4637-9103
Jung Woo Lee, https://orcid.org/0000-0003-4705-9248
Jung-Yeul Yun, https://orcid.org/0000-0003-4135-1301

References

[1] S. Rashidi, J. A. Exfahani and A. Rashidi: Renewable and Sustainable Energy Rev., **73** (2023) 1198.
[2] B. Zhu, M. Duke, L. F. Dumee, E. Des Ligneris, L. Kong and S. Gray: Membranes., **8** (2018) 83.
[3] G. Korotcenkov and B. K. Cho: Crit. Rev. Solid State Mater. Sci., **35** (2010) 1-37.
[4] H. Föll, J. Carstensen and S. Frey: J. Nanomater., **2006** (2006) 091635.
[5] Y. Lee, H. S. Kim and J. H. Lee: J. Semiconductor Tech. Sci., **22** (2022) 145.
[6] R. L. Smith and P. K. Chatterjee: J. Vac. Sci. Technol., A, **14** (1996) 1761.
[7] Semiconductor Solutions Catalog, Mott Corporation (Published June 2025).
[8] J. Park, H. J. Ryu and H. K. Seok: J. Powder Mater., **21** (2014) 160.
[9] J. Banhart and J. Baumeister: MRS Online Proceedings Library (OPL)., **521** (1998) 121.
[10] W. E. Frazier: J. Mater. Eng. Perform., **23** (2014) 1917.
[11] T. DebRoy, H. Wei, J. S. Zuback, T. Mukherjee, J. W. Elmer, J. O. Milewski and W. Zhang: Prog. Mater Sci., **92** (2018) 112.
[12] D. Herzog, V. Seyda, E. Wycisk and C. Emmelmann: Acta

Mater., **117** (2016) 371.
[13] M. Vaezi, H. Seitz and S. Yang: Int. J. Adv. Manuf. Technol., **67** (2013) 1721.
[14] L. E. Murr, S. M. Gaytan, D. A. Ramirez, E. Martinez, J. Hernandez, K. N. Amato and R. B. Wicker: J. Mater. Sci. Technol., **28** (2012) 1.
[15] A. G. Demir and B. Previtali: CIRP Annals., **68** (2019) 793.
[16] A. I. Nurhudan, S. Supriadi, Y. Whulanza and A. S. Saragih: J. Manuf. Processes., **66** (2021) 228.
[17] J. Gonzalez-Gutierrez, S. Cano, S. Schuschnigg, C. Kukla, J. Sapkota and C. Holzer: Mater., **11** (2018) 840.
[18] P. Sevilla: J. Alloys Compd., **439** (2007) 67.
[19] M. J. Lee, Y. J. Yi, H. J. Kim, M. H. Park, B. K. Kim and J. Y. Yun: Arch. Metall. Mater., **64** (2019) 547.
[20] M. J. Lee, Y. J. Yi, H. J Kim, M. H. Park, B. K. Kim and J. Y. Yun: J. Powder Mater., **25** (2018) 415.
[21] P. Liu and G. F. Chen: Porous Materials., Elsevier (2014), 10.
[22] C. Osburn, H. Berger, R. Donovan and G. Jones: J. Environ. Sci., **31** (1988) 45.
[23] M. N. Rahaman: Ceramic Processing and Sintering., CRC Press (2017), 497.
[24] R. M. German: Sintering Theory and Practice., Wiley (1996), 135.

Research Article

pISSN 2799-8525 · eISSN 2799-8681
J Powder Mater 2025;32(4):309-314

Journal of
Powder Materials

Type 316H 스테인리스강 기판 위에 high velocity oxy-fuel 및 directed energy deposition 공정을 통한 순수 Ni 적층 및 기계적 특성 평가

이원찬[1], 남승주[1], 윤지현[2], 김정한[1,*]

[1]국립한밭대학교 신소재공학과
[2]한국원자력연구원 재료안전기술연구부

Evaluation of Mechanical Properties of Pure Ni Coatings on a Type 316H Stainless Steel Substrate via High-Velocity Oxy-fuel and Directed Energy Deposition Processes

Won Chan Lee[1], Seung Ju Nam[1], Ji-Hyun Yoon[2], Jeoung Han Kim[1,*]

[1]Department of Materials Science & Engineering, Hanbat National University, Daejeon 34158, Republic of Korea
[2]Department of Nuclear Materials Safety Research Division, Korea Atomic Energy Research Institute, Daejeon 34057, Republic of Korea

This study compares pure Ni coatings deposited on type 316H stainless steel using high-velocity oxy-fuel (HVOF) and directed energy deposition (DED) processes. Microstructural analysis showed that DED produced more uniform claddings with fewer pores, while HVOF resulted in incomplete melting and cracks. Elemental diffusion of Cr and Fe from the substrate into the cladding was evident in DED samples, especially at higher laser power, but minimal in HVOF due to low heat input. Vickers hardness testing revealed that DED claddings had higher hardness near the interface, which was attributed to solid solution strengthening and reduced porosity. Although HVOF better suppressed diffusion, it exhibited inferior mechanical properties due to internal defects. Overall, the DED process demonstrated superior coating quality and mechanical performance, suggesting its suitability for corrosion-resistant applications requiring both structural integrity and thermal stability, such as molten salt reactors.

Keywords: Molten salt reactor; HVOF; DED; Nickel; Cladding

Received: June 12, 2025
Revised: July 30, 2025
Accepted: July 31, 2025

***Corresponding author:**
Jeoung Han Kim
E-mail: jh.kim@hanbat.ac.kr

1. Introduction

용융염 원자로(Molten Salt Reactor, MSR)는 지속 가능한 에너지 생산을 목표로 개발 중인 차세대 원자로로, 기존의 경수로형 원자로(Light Water Reactor, LWR)에 비해 높은 열효율, 우수한 피동형 안전 시스템, 운전의 유연성 등 다양한 장점을 지닌다[1-3]. 특히, 소형 모듈 원자로(Small Modular Reactor, SMR) 형태로 구현이 가능하여 항공기, 선박, 원격지 전력 공급 등 다양한 응용 분야에서 주목받고 있다. MSR의 가장 큰 특징은 고온에서 액체 상태를 유지하는 용융염을 냉각재이자 핵연료 용매로 사용하는 설계 구조에 있으며, 이는 기존 원자로와 뚜렷이 구별된다. 이러한 설계는 고온 열전달 성능 향상과 함께 시스템의 안전성을 크게 제고한다. 예를 들어, 중대사고 발생 시 용융염이 누출되더라도 대기 중에서 빠르게 고화되어 2차 확산을 억제하는 성질을 가지고 있어, 안전성 측면에서 유리하다. 그러나 이러한 이점에도 불구하고, 염화물계 용융염은 고온에서 구조재에 심각한 부식을 유발하는 문제가 있어 MSR의 상용화를 저해하는 핵심 기술적 과제로 지적되고 있다[4, 5]. ASME Boiler & Pressure Vessel Code Section III Division 5에 따르면, MSR에 적용 가능한 구조재는 2.25Cr-1Mo, Modified

https://doi.org/10.4150/jpm.2025.00185

9Cr-1Mo 강, Type 304H, Type 316H, Alloy 800H, Alloy 617로 매우 제한적이다. 본 연구에서는 고온 크리프 저항성과 중성자 조사 저항성이 우수한 Type 316H를 구조재로 선정하였다. 그러나 기존 연구들에 따르면, Type 316H는 염화물계 용융염 환경에서 내식성이 매우 낮은 것으로 보고되고 있다[6, 7]. 이러한 한계를 극복하기 위해, ASME 코드에서는 등재된 재료를 사용할 경우 전체 두께의 10% 이내 범위에서 코드 미등재 재료를 클래딩(cladding) 형태로 적용하는 것을 허용하고 있다. 이에 본 연구는 염화물계 용융염 환경에서 우수한 내식성을 지닌 순수 니켈(Ni)을 스테인리스강 표면에 클래딩하는 방안을 검토하였다. 니켈은 철(Fe)이나 크롬(Cr)에 비해 환원-산화 전위(redox potential)가 높아 용융염과의 반응성이 낮으며, 열촉매와의 반응성도 적어 화학적으로 매우 안정적인 특성을 나타낸다[8]. 따라서 부식 저항성 측면에서 유망한 클래딩 소재로 평가된다. 특히 열교환기 부품의 경우, 두께가 4~5 mm 수준으로 얇기 때문에 클래딩 두께는 400~500 ㎛ 이내로 제한되어야 한다. 또한, Cr이나 Fe와 같은 용융염에 취약한 원소의 확산을 최소화하기 위해 비교적 낮은 입열량을 갖는 Directed energy deposition (DED) 및 High velocity oxy-fuel (HVOF) 공정이 적합한 것으로 판단된다[9-11]. 본 연구에서는 스테인리스강에 니켈 클래딩을 적용하기 위한 두 가지 공정, DED와 HVOF를 비교하여 최적의 클래딩 방안을 도출하고자 하였다. DED 공정은 정밀한 소재 증착이 가능하며, 다중 분말 공급을 통해 합금 조성을 자유롭게 조절할 수 있고, 기판과의 용융 접합을 통해 높은 결합 강도를 확보할 수 있다. 반면, HVOF 공정은 고속 입자의 충돌을 통해 치밀하고 기공이 적은 클래딩층을 형성하며, 기계적 결합 기반으로 높은 접착 강도를 가지는 동시에 낮은 열 입력으로 기판의 열 변형을 최소화하는 장점이 있다. 본 연구에서는 이러한 두 공정을 비교, 분석함으로써 MSR 운전 환경에 적합한 최적의 니켈 클래딩 공정을 도출하고자 하였다.

2. Experimental Section

본 연구에서는 금속 적층 제조 방식 중 하나인 directed energy deposition (DED) 공정을 이용하여 순수 니켈(Ni) 분말을 STS316H 스테인리스강 기판 상에 적층하였다. 적층 장비는 AM Solutions사(대한민국)에서 제작한 L-DED 시스템을 사용하였다. 기판으로는 두께 4 mm의 STS316H 판재를 사용하였으며, 주요 화학 조성은 Table 1에 제시하였다.

적층에 사용된 분말은 Hoganas(스웨덴)에서 제조한 순도 99.99 wt% 이상의 Ni 분말이며, 제조사로부터 제공된 불순물의 최대 함량은 Mo < 0.01 wt%, Mn < 0.002 wt%, V < 0.001 wt% 수준이다. 분말은 50 μm 및 150 μm 체를 사용하여 입도 분포를 50–150 μm 범위로 조정하였으며, ImageJ 소프트웨어를 활용한 광학 현미경 이미지 분석을 통해 평균 입도는 약 102 μm로 측정되었다[12].

적층 시 분말 공급 속도는 3.1 g/min, 분말 운송 가스로는 순도 99.99%의 Ar 가스가 사용되었다. 또한 용융풀의 산화를 방지하기 위해 동일한 Ar 가스를 레이저 건 입구에서 300 mL/min의 유량으로 보호가스로 분사하였다. 열원은 Raycus 1500 W급 다이오드 레이저를 사용하였으며, 450 W 및 550 W의 두 가지 레이저 출력 조건으로 각각 시편을 제작하였다. 두 시편 모두 스캔 속도 850 mm/min, 스캔 간격 0.5 mm, 적층 간격 0.10 mm, 적층 경로는 CFCFC 패턴(외곽 Counter - 내부 Face 반복)으로 동일하게 유지하였다. DED 공정은 챔버 내에서 상온·상압 조건 하에서 수행되었으며, 상대습도는 10% 이하로 제어하였다.

비교 실험을 위하여, 동일한 STS316H 기판과 순수 Ni 분말을 이용한 HVOF (High Velocity Oxygen Fuel) 방식의 코팅 시편은 한국원자력연구원(KAERI)으로부터 제공받았다. 해당 시편은 HVOF 방식으로 순수 Ni 분말을 Type 316H 스테인리스강 직육면체 시편(4 mm × 20 mm × 10 mm) 전체 표면에 코팅한 것으로, 코팅 두께는 약 400 μm이다. 이때, 분말 공급 속도는 70–80 g/min, 연료로는 산소(O_2)와 등유(kerosene)가 사용되었으며, 분말 캐리어 가스로는 아르곤(Ar)이 사용되었다.

제작된 모든 시편에 대해 주사전자현미경(SEM, JSM-IT500, JEOL)을 사용하여 단면 및 표면의 기공 분포, 용융풀 경계 및 미세조직 관찰을 수행하였고, 에너지 분산형 분광기(EDS, EDAX Instruments)를 이용하여 시편 단면의 선(line) 및 면(mapping) 성분 분석을 병행하였다. 경도 측정은 비커스 경도계(Duramin-40M1, Struers)를 이용하여 수행되었으며, 하중은 100 gf (HV0.1), 유지시간은 10초로 설정하였다. 각 시편에 대해 3회 반복 측정을 통해 평균 경도값 및 표준편차를 도출하였다.

Table 1. Chemical composition of as-received STS316H metal analyzed by SEM-EDS and inductively coupled plasma-optical emission spectrometry (weight %)

Component	Fe	Cr	Ni	Mo	Mn	V
STS316H	Bal.	17.07	10.06	2.16	0.7	0.04
Pure Ni powder	-	-	Bal.	< 0.01	< 0.002	-

SEM-EDS, scanning electron microscopy with energy dispersive X-ray spectroscopy

3. Results and Discussion

3.1 클래딩 후 시편 표면 특성

그림 1은 HVOF 및 DED 방식으로 적층된 형상을 나타낸다. 그림 1-(a)는 HVOF 코팅 후 약 400 μm의 두께를 목표로 표면을 연삭한 후의 형상을 보여준다. 이때, 모서리 부분에서는 코팅이 균일하게 형성되지 않았음을 확인할 수 있었다. 반면, 그림 1-(b)는 DED 공정을 적용한 이후의 시편 형상을 나타내며, 전체적으로 균일하고 정밀한 형상이 관찰되었다.

3.2 미세조직 분석 및 공정비교

그림 2는 HVOF 공정 후 획득한 단면을 주사전자현미경(SEM)으로 분석한 결과이다. 클래딩층의 두께는 약 359 μm로 측정되어 목표 두께인 400 μm에 근접하였으나, 내부에 다수의 기공과 크랙이 관찰되어 공정 제어의 한계를 드러낸다. 코팅층과 STS316H 기판 사이에는 뚜렷한 계면이 형성되었으며, 일부 영역에서는 불완전 용융된 분말도 확인되었다. 이는 분말이 분사 과정에서 충분한 열처리를 받지 못했음을 나타낸다.

라인 프로파일 분석 결과, 기판에 직접적인 열이 가해지지 않고 코팅이 이루어졌기 때문에 기판과 클래딩층 사이의 조성 경계가 명확하게 구분되었다. 이러한 미세결함들(기공, 크랙, 불완전 용융 입자)은 코팅층의 품질 및 장기 내구성에 부정적인 영향을 미칠 수 있으므로, 향후에는 결함 발생 원인을 체계적으로 규명하고, 이를 최소화할 수 있는 최적의 분사 조건 도출이 필요하다.

DED 공정에서 적용되는 레이저 출력의 변화는 입열량(heat input)에 직접적인 영향을 미치며, 이는 미세조직 형성과 원소 확산 거동에 중대한 차이를 유발할 수 있다. 본 연구에서는 식 (1)을 통해 입열량 Q를 산출하였다.

$$Q = (P \times \eta)/V_S \quad (1)$$

여기서 P는 레이저 출력(W), VS는 스캔 속도(mm/s), η는 열 효율(thermal efficiency)로 본 연구에서는 0.8로 설정하였다[13]. 실험에서는 VS를 14.2 mm/s (= 850 mm/min)로 고정하고, P를 각각

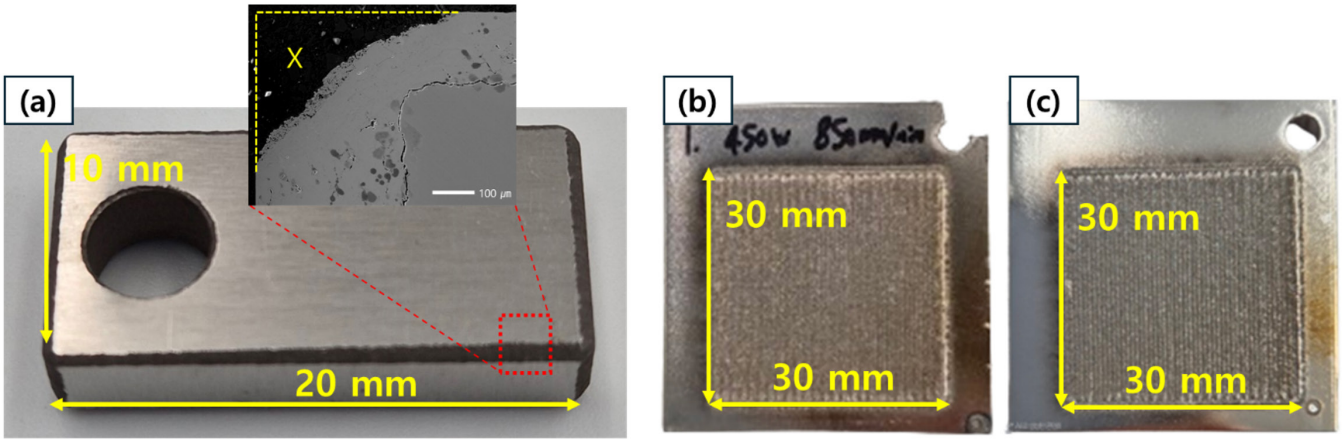

Fig. 1. Post-cladding surface morphology: (a) high-velocity oxy-fuel, (b) 450 W directed energy deposition (DED), (c) 550 W DED.

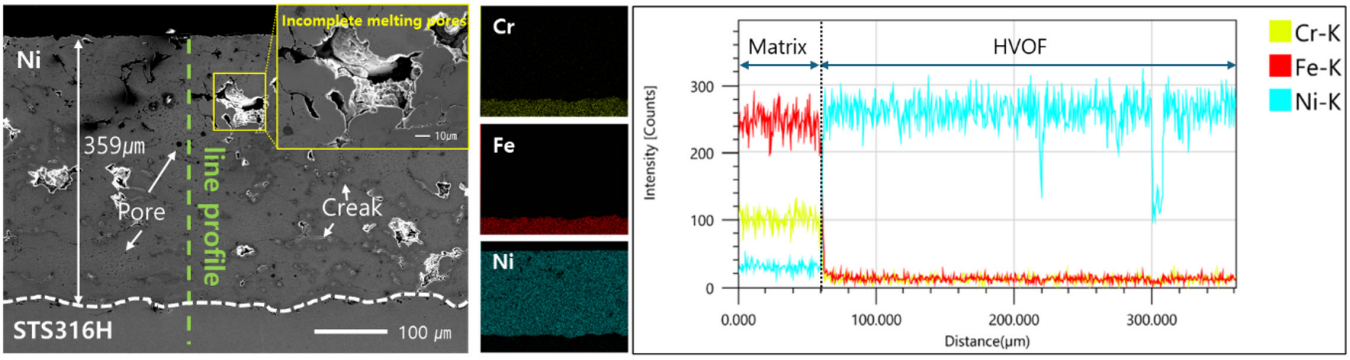

Fig. 2. Cross-sectional scanning electron microscopy image and compositional line profile of the high-velocity oxy-fuel-coated layer.

450 W와 550 W로 설정하였으며, 이에 따른 입열량은 각각 25.4 J/mm 및 31.1 J/mm로 계산되었다. 이와 같이 입열량이 증가하면 기판으로부터 클래딩층 방향의 원소 확산 거리 확대 및 열적 균열 발생 가능성 증가 등 공정 결과에 뚜렷한 차이를 초래할 수 있다.

그림 3은 DED 공정 후 STS316H 기판 상에 형성된 Ni 클래딩층의 미세조직 및 조성 분석 결과를 나타낸다. 그림에 표시된 녹색 점선은 STS316H 기판 표면부터 클래딩층 상부까지 약 400 μm의 거리를 의미하며, 라인 프로파일 분석 구간을 나타낸다. 그림 3-(a)는 레이저 출력 450 W, 스캔 속도 850 mm/min 조건에서 적층된 단면이며, 그림 3-(b)는 동일한 스캔 속도(850 mm/min)에서 레이저 출력을 550 W로 증가시켜 적층한 단면을 보여준다. 두 조건 모두에서 클래딩층과 기판 사이에는 뚜렷한 용융풀 경계가 형성되었으며, Cr, Fe, Ni 성분의 농도 분포를 통해 기판과 클래딩층 간의 조성 경계가 명확하게 구분된다. 450 W 조건에서는 일부 기공이 관찰되었으나, 크랙은 확인되지 않았다. 반면, 550 W 조건에서는 기공뿐만 아니라 계면 인근을 포함한 클래딩층 전반에서 크랙이 관찰되었다. 본 연구에서는 해당 균열이 잔류 인장응력에 기인한 것인지에 대한 정량적 해석은 수행되지 않았으므로, 크랙 발생 메커니즘에 대한 단정적인 해석은 지양되어야 한다. 다만, 레이저 출력 증가로 인해 용융 영역이 확대되고 그로 인해 열적 응력 또는 열 기계적 불균형이 유도되었을 가능성이 있으며, 이는 향후 잔류 응력 해석을 통해 보다 명확히 규명될 필요가 있다. 한편, 본 절에서 이어지는 Cr 및 Fe의 조성 확산 분석은 공정 조건에 따른 입열량 차이에 기인한 현상으로, 균열 발생과는 독립적인 메커니즘으로 판단된다.

그림 4는 STS316H 기판에서 Ni 클래딩층까지의 Cr 및 Fe 성분 확산 거리를 EDS 점분석을 통해 정량적으로 나타낸 것이다. 그림 4-(a)는 Cr의 조성 분포를, 그림 4-(b)는 Fe의 조성 분포를 각각 보여주며, DED 공정 조건과 HVOF 공정 간의 차이를 비교하였다. 분석 결과, HVOF 공정에서는 그림 2의 선분석 결과와 동일하게 클래딩층 내부에 Cr 및 Fe 성분이 확산되지 않았다. 반면, DED 공정에서는 기판으로부터 클래딩층 방향으로 뚜렷한 성분 확산이 관찰되었다.

특히, 레이저 출력이 높은 550 W 조건에서는 450 W 조건에 비해 확산 거리가 더 길게 나타났으며, 이는 열 입력의 증가에 따라 합금 원소의 확산 범위가 확대되었음을 보여준다. 이러한 결과는 DED 공정에서 레이저 출력이 Cr 및 Fe와 같은 합금 원소의 클래딩층 내 확산 거리에 큰 영향을 미친다는 것을 시사한다.

3.3 클래딩 경계부에서의 미소경도특성

그림 5는 STS316H 기판과 Ni 클래딩층에 대해 수행한 비커스 경도(Vickers hardness, HV0.1) 측정 결과를 나타낸다. 경도 측정은 클래딩과 기판의 계면을 기준점(0 ㎛)으로 설정하여 수행되었다. DED 공정(레이저 출력 450 W)으로 제조된 클래딩층은 내부 기공의 형성이 적어, HVOF 공정 대비 전반적으로 높은 경도 값을

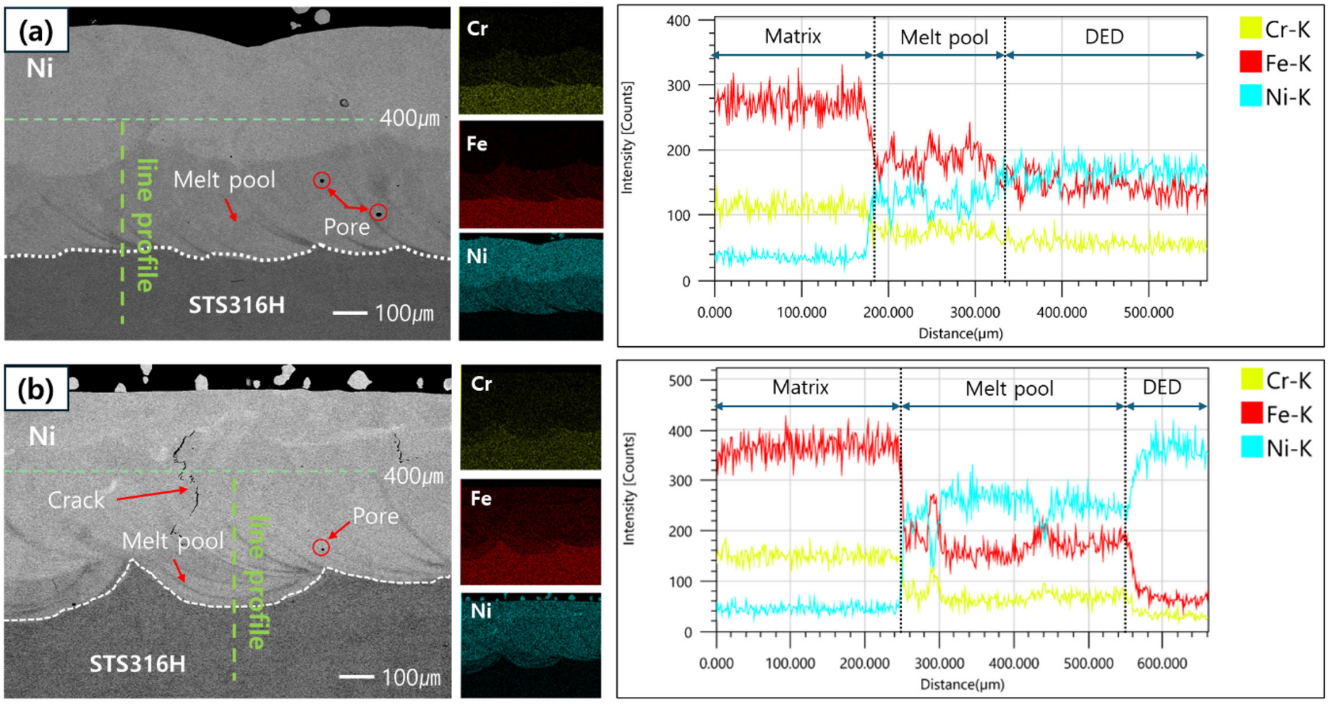

Fig. 3. Cross-sectional scanning electron microscopy image and compositional line profile of the directed energy deposition-processed layer: (a) laser power 450 W, (b) laser power 550 W.

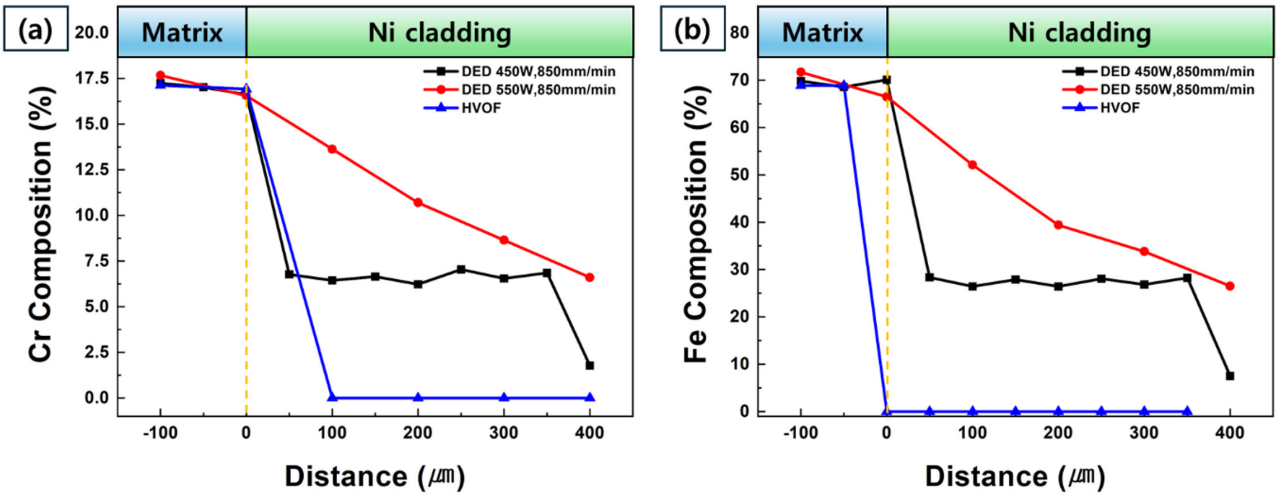

Fig. 4. Energy-dispersive X-ray spectroscopy point analysis of elemental diffusion from substrate to cladding: (a) Cr diffusion, (b) Fe diffusion.

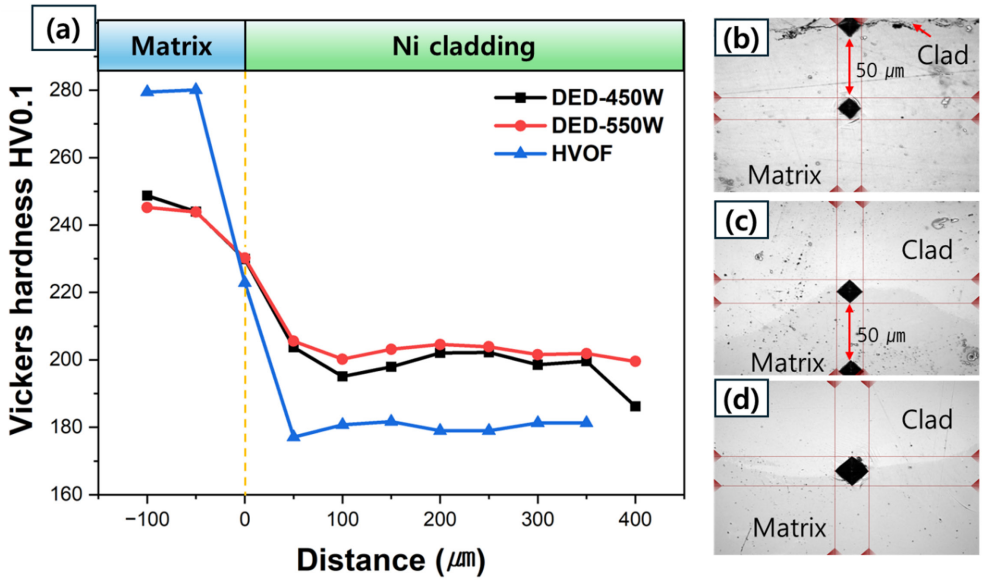

Fig. 5. Vickers hardness test results: (a) Vickers hardness distribution across the cladding–substrate interface, (b) HVOF indentation, (c) DED-450W indentation, (d) DED-550W indentation. HVOF, high-velocity oxy-fuel; DED, directed energy deposition.

나타냈다. 특히 계면 부근에서는 Cr 및 Fe의 열적 확산으로 인해 순수 Ni 대비 경도가 상승하는 현상이 관찰되었으며, 이는 고용 강화 효과가 일부 기여했을 가능성이 있다. 한편, 550 W 조건에서는 입열량 증가로 인해 원소 확산 거리가 확대되었고, 그 결과 고용 강화 효과가 미세하나 추가적으로 발생하여 계면 부근에서의 경도가 450 W 조건보다 소폭 향상되었다.

반면, HVOF 공정으로 제작된 클래딩층은 다수의 기공 및 크랙이 존재하여 기계적 물성이 저하되었으며, 이에 따라 경도 값도 상대적으로 낮은 수준을 보였다. 이러한 결과는 두 공정 간의 미세조직 차이가 경도에 직접적인 영향을 미친다는 점을 시사하며, 공정 선택 및 최적화가 코팅층의 기계적 특성 확보에 있어 중요함을 보여준다. 참고로, 비교 기준이 되는 벌크 소재 Ni-201 (Pure Ni)의 평균 비커스 경도는 약 171 HV로 측정되었다.

4. Conclusion

본 연구에서는 STS316H 기판에 순수 Ni 클래딩을 적용하기 위해 HVOF와 DED 두 공정을 비교하고, 미세조직, 원소 확산, 기계적 특

성을 종합적으로 평가하였다. 그 결과, DED 공정은 균일한 증착 형상과 낮은 기공률, 높은 경도를 보여 우수한 코팅 품질과 기계적 신뢰성을 나타냈다. 특히, Cr 및 Fe의 확산이 뚜렷하게 확인되었으며, 이는 레이저 출력에 따라 확산 거리가 증가하는 경향을 보였다.

HVOF 공정은 낮은 열 입력으로 인해 Cr, Fe 확산을 효과적으로 억제하는 장점을 보였으나, 기공과 크랙이 다수 발생하여 코팅층의 기계적 특성이 저하되었다. 이는 고온에서의 구조 신뢰성을 요구하는 환경에서는 한계로 작용할 수 있다.

결론적으로, DED 공정은 우수한 기계적 성능과 증착 안정성을 바탕으로 용융염 원자로와 같은 고온 환경에 적합한 공정으로 판단된다. Cr 및 Fe 확산 억제를 위한 공정 제어를 병행한다면 내식성 클래딩으로 활용이 가능할 것으로 보인다. 한편, HVOF 공정 역시 결함을 최소화하는 최적화가 이루어진다면, 확산 억제 특성을 바탕으로 내식성 중심의 응용 분야에 적합한 대안이 될 수 있을 것으로 보인다.

Funding

This work was supported by Korea Research Institute for defense Technology planning and advancement (KRIT) grant funded by the Korea government (DAPA (Defense Acquisition Program Administration)) (KRIT-CT-22-017, Next Generation Multi-Purpose High Power Generation Technology (Liquid Fueled Heat Supply Module Design Technology), 2022). This work was also supported by the Korea Institute for Advancement of Technology (KIAT) by the Korea Government (MOTIE) (RS-2024-00406598, HRD program for Industrial Innovation).

Conflict of Interest

JH. Kim serves as an editor of the Journal of Powder Materials editing, but has no role in the decision to publish this article. Except for that, no potential conflict of interest relevant to this article was reported.

Data Availability Statement

All dataset files used in this study are already provided in the manuscript.

Author Information and Contribution

Won Chan Lee: Analyzed the data and wrote the original draft of the manuscript.
Seung Ju Nam: Assisted with the experiments.
Ji-Hyun Yoon: Provided materials. Reviewed a manuscript.
Jeoung Han Kim: Conceived and designed the experiments.
All authors reviewed and approved the final manuscript.

Acknowledgments

None.

References

[1] J J. Serp, M. Allibert, O. Beneš, S. Delpech, O. Feynberg, V. Ghetta, D. Heuer, D. Holcomb, V. Ignatiev, J. L. Kloosterman, L. Luzzi, E. Merle-Lucotte, J. Uhlíř, R. Yoshioka and D. Zhimin: Prog. Nucl. Energy, **77** (2014) 308.
[2] R. Roper, M. Harkema, P. Sabharwall, C. Riddle, B. Chisholm, B. Day and P. Marotta: Ann. Nucl. Energy, **169** (2022) 108924.
[3] J. Wu, J. Chen, X. Cai, C. Zou, C. Yu, Y. Cui, A. Zhang and H. Zhao: Energies, **15** (2022) 8296.
[4] N. S. Patel, V. Pavlík and M. Boča: Crit. Rev. Solid State Mater. Sci., **42** (2017) 83.
[5] D. Zhang, L. Liu, M. Liu, R. Xu, C. Gong, J. Zhang, C. Wang, S. Qiu and G. Su: Int. J. Energy Res., **42** (2018) 1834.
[6] L. Guo, Q. Liu, H. Yin, T. Pan and Z. Tang: Corros. Sci., **166** (2020) 108473.
[7] K. I. Choudhry, S. Mahboubi, G. A. Botton, J. R. Kish and I. M. Svishchev: Corros. Sci., **100** (2015) 222.
[8] S. Guo, J. Zhang, W. Wu and W. Zhou: Prog. Mater. Sci., **97** (2018) 448.
[9] D.-G. Ahn: Int. J. Precis. Eng. Manuf.-Green Technol., **8** (2021) 703.
[10] M. Das, B. Zheng, A. L. Vyatskikh, S. Bose, A. Bandyopadhyay, J. M. Schoenung, E. J. Lavernia and N. Eliaz: Mater. Today, **49** (2021) 271.
[11] B. Wielage, A. Wank and H. Pokhmurska: Surf. Coat. Technol., **201** (2006) 2032.
[12] U. Ko, W. C. Lee, G. S. Shin, J.-H. Yoon and J. H. Kim: J. Powder Mater., **31** (2024) 220.
[13] W. C. Lee, J. W. Park, S. J. Nam, J.-H. Yoon and J. H. Kim: Powder Metall., **68** (2025) 342.

Research Article

pISSN 2799-8525 · eISSN 2799-8681
J Powder Mater 2025;32(4):315-329

Journal of
Powder Materials

Enhanced Compressive Strength of Fired Iron Ore Pellets: Effects of Blending Fine and Coarse Particle Concentrates

Ngo Quoc Dung[1], Tran Xuan Hai[1], Nguyen Minh Thuyet[1], Nguyen Quang Tung[2], Arvind Barsiwal[1], Nguyen Hoang Viet[1,*]

[1]Faculty of Materials Engineering, School of Materials Science and Engineering, Hanoi University of Science and Technology, Hanoi 100000, Vietnam
[2]Hoa Phat Dung Quat Steel Joint Stock Company, Binh Son, Quang Ngai 570000, Vietnam

This study investigated the effects of oxidative firing parameters and raw material characteristics on the pelletization of Australian and Minh Son (Vietnam) iron ore concentrates. The influence of firing temperature (1050°C–1150°C) and holding time (15–120 min) on pellet compressive strength was examined, focusing on microstructural changes during consolidation. Green pellets were prepared using controlled particle size distributions and bentonite as a binder. Scanning electron microscopy and energy-dispersive X-ray spectroscopy analyses revealed that grain boundary diffusion, liquid phase formation, and densification significantly improved mechanical strength. X-ray diffraction confirmed the complete oxidation of magnetite to hematite at elevated temperatures, a critical transformation for metallurgical performance. Optimal firing conditions for both single and blended ore compositions yielded compressive strengths above 250 kgf/pellet, satisfying the requirements for blast furnace applications. These results provide valuable guidance for improving pellet production, promoting the efficient utilization of diverse ore types, and enhancing the overall performance of ironmaking operations.

Keywords: Iron ore pelletization; Oxidative firing; Compressive strength; Microstructural evolution

Received: April 30, 2025
Revised: June 25, 2025
Accepted: July 10, 2025

***Corresponding author:**
Nguyen Hoang Viet
E-mail: viet.nguyenhoang@hust.edu.vn

I. Introduction

Pelletizing iron ore fines has become an essential step in modern iron and steel production, driven by the declining availability of high-grade lump ores and the growing need to make effective use of finer iron-bearing materials [1-8]. By agglomerating fine particles into pellets, the process not only improves furnace efficiency but also enhances key metallurgical properties such as reducibility and mechanical strength. In addition to pelletization, other agglomeration techniques such as compacting and briquetting are also gaining attention as viable routes for recycling iron ore fines and waste streams [9-12]. These technologies offer greater flexibility in raw material use and can be adapted for various reduction environments, supporting both sustainability and cost-effectiveness in ironmaking.

Pelletization technology originated in Sweden and Germany in the early 20th century, where initial advancements demonstrated that pelletized fines outperformed lump and sintered ores in reduction efficiency. In the mid-20th century, the United States further industrialized the process, particularly with low-grade Taconite ores. Since the 1960s, pellet production has expanded globally, reaching hundreds of millions of tons annually [5, 13-15].

Ongoing research has focused on improving pellet quality [1, 16-18]. Studies have explored the development of new organic binders (e.g., Pefidur) to replace traditional bentonite, thereby reducing impurities and enhancing metallurgical properties. Other investigations have aimed to modify the mineral structure of pellets, producing self-fluxing or dolomite-containing pellets to improve blast furnace performance. Enhancing energy efficiency through heat recovery and the use of alternative fuels has also been widely investigated [19-23].

In Vietnam, iron ore pellets are increasingly incorporated into blast furnace operations at facilities such as Hoa Phat Dung Quat Steel Joint Stock Company and the Viet - Trung

https://doi.org/10.4150/jpm.2025.00129

Mining and Metallurgy Co.,Ltd. Reports indicate that incorporating 20–25% pellets into the blast furnace charge enhances productivity, reduces coke consumption, and lowers the cost of pig iron production. Moreover, pellet usage addresses the challenge of limited domestic reserves of high-grade magnetite ore.

Despite global progress in pelletization research, systematic studies examining the specific influence of oxidative firing parameters—particularly firing temperature and holding time—on the mechanical performance of pellets from local Vietnamese ores are lacking. These factors are essential for maximizing pellet quality and ensuring the viability of domestic ores in high-efficiency blast furnaces [10-12, 24].

This study aims to fill that gap by systematically examining the effects of oxidative firing temperature and duration on the compressive strength of iron ore pellets made from Australian and Minh Son concentrates. By correlating microstructural evolution with mechanical performance, the research seeks to define optimal firing conditions that enhance pellet strength—supporting the development of efficient and localized pellet production technologies in Vietnam.

II. Materials and Methods

2.1. Raw Materials and Pellet Preparation

Iron ore concentrates sourced from Australia and Minh Son Company (Vietnam) were used in this study. Both materials were supplied by Hoa Phat Hai Duong Steel Joint Stock Company [10, 11]. Indian bentonite, with the chemical composition shown in Table 2, was added as a binder at an addition rate of approximately 1.5 wt%. Fig. 1 presents SEM images and particle size distributions of the Australian and Minh Son iron ore concentrates. In Fig. 1a, the Australian concentrate exhibits a fine and relatively homogeneous microstructure, with particles displaying mostly angular shapes and narrow size variation. In contrast, the SEM image of the Minh Son concentrate (Fig. 1b) reveals a coarser texture, where particles are larger, more irregular in shape, and display a broader size range. The corresponding particle size distribution curves (Fig. 1c and 1d) quantitatively confirm these observations. The Australian ore features a much finer distribution, with a median particle size (d_{50}) of approximately 13 μm, while the Minh Son ore shows a d_{50} of around 50 μm, indicating the presence of significantly coarser grains.

2.2. Firing, Mechanical Testing, and Microstructural Characterization

In this study, four iron ore compositions were prepared: 100% Australian ore (denoted as IO: 100A), 100% Minh Son ore (IO: 100M), and two blends — 90% Australian + 10% Minh Son (IO: 10A–90M) and 20% Australian + 80% Minh Son (IO: 20A–80M). Green pellets were formed using a disc pelletizer, incorporating bentonite and water under controlled conditions. Following pelletization, the green pellets were evaluated for mechanical intergrity using a 5 kgf press [25]. As shown in Fig. 2, all samples satisfied the typical requirement of approximately 1 kg per pellet [1, 2], consistent with reported values for blended magnetite–hematite ores (1.25–1.55 kgf/pellet) [26]. The pellets were subsequently oxidatively fired in a silicon carbide (SiC) electric furnace at target temperatures of 1050°C, 1100°C, and 1150°C, with holding times of 15, 30, 45, 60, 90, and 120 min. Compressive strength was then measured post-firing, based on testing a minimum of five pellets per condition to ensure statistical reliability.

The schematic diagram of the pelletization process is presented in Fig. 3. It illustrates the drying of iron ore concentrates, followed by blending with a binder and water spraying, green pellet formation, heat hardening to produce fired pellets, and subsequent evaluation of their properties.

Table 1. Chemical composition of iron ore concentrates

Ore type	Chemical composition, %wt							
	TFe	FeO	SiO_2	Al_2O_3	CaO	MgO	S	P
Australia	65.5	26.80	8.0	0.5	0.2	0.5	0.001	0.014
Minh Son	66.5	20.67	5.0	0.7	0.1	0.1	0.061	0.002

Table 2. Chemical composition of Indian bentonite powder

Binder material	Chemical composition, %wt				
	Fe_2O_3	SiO_2	Al_2O_3	CaO	MgO
Indian bentonite type	12.37	62.99	20.67	1.14	1.32

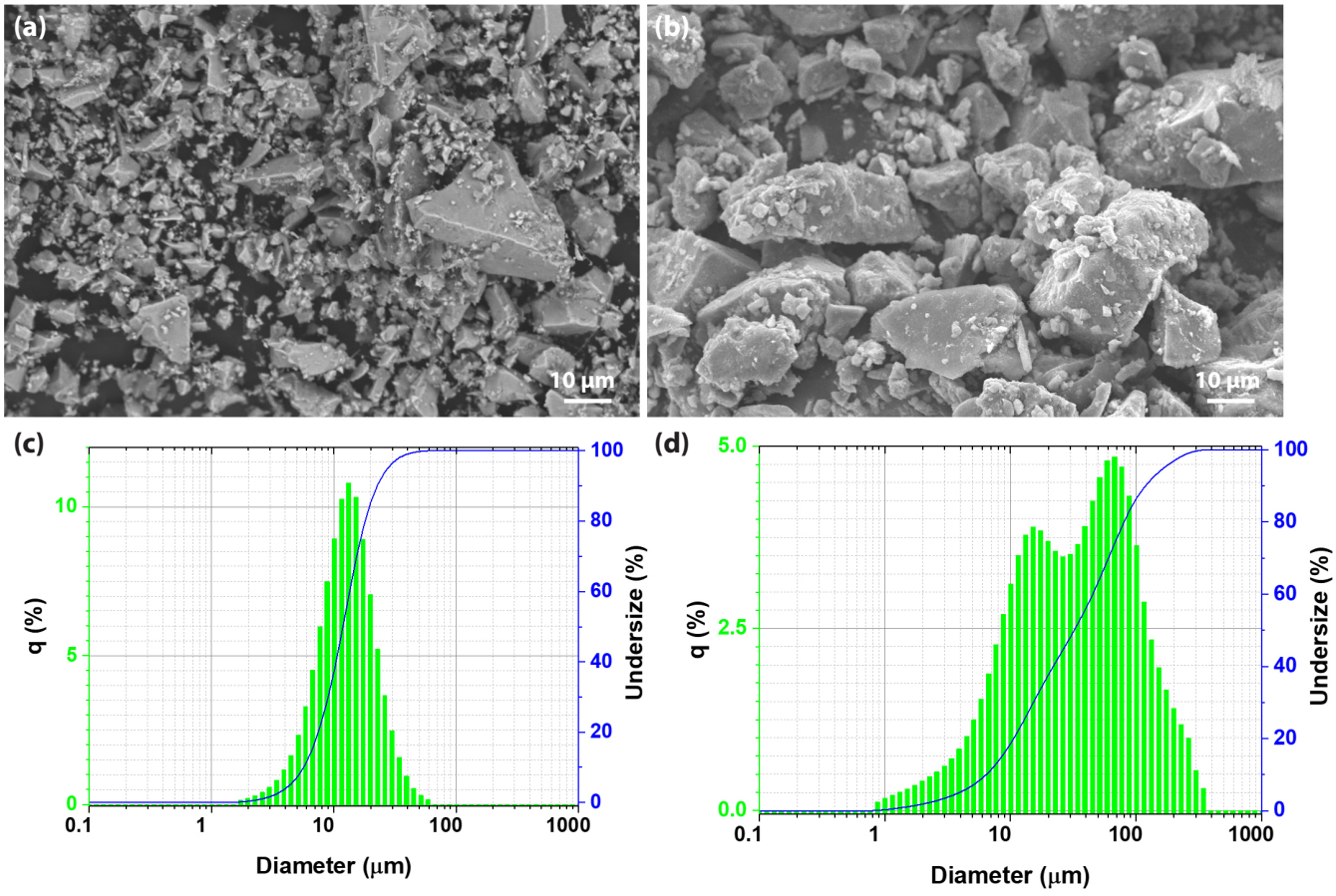

Fig. 1. Scanning electron microscopy images and particle size distribution of (a, c) Australian and (b, d) Minh Son iron ore concentrates.

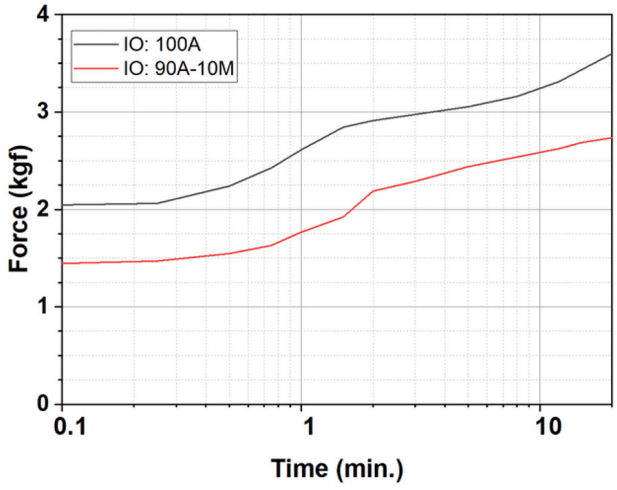

Fig. 2. Strength of green pellets over time.

Microstructural analysis of the fired pellets was performed using scanning electron microscopy (SEM). Elemental distribution was investigated via energy-dispersive X-ray spectroscopy (EDS) on fracture surfaces and cross-sections. Phase identification was conducted using X-ray diffraction (XRD), with powdered samples obtained from ground fired pellets. The diffraction data were analyzed using Profex software and supporting tools [27, 28] to identify crystalline phases and assess oxidation transformations.

III. Results and Discussion

3.1. Compressive Strength Testing

Fig. 4 presents the compressive strength of oxidatively fired pellets at various temperatures and holding times. At 1050°C, the pellets exhibited relatively low strength, with the 100% Australian ore (IO: 100A) reaching only 122.78 kgf/pellet. Extending the holding time led to progressive improvement, achieving

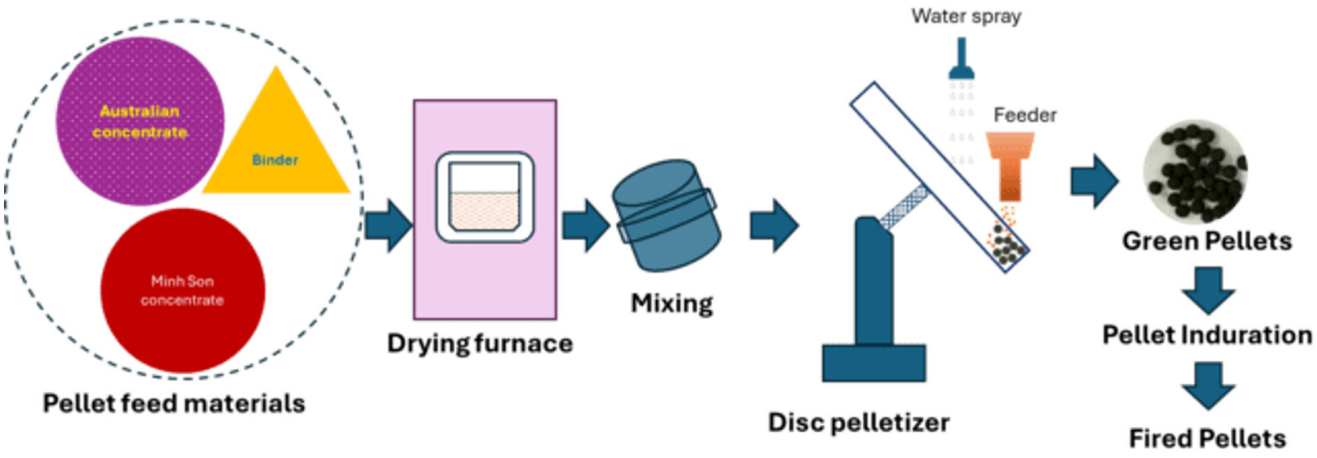

Fig. 3. Schematic representation of the iron ore pelletization process.

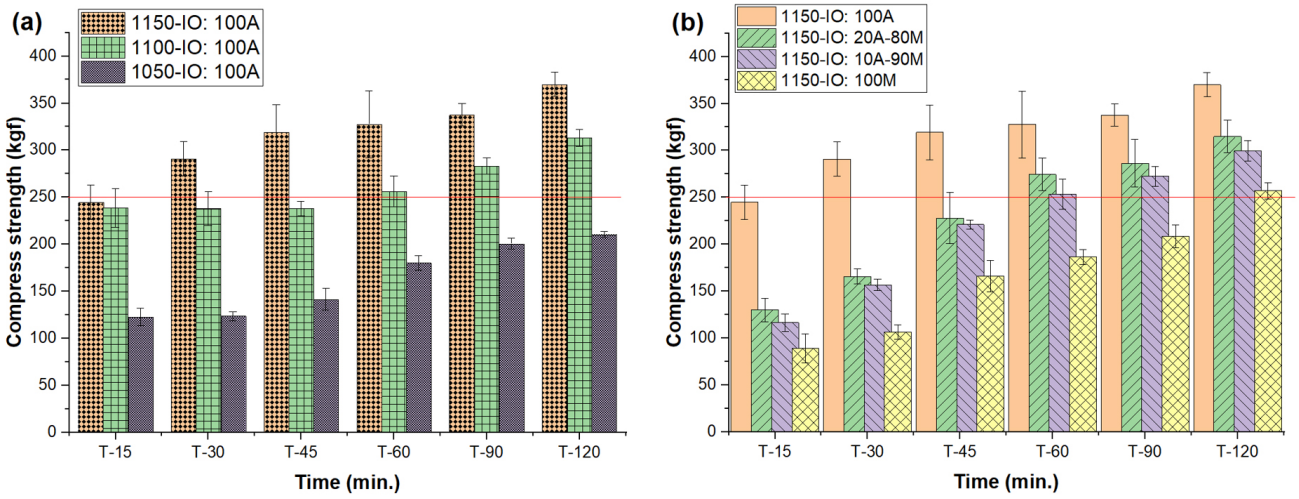

Fig. 4. Compressive strength of (a) IO: 100A pellets fired oxidatively at 1050°C, 1100°C, and 1150°C, and (b) blended pellets fired at 1150°C with holding times of 15, 30, 45, 60, 90, and 120 min.

180.26 kgf/pellet after 60 min and 210.36 kgf/pellet after 120 min. As the firing temperature increased, a notable enhancement in mechanical performance was observed. At 1100°C and 1150°C, the IO: 100A pellets achieved compressive strengths of 238.54 kgf/pellet and 244.77 kgf/pellet, respectively, after just 15 min of holding. Further increases in holding time at 1150°C resulted in continued strength gains: 244.77 kgf/pellet at 15 min, then increasing to 290.94 kgf/pellet at 30 min, 319.18 kgf/pellet at 45 min, 348.86 kgf/pellet at 60 min, and a maximum of 370.01 kgf/pellet at 120 min.

The performance of blended compositions at 1150°C also followed a similar trend, with compressive strengths measured at 60, 90, and 120 min as follows: 327.59, 337.59, and 370.01 kgf/pellet for IO: 100A; 274.48, 286.27, and 314.84 kgf/pellet for the 20% Australian + 80% Minh Son blend (IO: 20A–80M); 253.43, 272.31, and 299.57 kgf/pellet for the 10% Australian + 90% Minh Son blend (IO: 10A–90M); and 186.00, 208.00, and 257.00 kgf/pellet for 100% Minh Son (IO: 100M). These results indicate that the minimum strength requirement for blast furnace feedstock (≥250 kgf/pellet) [23, 29] was satisfied under specific conditions. The IO: 100A pellets met the requirement after 60 min at 1100°C and from 30 min onward at 1150°C. Blended pellets (IO: 20A–80M and IO: 10A–90M) reached the threshold after 60 min at 1150°C, while IO: 100M required 120 min.

The improvement in compressive strength with increased temperature and holding time is attributed to the melting of the bentonite binder and localized fusion at ore particle interfaces, which enhance densification and the mechanical integrity of the fired pellets [2].

3.2. Morphological Changes of Fracture Surfaces

Fig. 5 presents the X-ray diffraction (XRD) patterns of (a) the initial Minh Son and (b) Australian iron ore concentrates, and (c) typically fired pellet. In these patterns, label (1) corresponds to the main diffraction peaks of the magnetite phase, and label (2) corresponds to the main diffraction peaks of the hematite phase. The analytical results are consistent with the initial information indicating that the Australian and Minh Son ores are primarily magnetite-type ores.

Fig. 6 shows the observation of the fracture surfaces after compressive strength testing clearly revealed changes in color and morphology of the IO: 100A pellets. At firing temperatures of 1050°C and 1100°C, the pellets exhibited a dark brown color, characteristic of Fe_2O_3 (hematite) powder. At 1100°C, the color became lighter brown due to the transformation of coarse Fe_2O_3 crystals. Fracture surfaces at these temperatures also showed fragmented powder remnants after strength testing, indicating weak bonding between ore particles. At 1150°C, the brown color significantly faded, and the pellets exhibited a grayish-blue color. The fracture morphology shifted to larger fragments instead of powdery breakage as observed at lower temperatures, and no fine powder residues were collected after testing. This suggests that inter-particle bonding was signifi-

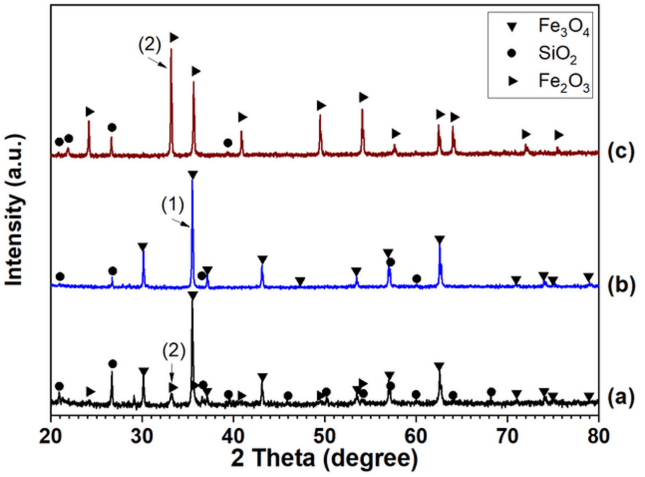

Fig. 5. X-ray diffraction patterns of the original ore samples: (a) IO: 100M and (b) IO: 100A concentrates, (c) fired pellet.

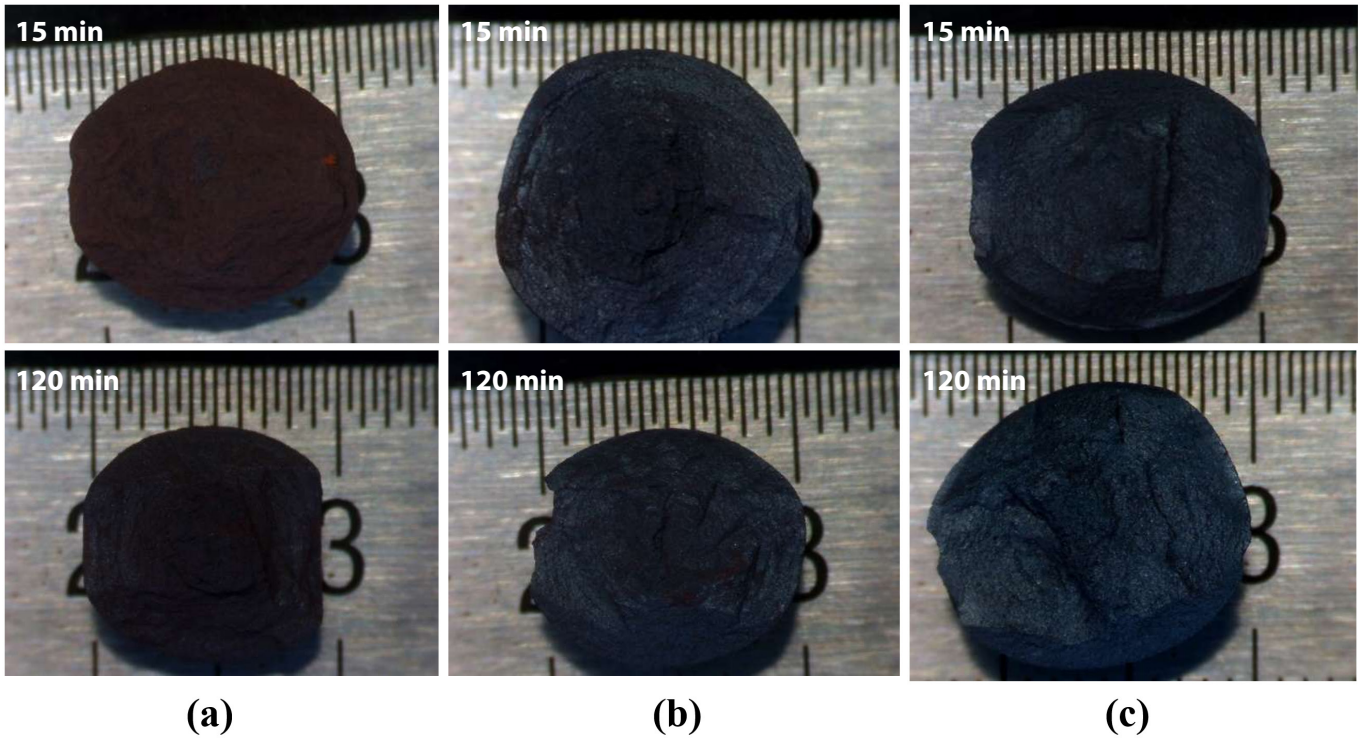

Fig. 6. Fracture surfaces of Australian pellets oxidatively fired at (a) 1050°C, (b) 1100°C, and (c) 1150°C for holding times of 15 and 120 min.

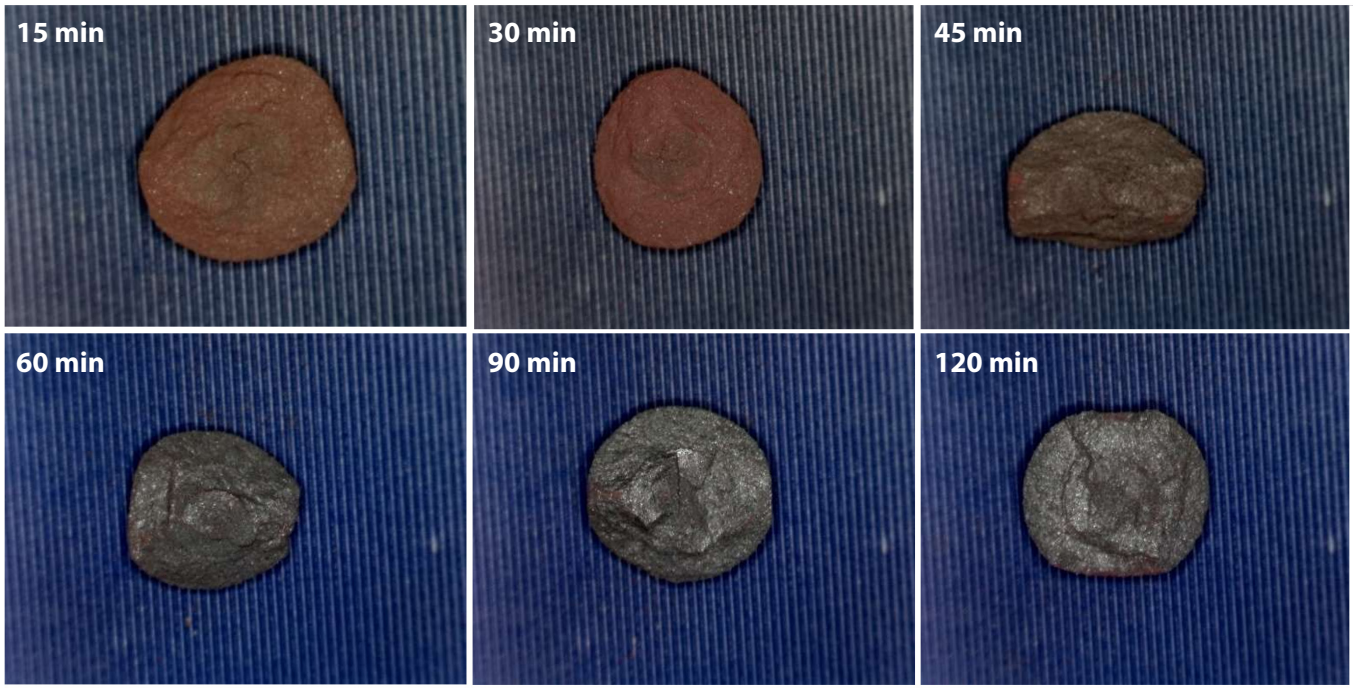

Fig. 7. Fracture surfaces of Minh Son pellets oxidatively fired at 1150°C for 15, 30, 45, 60, 90, and 120 min.

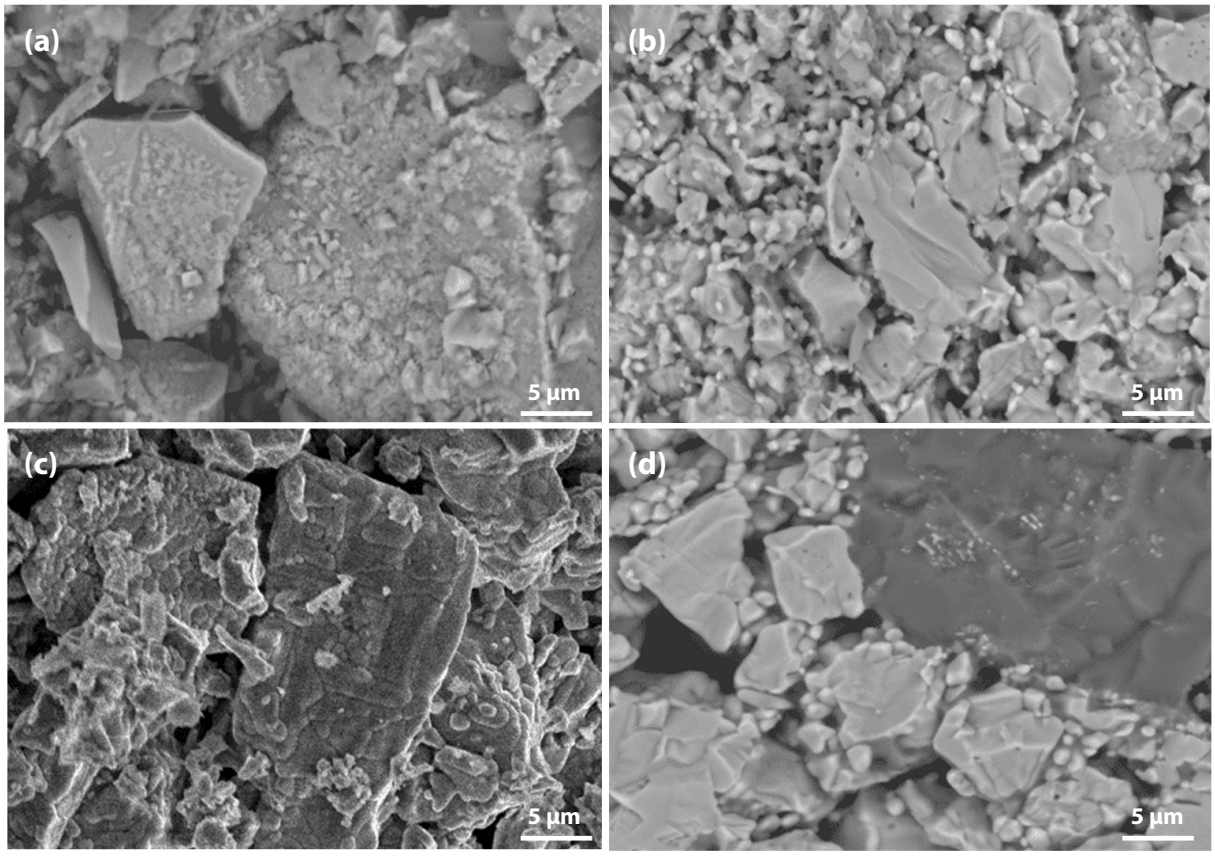

Fig. 8. Scanning electron microscopy images of fracture surfaces of Australian pellets oxidatively fired at (a) 1050°C for 30 min, (b) 1100°C for 30 min, (c) 1100°C for 120 min, and (d) 1150°C for 30 min

cantly enhanced, likely due to the formation of a liquid phase during firing, contributing to the densification and strengthening of the pellets.

Consistent with these observations, Fig. 7 shows the fracture surfaces of IO: 100M pellets (100% Minh Son ore) oxidatively fired at 1150°C for varying holding times. Clear changes in surface color and morphology were observed with increasing firing duration. At short holding times of 15 and 30 min, the pellets retained a reddish-brown hue, indicating incomplete oxidation and limited sintering. The fracture surfaces in this range were relatively powdery, suggesting weak inter-particle bonding. As the holding time increased to 45 and 60 min, the surface color gradually darkened, and fracture morphology began to show more coherent fragments. At 90 and especially 120 min, the pellets exhibited a grayish tone with denser and more compact fracture surfaces. The absence of fine powder residues and the shift toward blocky fracture pieces indicate improved sintering behavior, likely due to enhanced grain boundary diffusion and the onset of local liquid-phase formation. These observations are consistent with the increasing compressive strength reported for IO: 100M at extended firing times.

High-resolution scanning electron microscopy (SEM) images at ×3000 magnification of the fracture surfaces of Australian pellets fired at 1050°C for 30 min, 1100°C for 30 and 120 min, and 1150°C for 30 min are presented in Fig. 8. As shown in Fig. 8a, the fracture surface of the pellet fired at 1050°C for 30 min exhibited discrete, sharp-edged particles—characteristic of the raw ore powder—with weak interparticle bonding, which accounts for the low compressive strength observed. At a higher firing temperature of 1100°C for 30 min, both trans-particle and inter-particle fracture features were observed, corresponding to a compressive strength approaching 250 kgf. When the holding time was extended to 120 min at 1100°C, stronger bonding between particles became evident, sharp particle edges disappeared, and the fracture mechanism shifted toward grain boundary failure, indicating the formation of a more cohesive microstructure and resulting in compressive strength exceeding 250 kgf. Similarly, the pellet fired at 1150°C for 30 min showed significant improvement in grain boundary cohesion due to liquid phase diffusion, and trans-particle fracture was domi-

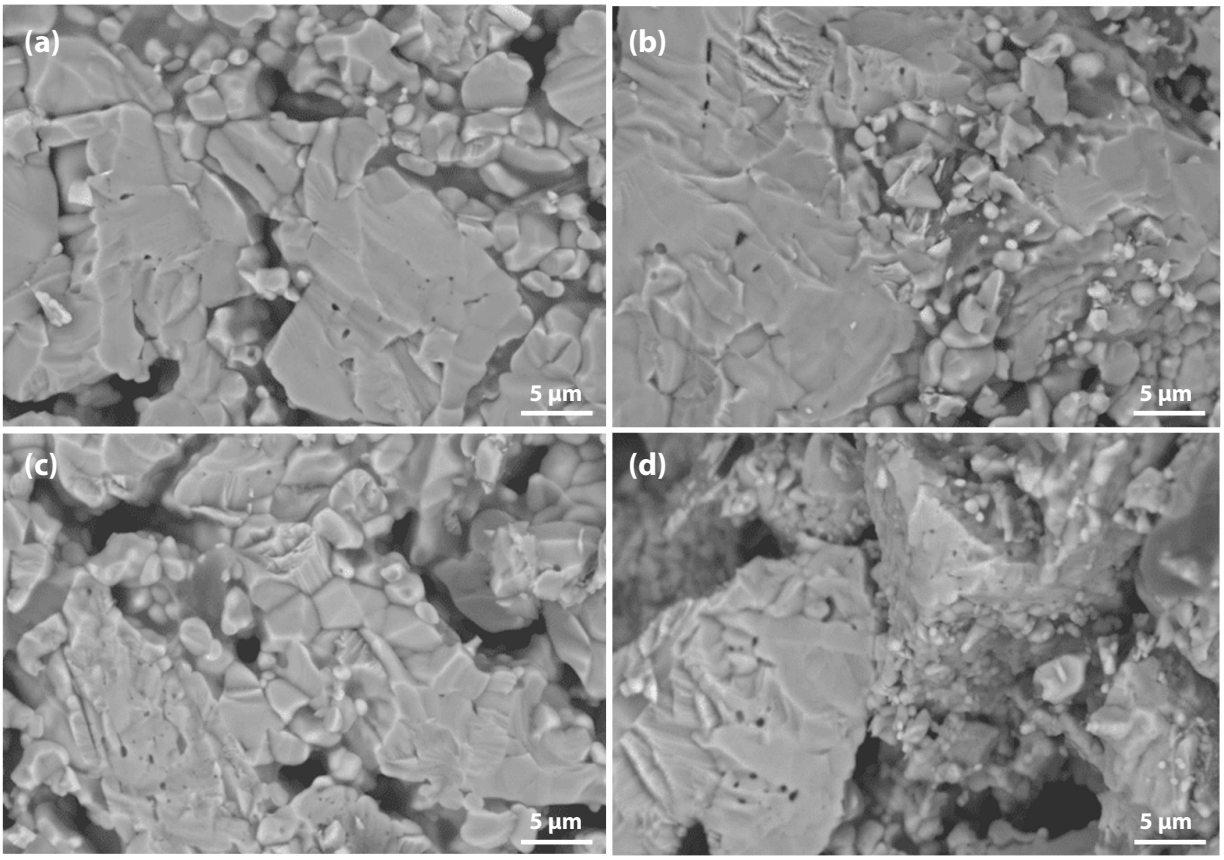

Fig. 9. Fracture surfaces of pellet samples oxidatively fired at 1150°C for 60 min: (a) 100% Australian ore, (b) 80% Minh Son + 20% Australian, (c) 90% Minh Son + 10% Australian, and (d) 100% Minh Son ore.

nant, achieving a compressive strength above 250 kgf.

The characteristic fracture surfaces of pellets fired at 1150°C for 60 min are shown in Fig. 9. It can be observed that pellet porosity varied notably:

- In Fig. 9(a) (100% Australian ore), most fractures occurred through particle breakage, corresponding to the highest compressive strength.
- In Fig. 9(d) (100% Minh Son ore), a mixture of large and small grains was observed, with fractures still occurring but with weaker interparticle bonding, resulting in the lowest strength.
- When blending (c) 10% and (b) 20% Australian ore into Minh Son ore, particle bonding was notably improved.

SEM image analysis showed that increasing the firing temperature from 1050°C to 1150°C or prolonging the holding time enhanced the solid bonding between fine ore particles. The edges of the ore grains became more rounded, and the dominant fracture mechanism shifted towards trans-particle fracture.The morphological changes of the fired pellets after oxidative firing can be explained by the following factors [18, 30-32]:

1. When fired at high temperatures in an oxidative atmosphere, magnetite ore particles begin to oxidize, forming Fe_2O_3 nanocrystals that grow and create bridging connections between particles. At 1050°C, this bonding can enhance pellet strength; however, due to the low temperature, the growth of Fe_2O_3 crystals is limited, resulting in insufficient compressive strength (only reaching 122–210 kgf/pellet), making the pellets unsuitable for blast furnace feedstock.
2. The recrystallization of Fe_2O_3 occurs when pellets are fired above 900°C. Complete transformation from magnetite to hematite takes place between 1050°C and 1150°C. Newly formed hematite crystals grow and bond tightly, significantly increasing pellet strength. The highest compressive strength was achieved for pellets oxidatively fired at 1150°C with a 2-h holding time.

3.3. Elemental Analysis in Fired Iron Ore Pellets

To gain deeper insight into the elemental distribution and its correlation with pellet structure and mechanical properties, energy-dispersive X-ray spectroscopy (EDX) and elemental mapping analyses were conducted on representative samples. These include fracture surfaces and cross-sections of pellets fired at 1150°C under varying conditions, as shown in Fig. 10 to 14.

Fig. 10 illustrates the EDX spectra obtained from various observation points on the fracture surface of an IO: 100A pellet (100% Australian ore) fired at 1150°C for 30 min. The analyzed area lies along the boundary between hematite particles and is marked by a higher concentration of Si in addition to Fe and O. This indicates the possible presence of SiO_2 at grain interfaces, which may lead to the formation of silicate-rich phases influencing sintering behavior and the bonding between particles. In contrast, points located within the grain interiors (e.g., Fig. 10b and 10d) were primarily composed of Fe and O, consistent with hematite (Fe_2O_3). Meanwhile, grain boundaries (e.g., Fig. 10a and 10c) exhibited enrichment in light elements such as Na, K, Mg, and Al, indicating localized concentrations of alkali and alkaline earth metal oxides. This segregation is believed to facilitate liquid-phase formation during firing, enhancing particle cohesion and promoting pellet densification [1, 33]. Elena Yazhenskikh's research [33] supports this, showing that eutectic temperatures in the Na_2O–SiO_2 and K_2O–SiO_2 binary systems are as low as 789 °C and 743 °C, respectively, while the ternary K_2O–Na_2O–SiO_2 system reaches a eutectic point at just 540 °C – critical for phase evolution during sintering.

Fig. 11 presents the EDS elemental mapping image of an IO: 100M pellet (100% Minh Son ore) fired at 1150°C for 120 min. The mapping clearly shows a heterogeneous microstructure with Si and O-rich phases distributed in isolated domains, while Fe-rich zones dominate the matrix. This microstructural contrast suggests incomplete homogenization, which correlates with the relatively lower strength of Minh Son pellets compared to Australian ore.

The corresponding EDX point spectra in Fig. 12 confirm these observations. Fe and O dominate the matrix composition, while isolated regions show higher concentrations of Si, Al, Na, and K. These regions likely represent residual gangue phases or partially sintered mineral inclusions.

For blended pellets, Fig. 13 and 14 show the elemental mapping and point spectra of IO: 20A–80M pellets fired at 1150°C for 60 min. The elemental maps indicate that Fe and O are more continuously present throughout the pellet matrix compared to IO: 100M, while Si-rich regions, although still observable, appear as smaller and less isolated domains that are more closely associated with the surrounding iron oxide phase. This integration of Si-rich areas into the Fe–O matrix, as opposed to forming large or segregated regions, is likely to facilitate stronger bonding between particles. These microstructural features are consistent with the higher compressive strength observed in the blended pellets compared to those made solely from Minh Son iron ore.

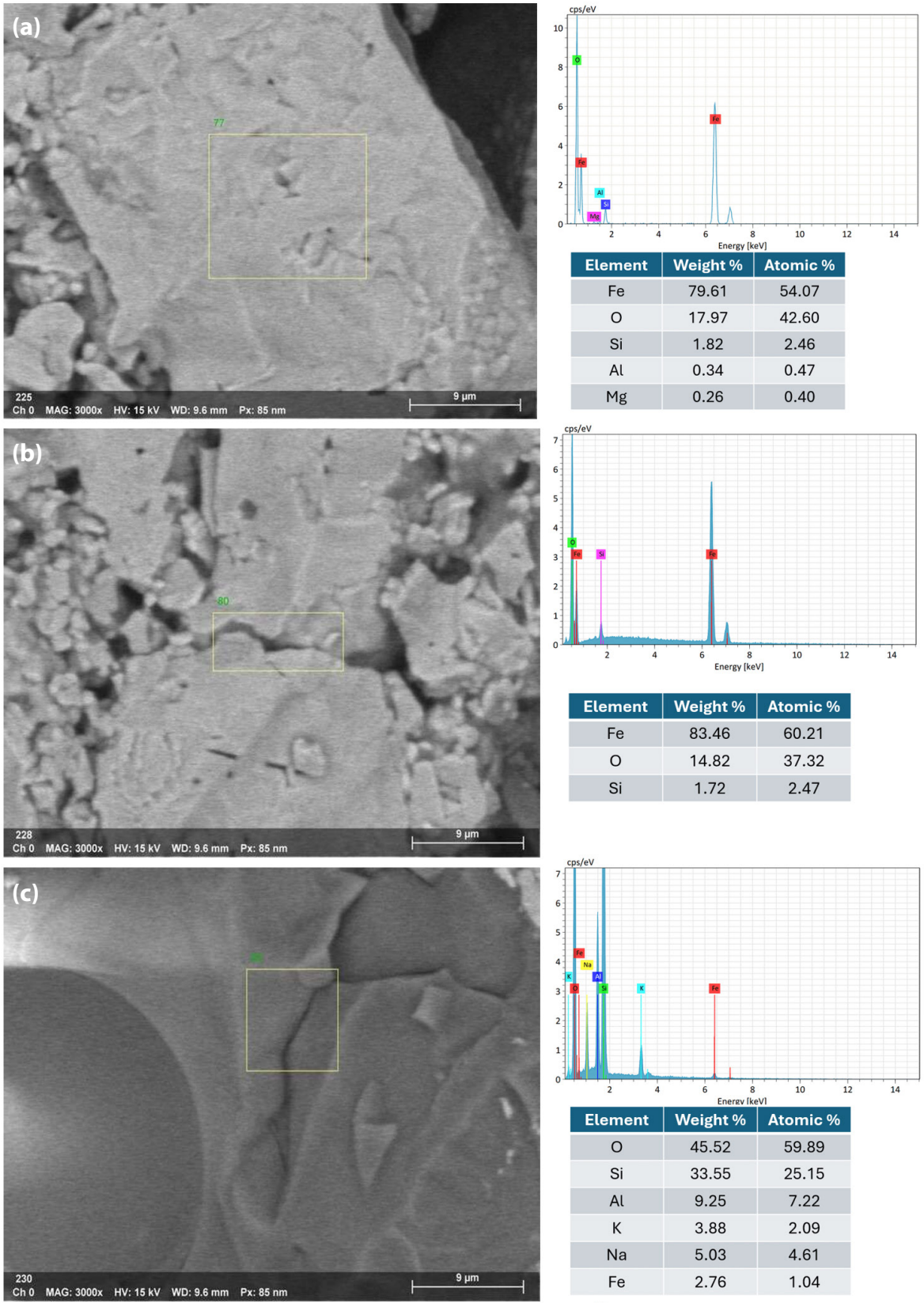

Element	Weight %	Atomic %
Fe	79.61	54.07
O	17.97	42.60
Si	1.82	2.46
Al	0.34	0.47
Mg	0.26	0.40

Element	Weight %	Atomic %
Fe	83.46	60.21
O	14.82	37.32
Si	1.72	2.47

Element	Weight %	Atomic %
O	45.52	59.89
Si	33.55	25.15
Al	9.25	7.22
K	3.88	2.09
Na	5.03	4.61
Fe	2.76	1.04

Fig. 10. Energy-dispersive X-ray spectroscopy elemental analysis spectra at specific observation points on the fracture surface of an Australian pellet fired at 1150°C for 30 min

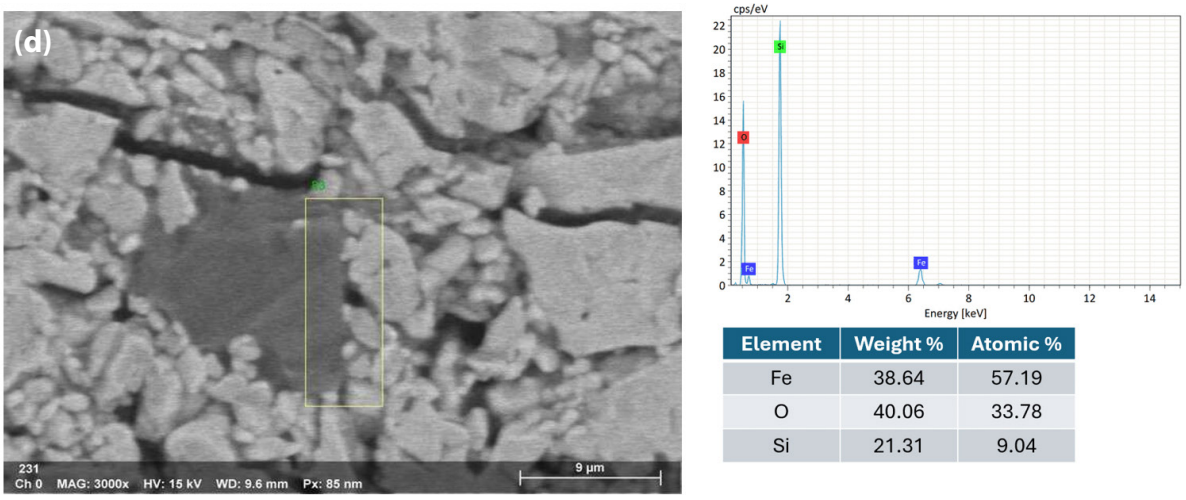

Element	Weight %	Atomic %
Fe	38.64	57.19
O	40.06	33.78
Si	21.31	9.04

Fig. 10. Continued.

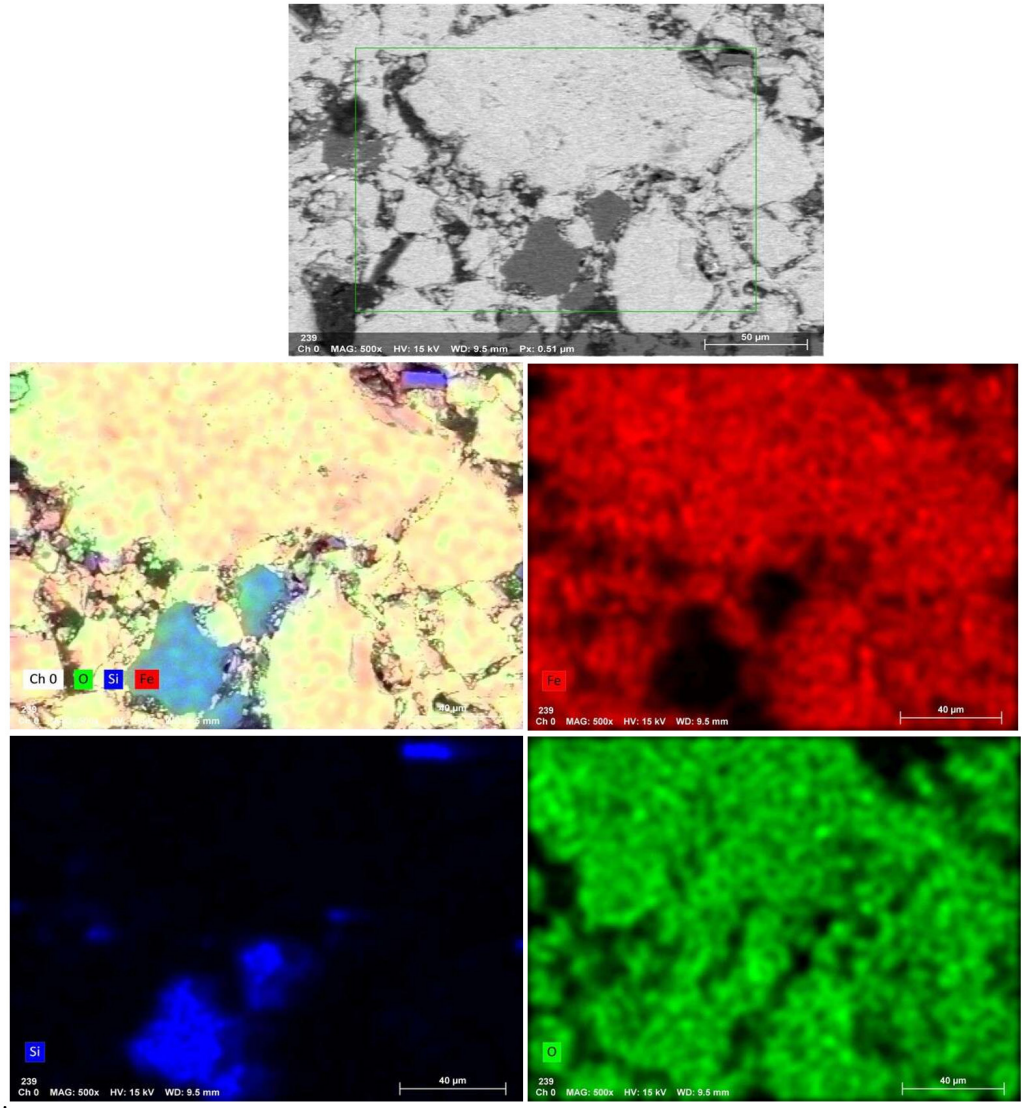

Fig. 11. Energy-dispersive X-ray spectroscopy mapping image of a Minh Son pellet fired at 1150°C for 120 min.

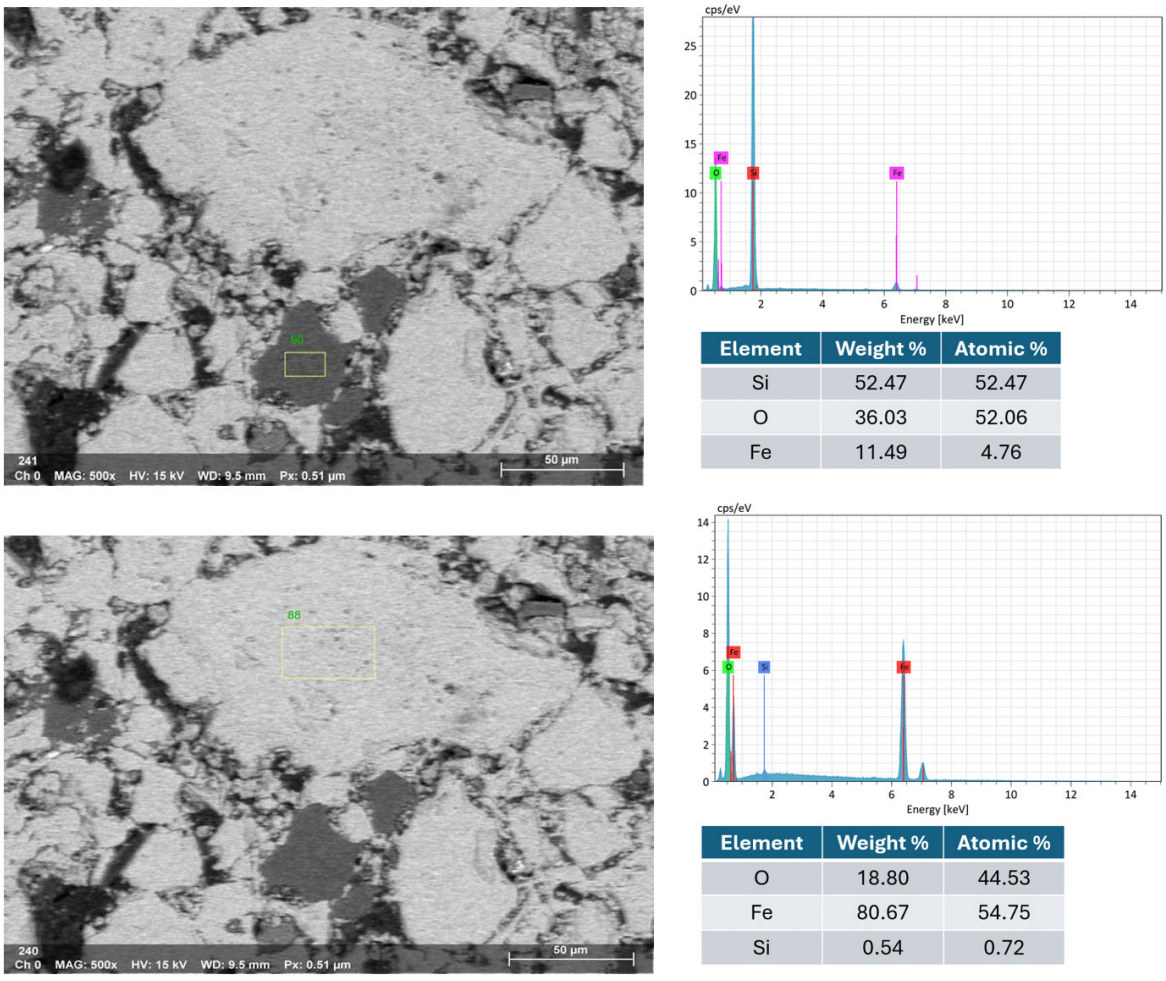

Element	Weight %	Atomic %
Si	52.47	52.47
O	36.03	52.06
Fe	11.49	4.76

Element	Weight %	Atomic %
O	18.80	44.53
Fe	80.67	54.75
Si	0.54	0.72

Fig. 12. Energy-dispersive X-ray spectroscopy elemental spectra at specific observation points on a Minh Son pellet fired at 1150°C for 120 min.

Moreover, the quantitative EDX data (in the inset of Fig. 10, 12 and 14) support these visual findings. For instance, pellets with higher compressive strength consistently exhibit Fe weight fractions above 80%, while lower-strength samples show elevated Si and alkali oxide content, especially at grain boundaries.

These results confirm that:

- Fe–O-rich domains correspond to well-sintered hematite phases contributing to strength,
- Si-rich and alkali-enriched regions tend to localize at boundaries or pores, potentially reducing interparticle bonding,
- and blending coarse Minh Son with fine Australian ore helps refine elemental distribution and promote consolidation.

Ultimately, elemental analysis via EDX demonstrates that chemical homogeneity and selective enrichment of sintering-aid oxides at key interfaces are critical for optimizing pellet strength under oxidative firing.

To further elucidate the improvement in homogeneity and compressive strength observed when blending Minh Son with Australian ore, it is useful to consider the micromechanical theory of particle bonding in porous media. According to the Rumpf equation [1, 21]:

$$\sigma_C = a\left[\frac{(1-\varepsilon)}{\varepsilon}\right] \cdot \frac{\gamma}{d} \cdot cos\theta_{sl}$$

where σ_C is the compressive strength, ε is the fractional porosity, γ is the liquid surface tension, d is the average particle size, and θ_{sl} is the liquid–solid contact angle. This relationship predicts that the compressive strength of the pellet is inversely proportional to the average particle size and porosity, and directly proportional to the degree of liquid-phase bonding at

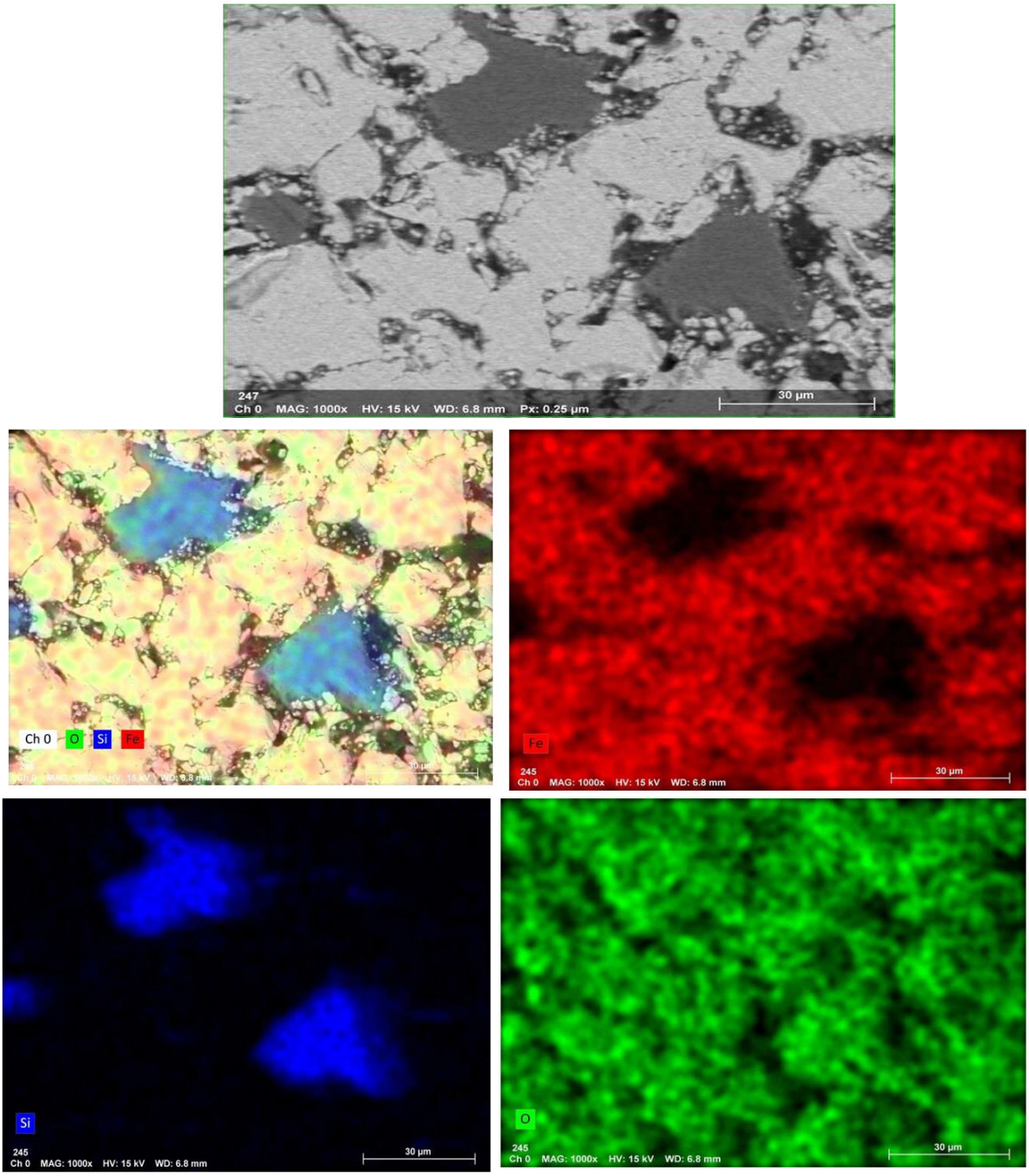

Fig. 13. Energy-dispersive X-ray spectroscopy mapping image of a blended pellet (80% Minh Son + 20% Australian) fired at 1150°C for 60 min.

particle contacts. Blending the finer Australian ore (d_{50} ≈ 13 μm) with the coarser Minh Son ore (d_{50} ≈ 50 μm) results in a more optimized particle packing, reducing the effective porosity (ε and average particle size (d) within the green pellet. This bimodal particle size distribution allows the fine Australian particles to fill the interstitial voids between coarser Minh Son grains, leading to a denser and more homogeneous microstructure. As predicted by the Rumpf equation, such improvements in packing and particle bonding - especially in the presence of liquid-phase sintering aids at high temperature—directly translate into increased compressive strength and structural uniformity of the fired pellets. Therefore, the enhanced homogeneity

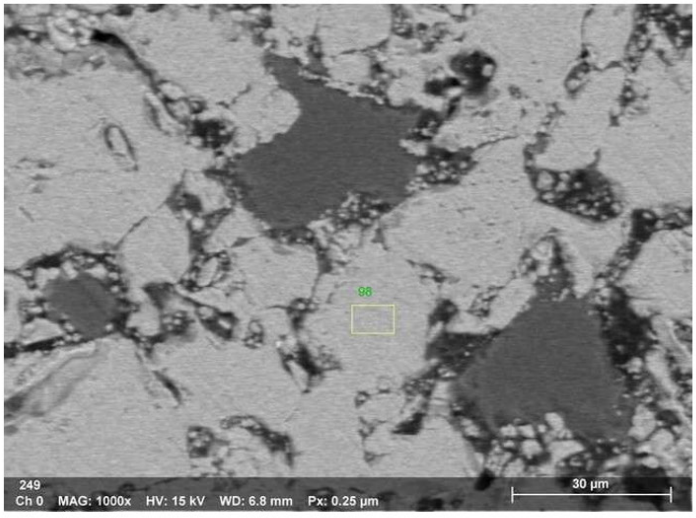

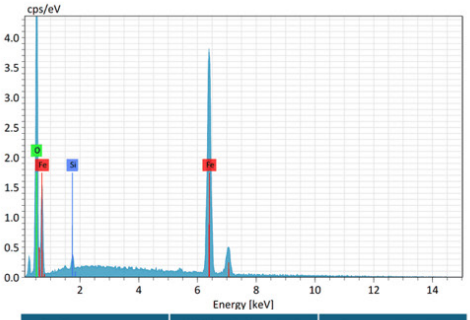

Element	Weight %	Atomic %
Fe	85.00	62.19
O	14.55	37.16
Si	0.45	0.65

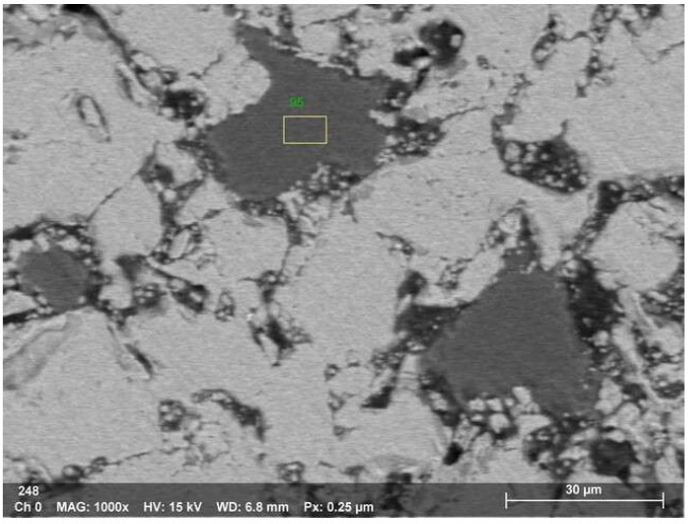

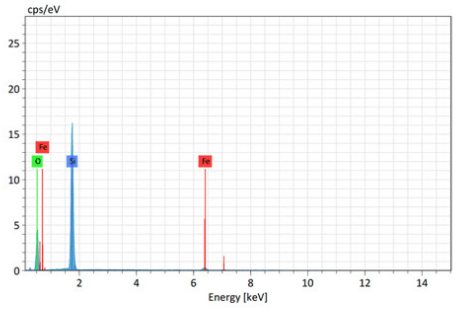

Element	Weight %	Atomic %
Si	59.08	49.68
O	31.34	46.27
Fe	9.58	4.05

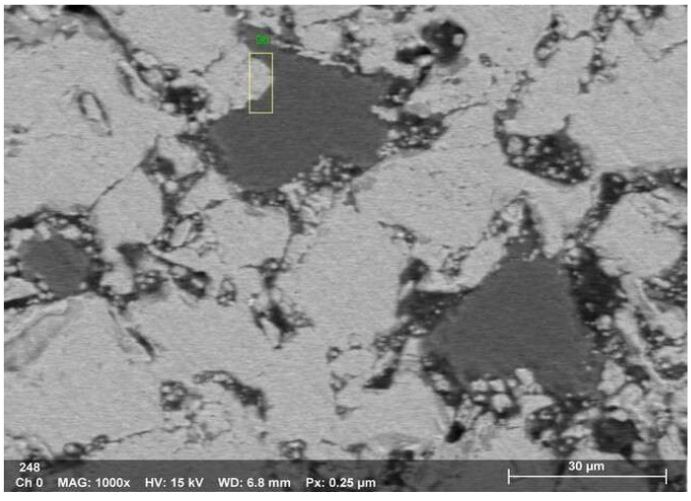

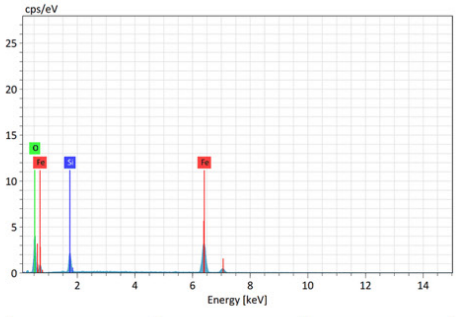

Element	Weight %	Atomic %
Fe	76.29	52.85
O	13.92	33.66
Si	9.79	13.49

Fig. 14. Energy-dispersive X-ray spectroscopy elemental spectra at specific observation points on a blended pellet (80% Minh Son + 20% Australian) fired at 1150°C for 60 min.

and mechanical properties of blended pellets can be quantitatively explained by this theoretical framework, in agreement with both the microstructural observations and mechanical testing results of this study [1, 17, 21].

IV. Conclusion

This study investigated the influence of oxidative firing parameters and raw material characteristics on the pelletization behavior and mechanical properties of iron ore concentrates. Pellets were prepared from Australian ore, Minh Son ore, and their blends, with firing conducted at temperatures ranging from 1050°C to 1150°C and holding times from 15 to 120 min. The results demonstrated that both firing temperature and duration significantly affect the compressive strength of the pellets, with higher compressive strength values achieved at 1150°C and prolonged holding times. Among all compositions, pellets made from 100% Australian ore (IO: 100A) exhibited the highest compressive strength, exceeding the industrial threshold of 250 kgf/pellet even at moderate firing durations.

Microstructural analysis revealed that improved strength is associated with the disappearance of sharp-edged particles, the development of trans-particle fracture, and enhanced grain boundary bonding. SEM-EDX and elemental mapping indicated that liquid-phase formation—facilitated by the localized enrichment of alkali and alkaline earth oxides—played a key role in promoting densification and interparticle bonding.

Furthermore, blending the coarser Minh Son concentrate with the finer Australian concentrate (e.g., IO: 20A–80M and IO: 10A–90M) led to noticeable improvements in pellet strength compared to using Minh Son ore alone. This highlights the effectiveness of optimizing particle size distribution and raw material composition. The results offer practical insights for improving iron ore pellet production from mixed ore sources, with clear benefits for sintering efficiency and mechanical performance in industrial-scale ironmaking.

Funding

This research is funded by Hanoi University of Science and Technology (HUST) under project number T2023-PC-056.

Conflict of Interest

The authors have no conflicts of interest to declare.

Data Availability Statement

All data generated or analyzed during this study are included in this article.

Author Information and Contribution

Ngo Quoc Dung: PhD candidate; responsible for conceptualization, experimental design and execution, original draft preparation, and acquisition of funding.

Tran Xuan Hai: Undergraduate student; contributed to experimental work and performed calculations related to the pelletization and mechanical testing processes.

Nguyen Minh Thuyet: PhD; supervised the research activities, provided critical revisions, and contributed to reviewing and editing the manuscript.

Nguyen Quang Tung: Research engineer; contributed to conceptualization and carried out computational analyses supporting experimental findings.

Arvind Barsiwal: PhD candidate; participated in reviewing and provided critical revisions.

Nguyen Hoang Viet: Professor; provided overall supervision, contributed to conceptual development, and participated in reviewing and editing the final manuscript.

Acknowledgments

The authors would like to extend their sincere appreciation to Hoa Phat Hai Duong Steel Joint Stock Company for generously supplying the raw materials and fuel essential to this research. Their contribution was instrumental in enabling the successful completion of our study.

References

[1] R. P. Bhagat: Agglomeration of Iron Ores, (2019).
[2] R. C. Gupta: Theory and Laboratory Experiments in Ferrous Metallurgy, (2010).
[3] A. K. Biswas: Principles of Blast Furnace Ironmaking: Theory and Practice, (Cootha), (1981) 528.
[4] A. Ghosh and A. Chatterjee: Ironmaking and Steelmaking: Theory and Practice, (PHI Learning Privated Limited), (2008).
[5] L. Lu: Iron Ore: Mineralogy, Processing and Environmental Sustainability, (2015) 1.
[6] M. Geerdes, R. Chaigneau, I. Kurunov, O. Lingiardi and J.

Ricketts: Modern Blast Furnace Ironmaking: An Introduction, 3rd ed., (PHI Learning Private Limited), (2015).
[7] A. Chatterjee: Sponge Iron Production by Direct Reduction of Iron Oxide, 2nd ed., (PHI Learning Privated Limited), (2012).
[8] H. B. Lüngen and J.-I. Yagi: Ullmann's Encyclopedia of Industrial Chemistry, (2019), 1.
[9] N. Q. Dung, N. M. Thuyet, N. T. H. Oanh, and N. H. Viet: Canadian Metallurgical Quarterly, (2025).
[10] Q. D. Ngo, M. T. Nguyen and H. V. Nguyen: Key Eng. Mater., **1005** (2024) 3.
[11] N. Q. Dũng, Đ. T. N. Ánh, N. S. Hiếu, N. Đ. Tuyên, N. Q. Tùng, C. T. M. Thu, L. V. Khởi, Đ. N. Q. Chiến, N. T. H. Oanh and N. H. Việt: J. Sci. Tech. Metals, **98** (2021) 2.
[12] N. H. Viet, P. N. D. Quynh and N. T. H. Oanh: J. Nanosci. Nanotechnol., **21** (2021) 2563.
[13] S. Moraes, J. R. B. Lima and T. R. Ribeiro, Iron Ores and Iron Oxide Materials, IntechOpen, (2018).
[14] A. Babich, D. Senk and H. W. Gudenau, Ironmaking, (2016).
[15] S. Kumar, B. Ravi, O. Sivrikaya and R. Nanda: Sci. Sinter., **51** (2019) 27.
[16] K. Sastry, P. Dontula and C. Hosten: Powder Technol., **130** (2003) 231.
[17] K. V. S. Sastry and D. W. Fuerstenau: Powder Technol., **7** (1973) 97.
[18] H. Elahidoost, S. Sheibani, S. Raygan, L. Hosseini and N. Esmaeili: Adv. Powder Technol., **33** (2022) 103883.
[19] V. Claremboux and S. K. Kawatra: Miner. Process. Extr. Metall. Rev., **44** (2023) 138.
[20] S. K. Kawatra and V. Claremboux: Miner. Process. Extr. Metall. Rev., **43** (2022) 813.
[21] S. K. Kawatra and V. Claremboux: Miner. Process. Extr. Metall. Rev., **43** (2022) 529–544.
[22] T. C. Eisele and S. K. Kawatra: Miner. Process. Extr. Metall. Rev., **24** (2003) 1.
[23] B. E. Monsen, E. S. Thomassen, I. Bragstad, E. Ringdalen and P. H. Hoegaas: Characterization of DR Pellets for DRI Applications, in AISTech 2015 Proceedings, vol. 1, Cleveland, OH, USA, May, (2015) 739.
[24] N. H. Viet, P. N. D. Quynh and N. T. H. Oanh: A study on the reduction of iron ore pellets in a bed of non coking coal, in Proc. National Scientific Conference on Metallurgy and Materials Technology, Hanoi, Vietnam, (2016) 185.
[25] P. K. Cuong, T. T. Dung, K. M. Tuyen, C. T. M. Thu and L. V. Khoi: Fabrication of a Compressive Strength Testing Device and Investigation of the Compressive Strength of Green Iron Ore Pellets, in Proc. Student Scientific Conference, Hanoi, Vietnam, (2020) KTVL.04.
[26] P. S. Kumar, B. P. Ravi, O. Sivrikaya and R. K. Nanda: Sci. Sinter., **51** (2019) 27.
[27] N. Doebelin and R. Kleeberg: J. Appl. Crystallogr, **48** (2015) 1573.
[28] N. Q. Dung, L. V. Khoi, N. L. Khoa, V. Hai, D. X. Thanh, P. Anh, N. T. H. Oanh, N. D. Tuyen, N. M. Duc, L. H. Thang, P. H. Long, H. T. M. Loan, C. T. M. Thu, T. T. Phong, B. L. Hung, M. K. Luan, N. Q. Huy, V. Hiep, P. M. Tuan, N. M. Thuyet, N. H. Viet: "Unveiling phase changes in iron ore reduction: X-ray diffraction analysis with a user-friendly Colab interface integrated with the Materials Project API," in Proc. Int. Conf. Adv. Mater. Technol. (ICAMT), Hanoi, Vietnam, Oct. 9–12, (2024) 171.
[29] k. b. Anand, k. k. Swapan and M. Kumar: IOP Conference Series: Mater. Sci. Eng., **178** (2017) 012003.
[30] T. Umadevi, N. F. Lobo, S. Desai, P. C. Mahapatra, R. Sah and M. Prabhu: ISIJ Int., **53** (2013) 1673.
[31] S. P. E. Forsmo, S. E. Forsmo, P. O. Samskog and B. M. T. Björkman: Powder Technol, **183** (2008) 247.
[32] G. Li, T. Jiang, Y. Zhang, and Z. Tang: Recrystallization of Fe2O3 During the Induration of Iron Ore Oxidation Pellets, in Recrystallization, K. M. Sztwiertnia (Ed.) IntechOpen (2012) 229.
[33] E. Yazhenskikh, PhD. thesis. Development of a new database for thermodynamic modelling of the system Na2O-K2O-Al2O3-SiO2, Rheinisch-Westfälische Technische Hochschule Aachen, (2005) 27.

Research Article

pISSN 2799-8525 · eISSN 2799-8681
J Powder Mater 2025;32(4):330-343

Journal of
Powder Materials

열역학 및 열 전달 해석을 활용한 Stellite 6 스크랩 재활용 공정과 분말화 기술 연구

이용관[1,2,†], 김현철[1,2,†], 김명석[1,2], 오승주[2], 박경태[1,*], 심재진[1,*]

[1]한국생산기술연구원 국가희소금속센터
[2]고려대학교 신소재공학과

The Recycling Process and Powderization Technology of Stellite 6 Scrap: A Thermodynamic and Heat Transfer Analysis

YongKwan Lee[1,2,†], Hyun-chul Kim[1,2,†], Myungsuk Kim[1,2], Soong Ju Oh[2], Kyoungtae Park[1,*], JaeJin Sim[1,*]

[1]Korea Institute of Industrial Technology, Incheon 21655, Republic of Korea
[2]Department of Materials Science and Engineering, Korea University, Seoul 02841, Republic of Korea

Co-Cr alloys are widely used in cutting tools and turbine components due to their high strength and resistance against wear and corrosion. However, scrap generated during hardfacing is often discarded due to impurities and oxidation, and research on its recycling remains limited. This study aimed to optimize the recycling process of Stellite 6 scrap to reduce waste and minimize costs while maintaining material quality. Melting, casting, and powdering processes were designed using HSC Chemistry, FactSage, and COMSOL Multiphysics, with optimization of key parameters such as the crucible material and temperature control. The recycled alloy and powder were analyzed using X-ray fluorescence analysis, inductively coupled plasma optical emission spectroscopy, and X-ray diffractometry, showing mechanical and chemical properties comparable to commercial Stellite 6. The Co and Cr contents were maintained, with a slight increase in Fe. These findings demonstrate the potential for producing high-quality recycled Stellite 6 materials, contributing to the sustainable utilization of metal resources in high-performance applications.

Keywords: Stellite 6; Cobalt-Chromium Alloy; Hard facing; COMSOL Multiphysics; Recycling

Received: April 30, 2025
Revised: June 25, 2025
Accepted: July 10, 2025

***Corresponding author:**
Kyoungtae Park
E-mail: ktpark@kitech.re.kr

***Corresponding author:**
JaeJin Sim
simjae@kitech.re.kr

†These authors contributed equally to this work.

1. Introduction

Co-Cr계 합금은 높은 강도 (500-1500 MPa), 높은 경도 (HRC 40-65), 그리고 우수한 내마모성과 내식성을 갖는 금속 재료이다[1-5]. 이러한 특성으로 인해 Co-Cr계 합금은 조성에 따라 다양한 형태로 개발되어 절삭 공구, 밸브 부품, 터빈 블레이드, 펌프 부품 등 여러 산업 분야에 널리 활용되고 있다[5-7]. 대표적으로, Co-Cr-Mo계 합금은 내식성 및 생체 적합성이 매우 높아 의료용 임플란트 등 생체 재료 분야에서 주로 사용된다[8-10]. Co-Cr-Ni계 합금은 고온 강도, 내산화성, 내마모성이 우수하여 항공기 엔진, 가스 터빈 등 고온·부식 환경에 적합한 산업용 소재로 활용된다[11, 12]. Co-Cr-W계 합금은 매우 높은 경도와 내마모성 및 내식성 물성으로 인해 하드페이싱 (Hardfacing) 용접 공정의 핵심소재로 활용되며, 특히 Stellite 6 (Kennametal Inc., USA) 라는 제품으로 가장 널리 알려져 있다[13-15].

이처럼 다양한 산업 분야에서 활발히 활용되는 Stellite 6을 기반으로, 많은 연구자들이 모재의 특성 향상 및 고온 환경에서의 코팅 효과 증진을 위한 연구를 수행해왔다. Jacek Górka et al. [16]은 Laser-Cladded Coatings 공정을 통해 Co 기반 합금(Stellite 6)에

https://doi.org/10.4150/jpm.2025.00136

경도와 미세구조를 개선 효과가 있는 타이타늄 카바이드 (TiC) 형성을 위해 다양한 농도의 Ti와 C를 첨가하여 내식성 향상 증진 및 침식 저항성 향상을 위한 연구를 수행하였다. 그 결과, Ti–W–C 복합 탄화물이 형성되어 소재의 마모 및 변형 저항성을 증가시켰으며, 이에 따라 모재의 내식성과 침식 저항성이 향상됨을 확인하였다. 또한, Dariusz Bartkowski et al. [17]은 다양한 WC, TiC 비율과 레이저 빔 출력에 따른 코팅 효과를 비교 분석하여, 생성된 탄화물로 인해 미세경도와 내마모성이 향상되며 모재의 침식 저항성과 내구성 역시 개선됨을 확인하였다.

Eyup Bagci et al. [18, 19]은 Stellite 6 합금의 페이스 밀링 (face milling) 공정에서 공구 마모, 칩 형상, 절삭력 변화가 모재의 제거율 (Material Removal Rate, MRR) 및 마모 특성에 미치는 영향을 체계적으로 분석하였다. 그 결과, 절삭 깊이 및 이송 속도에 따라 절삭력이 증가함에 따라 내식성이 향상되는 경향을 보였으며, 절삭속도와는 유의한 상관관계가 확인되지 않았다. 그리고, Joowon Suh et al. [20]은 지향성 에너지 적층 (Directed energy deposition, DED) 기반 적층 제조에 열간 등압 성형 (Hot Isostatic Pressing, HIP) 공정을 결합한 후처리 방법을 통해, 기존 주조 공정 대비 코발트 기지상의 감소 및 탄화물 형성이 경도 등 기계적 특성 향상에 기여하며, 결과적으로 내식성이 개선됨을 입증하였다.

뿐만 아니라, Stellite 6은 분말 형태로 열 스프레이 코팅, 고속 산소 연료 분사 (High Velocity Oxygen Fuel, HVOF) 공정에도 많이 활용되고 있다. 이와 관련하여 Alejandra Islas Encalada et al. [21]은 Stellite 6 분말에 탄화 크로뮴 (Cr_3C_2) 금속 바인더를 첨가하여 HVOF 공정을 수행함으로써, 마모 저항성 향상과 그 메커니즘에 대한 연구를 진행하였다. 해당 연구에서는 마모 특성에 중요한 영향을 미치는 Cr_3C_2의 장입을 통해 코팅 물성이 개선됨을 입증하였다. 또한, Žaneta Dlouhá et al. [22]는 탄소강 및 질화강 기판에 Stellite 6을 코팅하기 위해, HVOF 공정 전 레이저 텍스처링 (Laser Texturing) 전처리 공정을 적용하여 코팅 효율을 분석하였다. 그 결과, 탄소강에서는 기계적 고정력 (mechanical interlocking) 향상으로 인해 코팅 효율이 증가한 반면, 질화강은 표면의 얇고 취성 있는 질화층이 레이저 텍스처링 및 HVOF 분사 중 손상되어 계면에 크랙이 발생하였고, 이로 인해 코팅 성능이 저하됨을 확인하였다."

이처럼 Stellite 6 및 분말을 활용한 모재 특성 향상과 코팅 성능 개선에 관한 연구는 활발히 진행되고 있으나, 하드페이싱 공정 중 발생하는 Stellite 6 스크랩의 재활용에 대한 연구는 아직 미흡한 수준에 머물고 있다. Stellite 6 스크랩은 금속 산화물, 절삭유 등의 불순물이 혼입될 가능성이 높아 대부분 폐기되며, 이에 따른 경제적 손실과 자원 낭비가 발생하고 있다. 스크랩을 효과적으로 재활용할 경우 원자재 비용 절감뿐만 아니라 공정에서 소요되는 총 에너지 및 비용까지 절감할 수 있을 것으로 기대된다.

따라서, 본 연구에서는 Stellite 6 스크랩의 재활용 가능성을 검토하고, 스크랩 내 일정량의 기재가 포함된 경우에도 실용적인 재활용이 가능한지를 검토하고자 한다. 이를 위해 다양한 시뮬레이션 소프트웨어 (HSC Chemistry [23], FactSage 8.0 [24], COMSOL Multiphysics 6.1 [25])를 활용하여 재활용 공정을 최적화하고, 실제 산업 현장에서 발생한 Stellite 6 스크랩을 기반으로 재활용 Stellite 6 주조재를 제조하였다. 또한, 제조된 재활용 Stellite 6 주조재를 활용하여 열 스프레이 코팅 및 HVOF 사용 가능한 분말을 제조하였고, 최종적으로 재활용 소재의 물성 특성을 분석하여 상업용 Stellite 6 제품과 비교 분석함으로써 재활용 공정의 상업적 활용 가능성을 평가하였다.

2. Experimental Section

2.1 실험 방법

본 연구에서는 Stellite 6 스크랩의 재활용을 위한 최적의 공정을 도출하기에 앞서, 다양한 전처리 및 분석을 수행하였다. 실험에 사용된 스크랩은 ㈜삼신에서 발전소용 밸브 용접 공정 이후 실제로 발생한 산업용 Stellite 6 스크랩을 제공받아 활용하였다. 스크랩 내에 잔류된 절삭유 및 기타 유기 용매와 같은 다양한 불순물을 제거하기 위해 에탄올을 활용한 Ultrasonic 3시간을 진행하였다. 그 후 불순물이 제거된 스크랩의 밀도 향상을 위해 Vacuum-plasma melting 및 프레스 공정을 통한 Compaction을 진행하였다.

그 다음으로 Stellite 6 스크랩 재활용 공정 최적화를 위해 HSC Chemistry 8.0과 FactSage 8.0 Software를 활용하여 열역학적 계산을 수행하고, 이를 바탕으로 다양한 공정 조건을 도출하였다. 그리고 COMSOL Multi-physics Software를 이용한 유한요소해석 (Finite element method, FEM)을 통해 열 전달 및 물리 전산모사 계산을 진행하여 고주파 용해 조건을 선정하였다.

선정된 공정 조건을 기반으로 전처리된 스크랩 원료와 고주파 유도 용해 장비를 이용하여 Stellite 6 스크랩 용해 공정을 수행하였으며, 생성된 용탕을 제조한 몰드에 주조한 후, 4시간 냉각 과정을 거쳐 최종 제품을 회수하였다. 회수된 최종 제품에 대한 XRF, ICP-OES, FE-SEM, EDS, XRD 분석을 수행하였고, 상용 Stellite 6 제품의 물성과 비교하였다. 그리고, 제조한 재활용 Stellite 6 주조재와 아토마이저 공정을 통해 Stellite 6 분말을 제조하였다. 이후, 체질 공정을 통해 입자 크기별로 분리한 후, 다양한 기초 분석을 수행하여 상업용 분말과 비교 평가를 진행하였다. 최종적으로 제조된 재활용 Stellite 6 분말을 다양한 기초분석을 통해 상용 분말과의 물성 평가를 진행하였다.

2.2 특성 평가

본 연구를 통해 제조된 Stellite 6 주조재 및 분말의 성분분석을 위

해 Energy Dispersive Sepctroscopy (EDS) (Oxford, U.K사), ICP-OES (Inductively Coupled Plasma – Optical Emission Spectroscopy, Varian Vista Pro, USA), X-ray Fluorescence Analysis (XRF) (Thermo Fisher SCIENTIFIC, ARL PERFORM'X, USA)을 활용하여 진행하였다. 또한, 구조분석은 Field Emission Scanning Electron Microscope (FE-SEM) (JEOL사, Model: JSM-7100F), X-Ray Diffractometer(XRD) (BRUKER AXS사, Model: D8 ADVANCE)을 활용하여 특성 평가를 진행하였다.

3. Results and Discussion

3.1 열역학적 계산 결과

본 실험에 앞서 Stellite 소재의 열역학적 거동을 파악하기 위하여, FactSage 8.0 Software의 Phase Diagram 모듈을 활용해 시뮬레이션을 수행하였다. 두 가지 상태도 계산을 진행하였으며, 이는 Fig. 1에 제시하였다. Fig. 1(a)는 Stellite 합금의 주요 기지인 Co-Cr 이원계 상태도로, 다양한 Co/Cr 조성비와 온도 조건에서의 상 변화를 확인을 위한 상태도 계산 결과이다. 계산 결과에 따르면, Co 함량에 따라 α-Co (고온상), ε-Co (저온상), σ상, 그리고 액상 (Liquid)이 형성되는 것을 확인할 수 있다. 특히, α-Co 및 ε-Co 상은 Cr이 최대 40%까지 고용이 가능하고 σ상은 국부적인 Co 결핍 상태에서 석출된다고 알려져 있으며, 이는 Stellite 6 합금의 내부식성 저하와 연관이 있는 것으로 알려져 있다[20].

Fig. 1(b)는 다성분계 Stellite 6 합금에 대해 Cr 함량 및 온도에 따른 상평형 변화를 계산한 결과를 나타낸다. 계산 결과, 다양한 고상 및 탄화물 상이 존재하는 것으로 확인되었다. 또한, 상태도 내에 표시된 빨간색 범위는 상용 Stellite 합금에서 일반적으로 보고되는 Cr 함량 (약 25–30 wt%)을 반영한 것으로, 주요 합금 원소 (Co, Cr, W, Fe, Si 등)의 상대적 원자비 기준으로 환산할 경우 이 범위가 약 0.2–0.3의 조성 구간에 해당하므로 이를 적용하였다. 해당 조성 영역에서는 온도에 따라 탄화코발트 ($Co_xW_yC_a$) 및 복합 탄화물 상이 형성될 가능성이 있음을 시사한다. 마지막으로, Stellite 6 스크랩 재활용 시 σ상 형성과 Cr 탄화물 침전 방지를 위해서는, Co-Cr 기지 내 완전 용해 조건을 확보할 필요가 있으며, 이때 최소 1,500 ℃ 이상의 고온 조건이 요구된다는 결론을 도출하였다.

그리고 Stellite 6 스크랩의 재활용 공정에서 사용될 도가니 소재를 선정하기 위해, HSC Chemistry Software를 활용하여 다양한 후보 소재와의 반응성 계산을 진행하였으며 원료 및 도가니와의 반응으로 인한 생성물은 그래프 내 붉은색 글씨로 표시하여 강조하였다. Fig. 2(a)는 일반적으로 많이 사용되는 금속 도가니 소재와의 반응성 계산 결과를 나타내었다. 그 결과, 몰리브덴 (Mo), 티타늄 (Ti), 탄탈륨 (Ta)은 고온 공정 조건에서 원료 성분들과 반응하여 각각 이몰리브덴 (Mo_2), 크로뮴화 티타늄 ($TiCr_2$), 크로뮴화 탄탈럼 ($TaCr_2$) 등의 화합물을 형성하는 것이 확인되었다. 반면, 텅스텐 (W)과 지르코늄(Zr)은 원료와 반응하지 않는 것으로 나타나, 금속 도가니 소재로서 W 및 Zr이 적합한 후보로 판단되었다.

Fig. 2(b)는 다양한 세라믹 도가니 소재와의 반응성을 계산한 결과이며, 대부분의 세라믹 소재는 원료와 반응하여 여러 생성물이 형성되는 것으로 확인하였다. 생성물 확인이 어려운 소재의 경우, 그래프를 확대하여 추가로 제시하였으며, 그 중 지르코니아 (ZrO_2)는 예외적으로 원료와 반응하지 않고 안정한 거동을 나타내어, 세라믹 소재 중 가장 적합한 도가니 재료로 판단됩니다. 결론적으로, 용해 공정에서 도가니 소재로는 금속의 경우 W 또는 Zr, 세라믹의 경우 ZrO_2가 활용 가능함을 확인하였다.

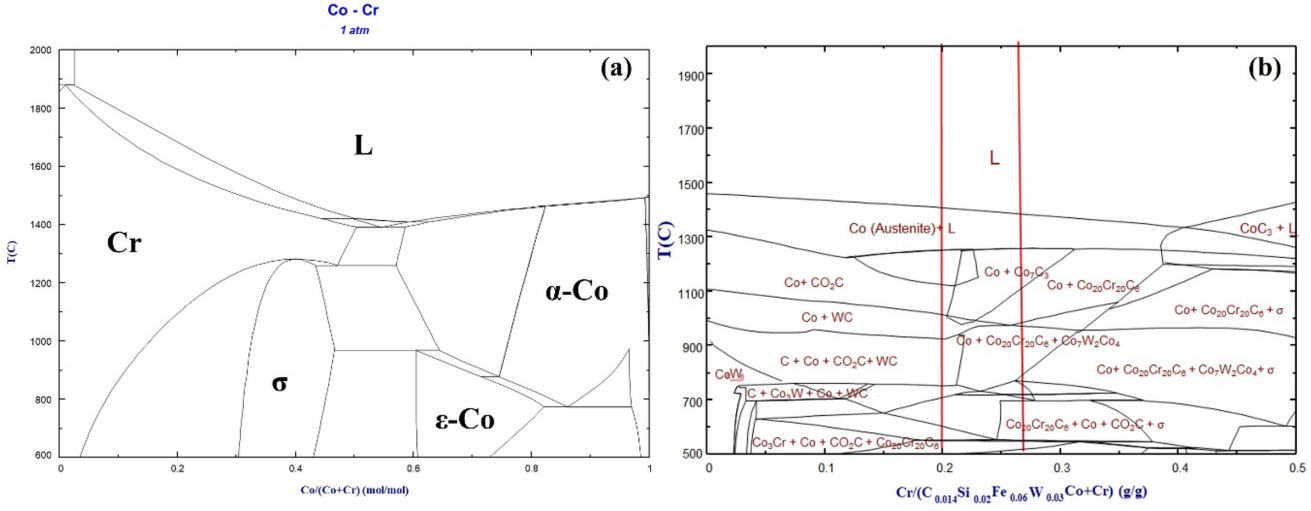

Fig. 1. Thermodynamic phase diagram prediction: (a) Co-Cr system, (b) Stellite 6 composition system

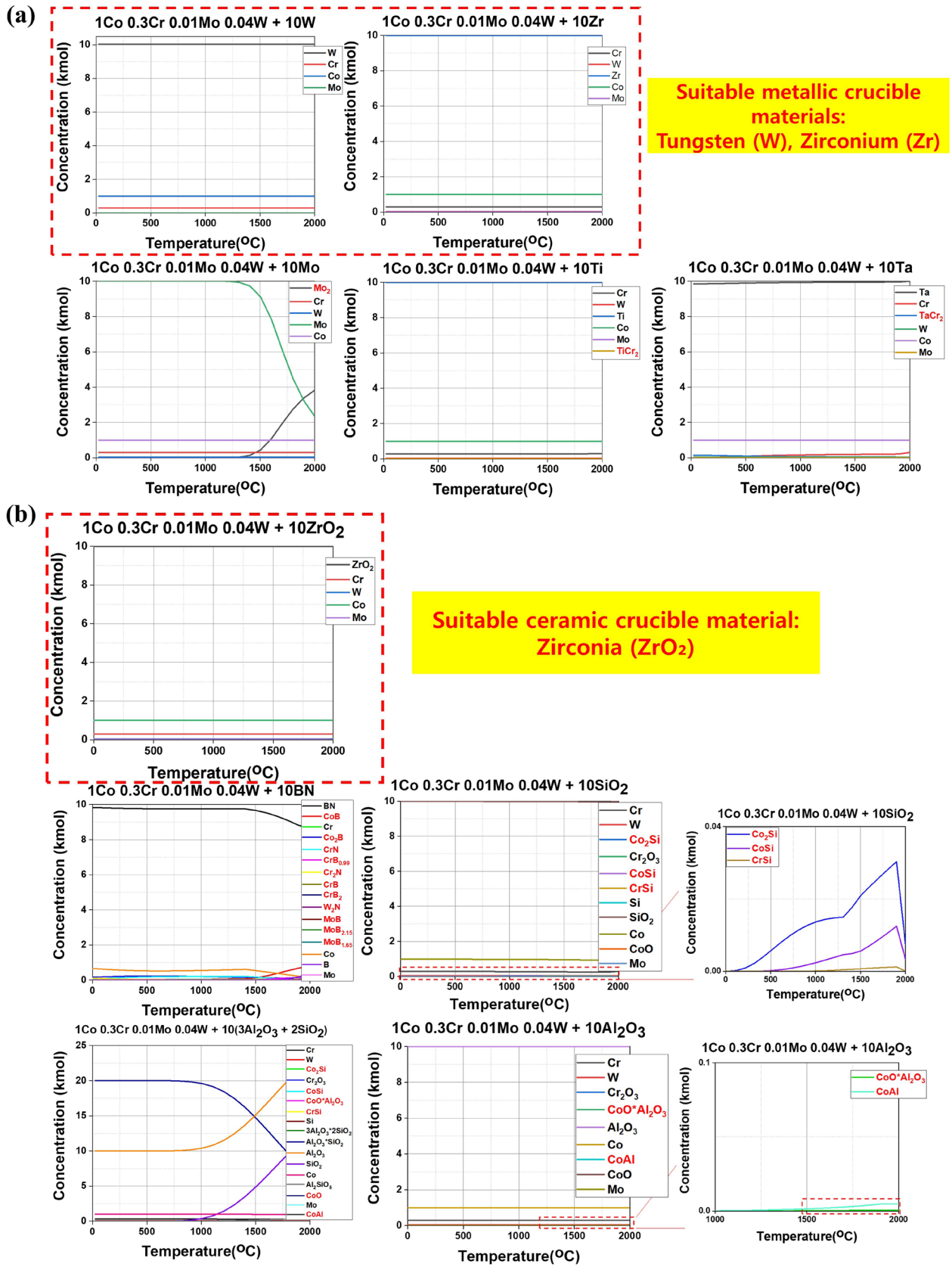

Fig. 2. Simulation results for reactivity with the crucible material based on thermodynamic calculations

3.2 열 전달 해석 결과

3.2.1 고주파 유도가열 공정 조건 확립을 위한 열 전달 해석 결과

다음은 Stellite 6 스크랩 재활용 공정에 활용된 고주파 유도가열 공정 조건 설정을 위해 COMSOL Multiphysics software를 활용하여 열 전달 해석을 진행하였으며 이때 활용된 메시 단면은 아래 Fig. 3에 나타내었다. 또한 활용된 지배방정식은 아래 Eq. (1)에 나타낸 내부 열에너지 변화 (ρCp·∂T/∂t + ρCp·∇T)는 내부 발생 열에너지 ∇·(k∇T) 및 외부 전자기장 열에너지 (Q_e) 온도변화로 계산하고 발산 및 내부로 전달되는 에너지 변화는 밀도에 따른 온도전달현상을 고려해서 열 전달 계산을 실시하였다. 이때 활용된 Stellite 소재의 물성 데이터베이스는 아래 Table 1에 나타내었다. 또한, 외부에 인가되는 전자기유도에 의한 열에너지 부여는 자기장에 의한 열원과 전기장에 의한 열원으로 나눠서 계산하고, 이에 대한 수식 설명은 아래 Eq. (2-4)에 나타내었다.

$$\rho C_p \frac{\partial T}{\partial t} + \rho C_p \cdot \nabla T = \nabla \cdot \left(k \nabla T \right) + Q_e \qquad (1)$$

ρ : *Density*

Cp: *Heat capacity*

k: Thermal conductivity

T: Temperature

∇: Gradient

Q_e: External heat source

$$Q_e = Q_{rh} + Q_{ml} \text{ (외부 총 열에너지)} \qquad (2)$$

Q_{rh}: Ohmic heating

Q_{ml}: Induction heating

$$Q_{ml} = \frac{1}{2} R e^{-i\omega B} \text{ (외부 자기장 열원)} \qquad (3)$$

R: Coil diameter

$e^{-i\omega B}$: Exponentially Decaying Term

ω: Angular frequency

B: Magnetic field

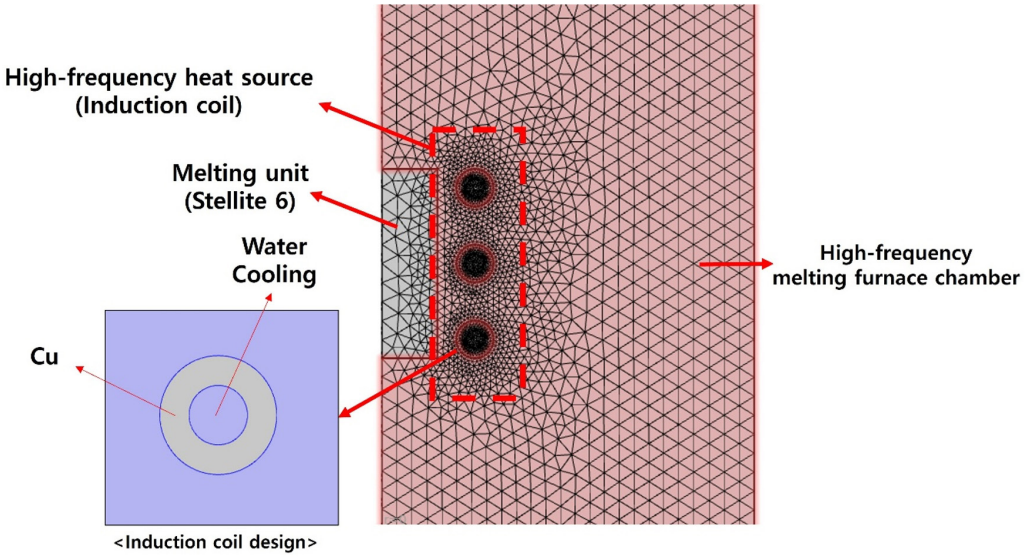

Fig. 3. Cross-sectional mesh structure applied to thermal-fluid analysis

Table 1. Material properties used for induction heating thermal-fluid calculations

Material Properties	Air	Water	Copper	Stellite
Density (Kg/m^3)	1,900	5,200	8,940	7,760
Thermal conductivity (W/m*K)	0.3	1,000	400	22.5
Specific heat capacity (J/Kg*K)	1,369	5,200	385	610
Electrical conductivity (S/m) or Electrical resistivity (ohm*m)	4E^{-3} (Electrical conductivity)	5.5E^{-6} (Electrical conductivity)	6E^{7} (Electrical conductivity)	2.5E^{-8} (Electrical resistivity)
Relative permittivity	4.5	1	1	1
Relative permeability	1	80	1	1

$$Q_{rh} = \frac{1}{2} Re^{E} \text{ (외부 전기장 열원)} \quad (4)$$

e^{E}: Heat generation function

다음과 같은 데이터 베이스를 활용하여 첫번째로, 출력 변화에 따른 자기장 밀도 계산을 진행하였다. 이때 주파수는 보유한 고주파 공정 장비의 가동 출력인 3 kHz에서 다양한 출력 조건 별 자기장 변화 및 밀도가 어떻게 형성되는지 계산을 진행하였다. 그 결과 Fig. 4(a)에서 확인되는 것처럼 출력이 증가함에 따라 자기장의 세기가 0.02에서 0.08 T까지 증가됨을 확인하였다. 이때, 표시된 T는 각 출력에서 발생하는 자기장의 세기를 의미하며 5 kW 이상의 경우 강한 자기장이 발생하여 소재 용해에 필요한 최소 온도인 1,500 ℃ 이상의 온도 상승을 위해 최소 5 kW 이상의 코일 전력이 요구된다고 판단된다.

Fig. 4(b)는 최적 출력 조건인 3 kHz 5 kW 조건에서 시간에 따른 소재 내부 온도 변화 시뮬레이션 결과를 나타내었다. 첫 번째 이미지는 0초 경과 시점에서 온도가 매우 낮은 상태(파란색)가 나타남이 확인되며 960초가 지나면 소재 내부가 서서히 가열되면서 온도가 상승하고, 2,880초와 3,600초에서는 내부 온도가 약 1900˚C 이상으로 높아져, 최종적으로 온도 분포가 붉은색으로 표시되며 온도 최고치에 도달하였다고 판단된다.

다음으로, 동일한 3kHz 주파수에서 코일 전력에 따른 온도 분포 시뮬레이션 결과를 아래 Fig. 5에 나타내었다. 계산 결과 2.0 kW 이상의 전력조건에서 소재 용융이 가능했지만 수 시간이 소요됨을 확인할 수 있다. 반면 5 kW 이상 조건에서는 30분 미만으로 용해가 가능하여 출력 별 자기장 발생 세기 계산 결과와 동일하게 코일 전력이 최소 5 kW 이상 조건이 적절하다 판단된다.

위 열 전달 해석 결과에서 소재의 용융에 필요한 최소 조건이 3kHz - 5kW으로 도출되었으나 같은 전력 조건이라 하여도 유도코일 조건 (간격) 및 소재의 국부 위치에 따라 자속밀도 및 온도 차이가 나타날 수 있다. 또한, 용융 시 상하좌우 간 온도 편차가 심하면 전체적인 가열을 위해 많은 열량이 필요하고 용해 시간이 길어질 수 있다. 최적의 코일 조건을 도출하기 위해 COMSOL multi-physics Software의 유한요소해석 (FEM) 법으로 자속 밀도 및 온도 구배 계산을 진행하였다. 이때, 고주파 열 전달 계산에 활용된 출력 조건 및 코일 간격 조건은 Table 2에 나타냈으며 시뮬레

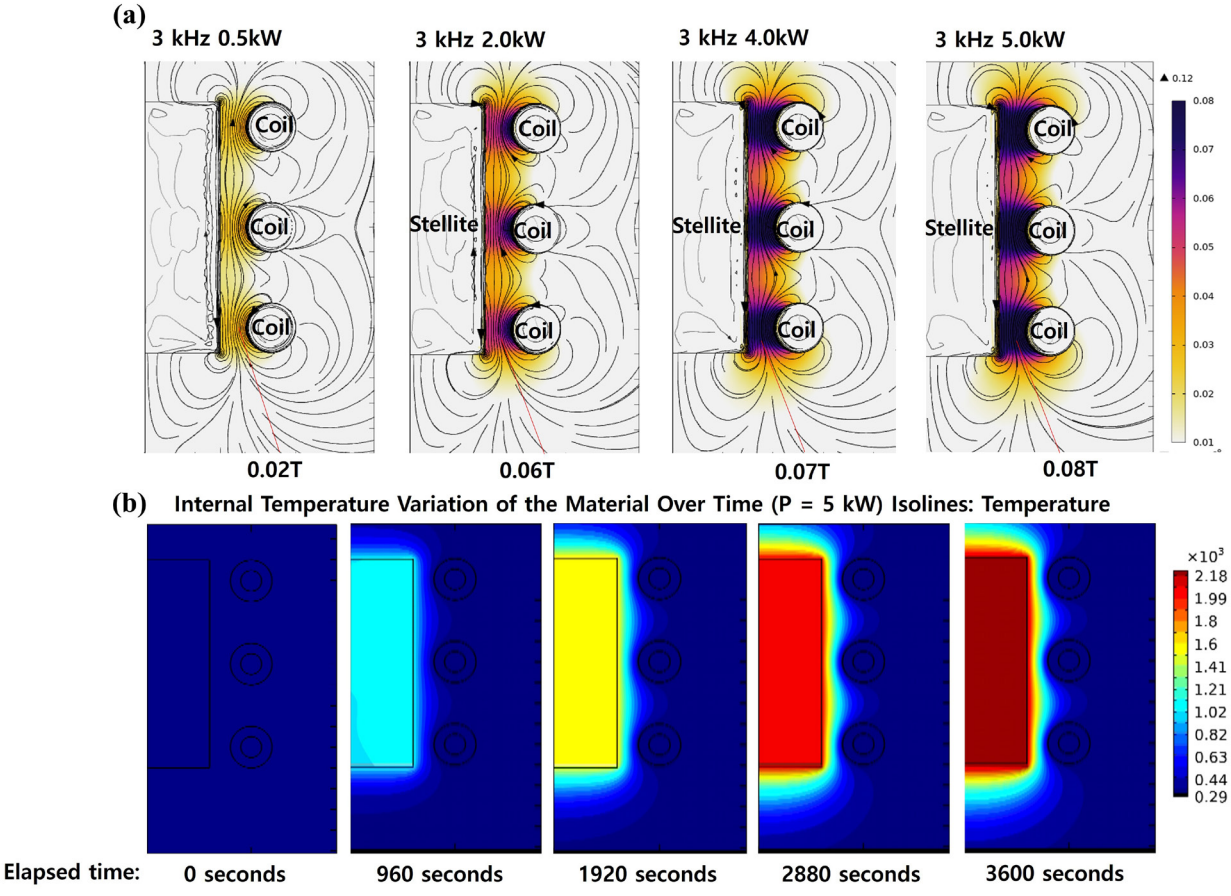

Fig. 4. (a) Magnetic field density variation with output changes, (b) temperature variation inside the material over time

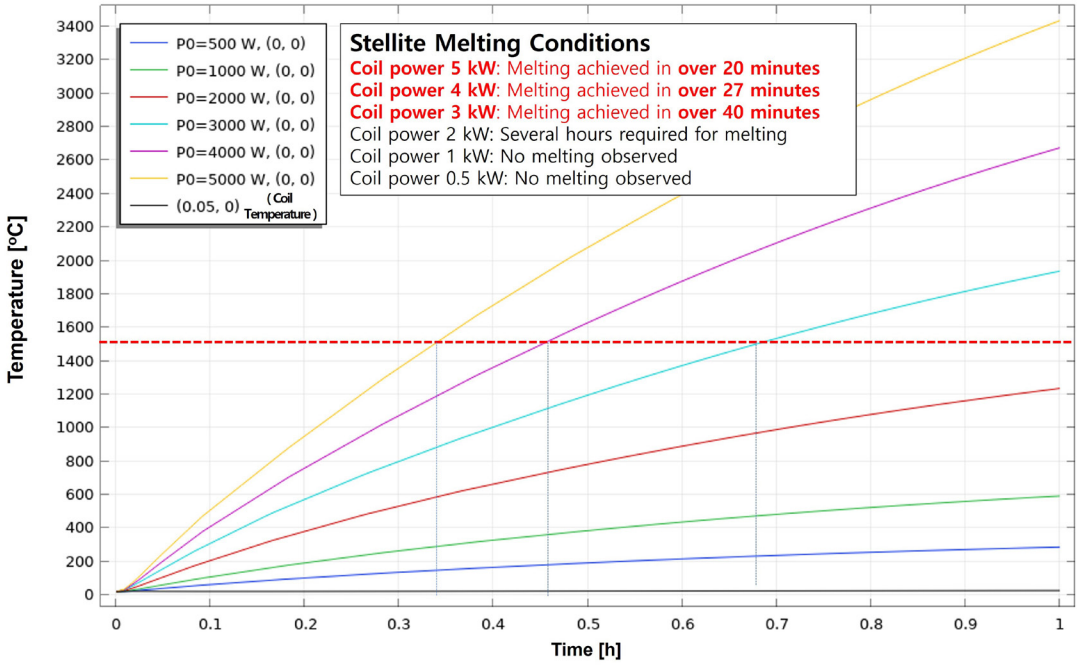

Fig. 5. Simulation results for temperature distribution in relation to high-frequency induction furnace output conditions

Table 2. Output and coil gap conditions used in high-frequency heat transfer analysis

Parameter	Value
Coil power [kW]	53 (Maximum operating power of the coil)
Frequency [kHz]	3
Operation Time [min]	50

C1 (m)	C2 (m)	C3 (m)	C4 (m)	C5 (m)
0.01	0.02	0.03	0.04	0.05

이션 결과는 아래 Fig. 6에 나타내었다.

그 결과 Fig. 6(a)는 코일 (C1 조건) 주변의 자속밀도 분포를 보여주며 색에 따른 자기장의 세기 확인이 가능하다. 이를 기반으로 (b)는 코일 간격에 따른 자기 밀도 변화 그래프 계산 결과이며, (c)는 코일 간격 별 온도 변화 확인을 위한 계산 결과이다. 계산 결과 코일 간격이 가장 가까운 C1 조건에서 최대 온도 (4,200 ℃)와 중심부에 가장 높은 자속밀도 (0.387 [T])를 지닌 것을 확인하였다. 또한, (d)는 Stellite 6 중심부 기준으로 모든 코일 간격 (C1-C5) 및 모든 시간 (0–50 min)을 자속밀도(X)/온도(Y)에 대하여 플롯 하였을 때, 약 167 ˚C/Guass의 기울기로 선형 비례하는 결과를 확인하였다. 이는 코일 간격과 관계없이 본 공정조건 (주파수 3 kHz, 코일 전력 53 kW)에서는 Y=167X-10 (Y: 온도 [℃], X: 자속밀도 [Gauss])의 관계가 있음을 도출하였다.

3.3 Stellite 6 스크랩 재활용 공정 주조재 분석 결과

앞선, 열역학 및 열 전달 해석을 통해 선정한 Stellite 6 스크랩 재활용을 위한 고주파 용해 공정을 진행하였다. 먼저, 아래 Fig. 7(a)는 본 공정에 실제로 활용된 Stellite 6 스크랩이며, (b)는 금속 도가니 대비 경제적 효율이 높은 세라믹계 도가니 중 Al_2O_3 도가니를 활용하였고 이때, 열역학 계산 결과 고온에서 원료와의 반응이 일어나지 않는 지르코니아 (ZrO_2) 성분의 이형제를 도포한 몰드를 활용하였다. 그리고, 열 전달 해석 결과 최적 공정 조건인 3 kHz-53 kW, 코일 간격 0.01 m 조건으로 스크랩이 완전히 용해될 때까지 약 30분정도 공정을 진행하였고 용해된 주조재를 (c)와 같이 제작한 세라믹 몰드 내 주입한 후 최종적으로 회수한 재활용 Stellite 6 주조재는 Fig. 7(d)에 나타내었다.

최종적으로 회수한 주조재의 주요 및 불순물 성분을 확인, 상용 Stellite 6와의 성분 비교를 위해 XRF 및 ICP-OES 분석을 수행하

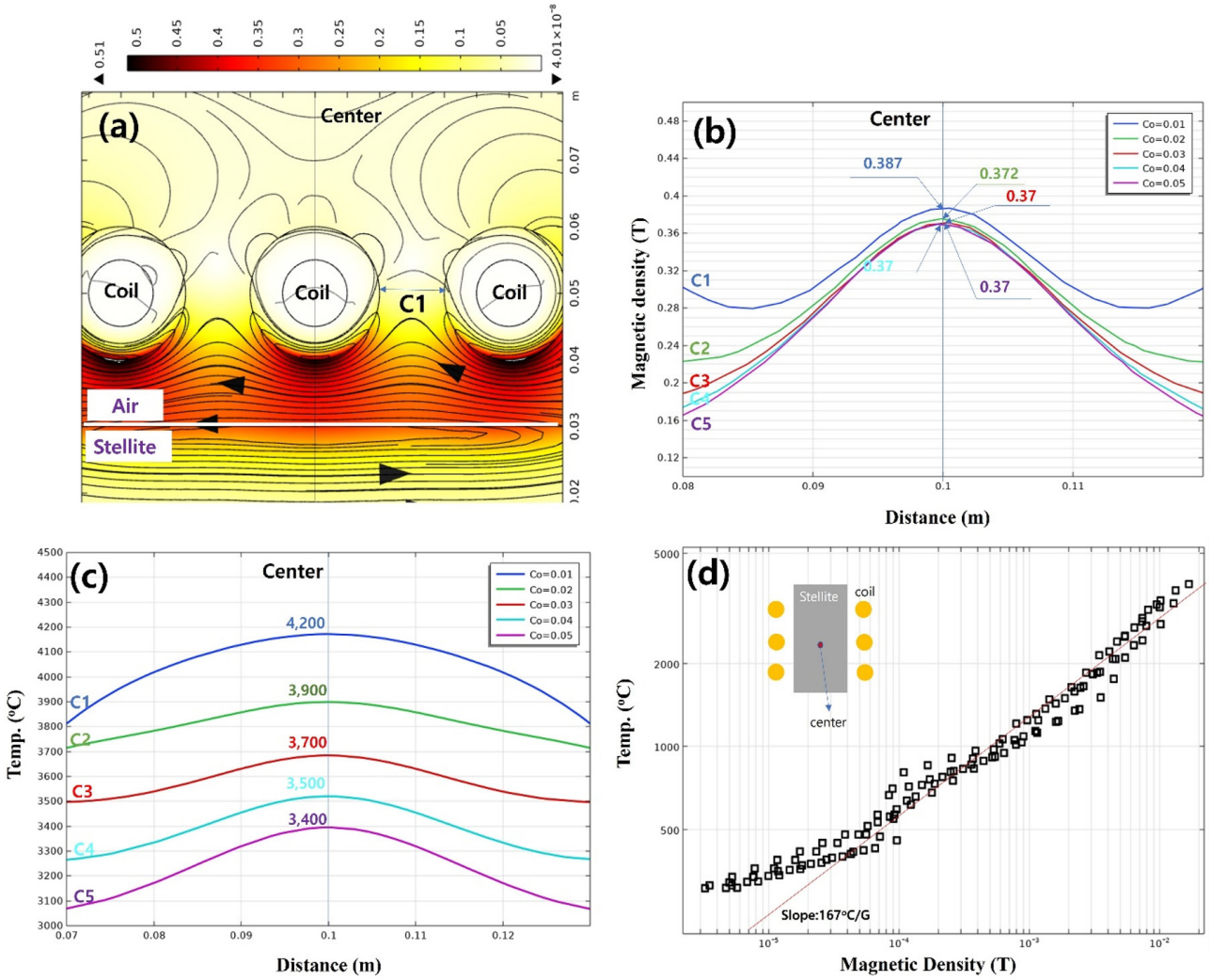

Fig. 6. Finite element analysis results: (a) magnetic flux density distribution around the coil (C1), (b) magnetic flux density intensity according to coil spacing, (c) temperature variation, and (d) correlation between magnetic flux density and temperature at the center of Stellite

였으며, 그 결과를 아래 Fig. 8에 나타내었다. Co 및 Cr 성분 비율 (Co/(Co+Cr)%)을 계산한 결과, XRF 분석 결과는 64.35% (50.9/(50.9+28.2)), ICP-OES 분석 결과는 64.22% (49.9/(49.9+27.8))로 측정되었다. 이는 원료로 사용된 용접봉 (64.66%) 및 스크랩 (64.07%)과 유사한 수준을 유지함을 나타낸다. 또한, 기타 합금 원소 (Fe, W, Ni 등)도 원료와 비교하여도 큰 차이가 나타나지 않았다.

그러나, Fe 성분의 함량은 원료로 활용된 스크랩 내 12.01%와 유사한 12.5~13.2%가 검출됨을 확인하였다. 이는 철강 산업에서 공정 후 발생하는 스크랩을 활용하였으므로 공정 중 Fe이 많이 유입되어 상용 Stellite 6 (평균 Fe 함량 5~10%)에 비해 높은 Fe 함량이 검출되었다고 사료된다. Stellite 6 내 과량의 Fe의 함량은 탄화물 감소에 영향을 주어 Stellite 6의 경도를 감소시킨다고 알려져 있다[26]. 따라서, 이는 향후 추가적인 공정 (진공증류 등)을 통한 후처리 공정 최적화 및 소재 고순도화 연구를 진행할 예정이다.

재활용 Stellite-6 주조재의 결정상 분석 결과, Peak의 위치는 일정하게 유지되었으나, Intensity 강도의 순서가 바뀐 것이 확인되며 이는 완전 용해 후 응고되면서 생긴 배향성과 Fe 성분의 portion 증가로 인해 이러한 현상이 발생되었다고 판단된다.

다음으로, 재활용 Stellite 6 주조재의 미세조직 비교를 위한 상용 Stellite 6, 스크랩, 재활용 Stellite 6 주조재 FE-SEM 분석을 진행하였으며 그 결과는 아래 Fig. 10에 나타내었다. 그 결과, 내부 미세조직으로는 전형적인 주조 조직이 관찰되었으며 레퍼런스 (Reference) 소재의 미세구조와 유사한 구조를 보였다. 또한, 상용 Stellite 6에서 스크랩화 시 확인되지 않은 배향조직이 재활용 Stellite 6에서 재형성되었으며, 조대화된 결정립도가 감소됨을 확인하였다[5, 27]. 이를 통해 상용 Stellite 6와 유사한 내부 미세조직을 가진

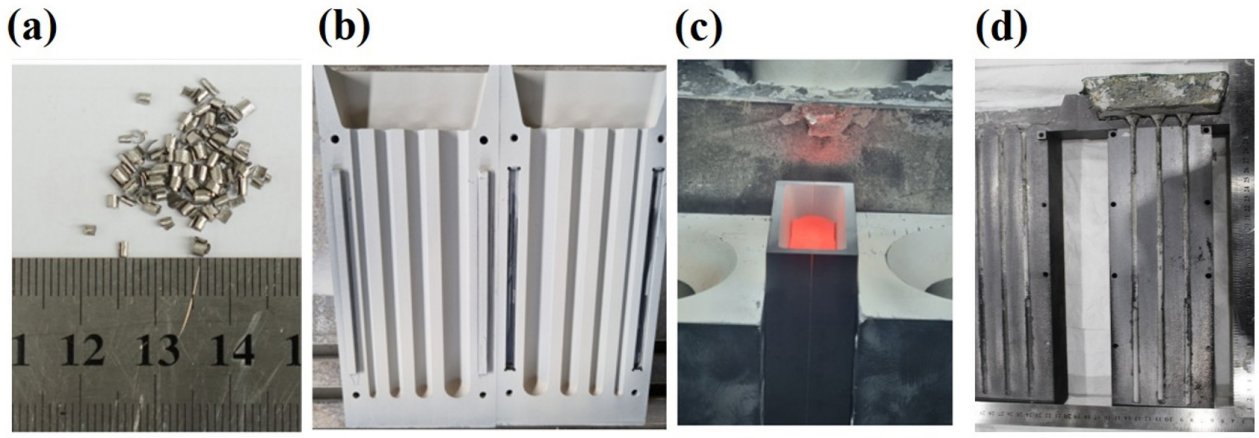

Fig. 7. Recycling process of Stellite 6 scrap: (a) Stellite 6 scrap, (b) ZrO_2-coated $Al2O_3$ crucible used for melting, (c) molten scrap alloy poured into the crucible, and (d) recycled Stellite 6 as-cast alloy obtained after casting.

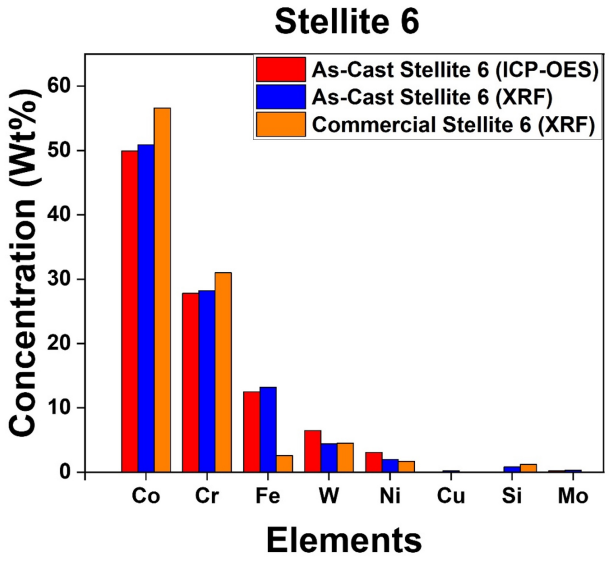

Fig. 8. Composition analysis of as-cast Stellite 6 (ICP-OES and XRF) and commercial Stellite 6 (XRF). ICP-OES, inductively coupled plasma optical emission spectroscopy; XRF, X-ray fluorescence analysis.

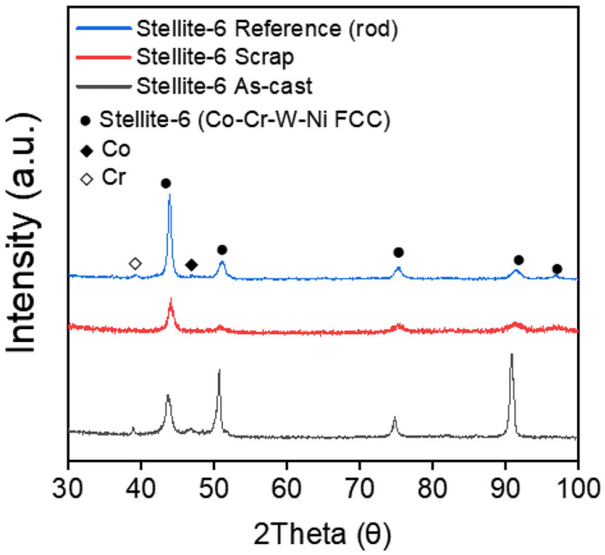

Fig. 9. X-ray diffraction analysis of commercial Stellite 6, scrap, and recycled Stellite 6 casting

재활용 Stellite 6 주조재가 회수됨을 입증하였다.

3.4 Stellite 6 재활용 분말 분석 결과

먼저, 상용 stellite 6 분말의 형상 및 성분 확인을 위한 FE-SEM, EDS 분석 결과를 아래 Fig. 11에 나타내었다. Fig 11(A)에서 확인되듯이 상용 Stellite 6 분말의 형상은 응고 조직상을 가진 구형 입자들로 구성되어 있음을 확인하였다. 그리고 (B)에 나타낸 EDS 분석 결과 주된 성분인 Co-Cr 합금의 성분이 검출되었으며, 추가적으로 W, Si, Zr 성분도 검출됨을 확인하였다.

앞서, 제조한 재활용 Stellite 6 주조재와 아토마이저 공정을 활용하여 HVOF 공정용 Stellite 6 분말을 제조하였고 아토마이저 장비 및 공정도는 아래 Fig. 12에 나타내었다. 그리고 본 연구에 활용된 아토마이저 공정은 장비 최대 전력인 23 kW에서 진행하였고 노즐 타입, 오리피스 직경, 분사 가스 및 압력 등 아토마이저 상세 공정 조건은 아래 Table 3에 나타내었다.

앞서, 공정 최적화를 통해 제조한 Stellite 6 스크랩 재활용 주조재를 활용한 아토마이저 공정을 통해 분말 제조 공정을 진행하였고, 제조된 분말을 분급 공정을 통해 입자 크기별로 분리한 후, 각

크기별로 물성 확인을 위한 다양한 기초분석을 진행하였다. Fig. 12에서 확인할 수 있듯이 XRD 분석 결과 주 성분인 Co, Cr 결정상이 검출되었으며, 입자 크기 별 큰 차이가 나타나지 않음을 확인하였다.

그러나, Fig. 9에 나타낸 재활용 Stellite 6 주조재의 Cr 및 Co의 XRD Peak 위치와 Fig. 13에 나타낸 재활용 Stellite 6 분말의 Cr 및 Co Peak 위치가 서로 다르게 검출됨을 확인하였다. 이러한 차이는 가스 아토마이징 공정 중 고속 응고 및 급격한 열 수축으로 인해 격자 내 응력이 잔류하게 되고, 이는 격자 상수의 변화를 유발하여 XRD 피크의 위치 이동 (peak shift)을 초래할 수 있다고 알려져 있다[28]. 특히 Co–Cr 계 합금은 Co (1.26 Å)와 Cr (1.27 Å) 간의 미세한 원자 반경 차이에도 불구하고 격자 왜곡에 민감하게 반응하는 특성을 가지는 것으로 알려져 있다[29]. 또한, Jitesh Kumar et al.[30]은 Co–Fe–Ni 계 합금에 Cr이 첨가되면 격자 내 왜곡(lattice distortion)이 증가하고, 이는 고용 강화 (solid solution strengthening) 효과를 유발한다고 보고된 바가 있다. 종합적으로 볼 때, 이러한 잔류응력에 기인한 격자 변형으로 인해 Co 및 Cr의 XRD 피크 위치가 변위 되었으며, 이에 따라 Fig. 9와 Fig. 13에서 상이한

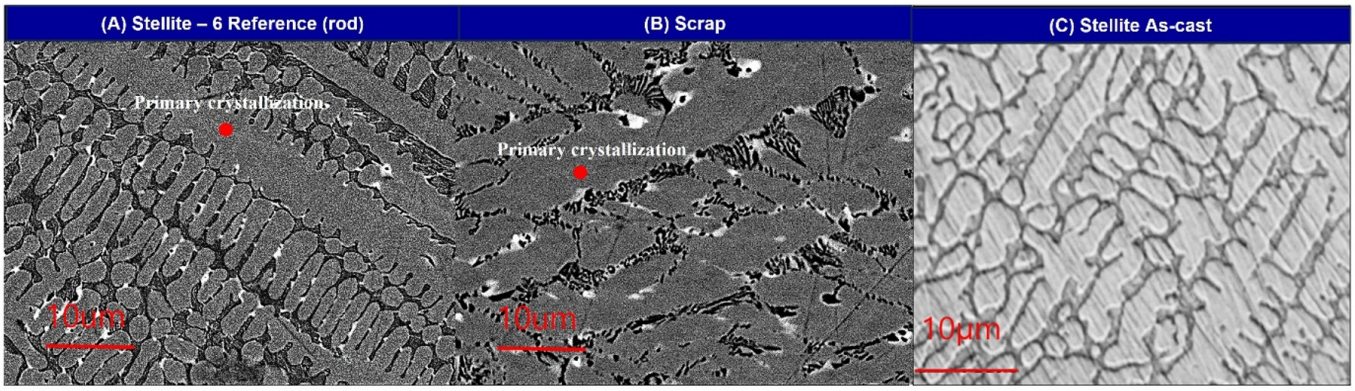

Fig. 10. Field-emission scanning electron microscopy analysis results for (A) commercial Stellite 6, (b) scrap, and (c) recycled Stellite 6 casting

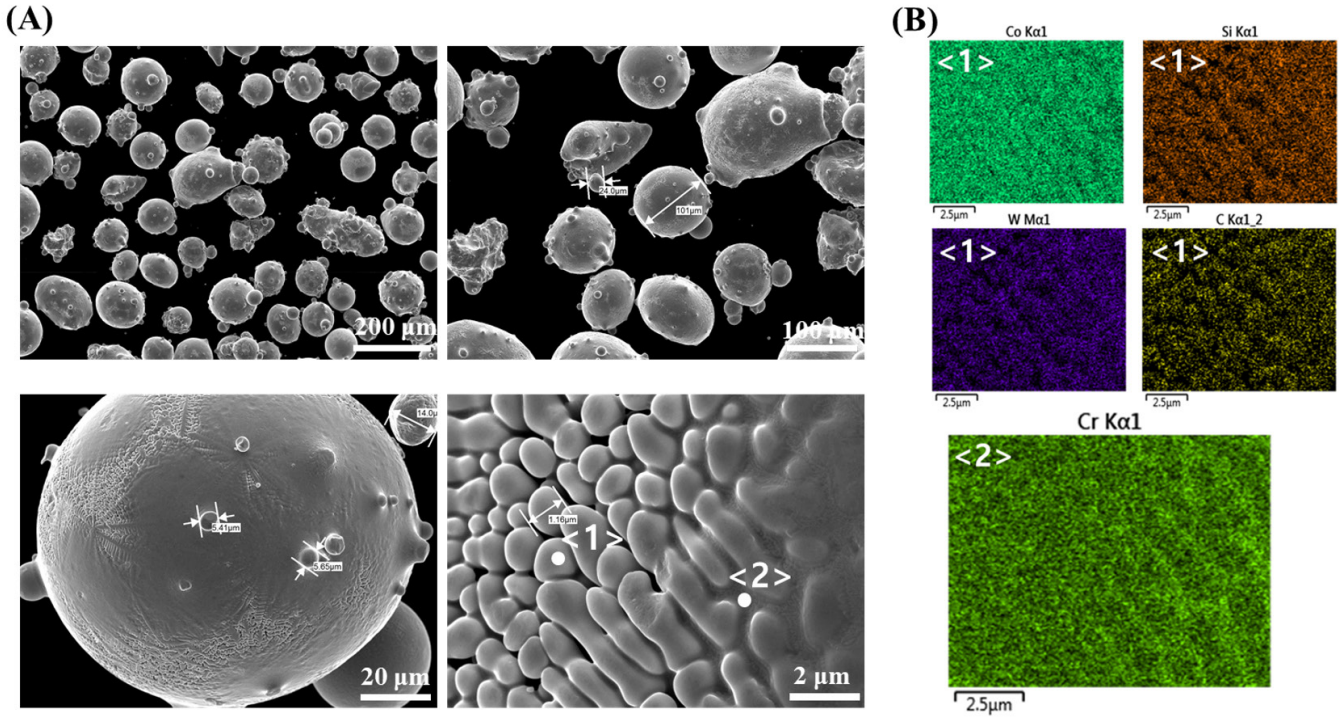

Fig. 11. Analysis results of commercial Stellite 6 powder: (a) field-emission scanning electron microscopy, (b) energy-dispersive X-ray spectroscopy.

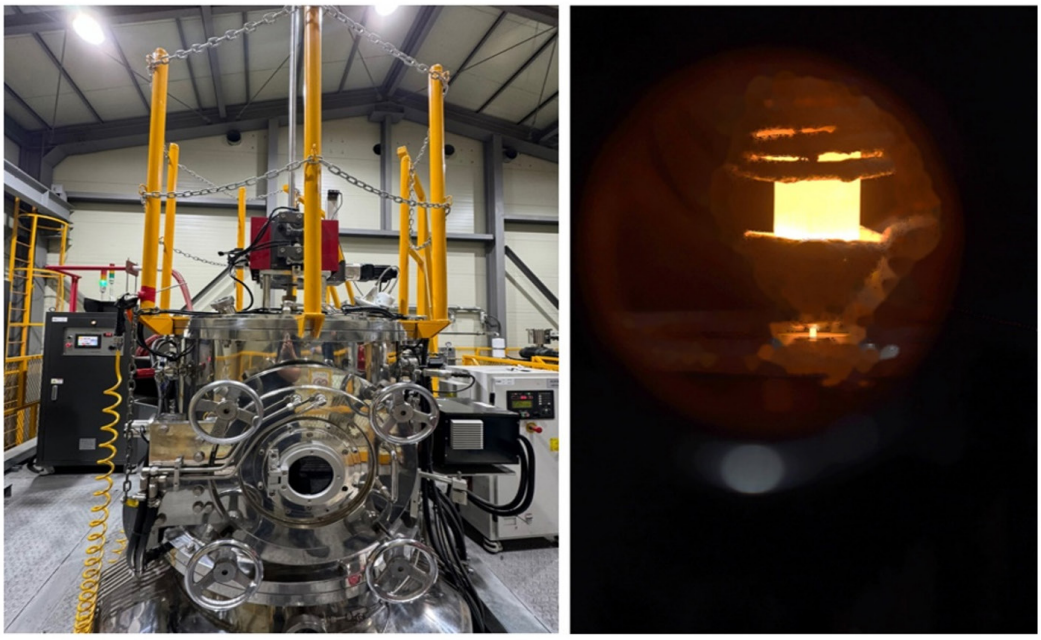

Fig. 12. Atomizer apparatus and in-process views for metal powder atomization

Table 3. Atomizing conditions applied to recycled Stellite 6 powder fabrication

Parameter	Value
Power [kW]	23
Vacuum level of vacuum chamber [Torr]	$9.0*10^{-2}$
Nozzle type	Direct injection type
Orifice diameter [mm]	4
Atomizing gas	Ar
Atomizing pressure [bar]	25

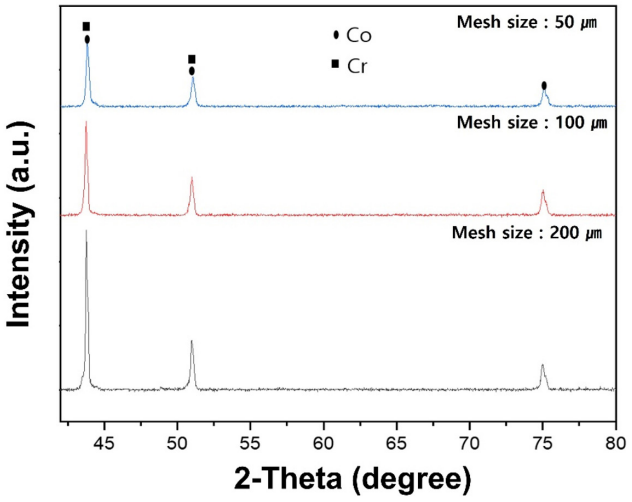

Fig. 13. X-ray diffraction analysis results of recycled Stellite 6 powder by particle size

피크 위치가 관찰된 것으로 판단된다.

다음으로, Fig. 14는 입자 크기 별 FE-SEM, EDS 분석 결과이며, 상용 분말과 동일하게 응고 조직상 및 구형 입자를 가진 분말이 제조됨을 확인하였다. 또한, EDS 분석 결과 XRD와 동일하게 주로 Co, Cr 성분이 검출됨을 확인하였으며, W, Si, Fe 역시 일부 검출됨을 확인하였다. 추가적으로, 재활용 Stellite 6 주조재를 분말화한 후 Fe 함량이 감소하는 경향이 확인되었다. 이러한 결과는 다음과 같은 원인에 기인한 것으로 사료된다. 첫번째로 분사 가스 압력이 증가하면 평균 입자 크기가 감소하고, 이에 따라 단위 질량당 표면적이 증가하여 산화 반응이 발생할 수 있는 면적이 확대되는 효과로 인해 Fe가 산화되었을 가능성이 높을 것으로 판단된다. 또한, 아토마이징 공정 시 높은 가스 분압은 분말의 비행 거리를 증가시키며, 이로 인해 고온 노출 시간이 길어져 산화도가 더욱 높아지는 것으로 보고되고 있다[31]. 이러한 현상으로 인해 Fe가 산화되어 미세 산화물 형태로 분리되거나 혹은 응고되기 전에 분말로 수거되지 않고 챔버 내에 증착 되었기 때문에 재활용 Stellite 6 분말 내 Fe 함량이 감소되었다고 판단된다. 그리고 일부 Fe가 액적 표면에 농축된 후 슬러지 또는 분진 형태로 분리되었을 가능성도 있다고 판단된다[32]. 따라서 본 연구를 통해 상용 Stellite 6 분말과 유사한 물성을 가진 재활용 분말이 제조됨을 확인하였다.

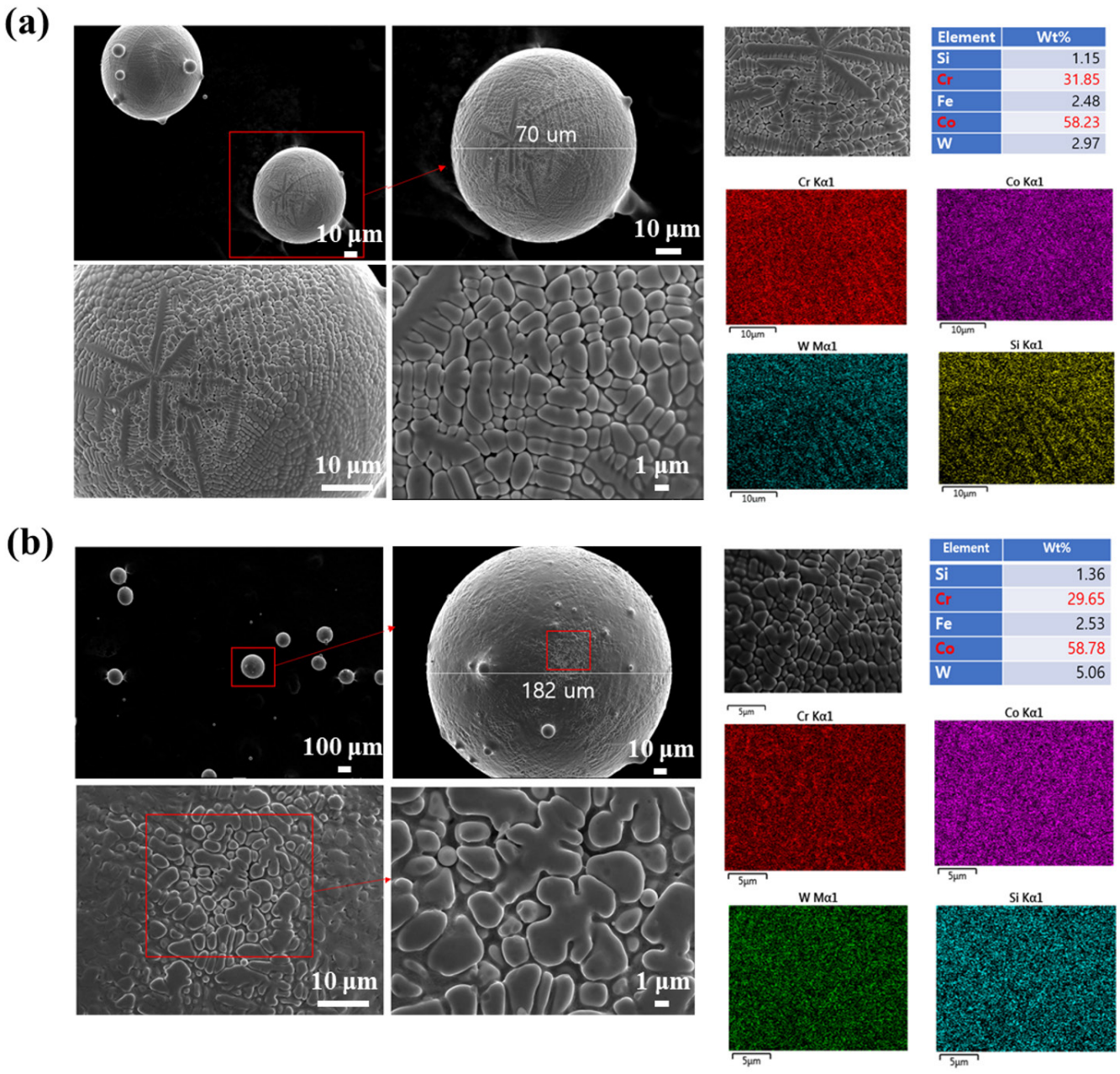

Fig. 14. Field-emission scanning electron microscopy and energy-dispersive X-ray spectroscopy. analysis results for recycled Stellite 6 powder: (a) 100 μm sieve size, (b) 200 μm sieve size

4. Conclusion

본 연구에서는 Stellite 6 스크랩의 재활용 공정을 통해 고순도 Stellite 6 주조재 및 분말을 제조하고, 그 물성을 상용 제품과 비교하여 재활용 공정의 타당성과 상업적 활용 가능성을 평가하였다.

1. 다양한 소프트웨어를 활용하여 열역학적 계산과 열 전달 해석을 통해 최적의 재활용 공정 용해 및 주조 조건을 도출하였다. 도가니 소재로 W, Zr, ZrO_2이 적합함을 확인하였고 경제성과 반응 안정성을 고려하여 Al_2O_3 내 ZrO_2를 도포한 도가니를 활용하였다. 그리고 열 전달 해석 결과를 바탕으로 주파수 3 kHz, 코일 가동최대 전력인 53 kW, 코일 간격 0.01 m 공정 조건에서 고순도 재활용 Stellite 6 주조재를 성공적으로 제조하였다.
2. 최종적으로 제조된 재활용 Stellite 6 주조재의 성분 및 미세조

직 분석 결과, 상용 Stellite 6과 유사한 특성을 보였으며, Fe 함량은 스크랩 특성상 소폭 증가하였다. 이는 향후 공정 개선 혹은 추가적인 후처리 공정을 통한 불순물 제어 연구를 진행할 예정이다.

3. 또한, 고순도 재활용 Stellite 6 주조재 및 아토마이저 공정을 활용하여 제조된 재활용 Stellite 6 분말의 다양한 물성 분석 결과를 통해 상용 분말과 유사한 입자 형상, 조직, 조성을 가진 분말이 제조됨을 확인하였다.

따라서 본 연구는 산업 현장에서 발생하는 Stellite 6 스크랩을 고부가가치 소재로 재활용할 수 있는 실질적인 공정 가능성을 제시하였으며, 이는 금속 폐기물 저감과 원자재 비용 절감 측면에서 지속 가능한 소재 활용 방안을 제공한다. 앞으로는 본 연구 결과를 기반으로 기계적 성능 및 내마모성 평가를 통해 산업 적용 범위를 확대하고, 공정 최적화 및 후처리 기술 개발을 통한 소재 고순도화 연구를 지속할 예정이다.

Funding

This study was supported in part by the internal research project of Korea Institute of Industrial Technology (Project No. EM220006, Development of material preparation/surface treatment/post-processing for molten metal-based hard-facing technology with higher than 40 HRC hardness) and by the government and local government-funded commissioned project (Project No. IZ250036, Development of TiC self-propagating high-temperature synthesis manufacturing process technology to develop advanced electrostatic chuck for semiconductor wafer fixation).

Conflict of Interest

The authors declare no conflict of interest.

Data Availability Statement

All dataset files used in this study can be available on request.

Author Information and Contribution

YongKwan Lee: Ph.D. Candidate; conceptualization, Investigation, Visualization, writing - original draft, Data curation, Software Hyun-chul Kim: Ph.D. Candidate; conceptualization, Investigation, Visualization, writing - original draft, Data curation, Software Myungsuk Kim: Ph.D. Candidate; Formal analysis, Data curation, Investigation Soong Ju Oh: Professor; Investigation, Conceptualization, Validation, Writing - Review & Editing Kyoungtae Park: Principal Researcher; Investigation, Conceptualization, Validation, Supervision, Project administration, Funding acquisition, Writing-Original Draft, Writing - Review & Editing JaeJin Sim: Senior Researcher; Investigation, Conceptualization, Validation, Supervision, Project administration, Writing-Original Draft, Writing - Review & Editing.

Acknowledgments

None.

References

[1] A. Shahroozi, A. Afsari, B. Khakan and A. R. Khalifeh: Surf. Coat. Technol., **350** (2018) 648.

[2] B. Venkatesh, K. Sriker and V. S. V. Prabhakar: Procedia Mater. Sci., **10** (2015) 527.

[3] W. C. Lin and C. Chen: Surf. Coat. Technol., **200** (2006) 4557.

[4] A. Motallebzadeh, E. Atar and H. Cimenoglu: Tribol. Int., **91** (2015) 40.

[5] Z. Li, Y. Cui, J. Wang, C. Liu, J. Wang, T. Xu, T. Lu, H. Zhang, J. Lu, S. Ma, H. Fan and S. Tang: Metals, **9** (2019) 474.

[6] V. Kuzucu, M. Ceylan, H. Celik and I. Aksoy: J. Mater. Process. Technol., **69** (1997) 257.

[7] F. Brownlie, T. Hodgkiess, A. Pearson and A. M. Galloway: Wear, **376** (2017) 1279.

[8] M. X. Yao, J. B. C. Wu and Y. Xie: J. Mater. Chem. A, **407** (2005) 234.

[9] K. Vutova, V. Stefanova, V. Vassileva and S. A. Vladimirova: Metals, **15** (2022) 4168.

[10] P. S. N. Mendes, J. F. C. Lins, P. S. N. Mendes, W. R. Prudente, R. P. Siqueira, R. E. Pereira, S. M. S. Rocha and A. R. Leoni: Int. J. Eng. Res. Appl., **7** (2017) 34.

[11] R. R. Garbade and N. B. Dhokey: IOP Conf. Ser.: Mater. Sci. Eng., **1017** (2021) 012033.

[12] T. Matkovic, P. Matkovic and J. Malina: J. Alloys Compd., **366** (2004) 293.

[13] N. Thawari, C. Gullipalli, J. K. Katiyar and T. V. K. Gupta:

MSEB., **263** (2021) 114799.
[14] J. C. Shin, J. M. Doh, J. K. Yoon, D. Y. Lee and J. S. Kim: Surf. Coat. Technol., **166** (2003) 117.
[15] Z. Hu, D. Zhanga, D. D. Wub, X. Zheng, J. Sun, P. Geng and N. Ma: Surf. Coat. Technol., **478** (2024) 130447.
[16] J. Gorka, T. Poloczek, D. Janicki, A. Lont, S. Topor, M. Zuk and A. Rzeznikiewicz: Materials, **17** (2024) 3101.
[17] D. Bartkowski, A. Bartkowska, J. Olszewska, D. Przestacki and D. Ulbrich: Materials, **16** (2023) 5000.
[18] E. Bagcı and S. Aykut: Arabian J. Sci. Eng., **39** (2014) 8135.
[19] E. Bagcı and S. Aykut: Int. J. Adv. Manuf. Technol., **29** (2006) 940.
[20] J. W. Suh, J. H. Koh, Y. B. Chun, Y. D. Kim, J. S. Jang, S. H. Kang and H. N. Han: J Powder Mater., **31** (2024) 152.
[21] A. I. Encalada, S. A. Alidokhta, P. Stoyanov, M. Makowiec, C. Moreau and R. R. Chromik: Wear, **546** (2024) 205310.
[22] Ž. Dlouhá, J. Duliškovic, M.F. Netrvalová, J. Naďová, M. Vostrák, S. Kraft, U. Löschner, J. Martan and Š. Houdková: Metals, **17** (2024) 5069.
[23] HSC Chemistry Software Ver. 8.0. https://www.outotec.com, 2018
[24] FactSage Software Ver 8.0. http://www.factsage.com/, 2021
[25] COMSOL Multiphysics® v6.1, Heat Transfer Module, COMSOL AB, Stockholm, Sweden (2022).
[26] M. A. Baek, G. B. Kang, G. C. Suk, S. C. Hong, Y. D. Kim and T. W. Na: Metals, **14** (2024) 244.
[27] A. Shahroozia, A. Afsarib, B. Khakana and A. R. Khalifeh: Surf. Coat. Technol., **350** (2018) 648.
[28] M. Belassel: SAE Int. J. Mater. Manuf., **5** (2012) 352.
[29] H. F. Zhang, H. L. Yan, H. Yu, Z. W. Ji, Q. M. Hu and N. Jia: J. Mater. Sci. Technol., **48** (2020) 146.
[30] J. Kumar, M. Radhakrishnan, S. Palaniappan, K. M. Krishna, K. Biswas, S. Srinivasan, R. Banerjee and N. B. Dahotre: Mater. Today Commun., **40** (2024) 109485.
[31] Y. Shi, W. Lu, W. Sun, S. Zhang, B. Yang and J. Wang: J. Mater. Sci. Technol., **105** (2022) 203.
[32] S. Yu. Manegin, S. D. Rozanov, I. A. Gulyaev, A. V. Mezhevov and P. O. Zhukov: J. Met., **66** (2022) 61.

Research Article

pISSN 2799-8525 · eISSN 2799-8681
J Powder Mater 2025;32(4):344-353

Journal of
Powder Materials

고함량 Gd_2O_3 첨가 UO_2 핵연료 소결체의 혼합 분말 입도에 따른 미세구조 영향 분석

이지환[1,2], 양재호[1], 윤지해[1], 김동주[1], 신동욱[2], 김동석[1,*]

[1]한국원자력연구원 경수로핵연료기술연구부
[2]한양대학교 신소재공학과

Influence of Powder Particle Size on the Microstructure of UO_2 Fuel Pellets with High Gd_2O_3 Content

Ji-Hwan Lee[1,2], Jae Ho Yang[1], Ji-Hae Yoon[1], Dong-Joo Kim[1], Dong-wook Shin[2], Dong Seok Kim[1,*]

[1]LWR Fuel Technology Research Division, Korea Atomic Energy Research Institute, Daejeon 34020, Republic of Korea
[2]Materials Science and Engineering Department, Hanyang University, Seoul 04763, Republic of Korea

The recent development of small modular reactors (SMRs) and the adoption of higher-enrichment fuels have intensified the need for advanced burnable absorbers to ensure effective reactivity control and extended fuel cycles. Among various designs, UO_2 fuels with high Gd_2O_3 (gadolinium oxide) content provide notable benefits; in particular, they are compatible with established fabrication methods for burnable absorber fuels. However, achieving a homogeneous dispersion of Gd_2O_3 at high loading levels remains challenging, and the frequent occurrence of phase segregation and non-uniform microstructures can limit fuel reliability and performance. Overcoming these limitations requires an understanding of the powder characteristics and mixing behaviors during fabrication. In this study, we investigate the effects of the initial particle size and mixing method of UO_2 and Gd_2O_3 powders on the microstructure and mixing homogeneity of high-Gd_2O_3-content fuels. The findings indicate that both the mixing method and the preparation state of the starting powders significantly affect the resulting microstructure and mixing uniformity.

Keywords: UO_2; Gd_2O_3; High Gd_2O_3; Burnable absorber; Nuclear; Nuclear fuel; Material

Received: June 4, 2025
Revised: August 18, 2025
Accepted: August 18, 2025

***Corresponding author:**
Dong Seok Kim
E-mail: dskim86@kaeri.re.kr

1. Introduction

가연성 흡수체(Burnable Absorber)는 원자로 초기 연료 장전 단계에서 잉여 반응도를 감소시키고 핵연료가 연소됨에 따라 반응도를 균형 있게 유지하는 역할을 수행한다[1]. 현재 상용 경수로에서는 가연성 흡수체로써 중성자 흡수 단면적이 큰 Gd원소를 주로 사용하며, 이는 Gd_2O_3(산화가돌리늄)형태로 UO_2 핵연료와 혼합하여 소결체로 제조된 후 원자로에 장전된다. 가연성 흡수체는 핵연료 집합체 내에서 배치되어 노심의 안정성을 확보하고 과도한 출력 상승을 방지할 뿐 아니라, 결과적으로 연료 활용도를 향상시킬 수 있는 필수적인 요소이다[2].

국내에서 추진하고 있는 혁신형 소형모듈원자로(SMR)의 개발에 있어, 무붕산 운전 적용이 계획 중이며, 원전의 경제성 향상을 위해 핵연료 연소 주기를 늘릴 목적으로 핵연료 농축도 상향도 고려되고 있는 지금, 초기 과도한 반응도를 효과적으로 제어할 수 있는 가연성 흡수체의 역할이 더욱 중요해지고 있다. 가연성 흡수체의 성능 향상에 있어, 기존보다 높은 중성자 흡수 성능을 확보하기 위해 동위원소 농축 [3, 4], 복합 형상 설계 [5, 6], 또는 고함량 첨가와 같은 다양한 개선 방안이 연구되고 있다. 그러나 동위원소 농축

https://doi.org/10.4150/jpm.2025.00178

은 생산 비용이 높고 농축 설비 및 규제 이슈로 인한 적용에 제약이 있으며, 복합 형상 설계는 제조 공정이 복잡하고 대량 생산에 어려움이 있다는 한계가 존재한다. Gd_2O_3 함량을 증가시키는 방안은 기존 제조공정과 평가기법을 그대로 활용할 수 있어, 보다 실질적이고 신속한 적용이 가능한 대안으로 고려될 수 있다. 다만, 고함량 조건에서는 제조 공정 최적화 및 추가 특성 평가가 필요할 수 있다.

현재 상용화된 가연성 흡수체 핵연료는 대부분 Gd_2O_3 함량이 약 10 wt.% 이하로 제한되어 있으며, 이보다 높은 함량을 적용한 경우에 대한 제조 공정, 평가 방법 및 물성 데이터는 충분히 구축되어 있지 않은 실정이다. 특히 Gd_2O_3 혼합 시 UO_2 핵연료의 열전도도가 저하되는 경향을 갖고 있어, 연료 성능에 부정적 영향을 미칠 수 있기 때문에, 이에 따른 열물성 변화에 대한 정밀한 데이터 확보가 반드시 필요하다. 일반적으로 가연성 흡수체 핵연료는 UO_2와 Gd_2O_3 분말을 혼합하여 성형 및 소결하는 방식으로 제조되며, 이때 혼합 과정에서의 분말 균질도가 소결체의 미세구조와 열물성에 직접적인 영향을 미친다[7]. 기존 연구에서는 단순 혼합(Simple Blending) [8, 9], 공동 분쇄 혼합(Co-Milling) [10, 11], 공침(Co-Precipitation) [12, 13] 등의 방법이 제안된 바 있으나, 대부분 10 wt.% 이하의 Gd_2O_3를 기준으로 수행되었고[14], 해당 함량 이상의 고함량 Gd_2O_3-UO_2 혼합체의 제조 및 미세구조 특성에 대한 연구는 부족한 상황이다.

본 연구에서는 현재 상용 핵연료에서 사용되는 8 wt.% 혼합 함량의 두 배에 해당하는 17 wt.%를 고함량 혼합 조건으로 설정하여, 분말 혼합 방법 종류에 따른 소결체의 밀도, 기공 분포 및 미세구조 변화를 분석하고, 혼합 분말의 입자 크기와 혼합 균질도가 소결체 미세구조에 미치는 영향을 규명하고자 한다. 이를 통해 고함량 Gd_2O_3 가연성 흡수체 제조 시 발생할 수 있는 공정상의 문제점을 극복하고, 향후 국내 혁신형 SMR에 적용 가능한 고함량 Gd_2O_3 첨가 UO_2 소결체 개발을 위한 기초 데이터를 확보하고자 한다.

2. Experimental

UO_2및 Gd_2O_3 분말 혼합 공정의 변수 조절을 통한 고함량 Gd_2O_3 가연성 흡수체 핵연료의 제조와 평가를 수행하였다. 시료의 분말 처리와 소결체 제조는 혼합, 분쇄, 성형, 소결의 일반적인 세라믹 제조 공정을 통해 진행하였다.

한국원자력연구원이 보유하고 있는 UO_2 분말 (ADU(Ammonium Di Uranate)공정 제조)과 가연성 흡수 물질 Gd_2O_3(99.99%, Sigma-Aldrich Ltd.) 분말, 그리고 소결체의 결정립 크기 확보를 위한 Al_2O_3(99.99%, Sigma-Aldrich Ltd.) 분말 (100 PPM)을 사용하였다. 후술할 혼합 공정에 따라 제조된 혼합 분말은 직경 10mm 의 성형 몰드를 사용하여 300 MPa의 압력으로 일축 압축하여 성형체를 제작하였다. Zn stearate(99.99%, Sigma-Aldrich Ltd.) 를 윤활제로 사용하였으며, 벽면 도포 윤활(die wall lubrication) 방식을 적용하였다. 성형체의 소결은 1730˚C, H_2 – CO_2(3%) 분위기에서 4시간 동안 진행하였다.

분말 혼합 방법 종류에 따른 영향을 평가하기 위해, 단순 혼합(Simple Blending), 체질 혼합(Sieve-Mixing), 그리고 유성 밀링(Planetary Milling)을 적용한 소결체를 각각 제조하였다. 단순 혼합으로는 Turbula™ mixer 를 사용하여 건식 분말 혼합을 이루었으며, 체질 혼합으로 실험용 체 (325 mesh, ~ 45 μm opening) 및 지르코니아 비드(5mm)를 사용하여 건식 혼합 및 응집체 해소를 유도하였다. 마지막으로 유성 밀링 장비((Pulverisett 6, Fristch)와 지르코니아 용기 및 비드(5mm)를 사용하여 UO_2 분말 및 Gd_2O_3 분말을 동시 습식 분쇄 및 혼합을 적용하였다.

초기 혼합 분말의 입자 크기 상대성 영향을 분석하기 위해, UO_2 및 Gd_2O_3 분말을 각각 따로 유성 밀링을 이용하여 분쇄하여 준비하였으며, 초기 분말 및 분쇄 분말의 적용 조합에 따라, 네 가지 조건에 따른 실험을 설계하였다. Table 1은 본 연구의 시편들을 변수

Table 1. Summary of specimen names and processing conditions used in this study

Specimen name	Mixing method	Gd_2O_3 content (wt%)
B8	Simple blending	8
B17		17
S8	Sieve mixing	8
S17		17
P8	Planetary milling	8
P17		17

Specimen name	Mixing method	Gd_2O_3 content (wt%)	UO_2	Gd_2O_3
S17-AA	Sieve mixing	17	As-received	As-received
S17-AP			As-received	Planetary milled
S17-PA			Planetary milled	As-received
S17-PP			Planetary milled	Planetary milled

별로 정리한 것으로, 각 시편의 혼합 공정과 입자 크기 등의 조건을 포함하고 있다.

제조된 소결체는 밀도 평가, X선 회절 분석, 미세구조 분석으로 평가를 수행하였다. 밀도는 ASTM B962-17을 준수한 아르키메데스법을 통해 측정하였으며, 물을 침투제로 사용하여 소결체의 건조, 수중, 포수 무게를 계산하였다. X선 회절분석기(Ultima IV, Rigaku) 을 통해 제조된 소결체의 결정구조를 평가하고 (20˚~90˚, 2 theta), UO_2-Gd_2O_3 소결체의 상 형성과 피크 분포를 확인하였다. 광학현미경(Optical Microscope, A1m, Carl Zeiss)과 주사전자현미경 (Scanning Electron Microscope, VEGA3, Tescan)을 통해 사용된 분말과 소결체의 결정립 크기, 분포와 같은 미세구조를 분석을 수행하였다.

고함량 Gd_2O_3가 첨가된 UO_2 핵연료의 혼합 분말 영향성을 정량적으로 분석하기 위해, 소결 시편의 광학현미경(OM) 미세구조 이미지를 ImageJ 소프트웨어(National Institutes of Health, version 1.50i)를 이용하여 분석하였다. 광학현미경으로 획득한 미세구조 이미지는 최적의 threshold 값을 설정하여 기공을 분리하였다. 기공만 분리된 이미지를 기반으로 입자 분석 기능을 이용하여 기공 크기, 면적 및 기공률(공극률)을 계산하였다. 정확성을 높이기 위해 시편당 최소 3장 이상의 이미지를 분석하였으며, 각 시편에 대해 얻은 데이터의 평균값을 통해 기공 크기 분포와 전체 기공률을 평가하였다.

3. Results and Discussion

3.1 Gd_2O_3 함량 증가 및 혼합 공정에 따른 입자 및 미세구조 영향 확인

Fig. 1은 UO_2와 Gd_2O_3 초기 분말의 SEM 이미지를 보여준다. UO_2 초기 분말(Fig. 1(a))과 Gd_2O_3초기 분말(Fig. 1(b))은 평균 입자 크기가 약 1–10 μm 범위로 분포하며, 일부 입자는 결합하여 20 μm 이상의 응집체를 형성하고 있었다. 이러한 대형 응집체와 불균일한 입자 분포는 혼합 균질성을 저하시켜 소결 과정에서 국부적인 치밀화 지연과 불균일한 기공 분포를 유발할 수 있다. 또한 Fig. 1(c, d)는 유성 밀링을 거친 후의 UO_2와 Gd_2O_3 분말을 나타낸다. 밀링 후 두 분말 모두 입자 크기가 약 1 μm 이하로 균일하게 감소하였으며, 초기 분말에서 관찰되던 불규칙한 형태의 응집체는 제거

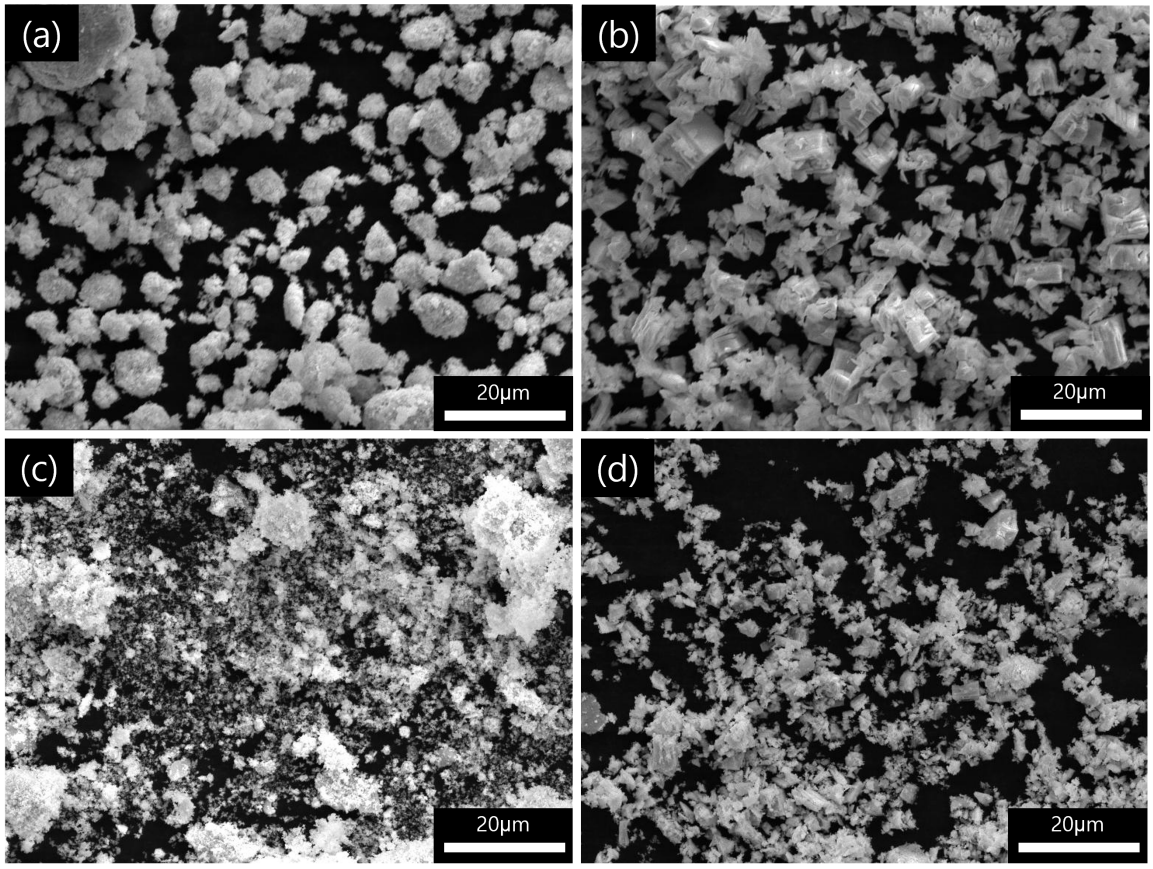

Fig. 1. Scanning electron microscopy images of as-received UO_2 and Gd_2O_3 powders : (a) As-received UO_2, (b) As-received Gd_2O_3, (c) Milled UO_2 powder, (d) Milled Gd_2O_3 powder.

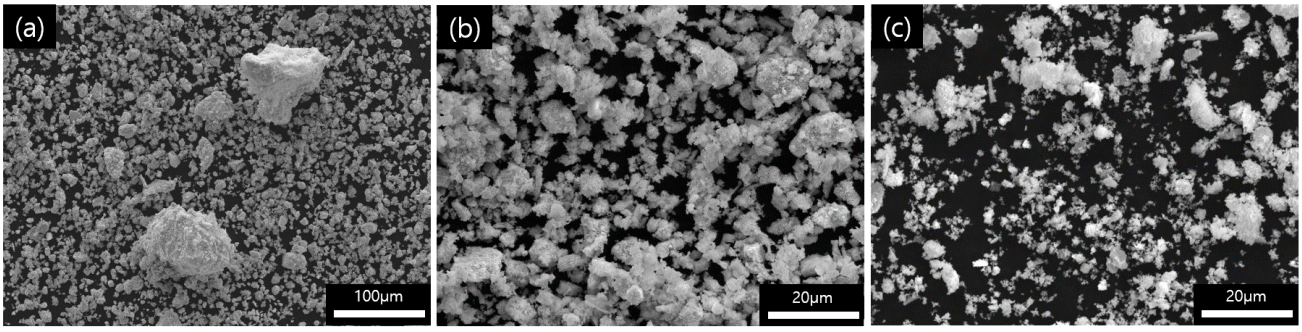

Fig. 2. Scanning electron microscopy images of UO_2–Gd_2O_3 mixed powders prepared by different mixing methods: (a) simple blending 17 (B17), (b) sieve mixing 17 (S17), (c) planetary milling 17 (P17).

되었다. 이러한 미세화 및 균일화는 입자 간 접촉 면적을 증가시켜 확산 거리를 단축시키고, 소결 밀도 향상과 균일한 미세구조 형성에 유리하게 작용할 것으로 판단된다.

Fig. 2는 UO_2와 Gd_2O_3 혼합 및 분쇄 공정을 거친 후의 변화를 SEM 이미지로 비교한 결과이다. B17 분말(Fig. 2(a))은 일부 Gd_2O_3 입자가 분산되어 있으나, 20 μm 이상의 대형 응집체가 여전히 존재해 혼합 균일성이 낮았다. 이러한 대형 응집체는 소결 시 UO_2와의 상호확산을 제한하고, 국부적인 치밀화 지연 및 기공 집중을 유발할 가능성이 높다.

S17 분말(Fig. 2(b))은 체질 혼합을 통해 Gd_2O_3 분포가 개선되고 응집체가 감소하여 혼합 균일성이 향상되었다. 이는 소결 과정에서 보다 균일한 입자 간 접촉을 가능하게 해, 기공 분포의 불균일성을 완화할 수 있다. P17 분말(Fig. 2(c))은 유성 밀링으로 입자가 더욱 미세해지고 UO_2와 Gd_2O_3가 균일하게 분산되어 응집체가 사라졌다. 이러한 미세화·균일화는 확산 거리를 줄이고, 소결 온도에서의 반응성과 치밀화를 촉진하여 균일한 미세구조 형성에 유리하게 작용한다.

Fig. 3는 혼합 공정과 Gd_2O_3 함량에 따른 소결체 밀도를 비교한 결과를 나타낸다. 혼합 공정이 소결체 밀도에 중요한 영향을 미치는 것으로 확인되었다. 단순 혼합 (B8, B17)은 가장 낮은 밀도를 나타냈으며, 이는 낮은 혼합 에너지로 인해 UO_2와 Gd_2O_3가 불균일하게 혼합되면서 소결 과정 중 기공 형성이 두드러졌기 때문으로 판단된다. 체질 혼합(S8, S17)은 단순 혼합 대비 밀도가 향상되었는데, 이는 체질 혼합을 통해 응집체가 사라지고 혼합 균질성이 개선된 결과로 보인다. 특히, 유성 밀링(P8, P17)은 가장 높은 밀도를 나타냈으며, 고에너지 혼합으로 입자 크기가 미세화되고 혼합 균일성을 크게 향상된 결과로 보인다. Gd_2O_3 함량이 8 wt%에서 17 wt%로 증가함에 따라, 이전 연구 결과와 마찬가지로[13] 전반적으로 소결체 밀도가 감소하는 경향이 나타났다. 이는 Gd_2O_3 함량 증가로 인해 소결 과정 중 기공 형성이 증가하고 치밀화가 저해된 결과로 판단된다. 이러한 경향은 단순 혼합(B17)에서 가장 크게 나타

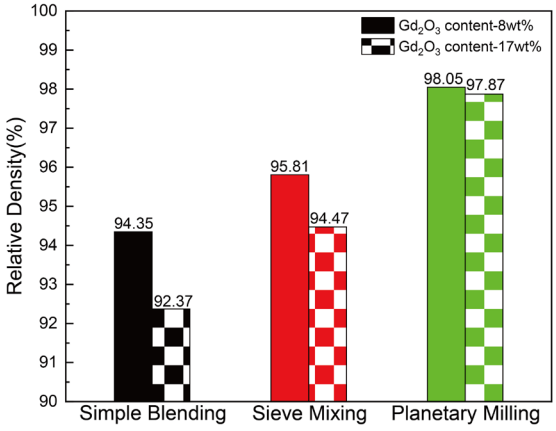

Fig. 3. Relative densities of UO_2–Gd_2O_3 pellets as a function of mixing method and Gd_2O_3 content.

났으며, B8 대비 약 2.10%의 상대 밀도 감소가 관찰되었다. 체질 혼합(S17)에서는 B17 대비 감소율이 작았으나, 여전히 밀도 저하 경향이 나타났다(1.40%). 한편, 유성 밀링(P17)에서는 감소율이 0.18%로 나타나, 고함량 조건에서도 상대적으로 높은 밀도가 유지되는 경향을 보였다.

U-Gd 혼합계에서 나타나는 기공 형성의 주요 원인으로 Kirkendall 효과가 알려져 있다[15]. 소결 과정에서 Gd_2O_3에서 UO_2로의 가돌리늄(Gd) 확산 속도가 UO_2에서 Gd_2O_3로의 우라늄(U) 확산 속도보다 빨라 물질 이동의 불균형이 발생하게 되는데[15, 16], 이 불균형으로 인해 Gd_2O_3 응집체가 존재하던 위치에 기공이 형성된다. 이는 본 연구에서 혼합 균일성이 낮은 단순 혼합 소결체에서 더욱 두드러지게 확인되며, 가돌리늄이 우라늄보다 UO_2 상으로 더 빠르게 확산되어 기공 형성을 유발하는 상호 확산 메커니즘을 뒷받침한다. 또한, 이러한 현상은 물질 간 확산율이나 용해도의 차이에 의해 발생하며 UO_2-Y_2O_3 시스템에서 관찰된 사례와 유사한 양상이 관찰된 바 있다[17-19].

Fig. 4는 혼합 방법과 Gd_2O_3 함량에 따른 저배율(50배) 미세구조 이미지를 나타낸다. Fig. 4.(a, d)는 단순 혼합으로 제조된 소결체(B8,17)의 미세구조를 보여주며, 두 시편 모두에서 Gd_2O_3 응집체가 관찰되었다. 특히 고함량 조건인 17 wt% (Fig. 4(d))에서는 응집체의 크기와 수가 현저히 증가하였다. 이는 혼합 분말 단계에서 이미 존재하던(〉20 μm) Gd_2O_3 응집체가 단순 혼합의 낮은 혼합 에너지로 인해 충분히 분산되지 못하고 잔존하였기 때문으로 판단된다. 반면, Fig. 4(b, c, e, f)는 체질 혼합 및 유성 밀링으로 제조된 소결체(S8, P8, S17, P17)의 미세구조로, 응집체가 관찰되지 않으며 Gd_2O_3 입자가 비교적 균일하게 분포하고 있다. 특히 Fig. 4(f)의 P17 시편은 고함량 조건임에도 불구하고 기공의 크기와 분포(수치)가 균일한 미세구조를 나타냈다.

Fig. 5는 혼합 방법과 Gd_2O_3 함량에 따른 고배율(500배) 미세구조 이미지를 나타낸다. B8 시편(Fig. 5(a))에서는 Gd_2O_3 응집체가 관찰되었으며, 응집체 주변에 미세한 균열이 형성된 것이 확인되었다. Gd_2O_3 함량이 증가한 B17 시편(Fig. 5(d))에서는 응집체의 크기가 더욱 커지고 응집체 주변으로 다수의 균열이 형성되었다. 두 시편 모두 Gd_2O_3 응집체가 존재했는데, 이는 낮은 혼합 에너지로 인해 입자 간 물리적 상호작용이 불충분하여 균질한 분포가 달성되지 않은 결과로 판단된다. 이러한 불균질한 혼합 상태는 응집체 주변에서 다수의 균열과 기공을 형성하여 소결 시 치밀화를 방해한 것으로 보인다. S8 시편(Fig. 5(b))은 단순 혼합에 비해 Gd_2O_3 입자가 비교적 균일하게 분포하였다. 고함량인 S17 시편(Fig. 5(e))은 Gd_2O_3 함량 증가로 인해 기공 수가 다소 증가했으나, 단순 혼합보다 입자 분포가 개선된 것을 관찰할 수 있었다. 두 시편 모두에서 Gd_2O_3 응집체는 발견되지 않았으나, 완전한 균질 혼합 상태에는 이르지 못하였다. 이는 체질 혼합이 단순 혼합보다 높은 혼합 에너지를 제공하여 혼합 균질성이 개선된 결과로 판단된다. Fig. 5(c, f)는 유성 밀링으로 제조된 소결체(P8, P17)의 미세구조를 나타낸다. P8 시편(Fig. 5(c))은 Gd_2O_3 입자가 고르게 분포하고, 기공 크기가 작으며 높은 밀도를 보여 우수한 혼합 균질성을 나타냈다. 고함량 조건의 P17 시편(Fig. 5(f)) 역시 Gd_2O_3가 고르게 분산되어 있으며, 기공 크기와 밀도가 더욱 감소된 가장 치밀한 미세구조를 형성하였다. 두 시편 모두에서 Gd_2O_3 응집체는 관찰되지 않았고, 일관된 미세구조 특성을 통해 혼합 균질성을 확보한 것으로 평가된다.

Fig. 6은 혼합 방법에 따른 소결체의 XRD 분석 결과를 나타낸다. Fig. 6(a)는 20°–90° 영역에서의 XRD 패턴을 보여주며, 모든 시편(B17, S17, P17)에서 UO_2의 주요 피크가 관찰되었다. 이는 소결 후에도 UO_2의 결정 구조가 유지되었음을 확인해 준다. 또한 UO_2에서 Gd^{3+}가 U^{4+} 자리를 치환하면 이온 반경 차이로 인해 격자가 수축하고, 이에 따라 $(U,Gd)O_2$ 고용체의 피크가 UO_2 대비 고각으로 이동한다. Fig. 6(b)는 고각도 영역(75°–80°)을 확대하여 UO_2 Peak (빨간 점선)와 U-Gd solid solution (파란 점선)의 피크 강도를 비교한 결과이다. 단순 혼합으로 제조된 B17 시편은 UO_2

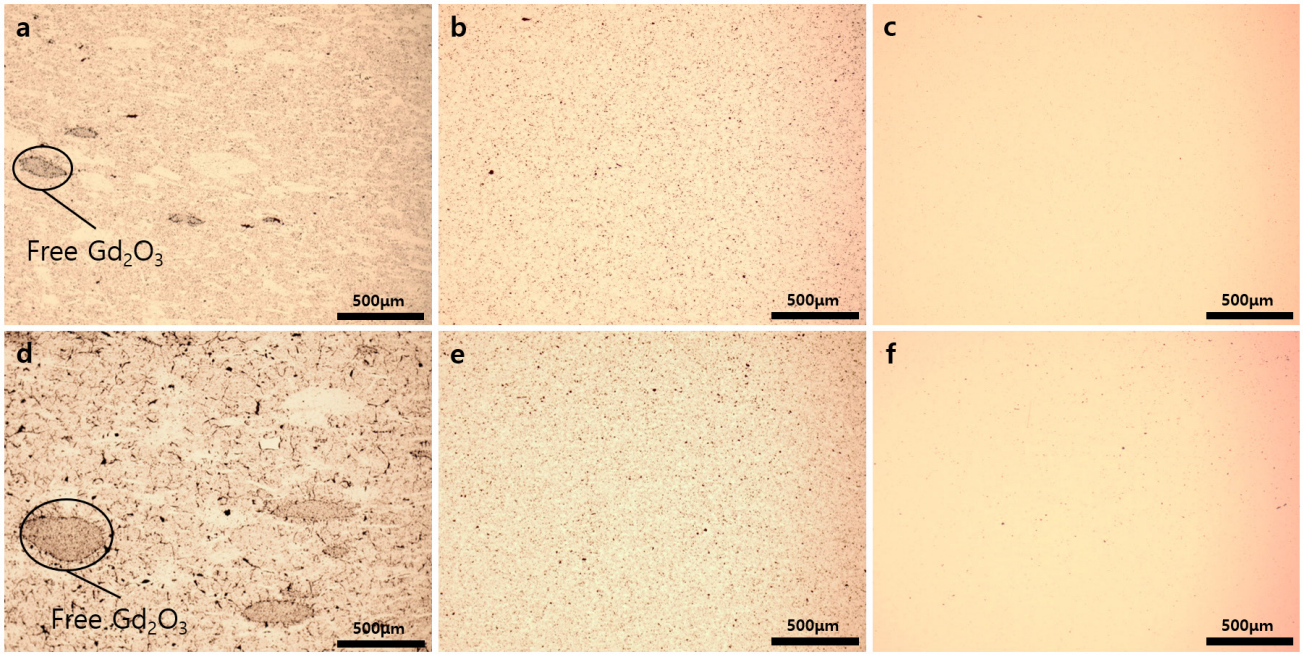

Fig. 4. Microstructures (optical microscopy) of UO_2–Gd_2O_3 pellets with different mixing methods and Gd_2O_3 contents (8 and 17 wt%): (a) simple blending 8 (B8), (b) sieve mixing 8 (S8), (c) planetary milling 8 (P8), (d) simple blending 17 (B17), (e) sieve mixing 17 (S17), (f) planetary milling 17 (P17).

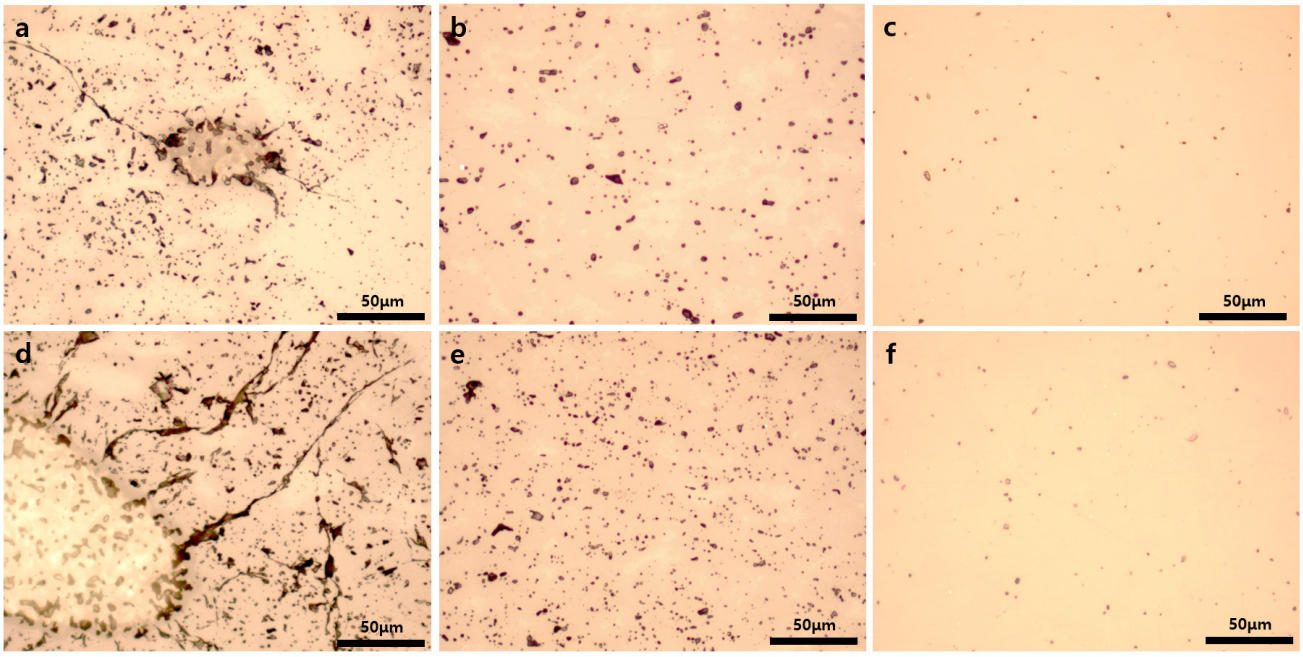

Fig. 5. Microstructures (optical microscopy) of UO_2–Gd_2O_3 pellets with different mixing methods and Gd_2O_3 contents (8 and 17 wt%) : (a) simple blending 8 (B8), (b) sieve mixing 8 (S8), (c) planetary milling 8 (P8), (d) simple blending 17 (B17), (e) sieve mixing 17 (S17), (f) planetary milling 17 (P17).

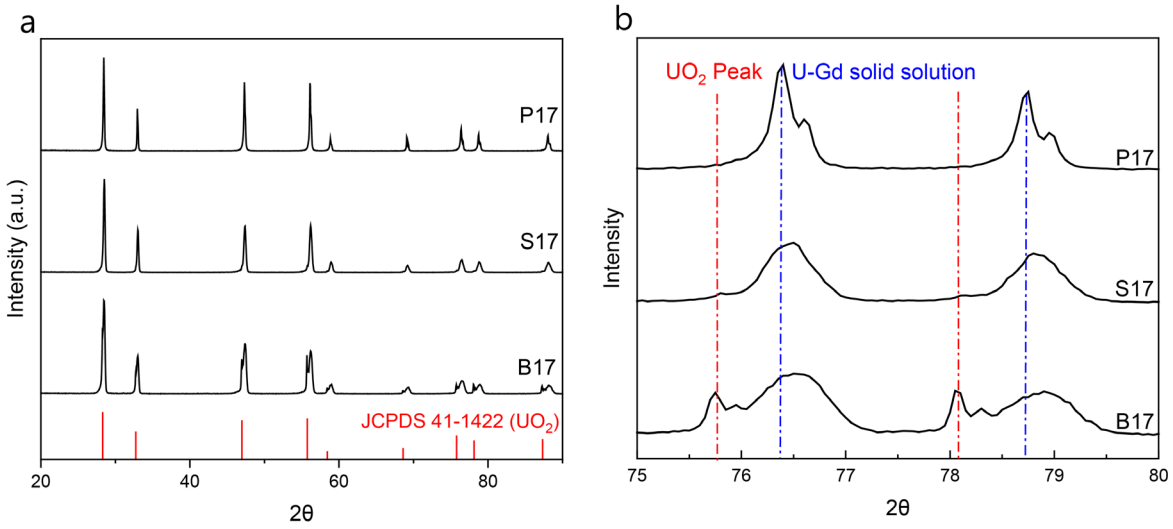

Fig. 6. Comparison of X-ray diffraction patterns of UO_2–Gd_2O_3 pellets with different mixing methods: (a) 20°–90°, (b) 75°–80°.

Peak의 피크가 뚜렷하게 나타났고, 상대적으로 U-Gd solid solution의 피크 강도가 낮았다. 이는 낮은 혼합 에너지로 인해 Gd_2O_3와 UO_2 간의 상호작용이 제한적이었으며, 결과적으로 Gd_2O_3가 UO_2 매트릭스 내에 균일하게 도핑되지 못한 것으로 판단된다. 체질 혼합으로 제조된 S17 시편에서는 UO_2 Peak 의 피크가 미약하게 존재하였고, 그 강도가 B17에 비해 감소했다. U-Gd solid solution피크 강도 또한 B17 에 비해 증가하였다. 이는 체질 혼합이 단순 혼합보다 혼합 균일성을 향상시켜 Gd_2O_3 입자가 UO_2 매트릭스에 더 효과적으로 도핑된 결과로 해석할 수 있다. 반면, 유성 밀링으로 제조된 P17 시편은 UO_2 Peak 의 피크가 사라지고, U-Gd solid solution의 피크가 명확히 관찰되었다. 이는 유성 밀링이 높은 혼합 에너지를 제공하여 Gd_2O_3를 UO_2 매트릭스에 효과적으로

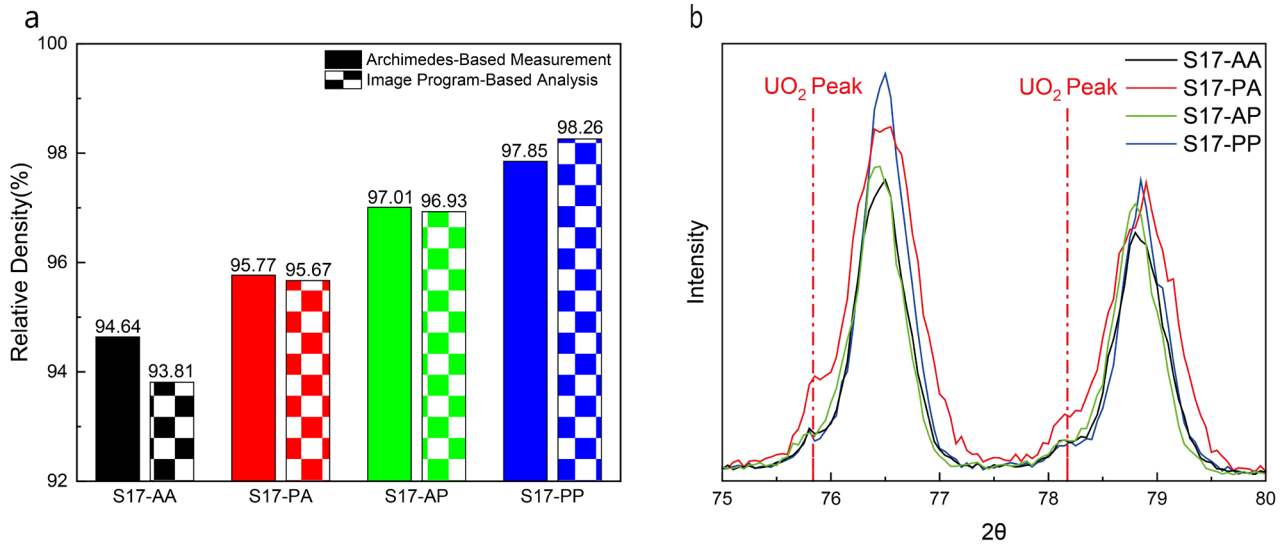

Fig. 7. (a) Comparison of relative densities of S17 samples (AA, PA, AP, PP) and P17 measured by Archimedes' method and image program-based analysis. (b) Comparison of high-angle X-ray diffraction patterns (75°–80°) of pellets fabricated with various UO_2–Gd_2O_3 powder size conditions (AA, PA, AP, PP) (right).

도핑하고 균일한 U-Gd solid solution을 형성했음을 나타낸다. 이러한 결과는 혼합 에너지가 증가할수록 UO_2 Peak 이 감소하고, U-Gd solid solution이 더욱 균일하게 형성됨을 보여준다.

3.2 초기 입자 크기 제어가 혼합 균질성과 소결 거동에 미치는 영향 확인

Fig. 7 (a)는 체질 혼합을 통해 제조된 S17 시편들의 상대 밀도를 아르키메데스법과 이미지 분석법을 통해 측정하여 비교한 결과를 나타낸다. 각 시편은 혼합 조건에 따라 S17-AA, S17-PA, S17-AP, S17-PP로 구분된다. 이미지 분석을 통해 산출한 상대 밀도는 아르키메데스법으로 측정한 값과 ±1% 이내의 차이를 보여, 이미지 분석 방법의 신뢰성을 확인할 수 있었다. S17-AA 시편은 밀링을 수행하지 않은 UO_2와 Gd_2O_3를 혼합하여 제조한 시편으로, 가장 낮은 밀도를 나타냈다. 이는 두 분말의 상대적으로 큰 입자 크기 차이로 인해 혼합 균질성이 저하되고, 그로 인해 소결 중 기공 형성이 증가했기 때문으로 해석된다. S17-PA 시편은 밀링한 UO_2와 밀링하지 않은 Gd_2O_3를 혼합한 시편으로, S17-AA에 비해 소폭 증가한 밀도를 보였다. 이는 UO_2 입자의 미세화가 혼합 균질성 향상에 일정 부분 기여한 결과로 판단된다. S17-AP 시편은 밀링하지 않은 UO_2와 밀링한 Gd_2O_3를 혼합한 시편으로, S17-AA 및 S17-PA보다 더 높은 밀도를 나타냈다. 이는 Gd_2O_3 입자 크기 감소가 혼합 균질성을 개선하고, 소결체 밀도 향상에 보다 큰 영향을 미친다는 것을 보여준다. S17-PP 시편은 두 분말 모두 밀링하여 혼합한 시편으로, 가장 높은 밀도를 나타냈으며, 이는 입자 크기 미세화로 인한 혼합 균질성 향상이 주요 원인으로 판단된다.

특히, S17-AP와 S17-PP는 유성 밀링을 적용하여 앞서 제조한 P17 시편(Fig. 3)과 유사한 수준의 높은 밀도를 보였다. 이는 습식 고에너지 혼합 공정을 사용하지 않더라도, 건식 혼합 공정을 통해 초기 입자 크기를 효과적으로 제어함으로써 소결체의 밀도 및 기본 물성을 향상시킬 수 있음을 시사한다. 또한, Gd_2O_3의 초기 입자 크기를 감소시키는 것이 혼합 균질성 개선과 소결체 밀도 향상에 결정적인 역할을 한다는 점을 실험적으로 확인할 수 있었다.

Fig. 7(b)는 입자 크기에 따른 소결체의 XRD (75°~80°) 분석 결과를 나타낸다. S17-PA 시편에서는 UO_2 Peak가 가장 높은 강도로 관찰되었으며, 이는 밀링되지 않은 Gd_2O_3의 혼합 불균질성으로 인해 응집이 심화되어 solid solution 형성이 제한되었음을 보여준다. S17-AA 시편 또한 UO_2 Peak가 확인되었으며, 강도는 PA보다는 낮았으나 여전히 명확히 존재하였다. 이는 밀링되지 않은 두 분말의 혼합으로 인한 균질성 저하와 불완전한 solid solution 형성으로 설명될 수 있다. 반면, S17-AP 및 S17-PP 시편은 UO_2 Peak가 매우 미약하거나 거의 나타나지 않았으며, 이는 Gd_2O_3가 보다 고르게 분산되고, solid solution이 효과적으로 형성되었음을 보여준다.

Fig. 8은 입자 크기에 따른 UO_2–Gd_2O_3 소결체의 고배율 미세구조(OM) 이미지를 보여준다. Fig. 8(a)는 S17-AA 시편으로, 미세구조상 다수의 크고 불균일한 기공이 관찰되었다. 이는 혼합 과정에서의 낮은 균질성을 반영하며, 소결 중 치밀화를 저해하여 기공의 형성과 잔존을 유도한 주요 원인으로 판단된다. Fig. 8(b)의 S17-PA 시편은 기공의 수는 감소하였으나, 상대적으로 큰 기공들이 관찰되었다. 이는 밀링되지 않은 Gd_2O_3의 큰 입자 크기가 혼합

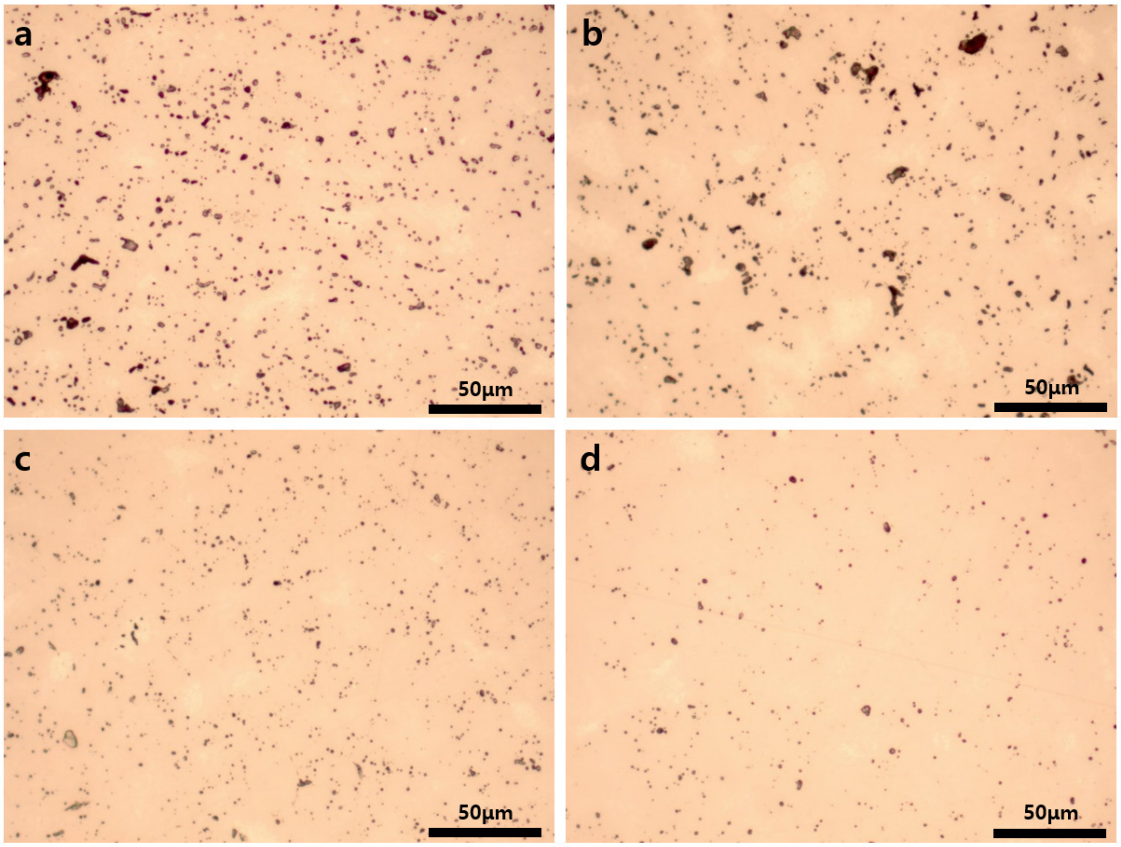

Fig. 8. Microstructures (optical microscopy) of UO_2–Gd_2O_3 pellets (17 wt% Gd_2O_3) with different powder size conditions: (a) S17-AA, (b) S17-PA, (c) S17-AP, (d) S17-PP.

균질성을 저해하고, 소결 중 국부적인 치밀화 불균형을 유발한 결과로 해석된다. 하지만 주성분인 UO_2가 충분히 미세하고 반응성이 높을 경우, 소결 반응이 활발히 일어나 일부 기공은 효과적으로 제거될 수 있음을 보여준다. Fig. 8(c)의 S17-AP 시편은 앞선 조건들에 비해 기공의 수가 적고, 비교적 균질한 미세구조를 형성하였다. 이는 Gd_2O_3의 입자 크기를 줄임으로써 혼합 균질성이 개선되었고, 확산 경로 단축을 통해 기공 형성이 억제되었기 때문으로 해석된다. 이러한 미세구조는 소결체의 밀도 향상에도 긍정적인 영향을 미쳤다. Fig. 8(d)의 S17-PP 시편은 기공의 수가 가장 적고, 분포 또한 매우 균일한 양상을 보였다. 이는 두 분말 모두를 미세화하여 혼합 균질성을 극대화한 결과, 치밀화가 효과적으로 이루어진 것으로 판단된다.

Fig. 9은 이미지 분석 프로그램을 활용하여 서로 다른 혼합 조건으로 제조된 UO_2–Gd_2O_3 소결체의 기공을 시각적으로 표현하고, 기공 크기 분포를 분석한 결과를 나타낸다. S17-AA 시편은 기공 크기 분포가 넓고 2 μm 이상의 큰 기공이 다수 관찰되었으며, 평균 기공 지름은 1.74 μm로 측정되었다. 이는 혼합 균질성이 낮고 소결 치밀화가 불완전했음을 보여준다. S17-PA 시편 역시 1.78 μm의 평균 기공 지름을 나타내며, 전체적인 기공 수는 다소 감소하였으나 여전히 큰 기공들이 존재하였다. 이는 밀링되지 않은 Gd_2O_3의 응집으로 인해 혼합 균질성이 저해된 결과로 해석된다. 반면 S17-AP 시편은 대부분의 기공이 1.5 μm 이하에 집중되었고, 평균 기공 지름은 1.24 μm로 감소하였다. 이는 Gd_2O_3 입자 미세화가 혼합 균질성과 소결성을 효과적으로 향상시켰음을 수치적으로도 입증한다. 특히 S17-PP 시편은 평균 기공 지름이 1.30 μm로 작고, 기공 크기 분포가 가장 좁은 특성을 보여주며, 두 분말의 미세화를 통해 높은 혼합 균질성과 치밀화 수준이 확보되었음을 확인할 수 있다.

특히, 혼합이 불균질할 경우 UO_2와 Gd_2O_3 입자 간의 소결 속도 차이에 의해 국부적인 체적 변화가 발생하고, 이로 인해 큰 닫힌 기공이 형성되어 최종 소결 밀도가 저하될 수 있다 [19].

4. Conclusion

본 연구에서는 다양한 제조 공정 변수들이 UO_2–Gd_2O_3 소결체의 밀도, 결정 구조, 및 혼합 균질성에 미치는 영향을 정량적으로

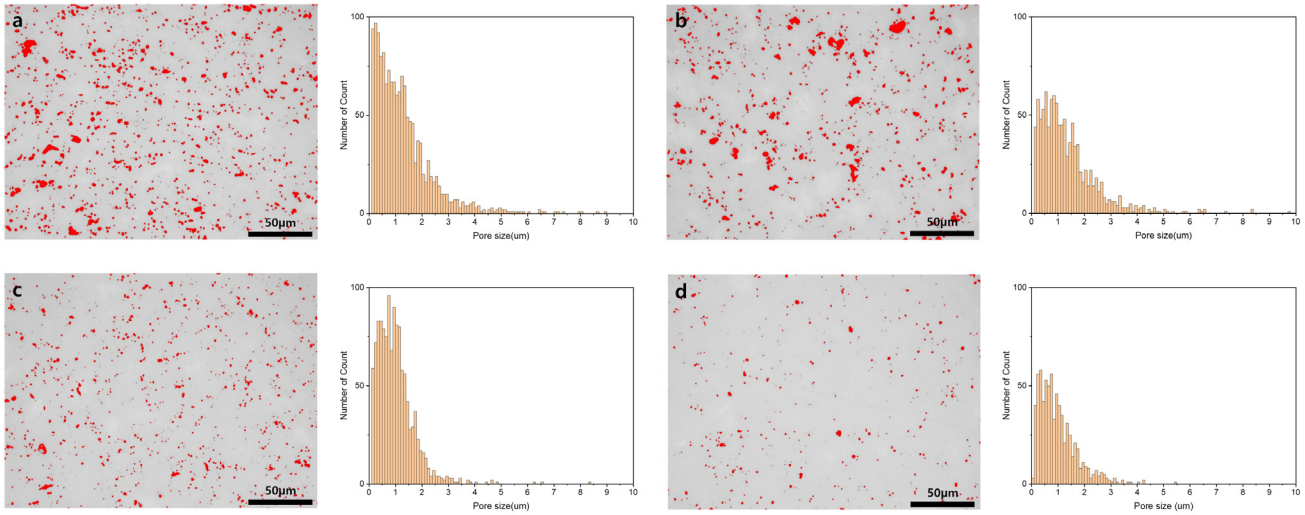

Fig. 9. Pore visualization (in red) of UO_2–Gd_2O_3 pellet microstructures using image analysis based on Fig. 8. and pore size distribution histograms of UO_2 – Gd_2O_3 pellets fabricated under different powder mixing conditions (a) S17-AA, (b) S17-PA, (c) S17-AP, (d) S17-PP.

분석하여, 향후 혁신형 SMR 고함량 Gd_2O_3 첨가 UO_2 소결체 제작에 필요한 기초 자료로 활용할 예정이다. 또한, 분말 혼합 방법 및 초기 분말 특성에 따른 소결체 미세구조 변화와 기공 특성에 대한 분석을 통해, 고함량 가연성 흡수체 핵연료의 제조 공정 최적화 및 성능 개선에 기여할 수 있을 것으로 기대된다.

고함량 Gd_2O_3 첨가 UO_2 핵연료 소결체를 제조하기 위해, 단순 혼합, 체질 혼합, 유성 밀링 세 가지 혼합 방식을 비교하였다. 단순 혼합은 낮은 혼합 에너지로 인해 Gd_2O_3 응집체, 기공, 균열이 다수 형성되어 소결체 특성이 저하되었고, 체질 혼합은 혼합 균질성이 향상되었으나 일부 기공이 잔존하였다. 유성 밀링은 고에너지 분산 효과로 가장 높은 혼합 균질성과 치밀한 미세구조를 달성하였다. XRD 분석 결과, 혼합 균질성 향상에 따라 Gd-rich 상이 감소하고 U-Gd solid solution 형성이 촉진되는 경향이 확인되었다. 이러한 결과는 고함량 Gd_2O_3 적용 시 혼합 공정이 소결체 특성과 밀도에 미치는 영향이 더욱 커지며, 고함량 조건에서는 혼합 방식의 최적화가 필수적임을 시사한다.

초기 입자 크기 제어가 혼합 균질성과 소결 거동에 미치는 영향을 평가하기 위해, UO_2와 Gd_2O_3 분말 조합을 달리한 네 가지 조건(S17-AA, -PA, -AP, -PP)을 비교하였다. Gd_2O_3 입자만을 미세화한 S17-AP 시편과 양 입자 모두를 미세화한 S17-PP 시편은 응집 현상이 줄어들고 기공 분포가 좁아져 혼합 균질성과 소결 특성이 크게 향상되었다. 그러나 미세화된 분말을 단순 혼합으로 혼합할 경우, 오히려 혼합 균질성이 저하되어 소결체 특성 개선에 부정적인 영향을 미치는 것으로 나타났다. 이는 미세화만으로 충분하지 않으며, 미세화된 분말에는 충분한 혼합 에너지가 병행되어야 혼합 균질성과 소결 특성이 효과적으로 향상될 수 있음을 보여준다. 또한, Gd_2O_3 는 비방사성 물질로 공정 제어가 용이하여, 입자 크기 제어를 통한 혼합 균질성 향상에 실질적 이점을 제공함을 확인하였다. 본 연구 결과는 고연소도 및 소형 모듈형 원자로용 고함량 가연성 흡수체 핵연료 개발에 기초 데이터를 제공할 수 있을 것으로 기대된다.

Funding

This work was supported by the Innovative Small Modular Reactor Development Agency grant funded by the Korea government (MOTIE) (No. RS-2023-00264675).

Conflict of Interest

The authors declare no competing financial interests or personal relationships.

Data Availability Statement

The dataset files are available on request.

Author Information and Contribution

Ji hwan Lee: Master's student; conceptualization, experiment, writing–original draft, formal analysis

Jae Ho Yang: Principal Researcher; data curation, formal

analysis

Ji-Hae Yoon: Senior Research Technician; data curation, formal analysis

Dong-Joo Kim: Principal Researcher; Validation, Project administration

Dong-wook Shin: Professor; Validation

Dong Seok Kim: Senior Researcher; writing–original draft, supervision, Writing – review & editing

Acknowledgments

None.

References

[1] J. A. Evans, M. D. DeHart, K. D. Weaver and D. D. Keiser: Nucl. Eng. Des., **391** (2022) 111726.

[2] M. Durazzo and H. G. Riella: Key Eng. Mater., **189–191** (2001) 60.

[3] K.-H. Bejmer and O. Soversbo: Prog. Nucl. Energy, **40** (2002) 251.

[4] D. Campolina, E. F. Faria, A. a. C. Santos, V. Vasconcelos, M. P. V. Franco, M. S. Dias and J. R. L. Mattos: Ann. Nucl. Energy, **118** (2018) 375.

[5] K. Iwasaki, T. Matsui, K. Yanai and R. Yuda: J. Nucl. Sci. Technol., **46** (2009) 673.

[6] M.-S. Yahya and Y. H. Kim: Nucl. Eng. Technol., **49** (2017) 851.

[7] IAEA-TECDOC-1686: Experiences and Trends of Manufacturing Technology of Advanced Nuclear Fuels, IAEA, Vienna (2012).

[8] M. Durazzo, A. C. Freitas, A. E. S. Sansone, N. A. M. Ferreira, E. F. Urano de Carvalho, H. G. Riella and R. M. Leal Neto: J. Nucl. Mater., **510** (2018) 603.

[9] L. R. dos Santos, M. Durazzo, E. F. Urano de Carvalho and H. G. Riella: J. Nucl. Mater., **493** (2017) 30.

[10] D.S. Kim, et al.: Trans. Korean Nucl. Soc., Autumn Meeting, (2023).

[11] A. Baena, T. Cardinaels, B. Vos, K. Binnemans and M. Verwerft: J. Nucl. Mater., **461** (2015) 271.

[12] A.L. Soldati, I. G. Watkins, A. F. Zuvich, F. Napolitano, H. Troiani, A. Caneiro and M. Prado: J. Nucl. Mater., **479** (2016) 436.

[13] A.G. Leyva and et al: J. Nucl. Mater., **303** (2002) 293–299.

[14] K.-S. Choi, M. Choi, C. H. Lee, S. Han and G. Y. Ji: Anal. Sci. Technol., **20** (2007) 131.

[15] M. Durazzo, A. M. Saliba-Silva, E. F. Urano de Carvalho and H. G. Riella: J. Nucl. Mater., **405** (2010) 203.

[16] M. Durazzo, A. M. Saliba-Silva, E. F. U. De Carvalho and H. G. Riella: J. Nucl. Mater., **433** (2013) 334.

[17] T. Takahashi and T. Yuda, IAEA-TECDOC-1036, IAEA, Vienna (1998) 105.

[18] K.W. Song, K. S. Kim, J. H. Yang, K. W. Kang and Y. H. Jung: J. Nucl. Mater., **288** (2001) 92.

[19] R. Yuda and K. Une: J. Nucl. Mater., **178** (1991) 195.

Research Article

pISSN 2799-8525 · eISSN 2799-8681
J Powder Mater 2025;32(4):354-360

Journal of
Powder Materials

Fe 와 Cr 첨가량이 β 타이타늄 합금의 ω상 형성에 미치는 영향

박선영*, 천영범

한국원자력연구원 재료안전기술연구부

Effect of Fe and Cr on ω Phase Formation in Metastable β-Ti Alloy

Sun-Young Park*, Young-Bum Chun

Materials Safety Technology Research Division, Korea Atomic Energy Research Institute, Daejeon 34057, Republic of Korea

This study investigated the effects of Fe and Cr contents on ω phase formation and transformation during solution treatment and the subsequent aging process, for which four model alloys with varying Fe and Cr contents but keeping Mo equivalent of ~ 12.6 were prepared by plasma arc melting and fabricated into plates by hot forging followed by hot-rolling. The atherrmal ω phase was observed in all Ti alloys after solution treatment followed by water quenching through XRD and TEM analysis. The largest volume fraction of athermal ω phase is formed in Ti alloy with only Fe 4 wt.% among all Ti alloys, leading to the highest Vickers value due to hardening effect ω phase. It was found that not only Mo equivalent but also each characteristic of β stabilizing elements should be considered to understand a microstructure evolution and mechanical properties.

Keywords: Beta titanium alloy; Aging; Omega phase; Hardness

Received: July 15, 2025
Revised: August 20, 2025
Accepted: August 21, 2025

***Corresponding author:**
Sun-Young Park
E-mail: sunyoung@kaeri.re.kr

1. Introduction

타이타늄(Ti) 합금은 우수한 인성, 뛰어난 내식성, 경량성, 열적 안정성을 가지고 있어 생체의료기기, 항공우주, 자동차, 해양 분야 등 다양한 분야에서 각광받는 소재로 알려져있다[1-6]. 특히, β-Ti 합금은 낮은 탄성계수, 낮은 밀도, 높은 내식성, 높은 비강도를 나타내 생체용 임플란트 소재 및 다양한 구조용 소재로 활용하고자 하는 연구가 이루어졌다. 지난 수십여년 동안 합금의 강도, 크리프 저항성, 성형성 및 용접성을 향상시키기 위해 V, Nb, Mo, Ta, Fe 등 다양한 합금 원소들을 이용한 합금화 방법에 대해 연구되었다[7-11]. 또한 합금 원소 및 함량 조절에 따라 합금 내의 상 조성, 분율 및 분포뿐만 아니라 상변태 거동을 제어하기 위한 연구가 이루어졌다. 그 중 여러 β-Ti 합금에서 ω 상의 형성이 보고되었으며, 이는 합금의 강도 향상 또는 연성에 영향을 미친다고 알려져 있다[12, 13]. 그러나 강도 증가가 ω 상의 형성 에 의한 것인지 또는 고용 원소에 의한 고용 강화 효과인지, 어떤 강화 효과 메커니즘이 더 지배적인 역할을 하는지에 대해 명확히 규명되지 않았다.

다양한 합금 원소 중 Fe과 Cr 은 높은 강화 효과뿐만 아니라 낮은 원가로부터 경제성을 가지고 있어 Ti 합금화 원소 중 효과적인 β 안정화 원소로 알려져 있다[9, 10, 14-17]. 특히, Fe은 인체 필수 원소로써 알레르기 반응 유발 가능성이 상대적으로 낮아 생체재료로써 높은 적합성으로 인해 치과용 소재로 활용하고자 하는 연구가 활발히 진행되고 있다[17, 18]. Cr은 Ti 의 양극 반응성을 조절하여 피막형성 경향을 증가시켜 내식성을 향상시키는 효과가 보고되었다[19]. 그러나 Ti 합금내에서 Fe 또는 Cr 합금원소가 ω 상 형성 또는 변태에 미치는 영향에 대한 연구는 미비하고, 합금화 원소의 증가량에 따른 β 상의 안정성 및 내식성에만 초점을 맞춘 경우가 대부분이다.

따라서 본 연구에서는 β-Ti 합금 내에서 Fe 와 Cr 원소의 함량에 따른 미세조직 변화와 기계적 특성에 미치는 영향에 대해 분석해보고자 한다. 본 연구에서는 상온에서 β 상을 안정적으로 유지하

https://doi.org/10.4150/jpm.2025.00220

기 위해 요구되는 Mo 당량(MoE)이 12가 되도록 유지하였으며 Fe과 Cr의 조성을 변화시켜 합금을 설계하였다. 주조, 단조, 압연 과정을 통해 합금을 판재로 제조하였고, 용체화처리(Solution treatment, ST), 시효 과정에 따른 미세조직을 분석하였으며 비커스 경도 시험을 통해 기계적 특성 변화를 분석하였다.

2. Experimental Section

합금원소 Fe과 Cr의 첨가량에 따른 미세구조 및 경도 특성 변화를 확인하기 위해 Ti-8Cr (8Cr), Ti-3Fe-2Cr (3Fe-2Cr), Ti-4Fe (4Fe) 로 합금 설계 및 제조를 진행하였다. Fe과 Cr의 첨가량은 상온에서 β상을 유지하는데 필요한 임계량 이상으로 설정하였으며, 진공아크용해 기법을 이용하여 500g 규모의 버튼형 잉곳으로 제조하였다. 그림 1(a)과 같이 판재 제조를 위해 열간단조, 열간압연 공정을 진행하였다. 1200℃ 온도에서 예열 한 후 70% 두께 감소율로 열간 단조 하였고, 1100℃ 온도에서 예열 한 후 2 번으로 나누어 50% 두께 감소율로 열간 압연 진행하여 약 4 mm 두께의 판재로 제조하였다. 상온에서도 β상을 유지할 수 있는 용체화처리(Solution Treatment, ST)를 위해 온도 950℃에서 30분 유지 후 수냉 공정을 진행하였고, 광학 현미경을 이용하여 압연 직후와 용체화처리 후의 미세조직을 관찰하였다.

합금의 성분 분석은 ICP-AES와 원소분석기(ONHP, Elatra)를 통해 확인하였고, 미세조직 관찰을 위해 시편을 압연 방향에 수직으로 절단 후 핫마운팅하여 #400~#2400의 SiC paper와 3 μm, 1 μm 다이아몬드 서스펜션을 이용하여 미세 연마하였다. 그 후 85% 증류수(H_2O) + 5% 불산(HF) + 10% 질산(HNO_3) 혼합액으로 에칭하였다. 광학현미경 및 투과전자현미경(Transmission Electron Microscope, TEM, JEM 2100F, JEOL)을 이용하여 합금 원소 함

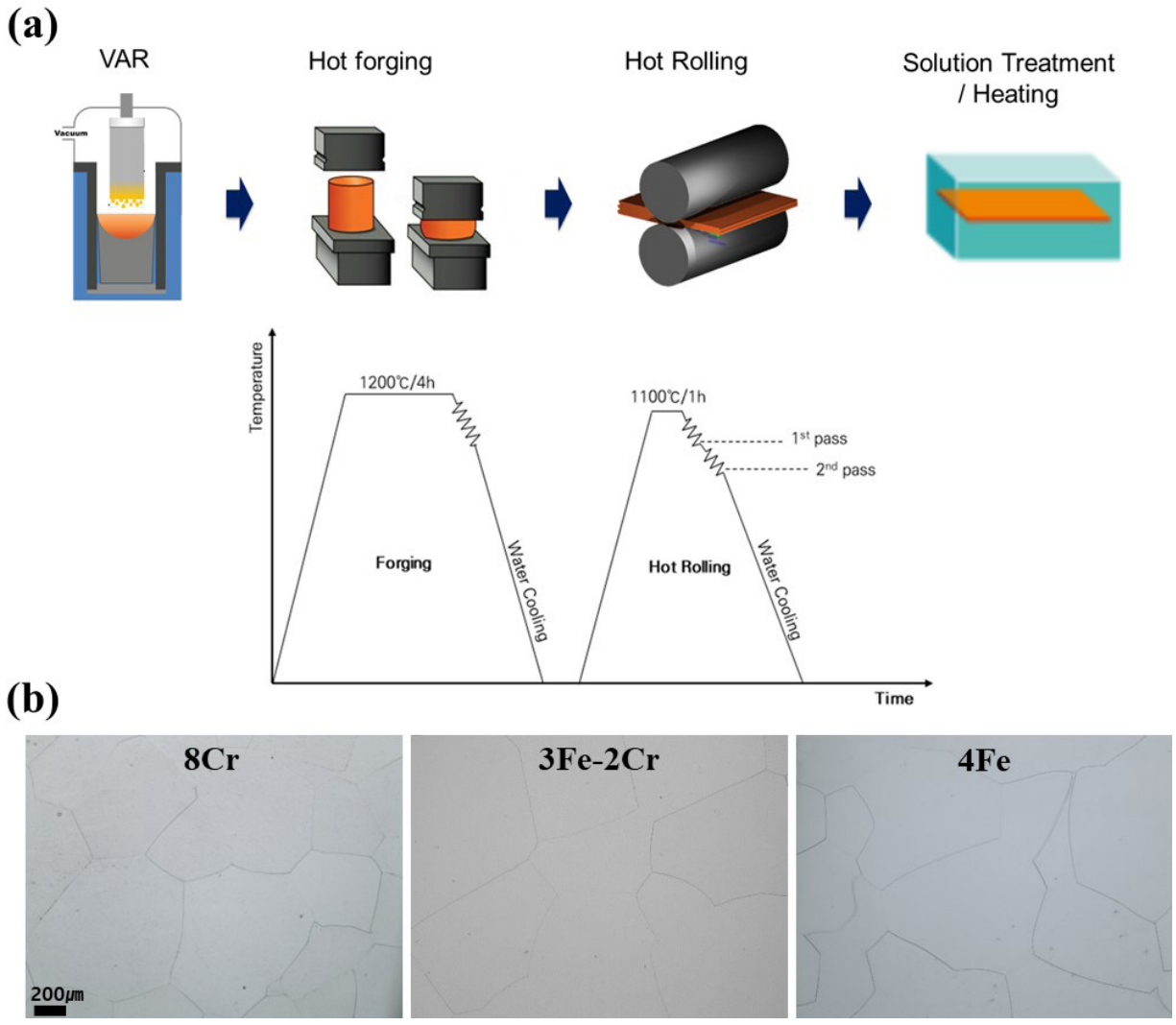

Fig. 1. (a) Schematic illustration of the procedure for fabricating Ti alloy plate (b) Typical optical microscopy images of Ti alloys.

량 변화에 따른 미세조직의 변화를 관찰하였다. 합금의 상 분석은 X선 회절 분석기(X-ray Diffraction, XRD, Empyrean, PANalytical) 를 통해 확인하였다. 또한, 상온에서의 기계적 특성을 평가하기 위하여 비커스 경도시험(Vickers hardness, HM-200, Mitutoyo)을 진행하였다. 비커스 경도시험은 0.2kgf 하중으로 10초 동안 유지하여 20 번 이상 측정하여 평균값을 도출하였다.

3. Results and Discussion

Ti 합금 내 β 상의 안정성은 일반적으로 Mo 당량 (MoE) 지수를 통해 정량화된다[20]. Cardoso와 Ho 등은 상온에서 β 상을 안정적으로 유지하기 위해 요구되는 최소 MoE 값이 약 10임을 보고하였다[3, 21]. 본 연구에서 설계된 Ti 합금은 다음 식 (1)을 기반으로 Fe와 Cr 원소의 중량비를 조절하였고, 표 1과 같이 모든 조성에서 MoE ≈ 12.6이 되도록 설계되었다.

$$\text{MoE (wt.\%)} = \text{Mo}+0.67\text{V}+0.44\text{W}+0.28\text{Nb}+0.22\text{Ta} +2.9\text{Fe}+1.6\text{Cr}+1.25\text{Ni}+1.7\text{Mn} \quad (1)$$

따라서, 본 합금계에서 β 상의 안정성은 강력한 β 안정화 원소인 Fe 및 Cr의 충분한 함량과 용체화 공정을 통해 확보되었으며, 그림 1(b)에서 볼 수 있듯이 모든 합금은 ST 후 평균 결정립 크기 약 363 μm의 등축 정립(equiaxed grains) 구조를 갖는 것을 확인하였다. 정확한 상 분석을 위해 측정한 XRD 분석 결과에 따르면, 그림 2와 같이 모든 Ti 합금에서 β 상이 주요 상으로 존재하는 것을 확인하였으며 β 상의 격자상수는 가장 강한 회절 피크인 β (110)에서의 회절 피크 값을 이용하였고, Bragg 및 구조식으로부터 a = 0.325 ± 0.6 nm로 계산되었다. 이는 ST 후에도 β 상이 안정적으로 유지되고 있음을 나타낸다. 또한, XRD 분석을 통해 β 상 외에 ω 상이 존재함을 알 수 있었고, 피크강도 비율(ω($11\bar{2}\bar{2}$)/β (110))을 비교하였을 때 4Fe 합금은 13.75%, 3Fe-2Cr 합금은 1.9%, 8Cr은 4.12%로 4Fe 합금에서 타 조성에 비해 현저히 많은 양의 ω 상이 존재함을 확인할 수 있었다. Ti 합금의 미세조직 및 상 분석을 보다 정밀하게 파악하기 위해 TEM 측정을 진행하였다. 그림 3에서 볼 수 있듯이 각 Ti 합금의 단일 결정립에서 취득한 선택영역 전자회절 (SAED, Selected-Area Electron Diffraction) 패턴을 통해 ω 상의 존재를 확인하였다[22]. β 상의 [110] zone axis SAED 패턴에서 β의 {112} 면 방향의 1/3 및 2/3 위치에 회절점이 추가로 관찰되며, 이로부터 ω 상이 합금 내에 형성되었음을 알 수 있었다. 강한 회절점(빨간 점선)은 β 상에서 발생하며, 상대적으로 약한 회절점은 서로 다른 결정학적 방향을 갖는 ω 상에 해당한다. 모든 Ti 합금에서 SAED 패턴 내ω 상에 의한 회절 강도가 명확하게 관찰되었으며, 이는 3Fe-2Cr합금과 8Cr 합금의 XRD 패턴에서 ω 상 피크가 뚜렷하게 나타나지 않았음에도 불구하고 합금 내에 ω 상이 형성되었음을 알 수 있다. 그림 3의 녹색 원으로 표시된 ($1\bar{1}00$)ω1 회절점으로부터 얻은 DF-TEM 이미지를 통해 β 상 내에 수 나노 크기의 ω 상 입자들이 분포되어 있는 것을 확인하였으며, XRD 패턴 결과 경향과 같이 3Fe-2Cr 및 8Cr 합금에서보다 4Fe 합금에서 ω 상 관찰이 뚜렷하게 나타났다.

합금 원소 및 첨가량에 따른 ω 상 형성이 기계적 특성에 미치는 영향을 확인하기 위해 실시한 비커스 경도 시험 결과는 그림 4와 같다. 8Cr 합금은 419±5.8 HV의 가장 낮은 경도 값을 나타냈으며, 3Fe-2Cr 합금은 484±3.8 HV, 4Fe 합금은 541±5.7 HV 경도를 나타냈다. 이로부터 Fe 함량 증가에 따라 합금의 경도 값이 뚜렷하게 증가하는 것을 알 수 있다. 또한 선행 연구 중 유사한 베타 안정화도를 갖는 Ti-12Mo 합금의 비커스 경도 값은 약 330HV정도로 Mo보다 Fe 및 Cr 합금에서 더 높은 경도 증가 효과를 주는 것을 알 수 있다[23]. 이러한 강화 거동에는2가지 요인이 있는데, 합금화로부터 나타난 고용 강화 효과 (Solid solution hardnening,

Table 1. Nominal composition (in wt.%) of Ti-Fe-Cr alloys, denoted 8Cr, 3Fe-2Cr, and 4Fe

	Ti	Fe	Cr	O	N	Moeq
Ti-8Cr	Bal.		7.69	0.15	0.001	12.6
Ti-3Fe-2Cr		3.15	2.03	0.16	0.002	12.7
Ti-4Fe		4.29		0.14	0.005	12.6

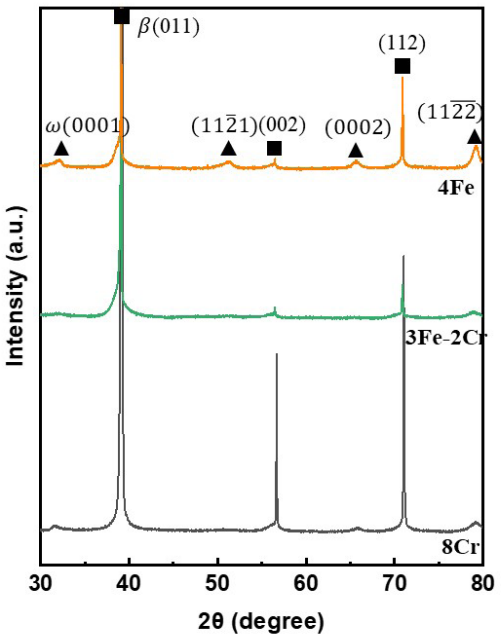

Fig. 2. XRD diffraction profiles of all Ti alloys after ST.

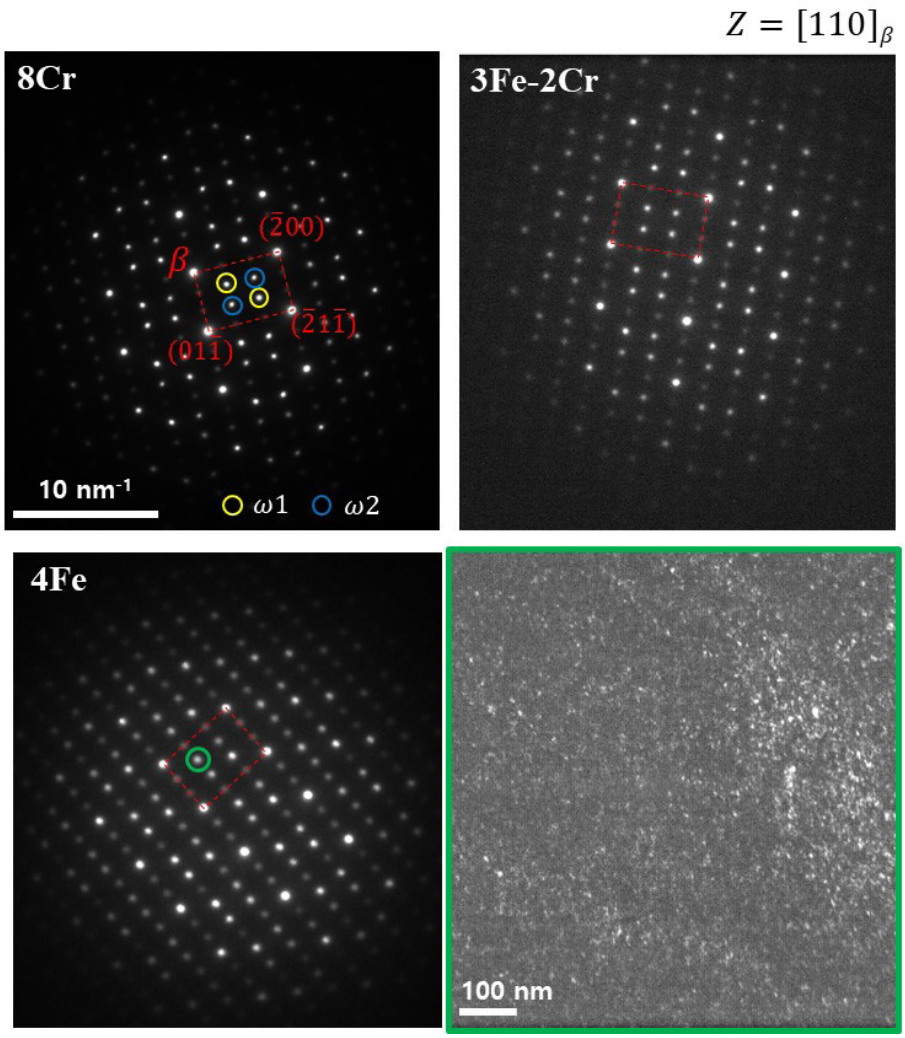

Fig. 3. SAED pattern corresponding [110]β zone axis of Ti alloys after solution-treated at 950°C for 30min followed by water-quenched and dark field image taken using the green circle diffraction spot.

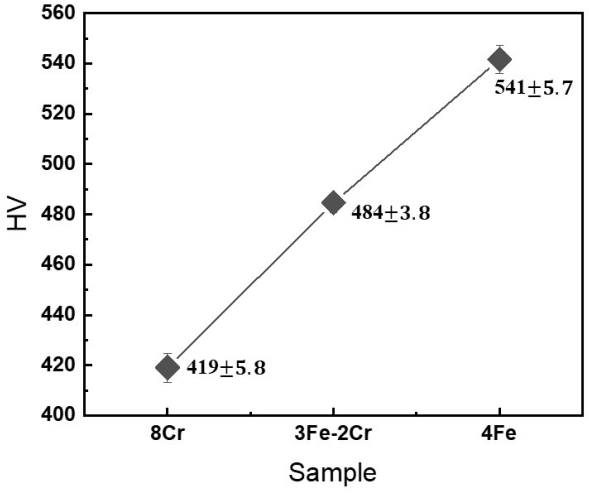

Fig. 4. The Vickers hardness of Ti alloys after ST.

SSH)와 ω 상 석출에 의한 강화 효과가 함께 기여하는 것으로 볼 수 있다. 고용강화효과의 경우, Gypen and Toda-Craballo식을 이용하여 합금화에 따른 수직응력 증가량을 예측해볼 수 있다. 그 결과, 4Fe의 경우 190.9 MPa, 8Cr 의 경우 286.4MPa 로 8Cr 합금에서 고용강화효과가 크게 작용 할 것으로 예상 할 수 있다. 한편, 앞서 XRD 결과(그림 2) 에서 본 것과 같이 4Fe 합금의 XRD 분석에서는 타 합금 대비 강한 ω 상 회절 피크가 나타났으며, 이를 통해 해당 합금에서 더 많은 양의 ω 상이 형성되었음을 알 수 있다. 4Fe 합금에서 가장 높은 비커스 경도를 나타낸 것으로부터 이는 ω 상이 β-Ti 합금 강화 효과에 중요한 요인으로 작용한 것을 알 수 있다. 또한 β 상 안정성 (Mo 당량)이 동일함에도 불구하고 4Fe 합금이 8Cr 합금보다 더 높은 ω 상의 체적 분율(volume fraction)을 갖는 것을 확인하였다. ω 상 형성에 영향을 주는 요인에는 크게 원자 크

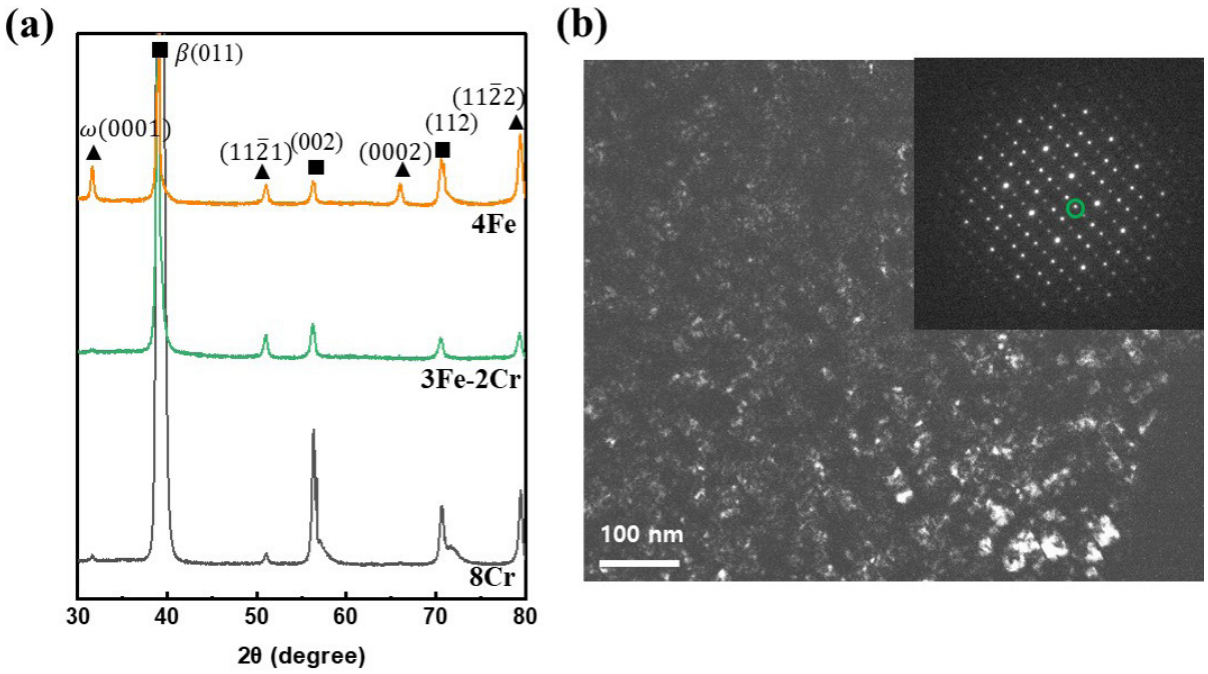

Fig. 5. (a) XRD diffraction profiles of all Ti alloys after aging time of 1hr at 400°C and (b) dark field TEM images of 4Fe alloy after aging time of 1hr at 400°C.

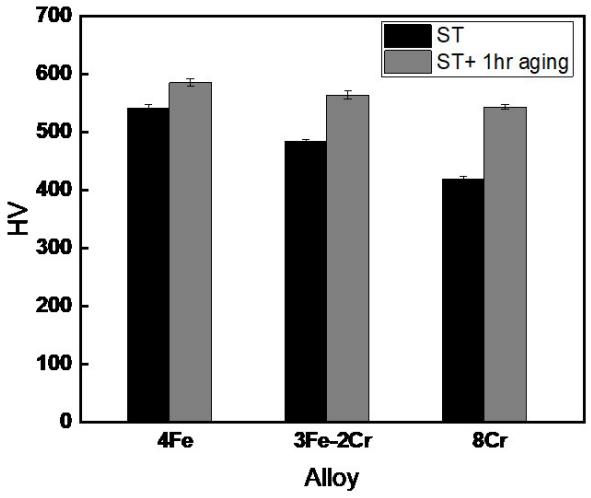

Fig. 6. The Vickers hardness of Ti alloys after ST and aging time of 1hr at 400°C.

기(atomic size)와 전자 구조(electronic effect, e/a)가 있다. 원자 크기의 경우 기지 금속인 Ti 원소와의 원자 크기 차이가 클수록 격자변형 및 응력을 유발하여 ω 상 형성을 촉진시킬 수 있다. Fe와 Cr은 각 126 pm, 128 pm 으로 Ti (147 pm)와 반경차이가 유사하므로 ω 상 형성에 미치는 영향은 유사할 것으로 볼 수 있다. 전자 구조의 경우, 같은 at.% 라고 고려할 때 Fe 원소가 Cr 보다 e/a 값을 두 배 높게 증가시키기 때문에 Fe 원소가 ω 상 형성에 미치는 영향이 클 것으로 예상할 수 있는데, 본 연구에서는 at.% 달리함으로써 e/a 값을 유사하도록 설계하였기 때문에 이 영향 또한 유사하다고 볼 수 있다. 비열적 ω 상은 고온에서 급속 냉각 과정에서 {111} β 면에서 중간 위치로 붕괴되는shuffle mechanism을 통해 생성되는 것으로 알려져 있다 [24-28]. 따라서 8Cr 합금의 경우 ω 상의 형성 과정에서 4Fe 보다 원자 농도가 높기 때문에 합금 내 원자의 이동이 억제되어 이로부터 ω 상의 형성이 억제 된 것으로 볼 수 있다. 결과적으로 4Fe 합금은 같은 원자량 대비 높은 β 안정화 효과를 보여주고 있으며, 4Fe 합금에서 풍부한 ω 상 석출 효과가 나타나며8Cr 합금보다 우수한 경도 값을 나타내었다.

ω 상의 성장 및 기계적 거동 효과를 확인하기 위하여 400˚C에서 1시간 시효처리를 진행하였고, XRD를 이용하여 상 분석을 진행하였다. 그림 5와 같이, 시효 1시간 이후에도 β 상이 주요 상으로 유지되었으며, ST 이후에 비해 ω 상에 해당하는 회절 피크의 세기가 모든 합금에서 월등히 증가한 것으로부터 시효 과정에서 ω 상의 성장 또는 석출 분율이 증가되었음을 알 수 있었다. 또한 TEM 측정을 통해 ω 상 크기가 ST 이후보다 성장한 크기 인 것을 확인하였다. 이에 따른 경도 변화를 확인하고자 하였으며, 그 결과는 그림 6과 같다. ST 이후의 상태와 비교했을 때 모든 합금에서 1시간 시효처리 후 경도가 증가하는 것을 확인하였다. 4Fe가 586±6.5 HV으로 가장 높은 비커스 경도 값을 보였으며 3Fe-2Cr 합금은 564±

7.0 HV 8Cr 합금은 544±3.6 HV 로, 여전히 Fe 함량이 높을수록 경도가 높은 경도값을 나타내는 경향이 나타났다. XRD와 TEM 분석 결과에서 확인한 것과 같이, 이러한 Ti 합금의 강화 현상은 400℃에서의 1시간 시효 처리 동안 ω 상의 성장으로부터 ω 상의 강화 효과가 여전히 효과적으로 작용한 것으로 볼 수 있다.

4. Conclusion

본 연구에서는 Mo 당량을 약 12.6으로 유지한 상태에서 Fe와 Cr의 조성을 달리하여 설계 및 제조된 β-Ti 합금의 미세조직 변화를 분석하고 경도 측정을 진행하였다. 소입(quenching) 과정 중 형성된 것으로 추정되는 ω 상은 모든 Ti 합금에서 관찰되었으며, 특히 Fe만 4 wt.% 첨가된 조성에서 가장 높은 체적 분율의 ω 상이 형성되었다. 이는 모든 합금에서 β 상 안정성이 유사함에도 불구하고 나타난 결과로, Fe원소가 Cr 보다 ω 상 형성에 효과적이며 이는 석출 강화 효과를 유도시켜 가장 높은 비커스 경도를 갖는데 기여하였다. 400℃에서 1시간 시효 처리 시, 모든 Ti 합금에서 ω 상의 크기가 ST 이후보다 증가하는 것을 확인하였다. 그 결과 뚜렷한 경도 강화 효과가 나타났으며 ST와 같이 4Fe합금에서 가장 높은 경도값을 나타내었다. 본 연구를 통해 β 상 안정성이 같더라도 합금화 원소에 따라 ω 상 형성 분율이 달라지며 이러한 미세조직 인자가 경도에 영향을 미침을 확인하였으며, 본 연구는 향후 Ti 기반 분말 합금 설계 또는 적층 제조 설계 시에 합금 원소 변수를 제시하는 기초 연구로 기여 할 수 있을 것으로 예상된다.

Funding

This study was supported in part by Korea Atomic Energy Research Institute R&D program (contract number: 524590-25) funded by the Korean Government (MSIT).

Conflict of Interest

The authors have no conflicts of interest to declare.

Data Availability Statement

All dataset files used in this study are already provided in the manuscript.

Author Information and Contribution

Sun-Young Park: Dr.; Conceptualization, Methodology, Validation, data curation, Investigation, and Writing

Young-Bum Chun: Dr.; Conceptualization, Funding acquisition, Review, and Editing

Acknowledgments

None.

References

[1] R. R. Boyer and R. D. Briggs: JMEP, **14** (2005) 681.
[2] H.-C. Hsu, S.-C. Wu, T.-Y. Chiang and W.-F. Ho: J. Alloys Compd., **476** (2009) 817.
[3] F. F. Cardoso, P. L. Ferrandini, E. S. N. Lopes, A. Cremasco and R. Caram: J. Mechanical Behavior of Biomedical Materials, **32** (2014) 31.
[4] J. D. Cotton, R. D. Briggs, R. R. Boyer, S. Tamirisakandala, P. Russo, N. Shchetnikov and J. C. Fannig: JOM, **67** (2015) 1281.
[5] R. Santhosh, M. Geetha and M. N. Rao: Trans. Indian Institute of Metals, **70** (2017) 1681.
[6] Y. Xu, J. Gao, Y. Huang and W. M. Rainforth: J. Alloys Compd., **835** (2020) 155391.
[7] D. Zhang, Y. F. Mao, Y. L. Li, J. J. Li, M. Yuan and J. G. Lin: Mater. Sci. Eng. A, **559** (2013) 706.
[8] H.-C. Hsu, S.-C. Wu, S.-K. Hsu, W.-H. Kao and W.-F. Ho: Mater. Sci. Eng. A, **579** (2013) 86.
[9] H.-C. Hsu, S.-K. Hsu, S.-C. Wu, C.-J. Lee and W.-F. Ho: Mater. Charac., **61** (2010) 851.
[10] T. Gloriant, G. Texier, F. Prima, D. Laillé, D.-M. Gordin, I. Thibon and D. Ansel: Adv. Eng. Mater., **8** (2006) 961.
[11] Y. Song, D. S. Xu, R. Yang, D. Li, W. T. Wu and Z. X. Guo: Mater. Sci. Eng. A, **260** (1999) 269.
[12] W. Chen, S. Cao, W. Kou, J. Zhang, Y. Wang, Y. Zha, Y. Pan, Q. Hu, Q. Sun and J. Sun: Acta Mater., **170** (2019) 187.
[13] W. Wang, X. Zhang and J. Sun: Phase stability and tensile behavior of metastable beta Ti-V-Fe and Ti-V-Fe-Al alloys. Mater. Charac., **142** (2018) 398.
[14] W.-F. Ho, C. -H. Pan, S.-C. Wu and H.-C. Hsu: J. Alloys Compd., **472** (2009) 546.
[15] W. Xu, K. B. Kim, J. Das, M. Calin and J. Eckert: Scr. Mater., **54** (2006) 1943.
[16] D.-J. Lin, J. C. Lin and C.-P. Ju: J. Mater. Sci. Mater. Medic.,

14 (2003) 1.
[17] D.-J. Lin, J.C. Lin and C.-P. Ju: Biomaterials, **23** (2002) 1723.
[18] H. Yamaguchi, M. Takahashi, K. Sasaki and Y. Takada: Dent. Mater. J., **40** (2021) 61.
[19] B. Gunawarman, M. Niinomia, T. Akahoria, T. Soumaa, M. Ikedac and H. Toda: Mater. Sci. Eng. C, **25** (2005) 304.
[20] R.P. Kolli and A. Devaraj: Metals, **8** (2018) 506.
[21] W. Ho, C. Ju and J. C. Lin: Biomaterials, **20** (1999) 2115.
[22] H. Liu, M. Niinomi, M. Nakai and K. Cho: Acta Mater., **106** (2016) 162.
[23] W. F. Ho, C. P. Ju and J. H. C. Lin: Biomaterials, **20** (1999) 2115.
[24] B. Hickman: J. Mater. Sci., **4** (1969) 554.
[25] S. Hanada and O. Izumi: J. Mater. Sci., **21** (1986) 4131.
[26] D. Moffat and D. Larbalestier: Metall. Trans. A, **19** (1988) 1677.
[27] M. J. Kriegel, A. Kilmametov, V. Klemm, C. Schimpf, B. B. Straumal, A. S. Gornakova, Y. Ivanisenko, O. Fabrichnaya, H. Hahn and D. Rafaja: Adv. Eng. Mater., **21** (2019) 1800158.
[28] D. Lin, J. C. Lin and C.-P. Ju: Mater. Chem. Phy., **76** (2002) 191.

Journal of
Powder Materials

Code of Ethics for the Journal of Powder

Established: 2007. 10. 23

Full Text

First published in April 1994, with the purpose for the revitalization of technical exchange between Academics & Industry in Powder Metallurgy related advanced studies. Journal of Powder Materials is currently published on a bi-monthly basis.

The Korean Powder Metallurgy & Materials Institute has prepared a code of ethics for a qualitative improvement to its journal. We can therefore secure the ethics required for scientific research through this code of ethics; and we intend to raise the value of our journal through the addition of originality and integrity to our journal. Therefore, all authors of theses, review committee members and editorial committee members shall observe this code of ethics in order to reject any dishonesty in the publication of theses and secure the integrity of any research.

Chapter 1. Matters to be observed by the author of thesis

1. The criteria of the authorship

The Author of academic paper means a person who meets all of the following criteria for authorship (based on the criteria of International Committee of Medical Journal Editors). Those who are not satisfied with any of the following criteria shall be divided into “contributor”.

A. Substantial contributions to the conception or design of the work; or the acquisition, analysis, or interpretation of data for the work.
B. Drafting the work or revising it critically for important intellectual content.
C. Final approval of the version to be published.
D. Agreement to be accountable for all aspects of the work in ensuring that questions related to the accuracy or integrity of any part of the work are appropriately investigated and resolved.

2. The duty of the author

The author of thesis shall explain the results and discussions of the research which the author has performed in a concise and accurate manner. When submitting the research results to the Journal of Powder Materials, an author of a thesis shall observe the code of ethics of this institute and conform to the honesty, accuracy and integrity of the research result submitted as such.

A. When submitting a thesis to the Journal of Powder Materials, the author of a thesis shall abide to the code of ethics as outlined by the Journal of Powder Materials
B. The author of a thesis shall reject any fabrication or falsification of the results for conducting all activities including the proposal, planning and execution of the research activities.
C. Submittal or publishing the same result to more than one journal simultaneously shall be regarded as an act of cheating and as such shall be eradicated.
D. The author of a thesis shall not submit and publish research results which were already published to this Journal.
E. An act of submitting another researcher's results under his/her own name shall be deemed as unethical and unacceptable.
F. An author who has submitted a thesis shall obtain proper consent from all existing co-authors and shall not include any inappropriate authors to the thesis. Co-authors shall contribute to the research academically and share the responsibility and achievements for the results altogether, and in the case of administrative and financial support for research, such shall be advised to state details through an "Acknowledgement".
G. An author of thesis shall obtain approval from the person concerned in advance with regards to submission if required, and confirm that there will be no future disputes of agreements and ownership.
H. The author of the thesis shall observe the regulations as provided in relevant laws, norms and as stated in the code of ethics; and to internationally accepted principles of the entire process of research and submission. Also, the author of such thesis shall also secure universality including the respect of human rights, the observation of bioethics, and the preservation of biological diversity and protection

for environments.

I. In the case of an error discovered in a submitted thesis during the publication process, the author of such thesis shall be obligated to correct any mistakes or withdraw the thesis altogether.

Chapter 2. Matters to be observed by the reviewer

The journal reviewer shall review a submitted thesis in compliance with this code of ethics and provide advice in regards to the publication of such thesis to the editorial committee members.

A. The journal reviewer shall review a submitted thesis fairly and objectively under consistent standards regardless of ethnicity, gender, religion, educational environment or acquaintance of the author of thesis.

B. The journal reviewer shall be obligated to review a thesis requested for review faithfully within the set period as determined in the review regulations.

C. The journal reviewer shall not disclose the information of the research results acquired through the review process to any third party or misuse such information.

D. The journal reviewer shall respect the personality of the author of the thesis and value the independence of intellectual ability. The journal reviewer shall prepare an amicable and supplementary written opinion without making subjective evaluations and shall avoid hostile expressions.

E. The journal reviewer shall request the author of the thesis to modify any inappropriate quoted contents and lead the author to quote references correctly. Also, the journal reviewer shall strictly review the thesis to determine is such has any similarity with previous published manuscripts that were presented in other publications.

F. The journal reviewer shall be obligated to reject review in the case of having any connection with the submitted thesis. The journal reviewer shall promptly notify such fact to the editorial committee members to appoint another journal reviewer.

Chapter 3. Matters to be observed by the editorial committee member

The editorial committee member shall retain full responsibility and authority to carry out the procedures to approve or reject a submitted thesis for publication in the journal. Each editorial committee member shall cooperate with the journal reviewer and other editorial committee members shall observe and carry out the following items.

A. The editorial committee member shall fairly evaluate the intellectual level of a thesis as submitted by the author regardless of ethnicity, gender, religion, educational environment or acquaintance of the author of a thesis.

B. The editorial committee member shall not delay the screening of a submitted thesis intentionally and shall perform prompt measures accordingly.

C. The editorial committee member shall screen the submitted thesis objective based on consistent standards, and the editorial committee member shall assume full responsibility and obligation for the required procedures.

D. The editorial committee member shall not release information regarding the submitted thesis to the public and shall not use such information for his/her own research purposes.

E. The editorial committee member shall be obligated to supervise any unethical behavior in a thesis submitted to the journal, and take any necessary measures for any wrongful acts. In the case of an appeal for wrongful acts, the editorial committee member and the review committee shall be obligated to investigate such matters.

F. The editorial committee member shall be obligated to reject screening in the case where editorial committee has written the thesis, or such has any connection with the submitted thesis. Another editing committee member shall be appointed for the screening process.

Chapter 4. Activities of the review committee

A. Clarifying integrity and responsibility of the research results – In the case where cheating has occurred, including plagiarism, duplicated submission or inappropriate citation is suspected, an investigation shall be carried out based on the editorial committee members recommendation The author of such thesis shall be responsible for any cheating including plagiarism, fabrication and falsification and duplicated presentation of the result.

B. In the case where any cheating is suspected in the process of a thesis submission and review, the editorial committee member shall submit such to the review committee and

request the review committee to investigate such in private. The review committee shall then carry out an inspection in compliance with the following guidelines to ensure that no victim shall suffer in good faith.

1. The review committee shall observe "the principle of presumption of innocence" until such is proven to be a wrongful act.
2. The review committee shall begin and perform such inspection fairly and without discrimination in private circumstances.
3. The review committee shall prepare, arrange and store documents in regards to the investigation.
4. The review committee shall suspend all process in regards to the thesis publication.
5. The review committee shall carry out an investigation promptly to reduce any damages due to delay.

C. The review committee shall carry out an investigation promptly and fairly at the editorial committee member's request. The investigation shall notify, carry out and finish based on the following guidelines.

1. The review committee shall notify any beginning of an investigation to the person or organization concerned that is questionable for cheating and also inform such as to any postponing of the publication of such thesis until the investigation is complete.
2. The review committee shall provide an opportunity for explanation to the person or organization subject to investigation within 30 days of written notice.
3. The review committee shall acquire and investigate any internal records or other publications related with cheating.
4. In the case of unintended mistakes or errors, the review committee shall finish the investigation promptly.
5. In the case where cheating is discovered, the review committee shall supervise measures for such cheating. The review committee shall return the submitted thesis to the author, notify the Institute's guideline to the author, remove or publish the withdrawal of the thesis in the case where such was already published, and restrict the author's thesis publication for 3 years afterwards.
6. In the case of a duplicated submission and publication with a joint publisher, such actions shall be notified to the relevant publisher and handled in conjunction with the relevant publisher.
7. All cases and investigations carried out by the review committee shall be documented and stored. In cases where cheating is not apparent, the relevant document shall be sealed.

Supplementary Provision

1. This code of ethics shall be in effect from October 23, 2007.
2. This Revised code of ethics shall be in effect from March 6, 2020.
3. This Revised code of ethics shall be in effect from February 10, 2022.

Journal of
Powder Materials

Journal of Powder Materials Research Misconduct-Related Regulations

Enacted: June 17, 2016

Chapter 1 General Provisions

1. Purpose

The purpose of this guide is to strengthen research ethics by setting the standards, operation, and discipline of research

2. Ethics Committee

① The ethics committee of The Korean Powder Metallurgy & Materials Institute will be formed to deliberate and decide on the regulations.

② The chair of the Research Ethics Committee shall be the Editor-in-chief of The Korean Powder Metallurgy & Materials Institute Committee. The chair convenes and presides over the Research Ethics Committee when the Editorial Committee proposes an issue as regards research misconduct.

③ The Research Ethics Committee shall consist of no more than five members. The committee members are appointed by the president of the society after the recommendation of the Editorial Committee.

Chapter 2 Research Misconduct

3. Subject of Research Misconduct

Research misconduct is directed to articles, documents, and data submitted or published to the Journal of Powder Materials.

4. Simultaneous Submission

Submitted papers may not be submitted to other domestic or foreign academic journals simultaneously, or as a duplicate, regardless of whether it is submitted beforehand or afterwards.

5. Duplicated Publication

① Dissertations published in other domestic or foreign academic journals may not be duplicated.

② When submitting a research report or a part of a doctoral or a master's thesis as it is, or if it is corrected or supplemented, the correct description must be clearly stated.

6. Plagiarism

① Plagiarism is the act of deliberate description of the content of academic ideas, opinions, expressions, and research results already published through all written media, including domestic or foreign journals, academic papers, research reports, master's or doctoral dissertations, books, magazines, and the internet without reference to the source.

② Plagiarism also applies when the researcher is the same as the author of the paper already published (self-plagiarism). However, it is not considered plagiarism if it describes widely used academic knowledge or research results without citation./td >

Forgery and Falsification Forgery or falsification involves the act of intentionally expressing, among others, numerical values and photographs of the data or results used in the research differently from the truth.

1. Forgery is the act of untruthful creation of false data or research results that do not exist.
2. Falsification refers to the act of artificial manipulation of research materials, equipment, processes, or distorting research contents or results by modifying or deleting data arbitrarily.

Chapter 3 Deliberation and Resolution Procedures

8. Judgment of Research Misconduct

① If there is a report on research misconduct within or outside the institute, the chair of the Editorial Committee must convene the committee to collect relevant data and confirm the credibility of the report.

② When the chair of the Editorial Committee confirms the authenticity of the report, he/she will submit the document of issue to the Research Ethics Committee.

③ The chair of the Research Ethics Committee gives the researcher an opportunity to document the proposed issues within two weeks in advance of the hearing..

④ The Research Ethics Committee shall make a unanimous

decision on whether there has been a case of research misconduct. If there is a disagreement between the two parties, it shall be decided by a vote of 3/5 of the attending committee members.

9. Discipline and Result Processing

① A person who violates research ethics shall be subject to and notified of a disciplinary action through the following measures:

1. Member expulsion
2. Prohibition of contributing to the Journal of Powder Metallurgy
3. If the article is published, the article will be deleted. Papers that are scheduled to be published cannot be published.
4. Relevant organizations will be notified of ethics violations.
5. Other disciplinary actions that are deemed necessary

② The content of the violated research ethics shall be posted on the homepage after a two-week protest period.

③ The contents of the disciplinary action in Items 2, 3, and 5 of Clause 1 shall be notified in the name of the editor-in-chief after the decision of the Research Ethics Committee. The contents of disciplinary action in Items

10. Objection

① A researcher who is judged for a research misconduct may file an objection only once within one month from the date of notification, if the decision of the Research Ethics Committee or the reason for misconduct is unreasonable.

② The Research Ethics Committee can review or revise the contents of the resolution by deliberating the validity of the objection.

Supplement

1. Amendment, Opening, and Closing of Regulations

This regulation may be amended, opened, or closed through the resolution of the Board of Directors.

2. Effective Date

1. This regulation shall be effective beginning on the date of the Board of Directors' approval (June 17, 2016).
2. This Revised code of ethics shall be in effect from February 10, 2022.

Written Oath of Observance of Research Ethics

Journal of
Powder Materials

Article title: _____

_____

Author name: _____

To Editor-in-chief of the Journal of Powder Materials

I, as a contributor to the Journal of Powder Materials, hereby declare that I have abided by the following Code of Research Ethics of The Korean Powder Metallurgy & Materials Institute while writing this article.

1. I swear that I shall observe The Korean Powder Metallurgy & Materials Institute's Research Ethics Code and regulations related to research misconduct, and have written this article through honest and rigorous research.
2. I swear that I have not published this article elsewhere and have no plan to submit this article in other journals until the deliberation is over.
3. I swear that I have not committed any research misconducts that can be defined as a violation of Research Ethics, such as forgery (falsification), alteration, plagiarism, duplicate publication, etc., that compromises academic integrity.
4. I swear that I acknowledge the legitimate efforts of participating researchers and did not make unreasonable authorship of those who have not contributed to the research.
5. I swear that I shall take full responsibility for all problems and disadvantages that may arise from noncompliance with the Research Ethics if found guilty of any of the above-mentioned research misconducts.

All authors must sign this Written Oath of Observance of Research Ethics, but in case of necessity, the correspondent author can obtain the consent of other authors and replace them.

All Authors:

_____ _____

Signature Date Signature Date

_____ _____

Signature Date Signature Date

One author on behalf of all co-authors:
"I warrant that I am authorized to execute this copyright on behalf of all the authors of the article referred to above."

Instructions for authors

Journal of
Powder Materials

The Korean Powder Metallurgy & Materials Institute, founded in 1994, is a research journal that primarily aims to publish original research papers on a bi-monthly basis.

1. Forms and contents of publication

- Original Papers: This form of publication represents original research articles on various aspects of powder metallurgy, namely fabrication, characterization, and forming of metal powders for advanced industrial applications.
- Letters or Rapid Communications: Short reports of original researches are accepted for publication.
- Critical Reviews or Reports : Invited or submitted review papers and technical reports are accepted.

The journal overall serves as a much-desired international platform for publications of wide researches in materials science. The emphasis, however, has been given on originality and quality of the paper rather than quantitative research. Short reports on material development, novel process or properties are also welcome. The following list of topics is of particular interest to the journal: (1) Powder fabrication techniques, (2) Characterization, (3) Compaction and sintering methods, (4) Heat treatment processes in powder metallurgy, (5) Industrial application of powders, (6) Powder process control, (7) Particle modification, (8) Particle motion and rheology, and (9) Particle growth.

2. Submission of papers

1) Manuscript should be submitted online at the KPMI homepage (http://www.kpmi.or.kr) or e-mail to the KPMI (journal@kpmi.or.kr)
2) File type: MS Word files according to instructions below. Pictures and photos should be submitted in JPG or TIFF format (300 dpi).
3) Prior to publications: Submitted manuscript must not previously been published in a journal and it is not being simultaneously considered for publication elsewhere.

3. Preparation of manuscripts

1) All papers should be written in English and SI units should be used throughout. Abbreviations should be defined the first time they occur in manuscript. Manuscripts should be typed on a paper of A4 format with 2.5 cm margins (right, left, top, bottom), and double-spaced, using Times Roman 11 font.

2) Structure of the manuscript:
The Title : The tile should be carefully chosen to indicate as clearly as possible the subject of the manuscript. The first letter of each word should begin with a capital letter except for articles, conjunctions, and preparations. The first word after a hyphen should also be capitalized such as "Variation of Magnetic Properties of Nd-Fe-B Sintered Magnets with Compaction Conditions".

Bylines should include all those who have made substantial contributions to the work. The first author should be the major contributor of the work. All authors' names should be written in full. At least one author should be designated with a sign as the corresponding author.

Affiliations should include the following information in the order of Institute, Department, City, Zip Code, and Country.

Abstract and Keywords : Each paper should include 120~200 words abstract and five key words for use in indexing.

3) Text: Description headings should be used to divide the paper into its component parts as below.

1. Introduction
2. Experimental
3. Results & Discussions
4. Conclusions

Acknowledgement (This is author's option.)
References
List of Table and Figure captions
Tables and Figures

4) References:
References should be indicated in the text by consecutive numbers in square parentheses, e.g. [1, 2, 5-7], as a part of the text, the full reference being cited at the end of the text. References should contain all the names of the authors together with their initials, the title of the journal, volume number (Bold type), year and the first page number as below. References to books should contain the names of the authors, the title (the names of

editors), the publisher name, location and year as below.

[1] J. D. James, B. Wilshire and D. Cleaver: Powder Metall., 33 (1990) 247.
[2] I. H. Moon: J. Korean Powder Metall. Inst., 1 (1991) 66.
[3] H. E. Exner and G. Petzow: Sintering and Catalysis, G. C. Kuczynski (Ed.), Plenum Press, New York (1976) 279.
[4] D. R. Dank and D. A. Koss: High Temperature Ordered Intermetallic Alloys, C. T. Liu (Ed.), MRS Symp. Proc. Vol. 133, Pittsburg, PA (1989) 561.
[5] Daido Steel: USA, US 5,193,607 (1993).
[6] M.G.Kim and J.H.Kim: Korea, KR 0041070 (2010).
[7] Germany: DIN EN ISO 11876N, Hardmetals.
[8] ASTM B213:03, Standard Test Method for Flow Rate of Metal Powders.
[9] J. C. Kim: M.S. Thesis, Title of Dissertation, Daehan University, Seoul (2011) 123.
[10] J. C. Kim: Ph. D. Dissertation, Title of Dissertation, Hankook University, Seoul (2011) 123.

5) Tables and Figures

Tables: type each table on the separate page, number consecutively in Arabic numerals and supply a heading. Figures for best results submit illustrations in the actual size (300 dpi) at which they should be published. The line drawings and the photographs should be originals and sharp images, with somewhat more contrast than is required in the printed version. Each figure should be typed on a separate page. The figure captions must be included.

6) Equations

Equations are placed must be clearly printed and numbered sequentially with Arabic numbers enclosed with round parentheses at the right-hand margin.

$$Ex)f = f\infty + (f0 - f\infty)\exp(-\gamma r/\gamma \tilde{} r) \quad (1)$$

4. Peer-review

All manuscripts are treated as confidential. They are peer-reviewed by at least 3 anonymous reviewers selected by the editor. Letters to the editor are reviewed and published on the decision of the editor. The corresponding author is notified as soon as possible of the editor's decision to accept, reject, or request revision of manuscripts. When the final revised manuscript is completely acceptable according to the KPMI format and criteria, it is scheduled for publication in the next available issue. Rejected papers will not be peer-reviewed again.

5. The accepted manuscript

1) Copyright:

Upon acceptance of a paper, the author(s) will be asked to transfer the copyright of the paper to the publisher, The Korean Powder Metallurgy & Materials Institute. This transfer will ensure the widest possible dissemination of the information.

2) Proofs:

Proofs will be sent to the corresponding author for checking before publication and will not be returned to the author, unless requested otherwise. Only typographical errors may be corrected. Any substantial alterations other than these may be charged to the author. All joint communications must indicate the name and full address of the author to whom proofs should be sent.

3) Reprints:

The authors are entitled to 50 reprints or a PDF file of the article without additional charge, but are charged for additional reprints exceeding 50 in addition to the nominal publication charge.

4) Publication charge:

The publication fee is US$200 up to 6 pages, and US$30 per additional page regardless of a member or a non-member. Additional fee for acknoledgement is US $100. For color printings, US$100 per color page is charged to authors regardless of the membership.

6. Code of ethics

We can secure the ethics required for scientific research through this code of ethics; and we intend to raise the value of our journal through the addition of originality and integrity to our journal. Therefore, all authors of theses, review committee members and editorial committee members shall observe this code of ethics in order to reject any dishonesty in the publication of theses and secure the integrity of any research. For the policies on the research and publication ethics not stated in this instructions, International standards for editors and authors (http://publicationethics.org/international-standards-editors-and-authors) can be applied.

Copyright transfer agreement

Journal of
Powder Materials

Article No: _____

Article Title: _____

_____

By: _____

It is hereby agreed that the copyright of the above article is transferred to The Korean Powder Metallurgy & Materials Institute. However, the author(s) reserves the following:

1. All proprietary rights other than copyright, such as patent rights.
2. The right to reuse all or part of this article in other works.
3. The right to use the article for the author's personal use provided the copies are not offered for sale.

All Authors:

_____ _____

Signature Date Signature Date

_____ _____

Signature Date Signature Date

One author on behalf of all co-authors:

"I warrant that I am authorized to execute this copyright on behalf of all the authors of the article referred to above."

signaturedate signaturedate

_____ _____

Signature Date Signature Date

This document must be signed by author(s) and be received by the production office before the article can be processed for publication. Please mail this document to the following address:

The Korean Powder Metallurgy & Materials Institute
Unit 706, (635-4, Yeoksam-Dong) 22, 7Gil,Teheran-Ro, Gangnam-Gu, 135-703 Seoul, Korea

Checklist

Journal of
Powder Materials

☐ 제목과 저자명, 저자 소속을 정확하게 확인하였습니다.

☐ 교신저자를 기호로 구분되어 표기하였으며, E-mail 주소와 연락처를 정확하게 표기하였습니다.

☐ Keyword는 학회지에 규정한 Keyword list에서 선정하여 정확하게 확인하였습니다.

☐ 그림과 그림설명이 잘 매치 되었는지 정확하게 확인하였습니다.

☐ 참고문헌은 한국분말재료학회지 작성 규정에 따라 정확하게 작성되었습니다.

☐ The paper title, authors' names, and authors' affiliations have been confirmed to be accurate.

☐ The corresponding author has been distinguished using symbol(s), and e-mail address(es) and contact number(s) have been indicated accurately.

☐ The keywords have been selected from the keyword list determined by the Journal and confirmed to be accurate.

☐ The figures and their captions have been confirmed to be matched accurately.

☐ The reference materials have been drawn up accurately according to the paper guidelines of the Journal of Powder Materials.

2025년도 임원명단

Journal of
Powder Materials

직 위	성 명	소 속
회장	김진천	울산대학교
수석부회장	이기안	인하대학교
대외협력부회장	이정구	한국재료연구원
학술부회장	홍순직	공주대학교
기술부회장	류성수	한국세라믹기술원
산업체부회장	이병윤	㈜창성
감사	김정곤	인천대학교
	장시영	한국항공대학교
편집위원장	김경태	한국재료연구원
편집이사	김정한	한밭대학교
	박귀일	경북대학교
	양민호	단국대학교
	이석재	전북대학교
	최현주	국민대학교
편집간사	강정신	서울대학교
	김정준	고등기술연구원
	박정민	한국재료연구원
	박태주	한양대학교
	배재웅	국립부경대학교
	변종민	서울과학기술대학교
	손석수	고려대학교
	신세은	순천대학교
	안창의	한국세라믹기술원
	양승민	한국생산기술연구원
	이 빈	경희대학교
	이동주	충북대학교
	조승기	한국재료연구원
	최병준	서울과학기술대학교
학술이사	강석훈	한국원자력연구원
	공만식	고등기술연구원
	노기민	한국지질자원연구원
	임경묵	한국생산기술연구원
	백연경	한국재료연구원
	이재범	충남대학교
	임효령	국립부경대학교
	채홍준	고등기술연구원
학술간사	김용주	국민대학교
	이지운	공주대학교
	정다운	한국생산기술연구원
	주수현	단국대학교
국제위원장	이창규	한국원자력연구원

직 위	성 명	소 속
국제이사	김범성	한국생산기술연구원
	류호진	KAIST
	안병민	아주대학교
	이근재	단국대학교
	이정구	울산대학교
국제간사	성효경	국민대학교
기술이사	김세훈	한국자동차연구원
	김영무	국방과학연구소
	박지환	엠티아이지
	윤중열	한국재료연구원
	이성희	목포대학교
	최한신	지아이텍
	황병철	서울과학기술대학교
기술간사	김연철	이화다이아몬드공업㈜
	김지원	고등기술연구원
	김충수	한국생산기술연구원
	정효연	한국생산기술연구원
	차희령	한국재료연구원
대외협력이사	강민철	3D프린팅연구조합
	박만호	㈜아스플로
	박진경	LG이노텍
	송인혁	한국재료연구원
	이찬기	고등기술연구원
	천영범	한국원자력연구원
	홍현선	성신여자대학교
대외협력간사	김영균	한국재료연구원
	이동근	순천대학교
	한준희	한국생산기술연구원
“지역이사 (지부장)”	권세훈	경상지부장 : 부산대학교
	김경훈	강원지부장 : 한국생산기술연구원
	오익현	호남지부장 : 전남테크노파크
	이진규	충청지부장 : 공주대학교
	현승균	경인지부장 : 인하대학교
지역간사	고원석	경인지부 : 인하대학교
	김태훈	호남지부 : 전남대학교
	양승민	강원지부 : 한국생산기술연구원
	엄두승	제주지부 : 제주대학교
총무이사	박경태	한국생산기술연구원
	이영인	서울과학기술대학교
총무간사	김태훈	한국재료연구원
	이 빈	경희대학교
	최상훈	고등기술연구원
	최현주	국민대학교
재무이사	변종민	서울과학기술대학교
	양상선	한국재료연구원
재무간사	송명석	한국생산기술연구원
	정재원	한국재료연구원

제16대 평의원

성 명	소 속	성 명	소 속	성 명	소 속
강 철	한라스택폴㈜	박귀일	경북대학교	이규수	MS가스
강두홍	(주)아스플로	박기봉	㈜엠케이	이근재	단국대학교
강민철	3D프린팅연구조합	박동규	경상대학교	이기안	인하대학교
강석중	KAIST	박만호	㈜아스플로	이동주	충북대학교
강석훈	한국원자력연구원	박성진	포스코홀딩스	이민하	한국생산기술연구원
고원석	인하대학교	박원욱	인제대학교	이민호	버추얼랩
공만식	고등기술연구원	박은수	서울대학교	이병윤	(주)창성
구용모	㈜창성	박은수	㈜이엠엘	이상관	한국재료연구원
권세훈	부산대학교	박정민	한국재료연구원	이석재	전북대학교
권영순	울산대학교	박정환	대광소결금속	이선영	한양대학교
권영태	한국재료연구원	박정효	국방과학연구소	이성모	HD현대중공업
김 폴	코오롱 미래기술원	박종관	㈜삼한	이성희	국립목포대학교
김경태	한국재료연구원	박지환	MTIG	이영인	서울과학기술대학교
김경훈	한국생산기술연구원	박진경	LG이노텍	이완재	한양대학교
김기범	세종대학교	박희동	이화다이아몬드공업㈜	이원식	한국생산기술연구원
김기한	용인전자(주)	백연경	한국재료연구원	이재범	충남대학교
김대현	(주)풍산홀딩스	백운형	한국전자재료	이재성	한양대학교
김덕주	하나테크	변종민	서울과학기술대학교	이정구	한국재료연구원
김동환	(주)성림첨단산업	석명진	강원대학교	이정구	울산대학교
김득중	성균관대학교	설재복	경상국립대학교	이지운	공주대학교
김범성	한국생산기술연구원	성효경	국민대학교	이진규	공주대학교
김병기	자화전자	손석수	고려대학교	이찬기	고등기술연구원
김상훈	산업연구원	손인진	전북대학교	이창규	한국원자력연구원
김세훈	한국자동차연구원	손현택	한국생산기술연구원	이학성	동아대학교
김신경	신한다이아몬드공업㈜	송광호	한국분말야금㈜	임경묵	한국생산기술연구원
김양도	부산대학교	송승철	한국회가내스㈜	임중경	대신강업주식회사
김영도	한양대학교	송용설	(주)아모그린텍	임효령	국립부경대학교
김영립	KAMI㈜	송인혁	한국재료연구원	장시영	한국항공대학교
김영무	국방과학연구소	신 훈	㈜아이피티	장태석	선문대학교
김용진	한국재료연구원	신광섭	일진다이아몬드공업㈜	정영근	부산대학교
김우종	(주)대건테크	신세은	순천대학교	정임두	울산과학기술원
김정곤	인천대학교	안동길	대구텍㈜	정재원	한국재료연구원
김정기	경상국립대학교	안병민	아주대학교	정형식	아주대학교
김정한	한밭대학교	안상호	포항산업과학연구원	조권구	경상국립대학교
김종렬	한양대학교	안인섭	경상국립대학교	조승기	한국재료연구원
김주용	리프로텍	안중호	안동대학교	조영철	현대자동차
김지순	울산대학교	안창의	한국세라믹기술원	좌용호	한양대학교
김진천	울산대학교	양동열	한국재료연구원	채홍준	고등기술연구원
김충수	한국생산기술연구원	양민호	단국대학교	천병선	충남대학교
김태규	한국원자력연구원	양상선	한국재료연구원	천영범	한국원자력연구원
김태훈	한국재료연구원	양승민	한국생산기술연구원	최병준	서울과학기술대학교
김택수	한국생산기술연구원	오승탁	서울과학기술대학교	최준필	한국기계연구원
김형섭	포항공과대학교	오왕근	(주)양우메탈	최한신	지아이텍
김홍물	하나에이엠티	오익현	전남테크노파크	최현규	현대제철

성 명	소 속	성 명	소 속	성 명	소 속
김효섭	한국생산기술연구원	유봉영	한양대학교	최현주	국민대학교
김휘준	한국생산기술연구원	유지훈	한국재료연구원	한유동	한국재료연구원
김희수	월드인덕션	윤덕용	KAIST	현승균	인하대학교
노기민	한국지질자원연구원	윤준철	현대제철	홍순직	공주대학교
류성수	한국세라믹기술원	윤중열	한국재료연구원	홍순형	KAIST
류시완	㈜풍산홀딩스	윤태식	대신강업㈜	홍현선	성신여자대학교
류호진	KAIST	은광용	㈜기술과가치	황득규	현대모비스㈜
박 준	제이피씨㈜	이 빈	경희대학교	황병철	서울과학기술대학교
박경태	한국생산기술연구원	이 성	국방과학연구소 민군협력진흥원		

본 학회지는 한국연구재단의 평가결과 등재학술지로 선정되었습니다.

"본 사업은 기획재정부의 복권기금 및 과학기술정보통신부의 과학기술진흥기금으로 추진되어 사회적 가치 실현과 국가 과학기술 발전에 기여합니다."